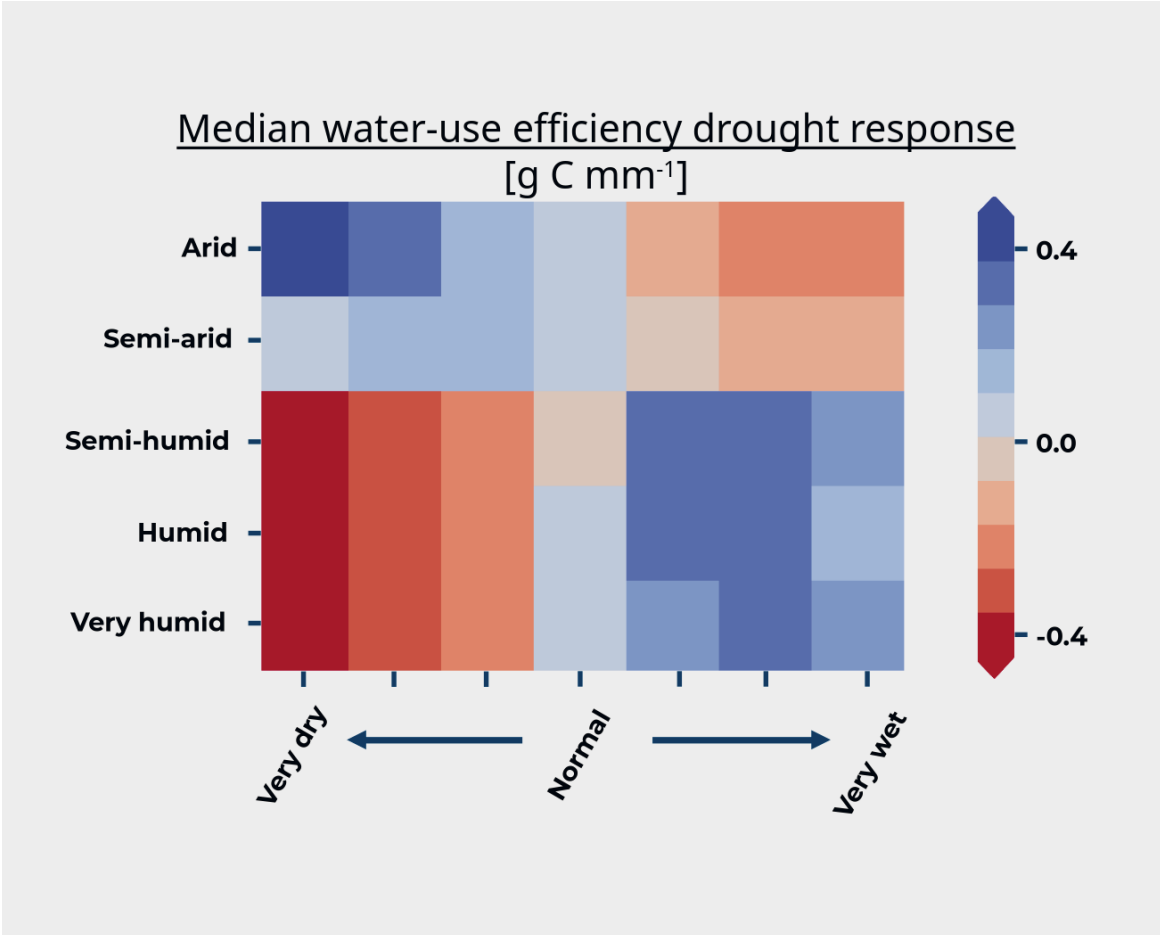

Drivers of spatiotemporal variability of European terrestrial ecosystem processes

Christian Poppe Terán

Energie & Umwelt / Energy & Environment
Band / Volume 705
ISBN 978-3-95806-905-3

Mitglied der Helmholtz-Gemeinschaft

JÜLICH
Forschungszentrum

Schriften des Forschungszentrums Jülich
Reihe Energie & Umwelt / Energy & Environment Band / Volume 705

Forschungszentrum Jülich GmbH
Institut für Bio- und Geowissenschaften (IBG)
Agrosphäre (IBG-3)

Drivers of spatiotemporal variability of European terrestrial ecosystem processes

Christian Poppe Terán

Schriften des Forschungszentrums Jülich
Reihe Energie & Umwelt / Energy & Environment Band / Volume 705

ISSN 1866-1793 ISBN 978-3-95806-905-3

Bibliografische Information der Deutschen Nationalbibliothek.
Die Deutsche Nationalbibliothek verzeichnet diese Publikation in der
Deutschen Nationalbibliografie; detaillierte Bibliografische Daten
sind im Internet über http://dnb.d-nb.de abrufbar.

Herausgeber und Vertrieb:	Forschungszentrum Jülich GmbH Zentralbibliothek, Verlag 52425 Jülich Tel.: +49 2461 61-5368 Fax: +49 2461 61-6103 zb-publikation@fz-juelich.de www.fz-juelich.de/zb
Umschlaggestaltung:	Grafische Medien, Forschungszentrum Jülich GmbH
Druck:	Grafische Medien, Forschungszentrum Jülich GmbH
Copyright:	Forschungszentrum Jülich 2026

Schriften des Forschungszentrums Jülich
Reihe Energie & Umwelt / Energy & Environment, Band / Volume 705

D 82 (Diss. RWTH Aachen University, 2025)

ISSN 1866-1793
ISBN 978-3-95806-905-3

Vollständig frei verfügbar über das Publikationsportal des Forschungszentrums Jülich (JuSER)
unter www.fz-juelich.de/zb/openaccess.

Summary

This thesis investigates the variability of ecosystem processes—gross primary production (GPP), evapotranspiration (ET), and water-use efficiency (WUE)—in Europe under climate change, with a focus on their trends and responses to droughts from 1995 to 2018. The work uses three complementary data sources: satellite-based remote sensing, in situ eddy covariance observations (ICOS), and land surface model simulations with CLM5. The thesis is structured around three main studies.

Study 1 (Chapter 3): Water-use efficiency is the amount of carbon assimilated per water used by an ecosystem and a key indicator of ecosystem functioning, but its variability in response to climate change and droughts is not thoroughly understood. Here, we investigated trends, drought response and drivers of three water-use efficiency indices from 1995 – 2018 in Europe with remote sensing data that considered long-term environmental effects. Inherent water-use efficiency decreased by -4.2% in Central Europe, exhibiting threatened ecosystem functioning. In European grasslands it increased by +24.2%, by regulated transpiration and increased carbon assimilation. Further, modulation of water-use efficiency drought response by hydro-climate and the importance of adaptive canopy conductance on ecosystem function is highlighted. These results imply that decoupling carbon assimilation from canopy conductance and efficient water management strategies could make the difference between threatened and well-coping ecosystems with ongoing climate change, and provide important insights for land surface model development.

Study 2 (Chapter 4): Evapotranspiration (ET) and gross primary production (GPP) are critical fluxes contributing to the energy, water, and carbon exchanges between the atmosphere and the land surface. Land surface models such as the Community Land Model v5 (CLM5) quantify these fluxes, estimate the state of carbon budgets and water resources, and contribute to a better understanding of climate change's impact on ecosystems. Past studies have shown the ability of CLM5 to model ET and GPP magnitudes well but emphasized systematic underestimations and lower variability than in the observations. CLM5's predictions of water and energy fluxes are evaluated using observations from eddy covariance stations from the Integrated Carbon Observation System (ICOS), remote sensing, and reanalysis data sets. We assess simulated ET and GPP from the grid scale ($CLM5_{grid}$) and the plant functional type (PFT) scale ($CLM5_{PFT}$). $CLM5_{PFT}$ exhibited a low systematic error in simulating the ET at the ICOS sites

(average bias of −4.68 %). GPP was underestimated by $CLM5_{PFT}$, especially in deciduous forests (bias of −43.76 %). The results showed an underestimation of the spatiotemporal variability in the simulated ET and GPP distribution moments across PFTs for both CLM setups compared to reanalysis data and remote-sensing products. These findings provide essential insights for improving land surface models, highlighting the need to enhance the CLM5's ability to capture the spatiotemporal variability in ET and GPP simulations across PFTs.

Study 3 (Chapter 5): Droughts significantly impact European ecosystems, but these effects vary due to the complex interactions among various hydrological compartments and across different temporal scales, making a comprehensive understanding challenging. 24 years (1995-2018) of high-resolution (3km) Community Land Model version 5 (CLM5) simulations over Europe are analyzed, applying a three-dimensional clustering algorithm to identify and characterize spatiotemporal drought events based on standardized indices of precipitation, vapor pressure deficit, soil moisture, runoff, and groundwater across multiple aggregation periods. The aggregation period strongly modulates drought duration, severity, and propagation speed, with more extended periods yielding more severe and persistent events. Notably, the severity of atmospheric droughts has increased over the study period ($0.22 \pm 0.11 \times 10^7$ km^2 days year^{-1}), while groundwater droughts have become less severe ($-0.28 \pm 0.38 \times 10^7$ km^2 days year^{-1}). Ecosystem responses, including transpiration, gross primary production, and water stress, show complex spatial patterns linked to plant functional types and aridity gradients, with compound droughts in soil and atmosphere causing the most widespread negative impacts. This event-based, multi-compartment study advances the understanding of drought impacts on ecosystem processes and informs holistic drought risk assessments and water management.

Together, these studies provide a robust assessment of how European ecosystems function and respond under increasingly frequent and severe drought conditions, offering insights for improving land surface models and informing future ecosystem management under climate stress.

Zusammenfassung

Diese Dissertation untersucht die Variabilität von Ökosystemprozessen – der Primärproduktion (GPP), der Evapotranspiration (ET) und der Wassernutzungseffizienz (WUE) – in Europa unter den Bedingungen des Klimawandels. Der Schwerpunkt liegt auf langfristigen Trends und den Reaktionen dieser Prozesse auf Dürren im Zeitraum von 1995 bis 2018. Die Arbeit basiert auf drei Datenquellen: Fernerkundung, In-situ Messungen (ICOS) sowie Simulationen mit dem Landoberflächenmodell CLM5. Die Dissertation ist in drei Studien gegliedert:

Studie 1 (Kapitel 3): Die Wassernutzungseffizienz – das Verhältnis von aufgenommenem Kohlenstoff zu transpiriertem Wasser – ist ein zentraler Indikator für die Funktionsweise von Ökosystemen, doch ihre Variabilität unter dem Einfluss von Klimawandel und Dürren ist bislang unzureichend verstanden. In dieser Studie wurden Trends, Dürreantworten und Einflussfaktoren von drei verschiedenen WUE-Indizes in Europa im Zeitraum 1995–2018 mithilfe von Fernerkundungsdaten untersucht, die langfristige Umwelteinflüsse berücksichtigen. Die inhärente Wassernutzungseffizienz nahm in Mitteleuropa um −4,2 % ab, was auf eine Gefährdung der Ökosystemfunktion hinweist. In europäischen Graslandschaften stieg sie hingegen um +24,2 % an, bedingt durch regulierte Transpiration und erhöhte Kohlenstoffaufnahme. Zudem wird gezeigt, wie die Reaktion der WUE auf Dürren durch hydro-klimatische Bedingungen moduliert wird und wie wichtig eine adaptive Blattleitfähigkeit für die Ökosystemfunktion ist. Die Ergebnisse verdeutlichen, dass eine Entkopplung der Kohlenstoffaufnahme von der Blattleitfähigkeit sowie effiziente Wasserbewirtschaftungsstrategien entscheidend dafür sein können, ob Ökosysteme unter dem Klimawandel gefährdet sind oder effizient damit umgehen können. Diese Erkenntnisse sind auch für die Weiterentwicklung von Landoberflächenmodellen von Bedeutung.

Studie 2 (Kapitel 4): Evapotranspiration (ET) und Brutto-Primärproduktion (GPP) sind entscheidende Flüsse im Energie-, Wasser- und Kohlenstoffaustausch zwischen Atmosphäre und Landoberfläche. Landoberflächenmodelle wie das Community Land Model Version 5 (CLM5) quantifizieren diese Flüsse, schätzen Kohlenstoffbilanzen und Wasserressourcen ab und tragen zum besseren Verständnis der Auswirkungen des Klimawandels auf Ökosysteme bei. In dieser Studie wird die Modellperformance von CLM5 durch den Vergleich mit Messungen von 42 Eddy-Kovarianz-Stationen des ICOS-Netzwerks,

Fernerkundungs- und Reanalyse-Daten bewertet. Es werden Simulationen auf Rasterebene ($CLM5_{grid}$) sowie auf Ebene der pflanzenfunktionalen Typen ($CLM5_{PFT}$) analysiert. $CLM5_{PFT}$ zeigte geringe systematische Fehler bei der Simulation von ET (mittlerer Bias −4,68 %). GPP wurde insbesondere in laubabwerfenden Wäldern stark unterschätzt (Bias −43,76 %). Diese Ergebnisse liefern wichtige Hinweise zur Verbesserung von Landoberflächenmodellen, insbesondere zur besseren Erfassung der raumzeitlichen Variabilität von ET und GPP über verschiedene Vegetationstypen hinweg.

Studie 3 (Kapitel 5): Dürren haben erhebliche Auswirkungen auf europäische Ökosysteme, doch diese Effekte sind aufgrund komplexer Wechselwirkungen zwischen verschiedenen hydrologischen Komponenten und zeitlichen Skalen schwer zu verstehen. In dieser Studie werden 24 Jahre (1995–2018) hochaufgelöster (3 km) Simulationen mit dem Community Land Model Version 5 (CLM5) analysiert. Mithilfe eines dreidimensionalen Clustering-Algorithmus werden räumlich-zeitliche Dürreereignisse identifiziert und charakterisiert, basierend auf Niederschlag, Dampfdruckdefizit, Bodenfeuchte, Abfluss und Grundwasser über mehrere Aggregationszeiträume hinweg. Bemerkenswert ist die zunehmende Schwere atmosphärischer Dürren ($0{,}22 \pm 0{,}11 \times 10^7$ km² Tage Jahr^{-1}), während Grundwasserdürren an Schwere abnahmen ($-0{,}28 \pm 0{,}38 \times 10^7$ km² Tage Jahr^{-1}). Die Reaktionen der Ökosysteme, zeigen komplexe räumliche Muster, abhängig von Vegetationstypen und Ariditätsgradienten. Besonders starke negative Auswirkungen wurden bei kombinierten Dürren in Boden und Atmosphäre festgestellt. Diese multikompartimentale Analyse verbessert das Verständnis der Dürreauswirkungen auf Ökosystemprozesse und liefert wichtige Impulse für umfassende Dürre-Risikoabschätzungen und nachhaltiges Wassermanagement.

Insgesamt liefern diese drei Studien eine robuste Bewertung der Funktionsweise europäischer Ökosysteme unter zunehmend häufigeren und intensiveren Dürren. Die gewonnenen Erkenntnisse tragen zur Verbesserung von Landoberflächenmodellen bei und sind relevant für das zukünftige Management von Ökosystemen unter klimatischen Belastungen.

Acknowledgements

I would like to express my deepest gratitude to everyone who has supported me throughout the journey of my thesis.

First and foremost, I am immensely grateful to my parents, my sister, and my wife for their unwavering love, patience, and encouragement. Their support has been the foundation that carried me through the challenges of this academic journey.

I am sincerely thankful to my supervisors, Dr. Bibi Naz, Prof. Dr. Harrie-Jan Hendricks-Franssen, and Prof. Dr. Harry Vereecken for their invaluable guidance, expertise, and continued support. Their mentorship and insight have played a crucial role in shaping this work.

My heartfelt thanks also go to the Early Career Researchers at IBG-3 in the Research Centre Jülich. The collaborative spirit and stimulating environment they foster have enriched both my academic and personal growth. I also gratefully acknowledge the Early Career Researchers of the eLTER project for their inspiring exchanges and shared dedication.

Last but certainly not least, I would like to thank my dear friends from Düren and Jülich (a.k.a. "Dürlich") for the laughter, conversations, and companionship that have made this time memorable.

List of Contents

List of Figures

List of Tables

List of Abbreviations

AVHRR	Advanced Very High Resolution Radiometer
BDS	Broadleaf Deciduous Shrub
BDT	Broadleaf Deciduous Tree
BES	Broadleaf Evergreen Shrub
BET	Broadleaf Evergreen Tree
BGC	Biogeochemical cycle
BI	British Isles
CABLE	Community Atmosphere Biosphere Land Exchange
CARDAMOM	Carbon Data Model Framework
CDF	Cumulative Density Function
CLM	Community Land Model
CMIP	Coupled Model Intercomparison Project
CORDEX	Coordinated Regional Climate Downscaling Experiment
COSMO	Consortium for Small-scale Modeling
CRO	Croplands
DBF	Deciduous Broadleaf Forest
DBSCAN	Density-Based Spatial Clustering of Applications with Noise
DEIMS-SDR	Dynamic Ecological Information Management System - Site and dataset registry
DOY	Day Of Year
EA	Eastern Europe
EC	Eddy covariance
ENF	Evergreen Needleleaf Forest

ER	Ecosystem Respiration
ERA5	European Centre for Medium-Range Weather Forecasts Reanalysis version 5
ERA5L	The European Centre for Medium-Range Weather Forecasts Reanalysis version 5 – Land
ESACCI	European Space Agency Climate Change Initiative
ESM	Earth System Model
ET	Evapotranspiration
EWUE	Ecosystem Water-Use Efficiency
FAO	Food and Agriculture Organization
FLUXNET	FLUX tower NETwork
FR	France
GLASS	Global Land Surface Satellite
GLDAS	Global Land Data Assimilation System
GLEAM	Global Land Evaporation Amsterdam Model
GPP	Gross Primary Production
GR / GRA	Grasslands
GRACE	Gravity Recovery and Climate Experiment
ICOS	Integrated Carbon Observation System
IGBP	International Geosphere-Biosphere Programme
IP	Iberian Peninsula
IPCC	Intergovernmental Panel on Climate Change
IWUE	Inherent Water-Use Efficiency
JULES	Joint UK Land Environment Simulator
LAI	Leaf-Area Index
LSM	Land Surface Model

LTER	Long Term Ecosystem Research
LUE	Light-Use Efficiency
LUNA	Leaf Utilization of Nitrogen for Assimilation
MD	Mediterranean
ME	Mid Europe
MF	Mixed Forests
MODIS	Moderate Resolution Imaging Spectroradiometer
NDT	Needleleaf Deciduous Tree
NEE	Net Ecosystem Exchange
NET	Needleleaf Evergreen Tree
PBIAS	Percent BIAS
PCMCI	Peter and Clark Momentary Conditional Independence
PDAF	Parallel Data Assimilation Framework
PFT	Plant Functional Type
PHS	Plant Hydraulic System
PRUDENCE	Prediction of Regional scenarios and Uncertainties for Defining European Climate change risks and Effects
RH	Relative Humidity
RI	Research Infrastructure
RMSD	Root Mean Square Difference
RMSE	Root Mean Square Error
RS	Remote Sensing
SAPFLUXNET	SAPFLUX NETwork
SC	Scandinavia
SM	Soil Moisture

SPI	Standardized Precipitation Index
SSI	Standardized Soil moisture Index
TWUE	Transpiration Water-Use Efficiency
UK	United Kingdom
VPD	Vapor Pressure Deficit
WAILS	Whole Systems Approach to In-Situ Research on Life-supporting Systems
WMO	World Meteorological Organization
WTD	Water Table Depth
WUE	Water-Use Efficiency

1 Introduction

1.1 Background

Since the dawn of civilization, human welfare has depended on balanced climatic and environmental conditions. These stable conditions have provided the basis for the rapid growth of the global human population and continuous economic and societal development. It has become evident that during this period of growth, human activities have had a substantial and irreversible impact on the Earth's face, e.g., by converting large portions of natural landscapes to cultivated land or urban areas. Consequently, humans altered natural ecosystems in abundance, extent, and diversity.

The period of growth in human society was accompanied and propelled by the exploitation of natural resources. For instance, water was extracted from naturally occurring sources in rivers, reservoirs, and aquifers to sustain large-scale agriculture in areas with limited rain. Rivers were dammed to store water for use in dry seasons and routed to make transportation with riverboats more efficient. Where atmospheric rain and surface water were absent, an agricultural economy was still possible by withdrawing groundwater accumulated in aquifers (Folke et al., 2009; Maxwell et al., 2016).

Furthermore, energy-dense carbon-based fossil fuels, such as coal and petroleum, have risen dramatically since the Industrial Revolution. Burning fossil fuels converts chemically stored energy to kinetic energy for powering machines, concurrently releasing carbon dioxide (CO_2) as a gas into the atmosphere. Consequently, the intensified use of fossil fuels in transportation, production of goods, electricity generation, and construction shifted considerable amounts of carbon stored belowground for millions of years into the atmosphere as carbon dioxide in a geologically short period (Crutzen, 2016).

In the atmosphere, CO_2 absorbs the energy wavelength spectrum that the Earth emits after being heated by sunlight (Foote, 1856; Tyndall, 1873). Consequently, the heat originating from incoming solar radiation that would radiate back into space remains in the Earth's system, causing an increase in temperature – the greenhouse effect (Arrhenius, 1896). Without greenhouse gases in the atmosphere, less solar radiation energy would be retained in the Earth system. The mean global surface temperature would be as low as -18 °C (Lacis et al., 2010), as opposed to the 14 °C experienced during a reference period from 1951 to

1980 (Hansen et al., 2010). The anthropogenically added CO_2 in the atmosphere reinforces the naturally occurring greenhouse effect, causing a continuous rise in the average annual global temperature (Hansen et al., 2010). The average global surface temperature has increased by over 1.5 K compared to the period from 1951 to 1980 (WMO, 2025), thus surpassing a global annual mean temperature of 15.5 °C. This relatively small temperature change induces a general shift in the global climate and has many implications for states and processes in the Earth System (IPCC, 2023a).

1.2 The main effect of climate change on the water cycle

The water cycle describes the flow of water through Earth System components, e.g., falling as precipitation onto the land surface, being frozen into glaciers, thawing, flowing as a stream to the ocean, and evaporating back again to the atmosphere. Changes in climate have a manifold impact on the global water cycle. Generally, increased temperatures favor an intensified hydrological cycle in the form of more extreme hydrological conditions through alterations in precipitation patterns and more frequent and severe atmospheric dryness (Guan et al., 2024; Loaiciga et al., 1996; F. Yang et al., 2003). In more detail, warmer air in the atmosphere can hold exponentially more water vapor, explained by the Clausius-Clapeyron relationship (Clapeyron, 1834; Clausius, 1850; Feynman, 2011). The atmosphere's vapor pressure deficit increases, and with unchanged water availability on the land, this results in a higher vapor pressure gradient between the land and the atmosphere. Where the available water (in streams, lakes, and soil) is sufficient, increased evaporation and transpiration will lead to larger magnitudes of water falling as heavy precipitation events, increasing the likelihood of floods (Brönnimann et al., 2022). Conversely, saturating warmer air will take longer, even with higher levels of land evapotranspiration, due to the exponential relationship between air temperature and vapor pressure at typical atmospheric conditions and constraints related to terrestrial water availability and physiological controls in vegetation (Budyko, 1974). This extends the periods between convective precipitation events, thus favoring more frequent and severe dry conditions on the land (Manning et al., 2019; Samaniego et al., 2018). This is additionally affected by changing atmospheric circulation patterns, such as increasing frequency and duration of blocking events (in Europe, these are often persistent high-pressure systems hampering westerly air flow), potentially prolonging dry conditions and exacerbating droughts (Bakke et al., 2023; Ionita

et al., 2022; Kautz et al., 2022). Notably, these changes in extreme conditions at small and medium temporal scales are not directly related to general drying and wetting trends, which alter the long-term hydroclimatic regime of a given location (Zaitchik et al., 2023).

1.3 Implications for ecosystem processes variability

Ecosystems are intricately affected by the changing climate and environment: The increased CO_2 concentration generally favors plant growth. However, the increased temperatures counteract this effect in temperate and tropical parts of the globe (Fernández-Martínez et al., 2019). Besides, there is increasing evidence of more complex indirect implications of increased atmospheric CO_2 on ecosystems, for example, a correlation with declining soil nutrients in forests (Penuelas et al., 2020), decreasing soil organic matter content (Terrer et al., 2021), and complex interactions with the land surface albedo (Graf et al., 2023). Moreover, the raised water demand of the drier atmosphere causes higher evaporation from the soil, which makes plant water stress more likely (Fu et al., 2021). Increased atmospheric dryness also clearly affects the phenology, changing the timing of the onset and duration of ecosystem activity during the warm and dry season by early depletion of the water stored in the soil (Rahmati et al., 2023). Thus, ecosystem responses to droughts in a later part of the year would be affected by these legacy conditions and exacerbate their impact on ecosystem processes, such as energy partitioning, carbon uptake, and transpiration (Bastos et al., 2020; Graf et al., 2020). Plants evolved water management strategies according to their long-term hydroclimatic environment, so in dry regions, vegetation has adapted to use water more efficiently to assimilate carbon for metabolism and growth (Joshi et al., 2022; Konings & Gentine, 2017; Moreno et al., 2024). Thus, the impacts of changing hydroclimatic conditions on ecosystem processes are heterogeneous over the land surface, depending on soil characteristics, hydroclimate, and especially plant type, among other factors (X. Feng et al., 2018). It is clear that the stability of ecosystem water and carbon processes is threatened by the steep hydroclimatic gradients and human modifications that affect functional diversity and drought resilience (W. R. L. Anderegg et al., 2018; Bastos et al., 2020; Y. Zhang et al., 2021). A holistic understanding of how and why processes in a particular ecosystem vary with shifting climatic conditions and droughts is important for sustaining the water cycle and managing water resources, agriculture, and other ecosystem services. Nevertheless, this understanding has not been established.

Two processes are of broad interest to studies of ecosystem functionality: gross primary production (GPP), which indicates the rate of carbon taken up from the atmosphere by photosynthesis into the vegetation, and evapotranspiration (ET), which summarizes water evaporation from the land surface and vegetation transpiration (T_r).

Carbon uptake is essential for vegetation to sustain metabolism and growth. At the same time, evapotranspiration is a vital water flux from the land surface to the atmosphere, returning more than half of the precipitated water to the atmosphere in the global average, thereby using more than half of the solar energy absorbed by the land surface (Jung et al., 2010; Oki & Kanae, 2006; Trenberth et al., 2009). Rising temperatures and increased CO_2 have intricate effects on GPP, over medium and long terms, even inducing physiological acclimation responses (Knauer et al., 2023; Lombardozzi et al., 2015). At the same time, more frequent and severe droughts can reduce GPP (Fu et al., 2022), and, in the worst cases, lead to vegetation dieback because of hydraulic failure and an increased risk of mortal pest infestation induced by inhibited defense metabolism (Christiansen et al., 1987; Schuldt et al., 2020; Sevanto et al., 2014). However, it is still unclear to what extent soil moisture deficits and vapor pressure deficits individually and combined induce a GPP reduction during droughts (Z. Deng et al., 2025; Fu et al., 2022, 2024; W. Li et al., 2022; Peng et al., 2024).

The potential ET increases during droughts, due to the increased atmospheric water demand and available energy. However, actual ET is often decreased by stomatal regulation of the plants to save water. Globally, drought often increases ET, but it has the potential to quickly deplete soil water resources, which will finally negatively impact ET (M. Zhao et al., 2022). Thus, severe drought events are the primary hazard to ecosystem functioning. Similarly, the generally increasing atmospheric water demand due to global warming impacts ET, depending on the available water. Where much water is available, ET will increase significantly, thus depleting available resources more quickly, with potential consequences for ecosystem functioning and human water supply (Condon et al., 2020). Further, plants slightly close (or reduce the density of) the stomata in response to the increased atmospheric CO_2, maintaining the carbon inflow relatively constant due to the raised concentration gradient, concurrently constraining water outflow and increasing water-use efficiency (Xu et al., 2016). As a result, the ET response to these factors depends on local aspects of the changing climate, drought frequency and severity, and the functioning of the present vegetation.

The water-use efficiency (WUE), which relates GPP to the unit of water used, is a key indicator of ecosystem functionality (Kühn et al., 2021; Migliavacca et al., 2021). Furthermore, it has important implications for efficient agriculture and conserving water resources (Callejas Moncaleano et al., 2021). It is fascinating because it couples the water and carbon cycles by adjusting plant stomatal conductance. It is affected by the intricate interplay of factors affecting GPP and T_r individually. WUE responses to climate change and droughts have also been observed to vary across spatiotemporal, hydroclimatic, and plant functional gradients (M. A. Adams et al., 2020; Bai et al., 2020; Beer et al., 2009; Cooley et al., 2022; Hatfield & Dold, 2019). Clear patterns in the long-term temporal WUE trends and the drought response are intricate to quantify because of the simultaneous sensitivity to drivers of GPP and T_r changes.

In conclusion, grasping the functional diversity related to the variability of water and carbon processes and their coupling in ecosystems, the alterations due to a changing climate and environment, and more frequent and severe dry conditions, remains a challenge.

1.4 Varying drought properties and ecosystem responses

Furthermore, droughts as emerging spatiotemporal phenomena have to be quantified and understood themselves, to contextualize their impact on processes in different ecosystems (Vicente-Serrano et al., 2025; W. Zhang et al., 2021). Droughts have been predominantly defined by anomalies of standardized drought indices, such as the Standardized Precipitation Index (SPI) (McKee et al., 1993). These indices facilitate the comparison of dry and wet conditions across different locations and periods, because the anomalies relate to local distributions over a reference period. Locations and periods identified as having drought conditions can be summarized by integrating regional and periodic deficits into discrete events (Andreadis et al., 2005; Cammalleri et al., 2023; Cammalleri & Toreti, 2023). The advantage of event-based analysis of droughts is that events additionally provide essential metrics such as spatial extent, duration, and propagation speed, and the associated drought points in each event are assumed to converge in terms of their drivers and ecosystem responses. This is necessary to find potential links between ecosystem drought responses and specific characteristics of an individual drought event.

While the effect of absolute plant water stress and critical soil moisture levels has received considerable attention (Franklin et al., 2020; Fu et al., 2024; Joshi et al., 2022; Stocker et al., 2023), the connection to droughts defined by hydrological variables remains elusive. On top of that, the emergent impacts of drought events on ecosystem processes and their trends remain poorly understood (Bradford et al., 2020; Crausbay et al., 2020; Vicente-Serrano et al., 2025), mainly because of the heterogeneity of physiological water management adaptations, the effect of plant physiology, e.g., root distribution in the soil, and the resulting drought responses.

In Europe specifically, increasing trends in drought frequency and severity have already been recorded (Rousi et al., 2022; Vautard et al., 2023). These trends have been projected to continue (Lehner et al., 2017). The societal impacts of European droughts include decreased agricultural yield, and reduced trade through hampered shipping in rivers, currently resulting in €9 billion economic loss in Europe, which is expected to increase drastically without climate action (Naumann et al., 2021). It expands to loss of property and lives, especially during multivariate extremes (Zscheischler et al., 2020).

1.5 Observations and models of ecosystem processes

Land surface models (LSMs) are tools for analyzing the variability of the terrestrial land surface (including hydrology, vegetation functioning, and nutrient cycling). They are essential components of larger Earth System Models (ESMs) that dynamically couple multiple component models (e.g., an atmospheric model, an LSM, and an ocean model). Essentially, LSMs deterministically solve the interconnected water, energy, and carbon cycles to predict the states and fluxes of natural and managed terrestrial ecosystems. Land surface heterogeneity is accomplished by distributed soil characteristics, discerning vegetation into plant functional types (PFTs), and implementing one set of equations and a corresponding set of parameters for each PFT in the model. Typically, PFTs are specified by morphological and phenological characteristics, distinguishing between leaf forms (needles, broad leaves, grasses), and phenology through leaf longevity (evergreen versus deciduous). Additionally, long-term precipitation and temperature patterns may categorize these to represent the vegetation's climatological adaptation functionally. Corresponding information on land cover, soil texture, and PFT distribution, among others, is derived from remote sensing or upscaled field measurements and then used as static input to LSMs.

Recent developments on transient land use, dynamic vegetation, carbon and nutrient cycling, plant hydraulics, crop management, and plant hydraulics have raised the number of processes represented in LSMs, thereby increasing their complexity. However, emergent non-linear interactions and feedbacks may reduce the ability of LSMs to accurately approximate ecosystem states and fluxes with increasing complexity (Fisher & Koven, 2020). Furthermore, more included processes may imply that more computational effort is required. Additionally, the high diversity of ecosystem responses and intricate heterogeneous interactions with the atmosphere require high-resolution simulations, which further increase the computational demand of such simulations (Wood et al., 2011; Naz et al., 2016; Prein et al., 2016).

LSMs have been successfully used to quantify, understand, and predict the interactions between the atmosphere and the land surface. They can provide critical information for agriculture and water managers (Belleflamme et al., 2023; Boas et al., 2023), to analyze the impacts of the changing climate and extreme events (Hartick et al., 2022), and to explore agricultural management options (Dombrowski et al., 2024). Further, they are critical for creating a scientific understanding of how the diverse processes on the land surface interact as a connected terrestrial system (Bonan, 2019; Fisher & Koven, 2020). However, the simulated projections always represent the status quo regarding the individual processes based on secluded experiments, thus potentially introducing untested, erroneous interactions between them. Further, misrepresentations of, e.g., nutrient dynamics (Davies-Barnard et al., 2020), management of ecosystems (Boas et al., 2021; Dombrowski et al., 2024), eco-evolutionary functional diversity (L. D. L. Anderegg et al., 2022; Harrison et al., 2021), and mechanistic drought responses (J. K. Green et al., 2024) affect the overall accuracy of the simulated energy, water, and carbon cycles by LSMs. Thus, critical variables of the model simulations must be rigorously evaluated in relation to the observations to provide essential context on the robustness of subsequent analyses.

The crucial advantage of LSMs is that they can simulate a set of physically consistent variables in a spatiotemporal uniform resolution, which facilitates large-scale and systematic studies of the complex interactions on the terrestrial land surface, and extend to future predictions by using environmental scenarios as input (Fisher & Koven, 2020; McColl et al., 2022). Meanwhile, in situ observation networks are still relatively sparse and introduce geographical bias by underrepresenting certain regions and ecosystems (Ohnemus et al., 2024; Wohner et al., 2021). Nevertheless, in situ observations are essential references to LSM

simulations, crucial to evaluating the simulated states and fluxes, and analyzing ground-truth feedbacks and responses.

While investments and developments in remote sensing missions and sensor technology provide ecosystem states and fluxes at high spatial resolution, the revisiting time dictates a relatively coarse temporal resolution of the data. Assumptions made while deriving ecosystem processes from sensor signals and differing sensor technologies make the physical accordance and captured feedback signals between variables inconsistent (G. Wang et al., 2005; Povey & Grainger, 2015). Nevertheless, the large spatial extent and the long-term coverage periods offer crucial references for regional to global-scale assessments and large-scale model evaluation.

Observations from the location of interest act as ground truth data for remote sensing and modelling evaluations. Global challenges such as climate change steered developments towards grouping stations across a country, continent, or globally, to provide spatially distributed sets of time series of local measurements in a standardized manner. Such research infrastructures provide standard protocols on, e.g., sensor technology to ensure consistent measurements across the station network and the represented period (Baatz et al., 2018; Pastorello et al., 2020). The eddy-covariance method is the gold standard for ecosystem processes measurements, providing observations of water, energy, and carbon fluxes between the land surface and the atmosphere in a high temporal resolution (Aubinet et al., 2012). The Integrated Carbon Observation System (ICOS) provides time series of energy, water, and carbon fluxes from eddy-covariance measurements across Europe (Heiskanen et al., 2022). The ICOS station network encompasses various PFT, ranging from forests to croplands and grasslands. Essentially, the eddy-covariance sensor operates atop a tower and represents an ideally homogenous ecosystem on a footprint area of up to 1 km^2. As a result, there is typically a scaling difficulty when comparing land surface model outputs, which generally output averages of the time series of multiple present PFT within a grid cell of thousands of km^2, with ICOS data. However, adding the subgrid PFT level of land surface models allowed the extraction of PFT-specific states and fluxes. Using these PFT-scale data from land surface models enhances compatibility with eddy covariance measurements and more robust evaluations.

To summarize, using remote sensing, LSM simulations, and in situ observations all have advantages and disadvantages in studying the variability of ecosystem processes. Using them appropriately can leverage their strengths, amplify the study's scope, and bring broad context to the overall study question.

1.6 Objectives and outline

As an overarching research goal, this thesis quantifies the variability of the critical ecosystem processes gross primary production (GPP), evapotranspiration (ET), and the water-use efficiency (WUE) over Europe, along a study period from 1995 to 2018, containing critical large-scale drought events. A special focus will be on their trends, drivers, and responses to drought events, using data from various sources (remote sensing, a land surface model, and in situ observations). Considering the scientific gaps and state-of-the-art outlined in Chapter 1, the individual scientific inquiries in this dissertation are as follows:

- Chapter 3: Quantifying the European trends and drought response of WUE as a proxy of ecosystem functioning using remote sensing and reanalysis data.
- Chapter 4: Evaluating a high-resolution simulation of GPP and ET with the Community Land Model version 5 (CLM5) over Europe with in situ data from a continental-scale observation network.
- Chapter 5: Analyzing drought events' properties, trends, and impacts derived from multiple hydrological compartments and various time scales from the evaluated European CLM5 simulation.

In more detail, Chapter 2 describes the underlying physical laws and methods of the European CLM5 setup. These include critical energy, carbon, and water cycle functions, such as radiative transfer through the canopy and water flow through the soil.

Chapter 3 uses an observation and reanalysis data set to quantify the trends, drought response, and drivers of WUE variability across Europe. This includes GPP from a revised light-use efficiency model for remote sensing data, ET from remote sensing, T_r and evaporation from a model-data-fusion framework, and meteorological data from an atmospheric reanalysis. Different approximations of the water-use term (T_r, ET, and canopy conductance) define different indicators of WUE. The trends are calculated using grid-cell-based Mann-Kendall trend analysis, revealing opposing trends among European regions and WUE indices. Droughts are calculated based on soil moisture droughts in the surface soil layers, and corresponding responses are identified across Europe for each WUE index.

In Chapter 4, the European setup of CLM5 is evaluated, and specifically, the simulated GPP and ET, where ICOS stations are located. Other data sources, like remotely sensed GPP and ET from reanalysis, which were used in Chapter 3, are

included for additional context. Time series from the corresponding PFT scale and the aggregated grid cell scale are compared to ICOS over 42 stations. The PFTs widely represented in the ICOS network are Evergreen Needleleaf Forest, Deciduous Broadleaf Forest, Grassland, and Croplands. Evaluation metrics (percent bias, root mean square error, correlation) comparing the variables for each station, as well as aggregated time series for each PFT, are calculated. Particularly, how well the seasonal cycle of GPP and ET is simulated across PFTs compared to the reference datasets is emphasized in this study. This evaluation provides crucial context on the ability of CLM5 to approximate ecosystem processes across Europe for the subsequent study of their drought response.

Chapter 5 is an in-depth study of identified droughts in the European CLM5 simulations and their impacts on ecosystem processes. First, drought indices are calculated based on the relative distribution at each grid cell of the European domain. A multivariate approach is facilitated by including multiple compartments of the water cycle, based on which the water deficits are determined: precipitation, vapor pressure, soil moisture, runoff, and groundwater. Further, four aggregation time scales, 31 days, 92 days, 183 days, and 365 days, represent a range of accumulated water deficits and their effect on ecosystem processes. These indices are used in a 3-dimensional clustering algorithm to distinguish spatiotemporal drought events from each other. Subsequently, the most significant event for each drought type is described and compared to events previously described in the literature, where applicable. The event-based drought approach facilitates the calculation of properties for each event, such as spatial extent, duration, and propagation speed. The study then compiles the distribution of these properties across events for each variable and identifies key differences in how drought events across compartments and aggregation times develop. Furthermore, the significant temporal trends of the drought event properties are determined. Lastly, this study connects the drought events with ecosystem processes by calculating the response of GPP, T_r, and water limitation to soil moisture, vapor pressure, and compound drought events.

Finally, Chapter 6 summarizes the conclusions of the three individual studies and outlines their contributions to answering the overarching research question. Specifically, the contributions to the general understanding of the functioning of terrestrial systems are highlighted, and future studies leveraging this research project are suggested. Ultimately, it outlines recommendations for further improvements on the European CLM5 setup, model development in CLM5, and integration between observations and models.

2 Theory

One of the underlying physical concepts behind calculating states and fluxes of energy and water is the conservation of energy, mass, and momentum. Land surface models solve these equations on the interface between the atmosphere and land to account for the albedo effect and energy partitioning on the surface. The heat and water balance equations for a simplified land surface and more resolved details on the implementation in the CLM5 will be presented in the following chapter as a theoretical introduction to this thesis. This is supposed to give a general idea of the coupling of energy, water, and carbon cycles in land surface models, rather than a detailed description of small-scale processes. For the latter, please check the referenced literature and the method sections of the following chapters.

2.1 The heat balance on the terrestrial surface

The heat balance on the land surface results from the partitioning of the incoming solar radiation:

$$R_{net} = \left(K_{\uparrow} - K_{\downarrow}\right) + \left(L_{\downarrow} - L_{\uparrow}\right) = \lambda E + H + G \qquad (2.1)$$

R_{net} [W m^{-2}] is the incident net radiation, calculated by summing the differences between atmospheric incoming ($\downarrow$) and outgoing ($\uparrow$) shortwave (K) [W m^{-2}] and longwave radiation (L) [W m^{-2}]. The atmospheric incoming radiation is an external input into land surface models, while the outgoing radiation is determined based on the surface albedo and emissivity. λ [J kg^{-2}] is the heat of vaporization or sublimation, and E [kg m^{-2} s^{-1}] is the evaporation rate; thus, λE [W m^{-2}] is the heat flux corresponding to energy transferred through evaporation and condensation. H [W m^{-2}] is the sensible heat flux, and G [W m^{-2}] is the heat flux from the surface to lower layers in the soil.

E results from water evaporated from the ground and vegetation. Ground evaporation is the sum of snow sublimation, soil evaporation, and surface water evaporation, considering their areal fractions on the land surface. Further, vegetation evaporation is the sum of water evaporated from the wet vegetation surfaces and transpiration from dry leaves. In CLM5, λ is a fixed constant (2.5×10^{6} J kg^{-2}), as its variation with the typical atmospheric temperatures is negligible. The individual water vapor fluxes are calculated using a model based on humidity

gradients and corresponding water vapor conductance (determined as the inverse of the resistance).

$$E = E_g + E_v \tag{2.2}$$

$$E_g = -\rho_{atm}\left[c_a^w \; q_{atm} + c_v^w \; q_{sat}^{T_v} - \left(c_a^w + c_v^w\right) q_g\right] \frac{c_g^w}{c_a^w + c_v^w + c_g^w} \tag{2.3}$$

$$E_v = -\rho_{atm}\left[c_a^w \; q_{atm} + c_g^w \; q_g - \left(c_a^w + c_g^w\right) q_{sat}^{T_v}\right] \frac{c_v^w}{c_a^w + c_v^w + c_g^w} \tag{2.4}$$

ρ_{atm} [kg m^{-3}] is the density of atmospheric air, and c_a^w, c_v^w, and c_g^w [m s^{-1}] are water vapor conductance from the canopy air to the atmosphere, from the leaf to the canopy air, and from the ground to the canopy air, respectively. In more detail, c_v^w c_g^w and c_a^w are calculated using physical properties of the surface, physiological properties of the vegetation, and the Monin-Obukhov (M-O) similarity theory (Monin & Obukhov, 1954), which avoids high computational demand from resolving small-scale turbulent flow by parametrizing aerodynamic resistance to water vapor. However, M-O neglects mesoscale circulations resulting from assuming uniform surface properties and states (e.g., soil moisture), and further neglects transient phenomena (e.g., rapid weather changes and stability issues). q_{atm}, q_g, and $q_{sat}^{T_v}$ [kg kg^{-1}] are the specific humidities of the atmosphere, the soil, and saturation at vegetation temperature. The vegetation conductance c_v is calculated by considering the leaf and stem area indices, their wet fraction, and stomatal conductance, including its soil moisture limitation, inter alia.

Similarly, the sensible heat components are calculated using a model based on temperature gradients and corresponding heat conductance.

$$H = H_g + H_v \tag{2.5}$$

$$H_g = -\rho_{atm} \; C_p\left[c_a^h \; \theta_{atm} + c_v^h \; T_v - \left(c_a^h + c_v^h\right) T_g\right] \frac{c_g^h}{c_a^h + c_v^h + c_g^h} \tag{2.6}$$

$$H_v = -\rho_{atm} \; C_p\left[c_a^h \; \theta_{atm} + c_g^h \; T_g - \left(c_a^h + c_g^h\right) T_v\right] \frac{c_v^h}{c_a^h + c_v^h + c_g^h} \tag{2.7}$$

C_p [J kg^{-1} K^{-1}] is the specific heat capacity of the air, and c_a^h, c_v^h, and c_g^h [m s^{-1}] are heat conductance from the canopy air to the atmosphere, from the leaf to the canopy air, and from the ground to the canopy air, respectively. Similarly to the

water vapor resistance, CLM5 approximates the aerodynamic resistance to heat with the M-O similarity theory. θ_{atm} [K] is the atmospheric potential temperature, and T_v and T_g [K] are the vegetation and ground temperatures. Finally, the ground heat flux G is calculated by inserting the incoming radiation S_{atm} from the atmospheric input, and the calculated E and H into the heat balance Equation (2.1).

The partitioning of energy between H and λE is the Bowen ratio B [dimensionless]:

$$B = \frac{H}{\lambda E} \tag{2.8}$$

B is highest in dry regions like deserts, where H dominates over LE ($B > 10$), whereas most energy is transferred as λE in humid areas or oceans ($B < 0.1$).

Further heat fluxes can substantially alter the balance over shorter periods at specific locations. For example, the energy used for photosynthesis is stored in plant biomass. During forest fires, this energy is released quickly and is a substantial factor in the heat balance. Minor factors are the dissipation of the mechanical energy of wind and waves and the energy flux resulting from the temperature difference between falling precipitation and the air.

2.2 Radiative transfer through the canopy

Equation (2.1) only includes a simplistic representation of the land surface as a two-dimensional interface. However, the plant canopy is critical in partitioning the incoming energy. In the CLM5, the incoming radiation ($S_{atm} = K_{\downarrow} + L_{\downarrow}$) is divided into the incoming direct (d) and diffuse (i) radiation (S^d_{atm} and S^i_{atm}), by ratios resulting from polynomial equations fitted to atmospheric modelling data (D. M. Lawrence et al., 2018). These are further partitioned into energy reflected and absorbed by the vegetation and soil per wavelength Λ [µm]:

$$R_{net} = S_{ground} + S_{veg} + \sum_{\Lambda} R^{d,\Lambda}_{atm} \; I^{d,\Lambda}_{\uparrow} + R^{i,\Lambda}_{atm} \; I^{i,\Lambda}_{\uparrow} \tag{2.9}$$

$$S_{ground} = \sum_{\Lambda} S^{d,\Lambda}_{atm} \; e^{-K(L+S)} \left(1 - \alpha^{d,\Lambda}_{ground}\right) \quad + \left(S^{d,\Lambda}_{atm} \; I^{d,\Lambda}_{\downarrow} + S^{i,\Lambda}_{atm} \; I^{i,\Lambda}_{\downarrow}\right) \left(1 - \alpha^{i,\Lambda}_{ground}\right) \tag{2.10}$$

$$S_{veg} = \sum_{\Lambda} S^{d,\Lambda}_{atm} \; I^{d,\Lambda}_{absorbed} + S^{i,\Lambda}_{atm} \; I^{i,\Lambda}_{absorbed} \tag{2.11}$$

K [dimensionless] is the optical depth of the direct beam per unit leaf. L [m^2 m^{-2}] is the exposed leaf area index, and S [m^2 m^{-2}] is the exposed stem area index. $\alpha_{ground}^{d,\Lambda}$ [dimensionless] is the albedo of the ground for the direct sun radiation beams at wavelength Λ. $I_{\uparrow}^{d,\Lambda}$ and $I_{\uparrow}^{i,\Lambda}$ [dimensionless] are the upward diffuse fluxes per unit direct beam and diffuse flux above the vegetation. The ratios by which the incident energy gets partitioned (the I's) are calculated by an analytical framework based on Sellers, 1985. $I_{\downarrow}^{d,\Lambda}$ and $I_{\downarrow}^{i,\Lambda}$ [dimensionless] are the direct downward diffuse fluxes below the vegetation per unit of direct beam and diffuse radiation. $I_{absorbed}^{d,\Lambda}$ and $I_{absorbed}^{i,\Lambda}$ [dimensionless] are the direct beam and diffuse fluxes absorbed by the vegetation per unit radiation. These partitioning ratios per unit direct and diffuse radiation and the albedos further consider the zenith angle of the incident beam.

The energy absorbed for photosynthesis Φ [W m^{-2}] is calculated as follows.

$$\Phi = \frac{\left(S_{atm}^{d,vis} \; I_{absorbed}^{d,vis} + S_{atm}^{i,vis} \; I_{absorbed}^{i,vis} \right)}{L} \tag{2.12}$$

Where $S_{atm}^{d,vis}$ and $S_{atm}^{i,vis}$ are the direct and diffuse solar radiation in the visible wavelengths ($\Lambda < 0.7 \;\; \mu m$). $I_{absorbed}^{d,vis}$ and $I_{absorbed}^{i,vis}$ are the absorbed direct beam and diffuse radiation fluxes in the visible spectrum per unit of direct beam and diffuse radiation. These fluxes are approached by two streams, i.e., separately for the sunlit and shaded leaf areas. Consequently, Φ is a primary factor determining the light limitation for C_3 and C_4 photosynthesis, besides rubisco and product limitation. Another major determinant of photosynthesis is the internal leaf partial pressure of CO_2, which is actively controlled by the adaptation of plant stomata depending on the water availability.

Clearly, through the water transported as vapor and latent heat, and because the stomata are an inlet and outlet for carbon and water simultaneously, the energy cycle is tightly coupled with the water and carbon cycles.

2.3 The water balance on the terrestrial surface

The land surface's water balance describes the incoming and outgoing water in solid, liquid, or gaseous form and is defined as:

$$P = E + Q + \Delta W \tag{2.13}$$

P [kg m^{-2} s^{-1}] is the atmospheric precipitation, i.e., falling rain, hail, or snow. E [kg m^{-2} s^{-1}] is the difference between evapotranspiration and condensation as calculated in Equations (2.2)-(2.4), Q [kg m^{-2} s^{-1}] is the horizontal surface and subsurface runoff, and ΔW [kg m^{-2} s^{-1}] is the change in water storage. CLM5 requires P as input from atmospheric data. Over relatively long periods (yearly), the change in storage, ΔW, is negligibly small compared to the other water cycle components during stationary conditions but may become significant under a changing climate, land cover and land use changes, and extensive human water extractions. Moreover, over short time scales, for example, during the melting season in glacial regions, ΔW can still be a dominant factor.

The runoff Q is composed of surface runoff and subsurface runoff. In CLM5, surface runoff is determined by the fraction of a location's saturated area and topographic properties, and the moisture input from precipitation and meltwater into the soil q_{in} [mm s^{-1}].

$$Q_{surface} = f_{sat} \; q_{\text{in}} \tag{2.14}$$

$$f_{sat} = f_{max} \; e^{0.5 \; f_{over} \; WTD} \tag{2.15}$$

The maximum saturated fraction f_{sat} [dimensionless] is defined as the share of the grid cell that is larger than the grid cell's mean compound topographic index, which quantifies the topographical control on runoff generation, based on the HYDRO1K dataset (Niu et al., 2005; Verdin & Greenlee, 1996).

Below the surface, CLM5 deploys a one-dimensional, multi-layer soil water model. Darcy's law describes the laminar flux of water across the soil depth and the layers q [mm s^{-1}] (Darcy, 1856; Dingman & Dingman, 2015) using the hydraulic potential, the sum of the soil matric potential ψ [mm] and the gravitational potential (here equal to the reference elevation z [mm], because the reference elevation is the surface).

$$q = -k \frac{\partial (\psi + z)}{\partial z} = -k \left(\frac{\partial \psi}{\partial z} + 1 \right) \tag{2.16}$$

k [mm s^{-1}] is the hydraulic conductivity, and varies with the volumetric soil water θ [mm^3 mm^{-3}] and soil texture per soil layer. The soil water mass conservation states:

$$\frac{\partial \theta}{\partial t} = -\frac{\partial q}{\partial z} - E \tag{2.17}$$

And substitution of q by the Equation (2.16) yields the Richards equation (Richards, 1931).

$$\frac{\partial \theta}{\partial t} = \frac{\partial}{\partial z}\left[k\left(\frac{\partial \psi}{\partial z} + 1\right)\right] - E \tag{2.18}$$

The rooting zone is parameterized per plant functional type, and the available water controls plant functioning. For example, the stomatal conductance is downregulated if the available soil moisture does not meet the transpiration demand.

The water cycle, vegetation productivity, and energy partitioning are intricately and non-linearly connected through processes, such as water vapor flux, vegetation physiology, ecosystem water use and management, and many more. This thesis will shed light on how these non-linear relationships appear across climate and ecosystem type gradients across the European continent, how they change with the climate, and with increasing severity and frequency of drought events.

3 Rising water-use efficiency in European grasslands is driven by increased primary production

This chapter is based on the journal article:

Poppe Terán, C., Naz, B.S., Graf, A., Qu, Y., Hendricks Franssen, H.-J., Baatz, R., Ciais, P., Vereecken, H., 2023. Rising water-use efficiency in European grasslands is driven by increased primary production. Commun Earth Environ 4, 95. https://doi.org/10.1038/s43247-023-00757-x

3.1 Introduction

The exchange rate of carbon between the land surface and the atmosphere determines the productivity of natural and cultivated ecosystems and influences the concentration of CO_2 in the atmosphere (Beer et al., 2010; Friedlingstein et al., 2022; C. Green & Byrne, 2004; Keenan & Williams, 2018; Reich, 2010). Through photosynthesis, vegetation drives the largest CO_2 flux from the atmosphere to the earth surface (Friedlingstein et al., 2022; Keenan & Williams, 2018), which is coupled to a simultaneous vapour outflux though open stomata (Cowan & Farquhar, 1977; Wright et al., 2004). Combining those fluxes by relating carbon assimilation flux to water loss, the water-use efficiency (WUE) (Cowan & Farquhar, 1977; Ehleringer et al., 1993; Hatfield & Dold, 2019) is a commonly used indicator to examine changes of ecosystem function (M. A. Adams et al., 2020; Beer et al., 2010; Belmecheri et al., 2021; Frank et al., 2015; M. Huang et al., 2015; Keenan et al., 2013; J. Liu et al., 2021; Peñuelas et al., 2011; Peters et al., 2018; J. Zhao et al., 2021) and ecosystem performance and fitness (Kühn et al., 2021). A recent study suggested that WUE constitutes one of three major axes of ecosystem function variability (Migliavacca et al., 2021).

WUE increased due to stomatal closure (M. A. Adams et al., 2020; Frank et al., 2015; Keenan et al., 2013; Marchand et al., 2020; M. Wang et al., 2018) in response to increasing atmospheric CO_2 since the beginning of the twentieth century. This effect of CO_2 on WUE is still not fully quantified and there is no consensus on its magnitude (Lavergne et al., 2019; Marchand et al., 2020). Moreover, changes of water supply and demand such as precipitation, soil moisture and vapour pressure deficit (VPD) have been identified as key factors influencing ecosystem

functioning and WUE variability (Beer et al., 2010; Belmecheri et al., 2021; Gu et al., 2021; Guerrieri et al., 2019; Lavergne et al., 2019; X. Liu et al., 2020; Mathias & Thomas, 2021). However, past large-scale spatiotemporal WUE analyses from remote sensing (RS) derived data rarely included long-term environmental effects (Lavergne et al., 2019) such as rising atmospheric CO_2 and atmospheric dryness and differ even in the sign of detected WUE trends (M. Huang et al., 2015; X. Liu et al., 2020; Tang et al., 2015). In addition, RS WUE studies investigating effects of a deficit of water resources, i.e. droughts, on WUE did not yet account for the plant physiological response to increased VPD during droughts by use of an adequate WUE index (L. Huang et al., 2017; M. Huang et al., 2021; Y. Yang et al., 2016). Hence, the spatiotemporal heterogeneity of WUE trends and effects of droughts remains poorly understood (Gu et al., 2021; M. Huang et al., 2021; M. Wang et al., 2021; Y. Yang et al., 2016). Their quantification from most recent RS data is important to enhance the understanding of impacts and feedbacks of climate change on ecosystem functioning across data sources and scales (Lavergne et al., 2019; Medlyn et al., 2017) as well as to provide insights to adequate functional discretizations and related parameter (Joshi et al., 2022; Keith et al., 2022) in land surface models.

Especially in Europe, where droughts were projected to increase in frequency and severity (Lehner et al., 2017), a detailed assessment of the WUE ecosystem function variability is required. Ranging from semi arid to very humid hydro-climates and from croplands and grasslands to evergreen forests, the pan-European domain also enabled analyses regarding the modulations of hydro-climate and land cover to the trends and drought response of WUE that have been found in past studies (Bai et al., 2020; Belmecheri et al., 2021; Cooley et al., 2022; Lavergne et al., 2019; Mathias & Thomas, 2021; Y. Yang et al., 2016). Nevertheless, a clear picture of the direction, magnitude and drivers of WUE trends and drought response in European hydro-climates and land cover has not yet been drawn. On top of that, the increasing availability of in-situ data on the continent provides a unique opportunity to assess the RS data quality and on the other hand the geographical, land-use and hydro-climatic coverage of those in-situ station networks.

In this study, we defined three WUE indices. Two by dividing carbon assimilation by ecosystem water-use, i.e. evapotranspiration (ET) and transpiration (T_r), resulting in EWUE and TWUE, respectively. Essentially, VPD has distinct effects on the carbon assimilation and the water-use of an ecosystem and is expected to increase during droughts. Therefore, the third WUE index relates carbon assimilation to canopy conductance (G_c) (IWUE) with a linear (Beer et al., 2010;

Keenan et al., 2013; Umair et al., 2020) implementation of VPD and captures the physiological response to drought by accounting for the regulation of transpiration to atmospheric water demand through adaptive stomatal opening. A more detailed description and their calculation is given in the Method section 3.2. Here we compared the trends and drought response of these WUE indices across hydro-climates and land cover to identify the adequate WUE index for estimations of ecosystem health and performance, as well as land surface model development.

The Global Land Surface Satellite (GLASS) photosynthesis (here rather: gross primary production, GPP) RS data (Liang et al., 2021; Zheng et al., 2020), includes the long-term effect of CO_2, VPD and temperature by use of the revised eddy covariance light-use efficiency model (Umair et al., 2020). So, we used the GLASS GPP and ET data (0.05° resolution, see Methods section 3.2 for more information on the data) and reanalysis data from the Global Land Evaporation Amsterdam Model (Martens et al., 2017) (GLEAM, T_r, 25km resolution), ERA5-Land (Copernicus Climate Change Service, 2019) (T_r, soil moisture, leaf area index, 9km resolution) and COSMO-REA6 (Bollmeyer et al., 2015) (meteorology, 6km resolution) from 1995 until 2018 over Europe. We aggregated the original data to 3km spatial resolution (to match future land surface model outputs) and 8-day temporal resolution (the coarsest resolution from the original data from GLASS RS). Relationships between ecosystem processes might vary with the seasons, e.g. different effect of droughts on WUE between during vegetation dormancy in winter and in summer, so we masked the data to the meteorological summer (June, July, August) to capture the most active period of the vegetation and to have a consistent signal of WUE drought response.

Finally, we (1) identified trends of summer WUE and differences between WUE indices on different land cover types, (2) detected the response of WUE to precipitation and soil moisture in summer drought conditions for hydro-climatic zones and (3) analyzed drivers of summer WUE variability using a discovery method for causal networks of ecosystem processes (Peter & Clark Momentary Conditional Independence (Runge et al., 2019), PCMCI+ (Runge, 2020)). Consequently, this work quantified regional variability of the summer WUE ecosystem function along recent decades and during droughts and identified distinct impacts of environment and ecosystem processes for different hydro-climate zones and land cover types. This work is important for the ongoing development of land surface models that incorporate functional variability to environmental factors and the assessment of ecosystem health and performance in the light of threatening changes in climate and environment.

3.2 Methods

3.2.1 GPP data

We used GLASS12B02 V40 (http://www.glass.umd.edu/introduction.html) (Liang et al., 2021) GPP data, which is in 0.05° spatial and 8 daily temporal resolution and was created with the revised EC-LUE model (Zheng et al., 2020) and includes long-term effects of CO_2, temperature (T) and VPD on GPP. While we left the assessment of the impact of the inclusion of those long-term environmental variables in GPP on WUE variability for future studies, we still validated this GPP product with FLUXNET2015 and ICOS Drought-2018 data (see their data descriptions below). To facilitate the data handling in this work and streamline comparisons with upcoming outputs from a land surface model, we aggregated this data from the original 0.05° resolution to the 3km European CORDEX domain (Giorgi et al., 2009) by bilinear interpolation. Then we compared the site GPP time series with those of corresponding grid cells in Table.A.3 and Table A.4 and the mean ET value of stations against the mean of corresponding grid cells in Figure A.10. We also plotted the geographical distribution of R^2 values between station and GLASS GPP in Figure A.2a. We assessed the validation as good (mean R^2 value of 0.67 across 60 FLUXNET2015 and 0.7 across 52 ICOS Drought2018 sites), but point out potential bias in regions where there less station density or no station data available at all (Southern and Eastern Europe).

3.2.2 ET data

The ET data used in this work is from GLASS11B02 V41 (http://www.glass.umd.edu/introduction.html), is calculated by a multi-model ensemble approach merging five process-based ET data (Liang et al., 2021) and has a 0.05° spatial and 8-daily temporal resolution. Similar to the GPP data described above, we linearly interpolated the GLASS ET data from the original 0.05° resolution to the 3km European CORDEX grid. Importantly, GLASS ET is given as latent heat in W m^{-2}, so we converted the values to mm day^{-1} by multiplying all values by 0.035, assuming a constant enthalpy of vaporization decoupled of variable temperature, which was applied in numerous studies before because of the small effect of variable enthalpy to the overall outcome of the conversion. Additionally to the validation with FLUXNET2015 and ICOS Drought-2018 ET (calculated from latent heat flux, see below) we also compared GLASS ET with reanalysis ET data from GLEAM3.5a (https://www.gleam.eu/), ERA5-Land (https://cds.climate.copernicus.eu/cdsapp#!/dataset/reanalysis-era5-

land). In Figure A.9 we plot mean FLUXNET2015 ET from stations against mean ET of the corresponding grid cell in GLASS, GLEAM and ERA5-Land ET. We decided to do our analyses with GLASS ET based on this result: The slope of GLASS ET against station ET shows better representation across sites than ERA5-Land and GLEAM. Again, in Table.A.3 and Table A.4 we present the R^2 between GLASS ET and station FLUXNET2015 and ICOS Drought-2018 ET time series. There is good agreement in the ET variability of GLASS and station ET, yielding mean R^2 across stations of 0.74 and 0.71 for FLUXNET2015 and ICOS Drought-2018 respectively. The geographical distribution of R^2 between stations and GLASS ET is also shown in Figure A.2b.

3.2.3 T_r data

Here we used GLEAM3.5a (https://www.gleam.eu/) T_r data (Martens et al., 2017) in all our analysis. The data is created in a land evaporation model and uses data assimilation of soil moisture from satellite observations. It is available in 0.25° spatial and daily resolution. We again bilinearly interpolated in space to the 3km European CORDEX grid, and aggregated the daily data to 8-daily means to make direct comparisons with the GLASS RS data. We compared GLEAM and ERA5-Land (https://cds.climate.copernicus.eu/cdsapp#!/dataset/reanalysis-era5-land) T_r with sap flow measurements from trees that we upscaled to forest stand T_r from SAPFLUXNET (Poyatos et al., 2020) (http://sapfluxnet.creaf.cat/). The results are shown in Table A.5. We opted for GLEAM T_r because of the higher mean R^2 across stations (0.42) than ERA5-Land (0.39). We add that the comparisons were biased because the upscaling from tree sap flow to tree stand transpiration did only represent one species (although this species dominated the forest) and did not represent understory transpiration at all while GLEAM transpiration represents whole ecosystem transpiration. Still, we were not aware of currently existing, more adequate homogeneous in-situ T_r data spanning multiple sites to verify transpiration directly at the moment and leave this out for future studies.

3.2.4 Meteorology data

Meteorological variables we used in this study were used to determine droughts (precipitation), hydro-climates (precipitation, annual sums (Jafari et al., 2018), see Figure A.1 and Table A.1) and/or environmental drivers in the PCMCI+ analysis (precipitation, temperature, shortwave incoming radiation, wind speed, relative humidity). All those values originated from the COSMO-REA6 (https://reanalysis.meteo.uni-bonn.de/?COSMO-REA6), a meteorological, high-resolution regional reanalysis over the European CORDEX domain in 6km spatial

and hourly time resolution with boundary conditions from ERA-Interim (Bollmeyer et al., 2015). Again, we bilinearly interpolated the data to 3km and aggregated to 8-daily means. This meteorological data also forces a land surface model, which will be used to elaborate on the current implementation of the WUE ecosystem function in Europe in an upcoming study. The VPD was calculated from the temperature and relative humidity after Allen et al., 1998:

$$E_s = 0.6108 \times e^{\frac{17.27 \times T}{T + 237.3}} \tag{3.1}$$

$$E_a = \frac{E_s \times RH}{100} \tag{3.2}$$

$$VPD = E_s - E_A \ [kPa] \tag{3.3}$$

Where E_S is the saturated vapour pressure and E_A the actual vapour pressure, T the temperature and RH the relative humidity.

3.2.5 Hydrology data and drought indices

We took soil moisture data from ERA5-Land (https://cds.climate.copernicus.eu/cdsapp#!/dataset/reanalysis-era5-land) at two different depth layers (0 – 7 cm, 7 – 28 cm). We bilinearly interpolated from the native 0.09° spatial resolution to the 3km European CORDEX grid and aggregated the daily values to 8-daily means. After we compared the WUE drought response based on drought indices of both, we opted to just use the surface soil moisture layer (0 – 7 cm) because the WUE response to soil moisture drought in both soil layers did not differ. The drought indices of precipitation and soil moisture of both layers were calculated using the climate indices python package (J. Adams, 2022) by fitting the soil moisture and precipitation of the whole 1995 – 2018 time series in every grid cell into a gamma distribution. Then we calculate standardized anomalies from the transformed time series:

$$SXI = \frac{X - \overline{X}}{\sigma_x} \tag{3.4}$$

Where X is the time series of the respective water resource (precipitation or soil moisture from both layers), and $\overline{X}$ and σ_x the mean and the standard deviation of the respective time series at the grid cell level. *SXI* represents the resulting standardized drought index, specific for the water resources, the standardized precipitation index (SPI) and the standardized soil moisture index (SSI) of the surface soil layer.

3.2.6 Leaf area index and land cover data

We obtained the leaf area index for the PCMCI+ analysis from the ERA5-Land. We bilinearly interpolated from the 0.09° native spatial resolution to the 3km European CORDEX grid and aggregated the daily data to 8-daily means.

The land cover data is IGBP-Modified MODIS 20-category data from MCD12Q1 (https://lpdaac.usgs.gov/products/mcd12q1v006/). We upscaled the data from 500m native spatial resolution to our 3km European CORDEX working grid by selecting the dominant land cover within the native grid cells whose centers lay inside the coarser 3km grid cell. Therefore, the land cover indications refer in this paper refer to the grid cell specific dominant land cover type by area.

3.2.7 In-situ observation data and validation

We used in-situ observation data from three different networks, that are FLUXNET2015 (Pastorello et al., 2020) (60 sites, 569 site-years) and ICOS Drought-2018 (Drought 2018 Team & ICOS Ecosystem Thematic Centre, 2020) (42 sites, 577 site-years) for GPP and ET and SAPFLUXNET (54 sites, 180 site years) for sap flux.

The ICOS Drought-2018 data used the FLUXNET format (Pastorello et al., 2020) and methodology that is also used in FLUXNET2015, so here we describe how we used them for both. We used the GPP variable estimated by night-time partitioning from net ecosystem exchange with variable threshold on friction velocity dependence ('GPP_NT_VUT_REF' variable). We masked this variable based on estimations of data quality of net ecosystem exchange ('NEE_VUT_REF_QC' variable), which is the measured variable before GPP gets partitioned from it. Similarly, to use in-situ ET observations, we took the measured latent heat flux from those data ('LE_F_MDS' variable) that uses the marginal distribution sampling technique (MDS) for gap filling. This variable was again masked by data quality measure ('LE_F_MDS_QC' variable). Then, we converted W m^{-2} to mm day^{-1} by multiplying all values by 0.035, assuming a constant enthalpy of vaporization decoupled of variable temperature, which was applied in numerous studies before because of the small effect of variable enthalpy to the overall outcome of the conversion.

As in-situ T_r data remains scarce, we opted to use a pan-European in-situ data of sap flux measurements and upscale them to the tree stand with the method seen in Nelson et al., 2020: We normalized daily tree sap flow values to the unit basal area of each tree and averaged the values for each species present in the stand. In

all stands, species where sap flow was measured covered 90% of the total stand basal area. Then we multiplied the species-specific sap flow per basal area by the basal area of each species in the stand and summed the resulting T_r of all species to obtain the stand level T_r in mm day^{-1}.

For the validation, we first found the closest grid cell in the 3km European CORDEX grid, which the spatial data where regridded to before (see above), to the coordinates of the observation station. Closest grid cell means the grid cell where the grid cell center has the shortest distance to the observation coordinates. We extract the GPP, ET and T_r variables from the aggregated spatial data and calculated R^2 between the time series of the station and the grid cell level data of the spatial data.

3.2.8 Determination of WUE drought response

We then identified the drought response in each location or grid cell as the difference of the median WUE only in drought years to the overall median WUE in that grid cell. For this, we defined a drought where the monthly SSI or SPI is less than -1. Similarly, drought severity categories were defined over the monthly SPI and SSI bins based on thresholds from Table A.2. Respective drought response refer to the difference between the median WUE when the drought index is within the given bin and the overall median WUE at this location.

3.2.9 Resulting European data for WUE analyses

We aggregated the spatial data to one single netCDF file. This data is in the 3km European CORDEX grid, in 8-daily time-steps from 1995 until 2018 and comprises of variables from GLASS remote sensing (GPP, ET), GLEAM reanalysis (ET, T_r, surface and root layer soil moisture), ERA5-Land reanalysis (ET, T_r, surface and first sub-surface layer soil moisture, leaf area index), and COSMO-REA6 meteorology (temperature, precipitation, relative humidity, incoming shortwave radiation, wind speed). The data can be made available upon request.

3.2.10 Water-use efficiency indices

The WUE indices are calculated from the data choices described above. We calculated the EWUE index based on the GPP and ET from GLASS remote sensing:

$$EWUE = \frac{GPP}{ET} \; [g \;\; C \;\; mm^{-1}] \qquad (3.5)$$

The TWUE index is based on GLASS GPP and GLEAM T_r:

$$TWUE = \frac{GPP}{T_r} \; [g \;\; C \;\; mm^{-1}] \tag{3.6}$$

To calculate the IWUE index, that considers the canopy conductance G_c rather than actual water-use per se, we first define G_c as:

$$G_c = \frac{T_r}{VPD} \; [mm \;\; kPa^{-1}] \tag{3.7}$$

With T_r from GLEAM and VPD calculated from COSMO-REA6 (see above). Therefore, IWUE results as:

$$IWUE = \frac{GPP}{G_c} = \frac{GPP}{T_r} \times VPD = TWUE \times VPD \; [g \;\; C \;\; kPa \;\; mm^{-1}] \tag{3.8}$$

3.2.11 Trend analysis

The WUE slope, intercept and p values were calculated in each grid cell using the non-parametric, seasonal Mann-Kendall analysis from the python package pymannkendall (Hussain & Mahmud, 2019) for monthly values from 1995 – 2018 masked to the summer months June, July and August. The slope is determined as the Theil-Sen estimator slope and the p value with a two-tailed test. We estimated median trends and intercepts of geographic regions and land cover by first determining the grid cells corresponding to a certain region or to one particular or a group of land cover and then calculating the median slope and intercept values corresponding to those grid cells, respectively. The relative median trend is then calculated by dividing the resulting scalars median trend by median intercept. We chose the intercept as the relative reference because it represents the regression value at the start of the time series, in our case i.e. beginning of 1995 and by multiplying with the number of years, i.e. 24, we got the total relative change of the trend regression during this study period.

3.2.12 Causal network analysis

PCMCI+ (Runge, 2020; Runge et al., 2019) is a causal network discovery method, which can estimate contemporary and lagged dependencies between time series. Important assumptions to entitle causality in PCMCI+ is causal and time series stationarity and causal sufficiency. To fulfill causal sufficiency, we included as many as 11 variables related to ecosystem process variability (i.e. GPP, ET, T_r, temperature, relative humidity, VPD, G_c, shortwave incoming radiation, wind

speed, precipitation, soil moisture and the leaf area index) and selected possible links of physically plausible relationships using the selected_links parameter and a significance level threshold of 0.01. Although some links of the network were not analysed here, their inclusion secured causal sufficiency (consideration of all possible common influencing factors to a variable) and they will be scrutinized in future investigations. We approximated causal stationarity by masking the time series to the summer season to omit changing relationships between variables, e.g. shortwave incoming radiation→GPP in deciduous forests is given in summer but not in winter (Krich et al., 2020). We further acknowledged changes in the causal relationships between the variables during special conditions, such as extreme high temperatures (Krich et al., 2022), and in the long-term over the 24-year period but we argue that they are negligible in the 8-day timely resolution in our data. Time series stationarity is satisfied by detrending and using seasonal anomalies of the time series of each variable that have already been masked to the summer months, before inputting into the PCMCI+ algorithm of the python package tigramite (https://github.com/jakobrunge/tigramite). We conducted three analyses whereby we added one respective WUE index to the input variables and adapted the selected_links parameter to match the possible links between the different components and their respective WUE index and no lag of causal relationships. Directed causal links between variables are iteratively found with conditional independence tests. We remark that some relationships among the selected links are of nonlinear nature. Nonlinear conditional independence tests in the PCMCI+ algorithm exist, however the detection power of linear links will be inhibited. We chose to assume a linear causal network as we are predominantly interested in how the strength of particular links vary across networks aggregations of regions, climates and land cover. Therefore we opted for the linear partial correlation conditional independence test for the cost of potential false positives and false negatives, but is still able to detect small nonlinearities. We minimized the impact of this uncertainty by limiting the network to physically possible and plausible links with the selected_links parameter as described above. For the full methodological description of PCMCI+ we refer to Runge, 2020. The network including all possible links through our selected_links control is shown in Figure A.11. Importantly, the total possible network may not make sense as such but enables PCMCI+ to unravel the different causal networks of hydro-climates and land cover. An exemplary causal graph output from PCMCI+ for a grid cell corresponding to the Wüstebach ICOS station (DE-RuW) for the EWUE index is shown in Figure A.12.

To identify shifts in the causal network resulting from a particular environmental condition, two causal networks have to be determined: One with time series including this particular effect and one without. The differences in the detected links and link strengths between those two networks are the effect of the environmental condition on the causal network. We investigated the effects of drought on the causal network by splitting the grid cell time series of all variables into two: one only containing values corresponding with SSI values lower than -1, and another non-drought time series, containing all other values. Then we subtracted the absolute link strengths of the non-drought from the drought network to have the difference network representing all link changes during droughts.

$$Link_{response} = Link_{drought} - Link_{non-drought} \tag{3.9}$$

Where *Link* is a chosen link of the causal network, $Link_{drought}$ the strength, or partial correlation, of the chosen link in the casual network during droughts and $Link_{non\text{-}drought}$ the strength of the chosen link in the non-drought causal network. Therefore, we applied PCMCI+ to each land surface cell in the study grid for three WUE indices and for non-drought periods, drought periods and overall, resulting in a high dimensional output with six causal networks from mentioned variables for each cell.

3.3 Results

3.3.1 All WUE indices decrease in Central Europe

Several aspects of ongoing global change (e.g. anthropogenically driven increased CO_2 and resulting changes and temperature and VPD) were found to affect the WUE (Beer et al., 2009; Dekker et al., 2016; Guerrieri et al., 2019; M. Huang et al., 2015; Keenan et al., 2013; Q. Zhang et al., 2019). To identify resulting long-term changes we conducted pixel-wise seasonal Mann-Kendall trend analyses that show spatially extensive, significant ($p < 0.05$) negative summer EWUE trends in Eastern and Central Europe (Figure 3.1a).

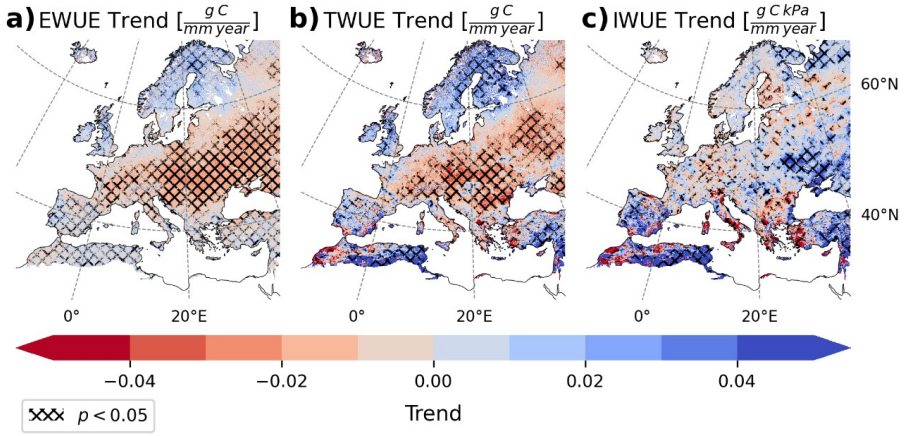

Figure 3.1: Albeit different directionality of trends elsewhere, all indices agree on decreasing summer WUE in Central Europe. In the summer seasons (June, July and August) over the years 1995 – 2018, EWUE (a), TWUE (b) and IWUE (c) trends were calculated over monthly time series for each grid cell with the seasonal Mann-Kendall analysis. The cross hatches mark areas where the trends are significant ($p < 0.05$).

There was a radial gradient from these continental regions outward towards significant increases in North and South Europe. The median relative change of the whole domain was -5.2%. The total relative changes here and later refer to the ratio of median of slopes of corresponding pixels to the median of intercepts of the same over the whole 24-year period 1995 – 2018. Therefore, the continental WUE change was dominated by the extensive negative trends in Eastern and Central Europe (Figure A.1 for the extents of the regions) which changed by -17.2% and -8.8%. The negative median decreasing trend agrees with MODIS products analyses by (Tang et al., 2015) who found decreasing global EWUE, although no resolved signal for Europe was shown. Other studies using MODIS data (L. Huang et al., 2017; Xia et al., 2015) outlined decreases of a much smaller extent in Eastern Europe until 2014 than we found here, but showed positive trends over most remaining parts of Europe. Importantly, the inclusion here of (1) the long-term influences of CO_2 and VPD to GPP and (2) recent years, 2014 until 2018, might be reasons for differences to mentioned studies. The decreasing trends in EWUE are also evident in station scale and spatially upscaled EWUE estimates from eddy-covariance (EC) measurements which show mostly negative trends in Europe, and a small increase in the southern, more arid areas of the continent (M. Huang et al., 2015; L. Zhang et al., 2020) as well. However, site network data was not able to confirm the decreases in Eastern Europe due to the lack of stations in that area (Figure A.2 for the distribution of EC stations in used data in Europe).

In Figure 3.1b, the summer TWUE trends show the same negative sign and a similar magnitude in Central and Eastern Europe as EWUE trends. The different trend slope from Central and East to Northern and Southern Europe was evident again. However, the extent of significant trends was not as coherent as with EWUE trends: Patchiness of the sign of TWUE trend implies higher spatiotemporal heterogeneity of T_r than of ET. Europe had a median TWUE change of -3.0%. Regionally, Eastern and Central Europe TWUE changed by -12.9% and -8.9% respectively. Scandinavia experienced a TWUE change of +10.7% during the whole study period. These trends agree better than EWUE with previous modeling studies (M. Huang et al., 2016).

In contrast, the median summer IWUE change across the region was positive (+4.6%). Further, in contrast to EWUE and TWUE, there were significant positive summer IWUE trends in Eastern Europe (Figure 3.1c). There, IWUE changed by a median of +5.2% and on the Iberian Peninsula by +10.0%. However, as for EWUE and TWUE, also IWUE shows a negative change in Central Europe by -4.2% over the 24-year study period. We also aggregated the trend slopes over areas of selected land cover types (Figure A.3 for a map of land cover types). We found that IWUE of evergreen needleleaf and deciduous broadleaf forests both changed by +3.0%. Further, in croplands IWUE increased by +5.6% and grassland IWUE changed by a higher margin of +24.2%.

An increase of forest IWUE was recorded in previous studies (M. A. Adams et al., 2020; Frank et al., 2015; Keenan et al., 2013; Lavergne et al., 2019; Marchand et al., 2020) and mostly explained by long-term elevated CO_2 concentration in the atmosphere. Nevertheless, the magnitude of the forest IWUE increase from tree-ring studies is still debated (Gong et al., 2022). Our results agree with the directionality of trends from eddy covariance towers of Keenan et al., 2013 and Mastrotheodoros et al., 2017, but here we had a more extensive time period including more recent years and state a substantially lower magnitude of IWUE trends (0.12% $year^{-1}$) in forests. Frank et al., 2015, also found IWUE increases in broadleaf and needleleaf forests solely driven by CO_2 based on tree ring isotope measurements. Here we did not find a distinct magnitude of increasing trends between needleleaf and evergreen forests, in contrast to tree-scale studies (Lavergne et al., 2019; M. Wang et al., 2018).

3.3.2 Contrasting drought response between WUE indices

We further analysed the Europe-wide impacts of precipitation and soil moisture summer droughts on WUE anomalies. We first calculated the standardized

precipitation index (SPI) and the standardized soil moisture index (SSI) over the whole study period for each grid cell on a monthly time scale (see Methods section 3.2 for more details). Then, we determined monthly anomalies of each WUE index when the drought index indicates drier than normal conditions, i.e. when it is lower than -1. Finally, the summer WUE drought response (Figure 3.2) at each location is the median of its drought anomalies over all summer seasons.

Generally, we found a larger response for SSI (Figure 3.2b, d, f) than for SPI droughts (Figure 3.2a, c, e) with all WUE indices. EWUE and TWUE both respond predominantly negative to drought, on over 80% of Europe for SPI, and on over 78.9% and 66.3% for SSI droughts, respectively. For each grid cell we estimated the relative drought response by relating the median drought response to the overall median WUE over the study period for that same grid cell. The median relative SPI drought response of EWUE and TWUE over the whole domain was -8.6% and -8.5%, respectively, and the response to SSI droughts were slightly larger for EWUE (-9.4%) and lower for TWUE (-7.6%). Notably, largest regional response of both, EWUE and TWUE, happened in Central Europe during SSI droughts, -15.3% and -14.4% , respectively. The Mediterranean, however, was the only region with a median positive TWUE response, which amounted to +2.6% during SSI droughts. In contrast, IWUE responded positively to drought virtually ubiquitous (over 90% of Europe for both drought types), so that the median response to SPI droughts was +17.3% and to SSI droughts was +23.6%. Same as with the other WUE indices, the response of IWUE was larger during SSI droughts. The highest regional response was in the Mediterranean, accounting for +31.7% and +23.1% during SPI and SSI droughts. Note a gradient from Northern humid regions with lower drought response toward higher response in drier areas in the South.

We found agreement on a generally negative EWUE drought response with other past studies based on site scale FLUXNET and spatial MODIS data (L. Huang et al., 2017; J. Zhao et al., 2021). In particular the study of Peters et al., 2018 based on atmospheric carbon isotope data also found increased IWUE during severe drought events for the Northern hemisphere. Using remote sensing data of ET and T_r and site-scale GPP, Gu et al., 2021 discovered discrepant EWUE (positive) and TWUE (negative) drought response. However, we found that our results showing mostly negative EWUE drought response of forests disagree with L. Huang et al., 2017, who used MODIS data and found mostly increasing EWUE in Europe. The usage of data of different scales (grid cell remote sensing water-use to site scale GPP) as well as analysis exclusively at EC site locations in their

analysis could explain the different EWUE drought response between their analysis and here.

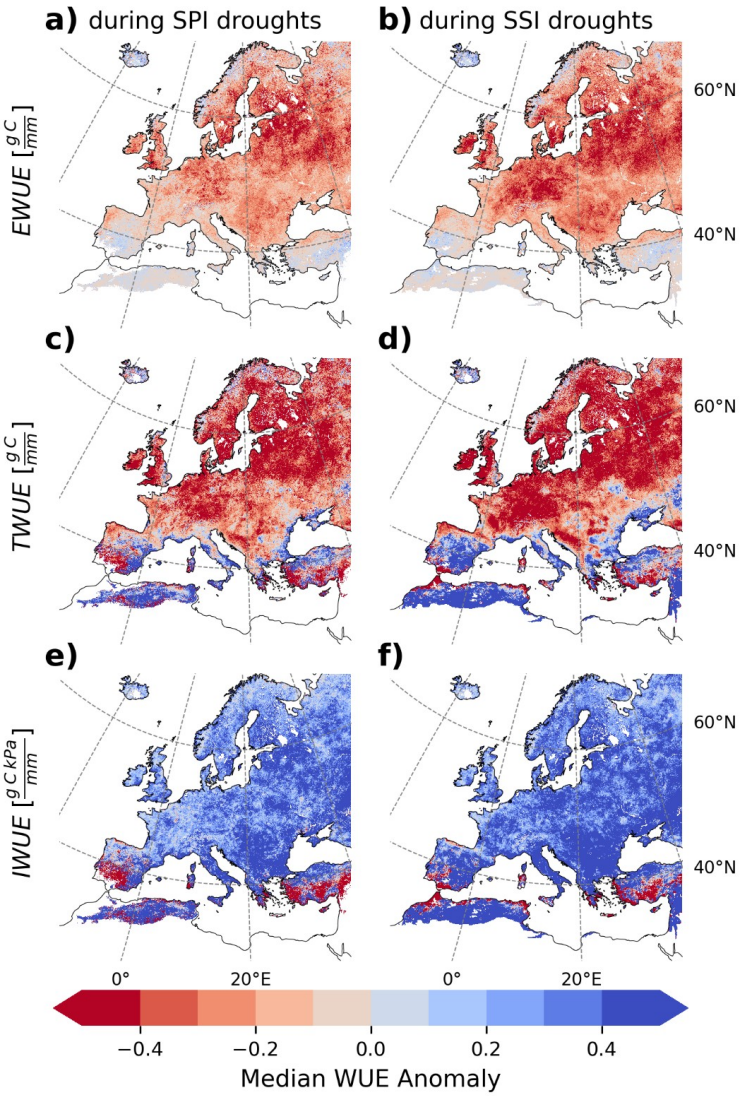

Figure 3.2: The magnitude of WUE response to droughts depends on the drought severity and the hydro-climate. Shown here are EWUE (a, b), TWUE (c, d) and IWUE (e, f) median anomalies (color map) to indicate the drought response during instances of standardized precipitation (SPI) (a, c, e) and soil moisture (SSI) (b, d, f) anomaly categories (x-axes) and hydro-climates (y-axes, Figure A.1, Table A.1 and Table A.2).

3.3.3 Gradient of WUE drought response across hydro-climates

We then analysed the WUE response to different summer drought categories in hydro-climates (Figure 3.3) to identify their relationship as well as conditions with an optimal WUE (Beer et al., 2009; Y. Yang et al., 2021; J. Zhao et al., 2021). For that, we determined zones of hydro-climates based on annual precipitation (Jafari et al., 2018) (Figure A.1 and Table A.1) and calculated median WUE anomalies (defined here as drought response) within the hydro-climate during occurrences of seven categories of summer SPI and SSI indices ranging between ≤ -2 and > 2 (Table A.2) on a monthly period.

In Figure 3.3a we uncovered two gradients of EWUE response to SPI categories: (1, along the x-axis) from negative response during dry conditions to positive response during wet conditions with larger response during more extreme conditions and (2, along the y-axis) increasing negative drought response in dry conditions across all hydro-climates. Here for EWUE, gradient (2) is exhibited by low response in very humid and arid and the largest response in semi humid hydro-climates. Both these gradients were more pronouncedly evident for SSI categories (Figure 3.3b). J. Zhao et al., 2021 also showed increasing negative EWUE drought response with drought severity from FLUXNET data, but in contrast to our study, they showed negative EWUE response during wet conditions.

Similarly, TWUE response also followed both gradients (1) and (2) in very humid to semi humid regions along SPI (Figure 3.3c) and SSI (Figure 3.3d) categories. But in semi arid and arid hydro-climates, we found generally smaller response of EWUE and TWUE along SPI categories and a reversed gradient (1) for TWUE along SSI categories, i.e. positive response during dry and negative during wet conditions.

This reversed gradient (1) was again observed in IWUE response but across all hydro-climates for both drought types (Figure 3.3e and f). Gradient (2) in the IWUE response to SPI droughts was directed towards the largest positive response in semi humid and humid hydro-climates, while during SSI dry and wet conditions it was towards semi arid regions.

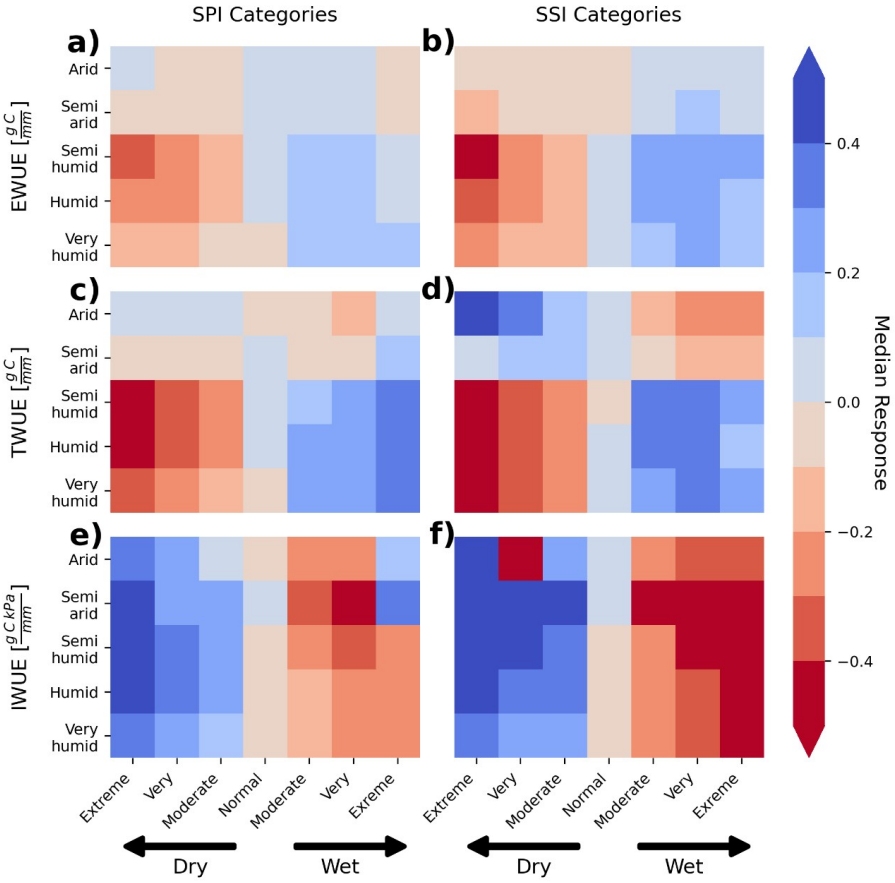

Figure 3.3: The magnitude of WUE response to droughts depends on the drought severity and the hydro-climate. Shown here are EWUE (a, b), TWUE (c, d) and IWUE (e, f) median anomalies (color map) to indicate the drought response during instances of standardized precipitation (SPI) (a, c, e) and soil moisture (SSI) (b, d, f) anomaly categories (x-axes) and hydro-climates (y-axes, Figure A.1, Table A.1 and Table A.2).

3.3.4 Drivers of WUE change and WUE drought response

We conducted a causal network discovery analysis to understand the relationships between meteorological, hydrological and biogeochemical variables and how they interacted to cause WUE variability for all summer months (Figure 3.4) and how these interactions differed during droughts (Figure A.8). In particular, we applied the PCMCI+ method (Runge, 2020; Runge et al., 2019) to create a causal network (see Methods section 3.2.12 and Figure A.11 and Figure A.12) out of the input time series of considered variables for each grid cell. We limited this analysis to the link strengths, i.e. partial correlations, where PCMCI+ yielded directed, significant ($p < 0.01$) causal links. It is clear that by definition, both, GPP and ET

cause WUE variability. However, their individual contribution to WUE changes might differ depending on geography and environment, so that either GPP or ET, or both similarly, are responsible for those WUE changes. Furthermore, it is important to understand that the resulting network does not directly yield the drivers of long-term changes of a selected variable. Rather, the network depicts the drivers of small-scale changes, identifying the contribution of a certain variable at the link source (arrow beginning) to the overall variability link destination (arrow head, see examples Figure A.11 and Figure A.12). The input time series to the PCMCI+ analysis were detrended and anomalized.

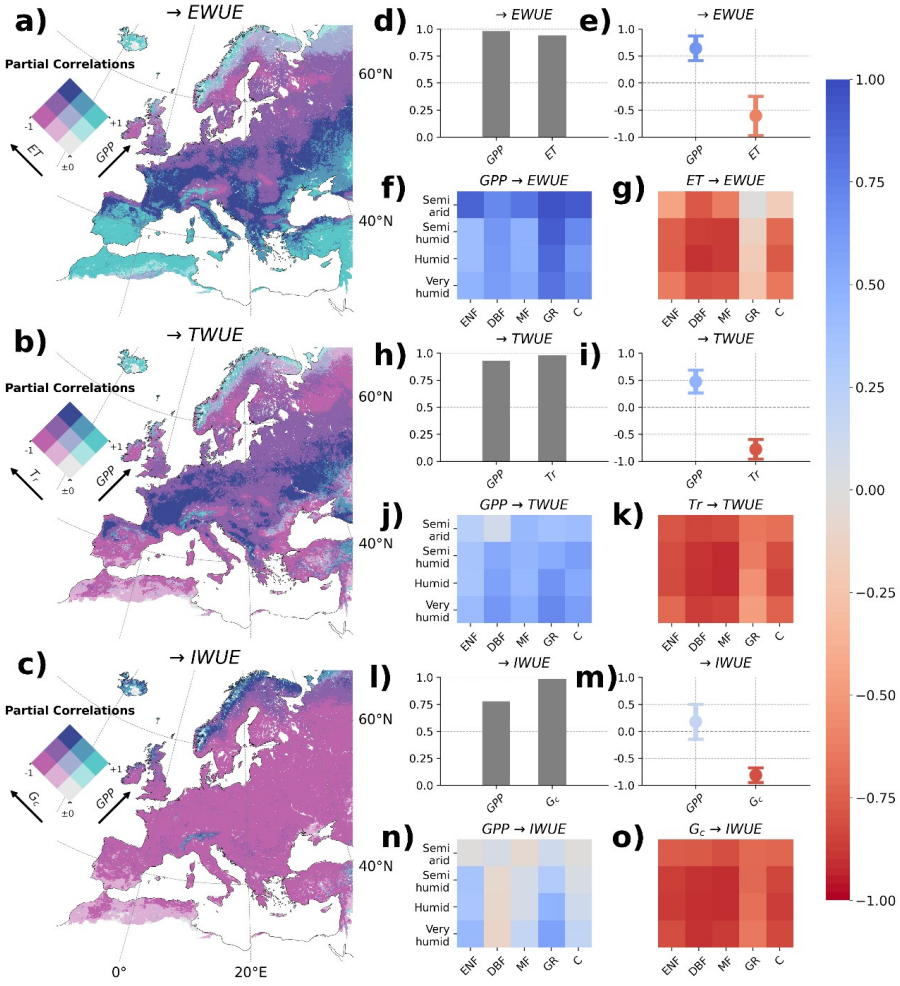

Figure 3.4: EWUE change is caused by gross primary production (GPP) on the Iberian Peninsula and evapotranspiration (ET) variability in Central and Eastern Europe, while we determined less directed causal links to TWUE and IWUE. Here we show partial correlations of GPP versus ET to EWUE (a), GPP versus transpiration (T_r) to TWUE (b) and GPP versus canopy conductance (G_c) to IWUE (c) from the PCMCI+

analysis. Green colors show a stronger link between GPP and WUE variability, and pink colors a stronger link between water-use and WUE, while gray shows low correlations and dark purple strong correlations of both. On the right side, we show for each map the relative area to the total land surface where PCMCI+ yielded directed links from GPP and water-use WUE (d, h, l) and the respective mean partial correlations (circle) across the continent with the standard deviation (error range marker) (e, i, m). Lastly, we aggregate the partial correlations of those links (f, g, j, k, n, o) over land cover (x-axes, ENF =Evergreen Needleleaf Forest, DBF = Deciduous Broadleaf Forest, MF = Mixed Forest, GR = Grasslands, C = Croplands) and hydro-climates (y-axes).

First, we scrutinized the causal networks resulting from all summer months (drought as well as non-drought months included). GPP was significantly linked to EWUE variability on a greater share of Europe than ET (Figure 3.4d) but both correlated on average and in absolute values almost equally strong with EWUE (+0.66±0.21 and -0.6±0.36, Figure 3.4e). On the Iberian Peninsula, GPP variability was the predominant cause of EWUE changes on 92.9% of its area (where the correlations of the link GPP→EWUE were above +0.66). Around France GPP and ET did both control EWUE. However, in Central and Eastern Europe 94.7% and 86.4% of the regions had rather ET caused EWUE changes, and a much smaller area with strong links between GPP and EWUE.

Generally, PCMCI+ determined less grid cells with directed links from GPP towards TWUE and IWUE than to EWUE (compare totals of Figure 3.4d, h, l). Further, the mean link strength between GPP and TWUE as well as IWUE was lower than to EWUE (compare Figure 3.4e, i, m). While the zones where GPP and water-use influence were both strong around France and north of the Black Sea remained when investigating TWUE (Figure 3.4b), the predominance of GPP influence in the Iberian Peninsula and the Mediterranean on TWUE was not present. Rather, TWUE was mostly transpiration controlled (Tr→TWUE < -0.66 on 76.8% of Europe). Only in Scandinavia along the coast and on Iceland GPP prevailed primal driver of TWUE. We found again less occasions where GPP caused IWUE (Figure 3.4l), and on at least 90% of the total area G_c dominated over GPP in the control of IWUE variability.

Then, we aggregated mean partial correlations from the directed links of the PCMCI+ analysis towards WUE (Figure 3.4f, g, j, k, n, o) and towards GPP, T_r and G_c (Figure A.6 and Figure A.7) over hydro-classes and land cover. In grasslands, the GPP→EWUE link was especially strong for all hydro-climates (Figure 3.4f), in exchange for a weak link between ET and EWUE (Figure 3.4g). Concurrently, also in grasslands, there was a weak connection between temperature as well as soil moisture to GPP (Figure A.6a and b) as well as strong T_r dependent G_c (Figure A.7b). We found that besides the predominance of the G_c control on IWUE in

other ecosystems, in grasslands and evergreen needleleaf forests GPP still accounted for a fair share of IWUE variability.

Just across hydro-climates, we discovered stronger links from GPP to EWUE (Figure 3.4f) and weaker links from ET to EWUE (Figure 3.4g) in semi arid than in more humid areas. An influence of hydro-climate on the GPP to TWUE link was only clearly visible for deciduous broadleaf forests and grasslands (Figure 3.4j, both towards stronger GPP→TWUE links in very humid areas), the strongest T_r→TWUE links, however, were in in semi-humid and humid hydro-climates (Figure 3.4k). Aside from the low average influence of GPP on IWUE across the continent that we described before, Figure 3.4n also shows that this link still played a role for evergreen needleleaf forests and grasslands and it was modulated by hydro-climate, so that the weakest GPP→IWUE links were in semi arid and the strongest in very humid areas. The G_c influence on IWUE shows lower correlations generally in semi arid zones throughout all land cover and in grasslands across all hydro-climates.

The input for a second PCMCI+ analysis were only those values in the time series of the considered variables that concurred with a soil moisture drought (SSI < -1). We did the same processing of the data to create the European interaction maps of GPP and ET links in Figure A.8a, b and c as we did in Figure 3.4a, b, and c. For the bars of relative area covered by significant links (Figure A.8d, h and l), the mean link strengths (Figure A.8e, i and m) and the aggregations of mean link strengths across hydro-climate and land cover (Figure A.8f, g, j, k, n and o), we rather show the absolute difference of the corresponding values between the drought and the non-drought PCMCI+ analyses, to highlight the aggregated response of the links to droughts (see Methods section 3.2.12 for a more detailed description).

The number of grid cells and therefore the relative area with significant links between GPP, water-use or G_c have generally decreased (Figure A.8d, h and l), but by a rather small magnitude (always less than 5%). Further, the influence of GPP on EWUE increased and the influence of ET on EWUE decreased during droughts (Figure A.8e). Geographically, this meant more extensive sole GPP control over EWUE in Southern Europe, and more co-control of EWUE by GPP in Central and Eastern Europe. This was noticeable through more green colors in the South and shifts from pink and purple to dark purple in Central and Eastern Europe between Figure 3.4a and Figure A.8a. Similarly, GPP influence on drought TWUE increased and T_r decreased (Figure A.8i), mostly noticeable in Central and Eastern Europe (compare Figure 3.4b and Figure A.8b). However,

droughts did not change the interactions of IWUE drivers much. The already small GPP influence on IWUE in general decreased during droughts (Figure A.8m), but the ubiquitous G_c influence persisted.

Furthermore, the aggregated drought response of GPP and water-use links to WUE along hydro-climate and land cover were more nuanced. We found a contrasting GPP→EWUE drought response between semi arid (negative) and more humid hydro-climates (positive), particularly in grasslands and croplands (Figure A.8f). The response of the ET→EWUE link to drought was also reversed (positive) in semi arid grasslands than in other ecosystems (negative). In deciduous broadleaf and mixed forests, as well as in croplands, the drought-related link strength reductions of ET to EWUE and T_r to TWUE, were most dominant, while evergreen needleleaf and mixed forests experienced the strongest increases in GPP influence on both EWUE and TWUE. The semi arid regions showed a contrasting response of the T_r→TWUE link in deciduous broadleaf forests, where T_r influence increased. Again inverted drought response of GPP→IWUE link in semi arid hydro-climates response was most dominant in grasslands and croplands, and for G_c→IWUE in deciduous broadleaf and evergreen needleleaf forests. The reduction of GPP influence on IWUE during droughts was most accentuated in very humid evergreen needleleaf forests.

3.4 Discussion

To comprehensively describe the variability of the important WUE ecosystem function along recent climate change, we conducted analyses on the summer-time trends, drought response and the causes of variability across the European continent using novel RS and reanalysis data. Here we did not include investigations on particular effects of the newly included influences of CO_2 and VPD in the RS GPP data on our WUE analysis. But these developments are welcome because the missing influences on GPP and resulting uncertainties on long-term WUE trends were a main point of criticism on RS-based WUE studies (Lavergne et al., 2019). Nevertheless, the RS GPP model implementations and underlying data uncertainty must still be scrutinized with respect to WUE. Future works might therefore use control data without these inclusions and test their incorporation to assess the effect on WUE variability.

A Mann-Kendall seasonal trend analysis showed EWUE and TWUE decreased in Central and Eastern Europe and increased in Northern Europe and the Iberian Peninsula. IWUE on the other hand mostly increased but aligns with the other indices on decreases in Central Europe. The dominant increase of IWUE was in

accordance with previous studies from different data sources and scales (M. A. Adams et al., 2020; Frank et al., 2015; M. Huang et al., 2015; Keenan et al., 2013; Lavergne et al., 2019; Marchand et al., 2020; M. Wang et al., 2018). But here we also showed highly resolved, spatially extensive, significant decreases of all three WUE indices in Central Europe and of EWUE and TWUE in Eastern Europe which could not yet be confirmed in in-situ data yet, due to the lack of eddy covariance measurements there.

As indicated by Kühn et al., 2021, increasing WUE is a trait that is related to enhanced plant performance and fitness irrespective of the WUE index at plant scale. We assumed the relationship of WUE on ecosystem performance and fitness to persist on grid cell scale, but found inconsistency of WUE trend direction between indices (negative for EWUE and TWUE and positive for IWUE). Therefore, we concluded that the IWUE index, which considers the eco-physiological adaptation of G_c and hence compares better with plant scale WUE, is best for inference of ecosystem performance and fitness. Consequently, declining IWUE from our trend analysis indicated ecosystems that potentially did not adapt well to environmental changes and have weakened functionality and performance: the Central European region, in the Central Alps, Balkan and western Turkey as well as Southern Finland (Figure 3.1c). Irrespective of the hydro-climate, we observed increased IWUE indicated enhanced ecosystem performance, particularly in grasslands (Figure A.4c), and decreased performance in mixed forests. Other land cover have contrasting directionality of IWUE trends and performance across hydro-climates. We note that increased plant IWUE is also a response to stress, and increased performance is not directly associated with increased ecosystem health. Nevertheless, plants and ecosystems that can efficiently adapt IWUE positively to changes in environmental conditions have an advantage with ongoing climate change. Future studies might verify the scaling and from plant to ecosystem and grid cell IWUE trends and the inference of ecosystem performance, but for that more extensive in-situ ecosystem observation data is needed. Because of the contradicting trends, drought-response and drivers between WUE indices, analyses on ecosystem performance from large-scale and spatiotemporal continuous data such as remote sensing, reanalysis and land surface model outputs might focus specifically on the IWUE index. These results create concrete functional references for land surface model developers as well as insights into relationships between ecosystem functioning and performance.

We did not find distinct IWUE trends between needleleaf and broadleaf forest land cover types, exhibiting the known discrepancy between leaf-scale and

ecosystem scale WUE (Lavergne et al., 2019). We hypothesized that the potential bias from representing spatial homogeneity of ecosystems by aggregation of grid cells by dominant land cover is not significant, because EC measurements (which are based on single land cover ecosystems) also did not show significantly different WUE trends between land cover either (Lavergne et al., 2019). The potential spatial aggregation bias also averaged off, by use of an adequately high number of grid cells with corresponding dominant land cover and might yield statistically more sound conceptual conclusions on discrete ecosystems than EC measurements from only a few dozen sites with short time series and underrepresented geographical regions and hydro-climates. Still, and importantly, the data used in our study was subject to several uncertainties. Those include lack of representation of vegetation and atmosphere interactions, e.g. the influence of WUE changes on above-canopy VPD that was not present in the meteorological data from COSMO-REA6 used here. Further, the remote sensing and reanalysis models are forced with different input data, so that drought response of leaf area index (and further GPP, ET and WUE) might occasionally be shifted in time. Though, we assess this effect over an 8-daily time resolution to be negligible. Furthermore, the vegetation response from long-term environmental effects from rising CO_2 and VPD in the used GLASS GPP data might not be reflected in e.g. ERA5-Land vegetation and soil moisture data, and cause bias in the TWUE and IWUE trends. We found that the GPP and ET data used in our study compared well with in-situ measurements by validating time-series from corresponding grid cells with time series from eddy covariance sites (See Methods section 3.2.1 - 3.2.3 and Table.A.3 and Table A.4). The T_r data was compared to plant sap flow measurements upscaled to forest stand (see Methods and Table A.5) but did not yield satisfactory results. This could be due to uncertainties in the scaling process and the different ecosystem representation of the grid cell data and upscaled sap flux data. However, large scale spatial and in-situ T_r data alternatives remain scarce. Further development of in-situ and spatial T_r estimates will be appreciated, and in future those should be evaluated on WUE ecosystem function estimations. WUE calculations, trends and drought response then depend on the combination of uncertainties for each variable, amplifying the uncertainty range for the WUE indices. A future study will compare WUE estimations from eddy covariance sites with corresponding grid cells in our data and land surface model output, to evaluate this uncertainty in more detail.

Further we found negative drought response of EWUE and TWUE to both precipitation and soil moisture droughts, while IWUE responded positively (Figure 3.2). All WUE indices showed larger response during more severe drought

conditions, and a gradient across hydro-climates (i.e. towards highest response at semi humid hydro-climates for EWUE, humid for TWUE and semi arid for IWUE). Despite a clear relationship between precipitation and soil moisture, we discovered more pronounced WUE response gradients during soil moisture droughts. We expected this higher sensitivity of WUE to soil moisture than to precipitation was due to its direct connection to the vegetation dynamics (vegetation uptake of water through roots in the soil). The intriguing contrasting TWUE drought response between arid and humid hydro-climates, for example, was much more pronounced during soil moisture drought (Figure 3.3d) and less distinctive during precipitation droughts (Figure 3.3c). It is noteworthy that the differing root depths of vegetation land cover (especially shallow versus deep rooted) might have influenced the drought response signal. We investigated the difference in WUE response between soil moisture droughts in different soil depth layers (see Methods section 3.2.5) and we did not discover apparent differences. So, we focused the further discussion only on WUE drought response to soil moisture droughts in the surface layer (0 – 7cm depth).

To conclude on these contrasting TWUE drought response between arid and humid hydro-climates, it is helpful to first discuss the gradient of IWUE drought response across hydro-climates. Those were exclusively positive with the largest response in semi arid hydro-climates (Figure 3.3f). We concluded two points from here: Firstly, the physiological drought response of G_c reduction was not accompanied by a proportional decrease of GPP, resulting in the ubiquitous positive response of IWUE. This is in accordance to the current understanding of plant biochemistry drought response (Y. Yang et al., 2021). Secondly, humid ecosystems responded much less sensitive to droughts than arid. This is evident in weaker responses in humid hydro-climates than in arid for all drought severity categories, and exhibits the two opposing drought water management strategies of plants: The isohydric strategy common in arid ecosystems, where the stomatal conductance is quickly regulated to limit transpiration during droughts, and the anisohydric strategy common in humid ecosystems, where the plants do not regulate G_c until close to dehydration to maximize carbon assimilation (Joshi et al., 2022; Sade et al., 2012). Importantly, our analyses were conducted at monthly time scale, where VPD and soil moisture were found to be coupled (Novick et al., 2016), and under such conditions, the isohydric – anisohydric framework is a good predictor for G_c variability (Novick et al., 2019). The results show that there was still some adaptation of the G_c in humid hydro-climates even during moderately dry conditions, expressed through slightly increased IWUE. This can be the result of upscaling heterogeneity of different plant dehydration thresholds and

occurrence of anisohydric species in humid climates. Additionally, the drought definitions by standardized indices did not differentiate between specific water needs of ecosystem types. Further, the different net water availability during same drought category between locations of different mean soil water magnitudes might also have confounded these gradients. However, the gradient towards more dynamically adapted stomata and G_c and increased IWUE in dry hydro-climates is clear, and there, it even resulted in increased TWUE (Figure 3.3d), which could be due to the fact that decreasing G_c let T_r decrease stronger than GPP, leading to a net water saving per carbon assimilated during droughts. That behaviour remained exclusive for arid and semi-arid ecosystems, suggesting that humid ecosystem functioning with their ineffective and "risky" water strategy behaviour that evolved with water resource abundance (Lehner et al., 2017; Sade et al., 2012), will possibly be inhibited by dehydration (and/or shift to more drought tolerant vegetation) along with the expected increase in drought occurrence and severity across the whole European continent. Upcoming studies should project ecosystem functioning and performance with future climate scenarios and assess the state of humid ecosystems by accounting for ecological instead of soil moisture drought categories.

We concluded with analyses of causal networks from PCMCI+ to determine differences between the detected drivers of WUE variability across regions, hydro-climates and land cover types in Europe. A striking result was the GPP caused EWUE variability in Southern Europe which is not evident for TWUE variability accordingly (Figure 3.4a and b). Therefore, the weaker link between ET and EWUE in Southern Europe comes from the inclusion of evaporation from soil. Especially in semi arid, less vegetated regions during dry conditions, soil evaporation will increase as long as there is water in the soil but Tr will decrease due to the closure of stomata (as seen in Figure 3.3d). that is even down regulated by the plants. Hence, the resulting ET variability is lower than Tr variability in semi arid regions and resulted in less significantly explained EWUE variability by ET and the predominance of GPP influence on EWUE (Figure 3.4f). However, TWUE variability showed the differences between isohydric, more T_r-controlled, arid ecosystems and anisohydric, less T_r controlled, humid ecosystems well (Figure 3.4b, j and k). In addition, the influence of GPP on that was present on EWUE and TWUE, but not obvious for IWUE suggested that IWUE variability was predominantly controlled by G_c through dependence of GPP on G_c (Figure 3.4c, m, n and o). Hence, IWUE depended mostly on the water management strategy and the physiological adaptability to environmental changes. Importantly though, in the most humid regions (near the coast of Norway, in

Iceland and the Alps), there is high influence of GPP on IWUE, potentially pointing at a decoupling of GPP and G_c.

We investigated the large increasing trend of grassland IWUE (Figure A.4 and Figure A.5) with respect to its drivers. For that, we depicted the linear regressions of relevant link strengths (as independent variables) as a function of the grassland IWUE trend (dependent variable) slope in Figure 3.5. Interestingly, the larger the slope of IWUE trend, the stronger was the GPP→IWUE and VPD→G_c and the weaker was the T_r→G_c link. This pattern matched to the regulation of G_c and T_r to dry conditions that we described above, through down regulated T_r variability and more GPP variability. Comparing the trends of relevant variables confirmed the emergent picture: high positive IWUE trends corresponded with positive GPP trends and negative G_c trends. Coincidentally, soil moisture droughts became less likely because of increasing soil moisture trends, but atmospheric water demand, VPD, rose, causing the described physiological responses of G_c and T_r in the long term. Combined with the GPP increase, which was presumably caused though the enhanced light-use efficiency with rising atmospheric CO_2 (Cai & Prentice, 2020), among other environmental factors, these resulted in the large IWUE increases in European grasslands. Future studies should look in more detail on the factors driving the large positive grassland GPP trends and its decoupling from G_c variability from in-situ data on smaller scales and whether this signal is represented in current land surface models.

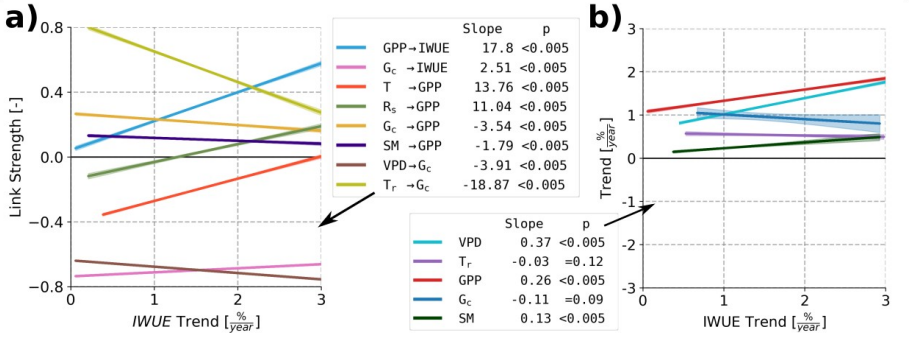

Figure 3.5: Strongly increasing IWUE in European grasslands are the result of regulated T_r and increasing GPP. We show in (a) the link strengths (y-axis, color lines) as linear regression function of the IWUE trend (x-axis). The 95% confidence interval was plotted but is minimal for all. The slope and p values of the regression are given in the figure legend. In (b) the linear regression of trend slopes of other relevant variables (y-axis, color lines) are plotted against the respective IWUE trend (x-axis). Again, the slope and p values are given in the figure legend. The stronger the positive IWUE trend, we note stronger GPP influence in (a, blue line) and the stronger the GPP trend slope, too (b, red line). At the same time, although vapour pressure deficit (VPD) is rising (b, light blue line), transpiration (T_r, b, purple line) was regulated by decreasing canopy conductance (G_c, b, dark blue line), resulting in the strong IWUE increases.

We saw the overarching pattern of semi-arid ecosystems reacting distinctively than humid, croplands and forested ecosystems in the drought response of causal networks (Figure A.8). Semi arid ecosystems effectively control T_r without inhibiting carbon assimilation, which was evident in unchanged GPP link strengths to EWUE and TWUE as shown in Figure A.8f and j, but partly strengthening the $T_r \rightarrow$TWUE link (Figure A.8k) and generally strengthening the $G_c \rightarrow$IWUE link (Figure A.8o). This underlines the conclusions on the opposing TWUE drought response between isohydric ecosystems in arid hydro-climates and anisohydric ecosystems in humid ecosystems through different water management strategies.

We also emphasize the response of causal networks in grasslands to drought that corresponded with the response to long-term increasing VPD described above. Grasslands showed a rather small change in the $T_r \rightarrow$TWUE link (Figure A.8k) and no changes to the G_c variability as well (Figure A.8o). Rather, GPP influence on IWUE increased especially in grasslands, again pointing at a potential decoupling of G_c and GPP through other environmental factors like increased atmospheric CO_2 that would also explain the large increasing grassland IWUE trend along with continuous drying of the atmosphere (see increasing VPD trend).

Long-term environmental changes and resulting in trends of ecosystem variables over the 24-year study period might have had an impact on influences between those variables, thus changing the causal network over time. Those long term effects on causal networks were not considered here. Prospective work will deal with differences in "decadal" causal networks around WUE to determine the changes in the drivers over time, that were not considered here. We included a wide range of meteorological, hydrological and ecosystem processes time series in the PCMCI+ analysis to comply with the causal sufficiency assumption and have as many possible confounding factors included as possible. But scarce and fragmentary data kept us from including factors that might have played a role on ecosystem processes change: local atmospheric CO_2 concentrations and human forest and crop management, inter alia.

All in all, the study advanced the understanding of the WUE ecosystem function, using new remote sensing data and relating results to existing studies from different data sources and scales. Concretely, we highlight:

1. Decreasing summer IWUE trend as indicator for potentially inhibited ecosystem function and performance in Central Europe;

2. High increasing European grassland summer IWUE trend despite atmospheric drying was caused by maintained T_r through adaptive G_c and increased, decoupled GPP;
3. Contrasting TWUE drought response and IWUE drought sensitivity across hydro-climates that demonstrated the contrast between isohydric and anisohydric plant water management.

In this study, we provided references for the further development of land surface models and its discretization and parametrization and assessments of European ecosystem functioning and performance changes. Future work will scrutinize whether these effects are detected by in-situ observations and the representation of these effects by current implementation and parametrization of plant functional types in state-of-the art land surface models.

4 Systematic underestimation of type-specific ecosystem process variability in CLM5 over Europe

This chapter is based on the journal article:

Poppe Terán, C., Naz, B.S., Vereecken, H., Baatz, R., Fisher, R.A., Hendricks Franssen, H.-J., 2025. Systematic underestimation of type-specific ecosystem process variability in the Community Land Model v5 over Europe. Geosci. Model Dev. 18, 287–317. https://doi.org/10.5194/gmd-18-287-2025

4.1 Introduction

Ecosystem processes, such as evapotranspiration (ET) and gross primary production (GPP), play an important role in cycling water, carbon, and energy between ecosystems and the atmosphere. Changes in the magnitude and variability of these fluxes can indicate ecosystems' inhibited performance due to changing environments (Kühn et al., 2021; Migliavacca et al., 2021). These changes can lead to short-term alterations and long-term trends in water resources and carbon pools in the atmosphere and the land surface. Thus, the accurate quantification of the variability of ecosystem processes is pivotal for developing climate change projections and formulating effective mitigation policies (Friedlingstein et al., 2023; Graf et al., 2023).

Notably, an accurate, functional understanding of land surface processes is essential to identify threatened ecosystems in the present and the future and facilitate carbon budget calculations. Land surface models (LSMs) serve as deterministic and process-based simulators of ecosystems, capturing energy, water, and carbon fluxes while considering their interactions and the heterogeneity of the land surface (Fisher & Koven, 2020) LSMs can complement point-scale observations from in-situ research infrastructures by providing spatiotemporally uniform and extensive high-resolution outputs. Their high-resolution process-based simulations contrast the often coarsely resolved remote sensing data. Hence, LSMs are frequently used tools for investigating and projecting the current understanding of ecosystem processes, such as GPP and ET, on various scales. However, there is uncertainty in the LSM structure, the parameters, the input data, and the initial conditions, which carry over to the

simulated variables. Therefore, assessing how well the general simulated ET and GPP variability compares to the observations is crucial. Such evaluations deliver essential context on LSM biases and form a basis for analyses of more complex ecosystem responses. Recent studies already found discrepancies between LSM simulations of ET and GPP and observations collected in the field and from remote sensing. For instance, these discrepancies are evident in their magnitude and variability (Boas et al., 2023; Cheng et al., 2021; De Pue et al., 2023; Strebel et al., 2023) and their response to drought (J. K. Green et al., 2024; Ukkola et al., 2016; H. Wu et al., 2020). Therefore, assessing the accuracy of LSMs in representing observed GPP and ET fluxes is crucial to test and improve our current understanding of ecosystem process variability and identify the limitations of state-of-the-art LSMs.

Current land surface models, e.g., the Joint UK Land Environment Simulator (JULES), the Community Land Model 5 (CLM5), or the Community Atmosphere Biosphere Land Exchange Model (CABLE), employ a tiling system within the grid cell to account for functional differences in distinct patches on the land surface. The natural and crop vegetation is grouped into plant functional types (PFTs), the entities for which ecosystem process calculations are resolved (Bonan et al., 2002; Fisher & Koven, 2020; Solomon & Shugart, 1993). Typically, PFTs are defined based on morphological and phenological characteristics of the vegetation (e.g., leaf type and leaf longevity) and climate (Bonan et al., 2002). However, the usefulness of this PFT definition, or at least its current coarsely resolved implementation, is a subject of debate (Caldararu et al., 2015; Van Bodegom et al., 2012). The primary argument against it is that observed plant traits implemented as PFT-related parameters vary to some extent in space and time in response to a changing environment. This spatiotemporal dependence of PFT traits is only marginally represented in LSMs. On top of that, most research assessing LSMs only used a handful of observation sites and did not analyze aggregated values for groups of sites observing the same PFT. Such analyses would provide essential insights; a recent study highlighted the differences between vegetation-type concepts used in observation networks, e.g., the International Geosphere–Biosphere Programme (IGBP) classification, and PFTs used in LSMs and underlined the importance of improving these PFT concepts (Cranko Page et al., 2024).

The phenology of ecosystem processes, i.e., their seasonal cycles and evolution through the year and the growing season length, have shifted in timing due to climate change. A recent study investigated which factors drive the changes in the mean annual dynamics of ecosystem processes in Europe (Rahmati et al., 2023),

and many of these discovered feedbacks, for instance, the effect of increased atmospheric dryness on growing season length, are only implemented simplistically in LSMs. Furthermore, robust simulations of LSMs for impact assessments become even more critical as ecosystems experience more disturbances, along with the changing climate. For example, projections show that droughts have recently become more frequent in Europe (Rousi et al., 2022; Vautard et al., 2023) and that these extreme events will become even more frequent and severe in the future (Lehner et al., 2017).While the combined effect of a higher occurrence of compound drought events is currently not fully understood, it is clear from observations that individual drought years, or droughts in general, have already had a profound impact on ecosystem processes in Europe (Graf et al., 2020; Poppe Terán et al., 2023; Van Der Woude et al., 2023). Given that the frequency and severity of extreme events affect GPP and the ET statistical distributions, investigating how the characteristics of the simulated distributions compare with the observed can contextualize findings of modeled ecosystem drought responses in Europe.

One predominantly used LSM is the Community Land Model version 5 (CLM5) (D. M. Lawrence et al., 2018, 2019). In the most recent version, CLM5 solves the biogeochemistry (BGC), i.e., the carbon and nitrogen cycles between the atmosphere, vegetation, and soil. CLM5 has been widely employed for quantifying and examining ecosystems at various scales, including global (D. M. Lawrence et al., 2019; Sitch et al., 2015; Xie et al., 2020), regional (Boas et al., 2023; Cheng et al., 2021), and site-scale (Fisher et al., 2019; Song et al., 2020; Strebel et al., 2023; Umair et al., 2020) applications. Several studies have highlighted the ability of CLM5 to simulate ecosystem processes close to the observations (Boas et al., 2023; Cheng et al., 2021; D. M. Lawrence et al., 2019; Wozniak et al., 2020; L. Zhang et al., 2023). However, they have also emphasized an underestimated magnitude and variability in the simulations across different timescales and under various conditions.

The present study assesses the CLM5's ability to capture ecosystem processes at a continental scale. To ensure comparability to point scale observations, we conducted high-resolution simulations at 0.0275° (approx. 3 km) resolution over the European Coordinated Regional Climate Downscaling Experiment (CORDEX) domain (Giorgi et al., 2009), resulting in 1544×1592 grid cells. Notably, the output contained variables from the subgrid scale, i.e., from within a 3 km grid cell, for PFTs present in the grid cell. We then compared the CLM5 grid level ($CLM5_{grid}$) and PFT level data ($CLM5_{PFT}$) to observations from a continental network of sites. The Integrated Carbon Observation System (ICOS) provides the

Warm Winter 2020 data (Warm Winter 2020 Team & ICOS Ecosystem Thematic Centre, 2022), which include eddy covariance measurements over a dense network of over 70 sites in Europe. It was named after and curated to support research on the effect of the warm winter of 2020 on terrestrial carbon fluxes. These ICOS data are regarded as the gold standard for calibrating and evaluating process-based models due to their ample spatial coverage as a network encompassing diverse land cover types. Thus, it offers an excellent opportunity to comprehensively assess simulated GPP and ET for specific PFTs from our CLM5 setup over Europe.

Additionally, we include remote-sensing data from the Global Land Surface Satellite (GLASS; Liang et al., 2021) and reanalyses from the European Center for Medium-Range Weather Forecasts Reanalysis 5 – Land (ERA5-Land; hereafter ERA5L; Copernicus Climate Change Service, 2019), as well as from the Global Land Evaporation Amsterdam Model (GLEAM; (Martens et al., 2017)) in our analyses to identify common patterns of ecosystem process variability between CLM5, in situ observations, reanalysis, and remote-sensing data.

In summary, this study uses ICOS observations as ground truth data. It compares them with grid level and PFT level CLM5 data and terrestrial surface fluxes from reanalyses and remote-sensing derivatives to the following:

1. Compare performance indices (root mean square error and percent bias) between the models and ICOS measurements on a per-site and PFT group basis to assess the systematic error and accuracy of ET and GPP simulations.

2. Investigate how the models represent the observed ET and GPP for different PFTs regarding their sub-annual averaged phenologies, standard deviation, and timing of important phenological events.

3. Evaluate the simulated PFT level ET and GPP statistical distributions and their moments (mean, variance, skewness, and excess kurtosis) to contextualize assessments of factors like droughts, which impact the shape of these distributions.

4. Compare the inter-site differences between ET and GPP time series within PFT groups to estimate how the observed intra-PFT variability is represented in the models.

Thus, these findings offer critical information for comparisons of GPP and ET from the evaluated models. Furthermore, this study also paves the way for a

better-informed analysis of the drought response of ET and GPP from the models being assessed over Europe. We expect the following:

1. There is a lower systematic bias, and the simulation is closer to the observations by the PFT scale than the grid scale CLM5 outputs and remote-sensing and reanalysis data.
2. The remotely sensed and modeled data approximate critical events in the phenologies of ET and GPP within the standard deviation of the ICOS measurements for sites of one PFT. However, this ability varies between PFTs.
3. The remotely sensed and modeled ET and GPP data distributions show a lower range among the moments within the PFT groups than the ICOS measurements.

4.2 Methods

4.2.1 Community Land Model version 5

We use the CLM5 (D. M. Lawrence et al., 2018, 2019), which is forced offline with custom input data. The land surface of a region in CLM5 is first disaggregated into grid cells, which are uniformly distributed and simulated individually. These grid cells are tiled into land units (i.e., natural vegetation, crops, lakes, urban areas, and glaciers) with a relative area coverage within the grid cell. Importantly, plants in the naturally vegetated land units compete for water in a single soil column. The vegetation is grouped into PFTs (P. J. Lawrence & Chase, 2007), which are distinguished through leaf habit (evergreen or deciduous), morphology (needle- and broadleaves, grass, and shrubs), and the bioclimate of the grid cell location (boreal, temperate, and tropical). While competition for soil moisture includes interactions among different PFTs, this is closer to natural conditions than separated soil columns and encourages evaluations on the PFT scale. Here, we use CLM5–BGC, which calculates vertical carbon and nitrogen pools and fluxes between the vegetation, soil, and atmosphere. In the following subsections, we briefly describe the essential processes in CLM5 that are particularly relevant to this study, as well as the input data and leading features of the European CLM5 setup.

Gross primary production and evapotranspiration

The stomatal conductance of plants (g_s) couples the water exchange with carbon uptake between vegetation and the atmosphere. In the CLM5, g_s is calculated by the Medlyn stomatal conductance model (Medlyn et al., 2011) as follows:

$$g_s = g_0 + 1.6\left(1 + \frac{g_1}{\sqrt{D}}\right)\frac{A}{c_s} \tag{4.1}$$

Where g_o is the Medlyn intercept and defaults to 100 mol m^{-2} s^{-1}, and g_1 is the Medlyn slope, a PFT-specific parameter. D is the vapor pressure deficit indicating atmospheric water demand, and c_s is the CO_2 partial pressure at the leaf surface relative to the total atmospheric pressure. A is the carbon assimilated through photosynthesis.

$$A = \frac{c_s - c_i}{1.6\, r_s} \tag{4.2}$$

The calculation of A is adapted from (Bonan et al., 2011). It is based on the Farquhar model (Farquhar et al., 1980) and limited by the photosynthetic capacity given by the LUNA model (A. A. Ali et al., 2016). It requires knowledge of the gradient of CO_2 concentration from the outside to the inside of the leaf and neglects CO_2 storage at the leaf surface. c_s and c_i are the leaf surface and internal partial CO_2 pressures, and r_s is the stomatal resistance, which is the inverse of g_s. Further, c_s and c_i are calculated.

$$c_s = c_a - 1.4\ r_b\ A \tag{4.3}$$

$$c_i = c_a - \left(1.4\ r_b + 1.6\ r_s\right)A \tag{4.4}$$

The factor of 1.4 refers to the diffusivity ratio between CO_2 and H_2O gases in the leaf boundary, and 1.6 is the same ratio in the stomata. The equations for A, g_s, c_i, and c_s are computed iteratively until c_i converges, using a hybrid algorithm with the secant and Brent methods (D. M. Lawrence et al., 2018). The photosynthesis is scaled to the canopy GPP by considering the effect of sunlit-to-shaded-area ratios of the total leaf area.

The water input from the atmosphere to the land surface can be snow accumulating on the ground, streamflow, lake water, moisture intercepted by the vegetation canopy, or water infiltrating the ground. The water in the ground percolates through 20 soil layers and is stored, directly evaporated, or taken up by

plant roots relative to their transpiration demand. Hydraulic stress in a plant is calculated in a hydraulic framework using Darcy's law for transient porous media flow (Bonan et al., 2014).

The transpiration flux T is calculated with the resulting r_s from above.

$$T = \frac{e_s - e_i}{r_s} \tag{4.5}$$

e_s is the H_2O vapor pressure at the leaf surface, and e_i is the saturation H_2O vapor pressure resulting from the leaf temperature. If T cannot meet the atmospheric water demand because of a soil moisture shortage, CLM5–BGC introduces water stress and attenuates g_s based on that transpiration deficit factor. Through decreased g_s, water stress also regulates photosynthesis, A.

Total evapotranspiration is then determined by summing the transpiration and evaporation from vegetation interception, surface water, the ground, and, potentially, snow.

Setup od the European CLM5

The European Coordinated Regional Climate Downscaling Experiment (CORDEX; Giorgi et al., 2009) domain delimited the extent of this study, matching with the extent of regional atmospheric models. With a resolution of 3 km (0.0275°), our grid contains 1544×1592 grid cells, including the ocean. We used standalone CLM5 with the activated BGC module and stub models for ice, sea, and waves.

The simulations were forced by the Consortium for Small-Scale Modeling (COSMO) Reanalysis 6 (Bollmeyer et al., 2015; Wahl et al., 2017), a 6 km resolution data set providing meteorological variables over the European CORDEX domain from 1995 to 2019. The main advantage of using this reanalysis is the high resolution and a better representation of seasonal precipitation intensities compared to a coarser resolved global reanalysis (Bollmeyer et al., 2015). Using this forcing in high-resolution LSM simulations should lead to a more accurate simulation of sub-surface and surface hydrological fluxes, especially in regions with a relatively heterogeneous land surface (Prein et al., 2016; Wahl et al., 2017).

The static surface information was initialized for the year 2000 and was determined using input data from a standard repository (D. M. Lawrence et al., 2018). These data include land use information (Hurtt et al., 2020), PFT distribution maps (P. J. Lawrence & Chase, 2007), soil texture (IGBP, 2000), and

slope and elevation information (Earth Resources Observation And Science (EROS) Center, 2017).

The CLM5–BGC needs initial conditions for the carbon pools. For that reason, a spin-up workflow is necessary to bring the carbon pools and fluxes of carbon to a steady state before starting with production simulations. The spin-up method consists of two steps. First, an accelerated decomposition simulation step, where carbon pools are artificially minimized. Second, a conventional simulation step, growing the carbon pools to the desired equilibrium state. During both spin-up steps, the atmospheric forcing from 1995 to 2012 was cycled (i.e., a cycling period of 18 years). The progress towards a steady state is monitored by assessing the difference in total carbon fixed in the ecosystem between a selected year within the last 18-year cycling period and the same year in the previous cycling period. $C_{tot,y}$ is the total ecosystem carbon (including vegetation and soil) in the year y, and $C_{tot,y-t}$ is the complete ecosystem carbon in the year $y-t$. A grid cell's carbon pools are in carbon equilibrium if the following is fulfilled:

$$\frac{\Delta C_{tot}}{t} < 1 \ g \ C \ m^2 \ yr^{-1} \tag{4.6}$$

The following conditions define the final steady state on the continental scale.

1. A total of 97 % of the grid cells (and the total area) is in equilibrium.
2. The change in continental ecosystem carbon across the continent is lower than 2 Tg C yr^{-1} for the three preceding cycle periods.

The soil organic matter carbon pools in high northern latitudes were the slowest to reach equilibrium, which was reached after just about 1500 simulation years.

After the spin-up, we conducted a 24-year (1995 until 2018) transient simulation starting with the initial conditions established by the spin-up. We output the simulated variables from two model levels for the analyses.

1. $CLM5_{PFT}$. This is the model's native resolution of vegetation-related states and fluxes calculation. Using output at this level (not the default configuration) allows for multiple time series per grid cell, with each corresponding to a single PFT. This enables a selection of modeled data as needed. For instance, when comparing model data to ecosystem level measurements, $CLM5_{PFT}$ relates to the simulated time series of the corresponding PFT, resulting in an adequate assessment of model functions. When comparing to in situ observations, we will refer to

$CLM5_{PFT}$ when we subset the ICOS site location and the agreeing PFT from the CLM5 data.

2. $CLM5_{grid}$. The grid cell level output aggregates the PFT and the other tiles (i.e., croplands, urban areas, and lakes) that compose the grid cell area. Consequently, these data do not relate to a single functional type. Instead, it informs us about the average state and fluxes in the grid cell area. In this study, $CLM5_{grid}$ designates CLM5 data extracted from the grid cell closest to the station's location.

4.2.2 Evaluation data

Station data

As ground truth data in the comparisons, we used the ICOS research infrastructure, which has a station observation network spanning 14 European countries (Heiskanen et al., 2022). Each station has at least one eddy covariance measurement tower and incorporates a processing workflow following a standardized protocol. We use the curated data, the Warm Winter 2020 data set (Warm Winter 2020 Team & ICOS Ecosystem Thematic Centre, 2022), which consists of homogenized variable time series following the ONEFlux data pipeline (Pastorello et al., 2020). The ICOS Warm Winter 2020 data have measurements of 73 stations totaling over 800 station years (available years are station-dependent) corresponding to multiple land cover types (see Figure 4.1 for a map with the station locations and Table for more information on the available years per station). Note that the land cover type indicated by the ICOS site metadata and represented in the measurements refers to the predominant PFT in the footprint of the eddy covariance station. We omitted the stations over wetland and mixed forest land cover types to ensure a coherent analysis because no PFT counterpart is implemented in $CLM5_{PFT}$. Also, shrub PFTs were not included in our analyses because there were insufficient shrubland sites in the ICOS data to support a robust evaluation. The analyses also excluded stations whose land cover type was not included in metadata sites (e.g., DEIMS-SDR at https://deims.org, last access: 20 February 2024), leaving a total of 42 stations for our analyses. Because the land cover types from the selected sites correspond well with PFTs in CLM5, we will also refer to them as PFTs.

The processing workflow of the Warm Winter 2020 data extracts daily time series for GPP, partitioned from the net ecosystem exchange (NEE), using the nighttime method and a dependence on a variable friction velocity threshold (in $g\,C\,d^{-1}$; GPP_NT_VUT_REF). We retained negative GPP values in these data, which stem

from the uncertainty in the NEE measurements and partitioning method, to avoid introducing bias into the GPP distributions (Pastorello et al., 2020; Reichstein et al., 2012). For the ET evaluation, we also extracted the gap-filled latent heat flux ($W\,m^{-2}$; LE_F_MDS). Importantly, we verified our results by checking for inconsistencies in the analysis of ICOS NEE (NEE_VUT_REF), ecosystem respiration (RECO_NT_VUT_REF), and energy-balance-corrected latent heat flux (LE_CORR).

The conversion of latent heat ($W\,m^{-2}$) into ET ($mm\,d^{-1}$) is achieved by multiplying with the factor 0.035, assuming a constant enthalpy of vaporization decoupled from temperature because variable enthalpy has a negligible effect on the overall outcome of the conversion.

Last, we use the leaf area index (LAI) from the ICOS archive final quality data set (ETC L2 Archive). LAI is measured but only sparsely available, starting from 2017, and thus only has 2 years intersecting with our study period (2017 and 2018). Furthermore, the data within this intersection period are only available for a smaller number (in relation to the eddy covariance (EC) data above) at evergreen needleleaf forest and cropland sites. Therefore, we do not include the analysis in the main text but include these results only in the Appendix for the context of the main analyses of ET and GPP.

Remote sensing and reanalysis data

To assess the CLM5 performance in the context of additional complementary data products, we include remotely sensed GPP data from the Global Land Surface Satellite (GLASS; Liang et al., 2021). The GLASS GPP product uses the Moderate Resolution Imaging Spectroradiometer (MODIS) and Advanced Very High Resolution Radiometer (AVHRR) sensors and the revised light use efficiency (LUE) model (Zheng et al., 2020) in eight-times-daily resolution in time and 0.05° resolution in space. We also compare the CLM5 outputs with GLASS ET data, which apply a multi-model ensemble (e.g., MODIS-ET and remote-sensing Penman–Monteith ET) to remote-sensing information to estimate eight-times-daily latent heat on a 0.05° grid. We convert latent heat to ET, as described above. Similarly, MODIS-derived GLASS LAI data (Ma & Liang, 2022) are used in this study to provide context to the ET and GPP analyses (same 0.05° grid and eight-times-daily resolution).

Last, we use LAI and ET reanalysis data for evaluation, which fuse observations and models. They are the European Center for Medium-Range Weather Forecasts Reanalysis 5 – Land product (ERA5L; Copernicus Climate Change Service, 2019),

which has a spatial resolution of 0.1° and hourly temporal resolution, and the Global Land Evaporation Amsterdam Model (only ET; GLEAM version 3.5a; Martens et al., 2017), which has a spatial resolution of 0.25° and daily temporal resolution.

4.2.3 Data processing

First, the remote-sensing and reanalysis data are bilinearly remapped to the 3 km European CORDEX grid and interpolated to eight-times-daily means for 1995–2018. The ICOS observation time series are interpolated to eight-times-daily means for each station whose data availability overlaps with our study period. Then, we extracted the $CLM5_{grid}$, GLASS, ERA5L, and GLEAM data from the grid cell closest to the location of each selected ICOS station. Furthermore, we select the time series in $CLM5_{PFT}$ that coincides with that grid cell and the station's predominant PFT. Importantly, we focus only on the four predominant PFTs represented in the entire ICOS station network, namely evergreen needleleaf forest (ENF), deciduous broadleaf forest (DBF), grasslands (GRA), and croplands (CRO), as outlined in Table 4.1. Finally, the periods for which station data are absent or of bad quality (determined by the corresponding measurement or gap-filling quality flag in the ICOS data) are discarded from the simulations to ensure we are comparing the same set of conditions.

Table 4.1: The predominant plant functional types (PFTs) in the Integrated Carbon Observation System (ICOS) WARM-WINTER-2020 observation dataset that correspond with the International Geosphere–Biosphere Programme (IGBP) land cover classifications, the number of corresponding sites, and the accordant PFTs in the European Community Land Model v5 (CLM5) setup.

ICOS IGBP PFT	# of Stations	Corresponding CLM5 PFT
Evergreen needleleaf forest (ENF)	18	Needleleaf evergreen tree – temperate Needleleaf evergreen tree - boreal
Deciduous Broadleaf forest (DBF)	8	Broadleaf deciduous tree – tropical Broadleaf deciduous tree – temperate Broadleaf deciduous tree – boreal
Grasslands (GRA)	8	C_3 arctic grass C_3 grass C_4 grass
Croplands (CRO)	8	C_3 Unmanaged Rainfed Crop C_3 Unmanaged Irrigated Crop

The ICOS observations were also interpolated to eight-times-daily means, encompassing a timescale with significant variability in ecosystem processes (De Pue et al., 2023), to match the coarsest time resolution of other data sets (i.e., GLASS remote sensing) and thus to facilitate comparison of processes at the same scale. For a consistent comparison, the analyses only account for time steps for which valid values are present for all data sources. We evaluate the data for each variable over each station and groups of stations with the same PFT.

4.2.4 Analyses

Yearly evolution and statistical distributions

We calculate ET and GPP PFT-specific phenology (mean sub-annual dynamics), resulting in day-of-year (DOY) plots. This is done by averaging the same eight-times-daily time step across years for each site and calculating the mean and standard deviation of site-specific DOY belonging to one PFT.

Furthermore, we determined the statistical distributions as probability density functions resulting from the Gaussian kernel density estimate (Scott, 1992). Subsequently, the distribution moments (mean, variance, skewness, and excess kurtosis) are calculated. The distributions and their moments are based on all eight-times-daily values corresponding to one PFT for each data source. The uncertainties in the distribution moments are calculated based on Harding et al., 2014.

Shift in phenological events

The three analyzed phenological events of ET and GPP – the start of the growing season, the peak, and the end of the growing season – are determined for each PFT group and data source as the average DOY of the event among the stations and available years within that PFT group for each variable. The eight-times-daily time series of each variable was first smoothed with a 1-dimensional Gaussian filter to rule out potential errors due to small-scale variability and dampen the effect of potential outliers. More specifically, the peak timing is the mean DOY of the overall maxima of the smoothed averaged yearly evolution across stations for each PFT and data source. The start and the end of the growing season were determined by the mean DOY of the two infliction points (N. Li et al., 2023; Lian et al., 2020; Whitcraft et al., 2015) of the smoothed yearly averaged evolution across stations for each PFT and data source. The shift in these events is simply the difference in the determined mean PFT-specific DOY between the models and the observations. As a measure of uncertainty in the mean PFT-

specific DOY, we also calculate the standard deviation of the DOY of the events across stations in each PFT group.

Performance metrics

The percent bias (PBIAS) measures systematic model error and is calculated as follows:

$$PBIAS = \frac{\sum_{i=1}^{n} X_{S,i} - X_{O,i}}{\sum_{i=1}^{n} X_{O,i}} \tag{4.7}$$

Where n is the number of time steps, $X_{S,I}$ is the simulated value of the variable X at the time i, and $X_{O,i}$ is the observed value of the variable X at the time i. If the PBIAS for variable X is positive then the model overestimates; if it is negative, it underestimates the observed variable X. In our analysis, X_i is the interpolated eight-times-daily mean.

Furthermore, we estimated the root mean square error (RMSE) to indicate model accuracy and the root mean square difference (RMSD) to indicate similarity. RMSE and RMSD are calculated the same. However, the term "error" assumes the truthfulness of the reference data. Hence, we use the RMSD when comparing data only between models.

$$RMSE = RMSD = \sqrt{\frac{\sum_{i=1}^{n} \left(X_{S,i} - X_{O,i} \right)^2}{n}} \tag{4.8}$$

A RMSE close to zero indicates that the model approximates the observations nicely. Similarly, a low RMSD reveals a high similarity between the two analyzed series. We calculate these metrics on a per-station basis and a set of stations belonging to the same PFT.

Modified Taylor diagrams

The Taylor diagram (Taylor, 2001) depicts multiple model performance indices in a single diagram by making use of the relationship of the calculation terms of the standard deviation, correlation, and RMSE. Their relationship can be summarized in the following equation of error propagation:

$$RMSE^2 = \sigma_O^2 \ \sigma_S^2 \ 2\sigma_O \ \sigma_S \ r \tag{4.9}$$

Where σ_O is the standard deviation of the observations, σ_S is the standard deviation of the simulation, and r is the Pearson correlation coefficient. The

multi-variate diagram can be constructed due to the geometric relationship between these statistical indices through the law of cosines. Thereby, plotting the calculated Pearson correlation against the standard deviation of the models and the observation on a trigonometric polar plane, the RMSE manifests as the polar Euclidean distance from the reference observations. We calculate the standard deviation and the Pearson correlation on the PFT-grouped stacked time series and plot these for *e* for each data source on one Taylor diagram per PFT. We modify the default Taylor diagram by scaling each marker's size by the absolute PBIAS for the corresponding source and PFT.

4.3 Results

4.3.1 Land surface representation

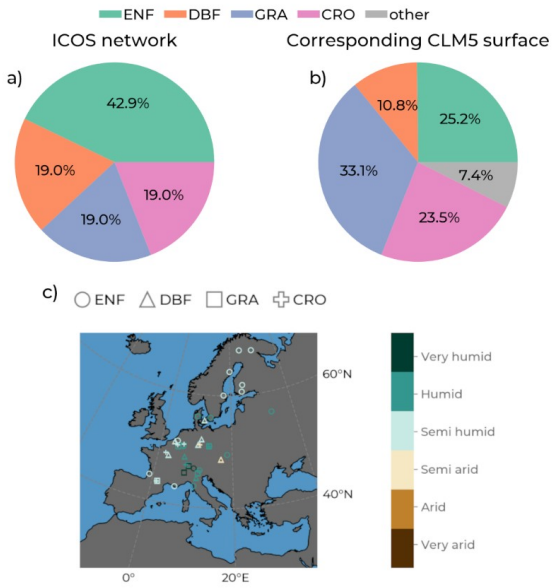

Figure 4.1: The share of represented plant functional types (by color: Evergreen Needleleaf Forest (ENF, green), Deciduous Broadleaf Forest (DBF, orange), Grasslands (GRA, purple), and Croplands (CRO, pink)) in a) in the ICOS station network used in subsequent analyses and b) in the corresponding grid cells in our European CLM5 setup. In c) is a map showing the locations of the ICOS stations, with the marker type indicating their PFT and the color of the marker indicating their hydro-climate (adapted from Jafari et al., 2018) based on the mean annual precipitation from the Consortium for Small-Scale Modeling (COSMO) -Reanalysis 6. Our 3 km European CLM5 simulation domain corresponds to the entire map box in c).

Before evaluating the GPP and ET variables from CLM5 and how they are compared with observations, we first assess if the PFT composition of the entire ICOS station network is comparable to the PFT composition in the respective

cells selected in $CLM5_{grid}$. This is important as GPP and ET magnitudes, variability, seasonality, drought responses, and trends strongly depend on the present vegetation type. In Figure 4.1, we observe that ENF, the PFT of almost half of the present ICOS stations, represents only around a quarter of the corresponding $CLM5_{grid}$ area. DBF also covers a smaller share of the area in those grid cells than in the ICOS station network. On the other hand, GRA and CRO are overrepresented in $CLM5_{grid}$ compared to the share of respective ICOS stations. Consequently, when comparing with the ICOS observations, the selected data from $CLM5_{grid}$ data are, on average, over-representing the functionality of GRA and CRO and underrepresenting ENF and DBF, which hampers the evaluation of $CLM5_{grid}$ with in situ ET and GPP. Hence, we also included the respective $CLM5_{PFT}$ GPP and ET in the subsequent analysis, enabling an accurate assessment of the functionality and relationships between PFT in the model. Additionally, we assess the similarities and differences between the two model scales, CLM_{grid} and CLM_{PFT}, and their approximation to the observations.

4.3.2 General model performance

This section presents model performance indices correlation, RMSE, and PBIAS, comparing each model's ET and GPP estimates with measurements from the ICOS sites. We compared the RMSE and PBIAS on a per-site basis (Table B.2 and Table B.3), which yielded good results for most sites. The focus of this study, though, is the performance of PFT aggregations through combining data from sites that belong to the same PFT.

Figure 4.2 shows modified Taylor plots visualizing the performance indices of the model ET against observations for each PFT. For more specific information, Table B.4 lists the number of ET eight-times-daily time steps that went into calculating these indices and their values. For ENF, all of the models indicate a correlation of around 0.8 with the ICOS observations, and $CLM5_{grid}$, $CLM5_{PFT}$, and GLEAM have a similar variability to ICOS. $CLM5_{PFT}$ has a higher absolute RMSE and a smaller absolute PBIAS than $CLM5_{grid}$ for ET across PFTs, except in CRO. Notably, the systematic bias in CLM5 is generally negative, with the same exception. On the other hand, ERA5L, GLASS, and GLEAM exhibit a generally positive systematic bias for ET. ERA5L and GLASS show more significant deviations from the ICOS ET observations at ENF and DBF than $CLM5_{PFT}$ and CLM_{grid} but have smaller RMSE values at GRA and CRO. GLEAM has generally low RMSEs and performs best among the models simulating ET at ENF and CRO. The most considerable systematic ET biases are found for ERA5L at CRO

and DBF sites, followed by GLASS for the same PFTs. The low absolute PBIAS of $CLM5_{PFT}$ across all PFTs and the lower correlation than the other model data at GRA and CRO points to potentially missing or simplistic representations of ecohydrological processes or management. Besides, all models approximate the ICOS ET observations fairly well, with correlations mostly over 0.8 but with partly high systematic biases by ERA5L at DBF and CRO sites.

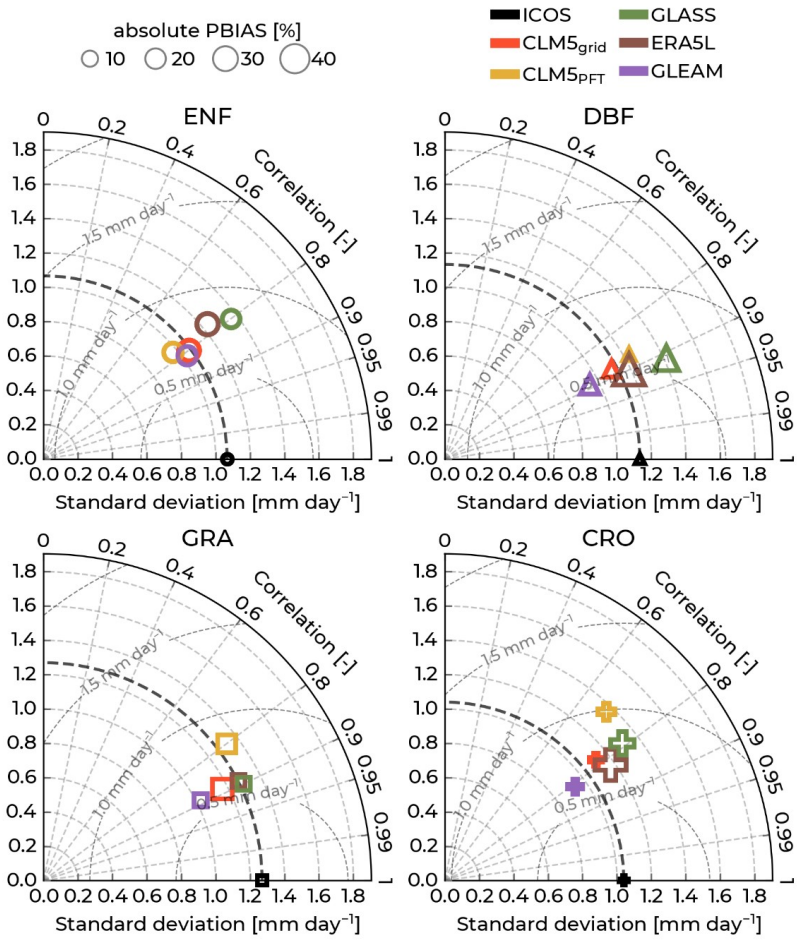

Figure 4.2: Modified Taylor diagrams with observations from the Integrated Carbon Observation System (ICOS) of evapotranspiration as reference (black markers) and showing model performances between the years 1996 – 2018 (years varying by station; see Table B.1. Data sources by color: Community Land Model v5 ($CLM5$), $CLM5_{grid}$: red, $CLM5_{PFT}$: yellow, Global Land Surface Satellite (GLASS): green, European Center for Medium-Range Weather Forecasts Reanalysis 5 – Land ($ERA5L$): brown, Global Land Evaporation Amsterdam Model (GLEAM): purple). Each diagram shows these plots for one plant functional type. Upper left: Evergreen Needleleaf Forest (ENF, circles), upper right: Deciduous Broadleaf Forest (DBF, triangles), lower left: Grasslands (GRA, squares), and lower right: Croplands (CRO, crosses). The azimuth angle indicates the Pearson correlation with the ICOS data, the radial distance is the standard deviation, and the

semicircles centered at the reference standard deviation show the root mean square error (RMSE). The size of each marker indicates the percent bias (PBIAS).

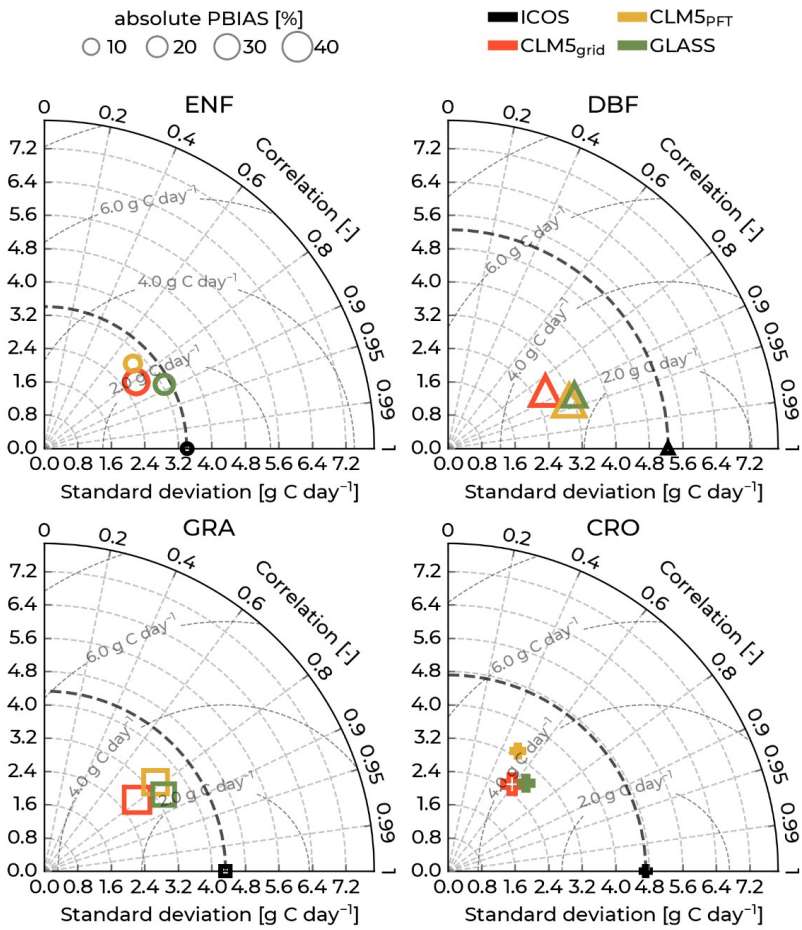

Figure 4.3: Modified Taylor diagrams with observations from the Integrated Carbon Observation System (ICOS) of gross primary production as reference (black markers) and showing model performances between the years 1996 – 2018 (years varying by station; see Table B.1. For colors, labels, and acronyms, refer to Figure 4.2.

In Figure 4.3, we show modified Taylor diagrams with the GPP performance indices of the models against the ICOS observations for each of the selected PFTs. For more specific information, Table B.5 lists the number of GPP eight-times-daily time steps that went into calculating these indices and their values. $CLM5_{PFT}$ performed better than $CLM5_{grid}$ in approximating the ICOS GPP observations at DBF sites, showing a higher correlation and lower RMSE and GRA sites. Conversely, $CLM5_{grid}$ is closer to the observations for ENF and CRO

PFTs. The GLASS data show the lowest GPP RMSEs and highest correlation values concerning ICOS measurements across all PFTs. All models approximated the ICOS GPP best (lowest RMSE) at ENF, and the worst performance was at CRO sites. Furthermore, all models exhibit a negative, systematic bias in simulating the observed GPP across all PFTs. Especially at DBF and GRA PFTs, $CLM5_{grid}$, $CLM5_{PFT}$, and GLASS show large systematic underestimations of the measurements. $CLM5_{PFT}$ has a notably small PBIAS related to the ICOS data for ENF and CRO sites. Especially at CRO sites, all models showcase comparatively low correlation values (<0.7). While the correlation is high (>0.75) for all models at DBF and GRA sites, especially for $CLM5_{PFT}$ and GLASS at DBF sites (0.93 and 0.92), the high PBIAS hints that modeled data do not incorporate important processes or management practices that cause to the high carbon uptake at DBF sites over the long term. Because of the slowly evolving carbon states in the terrestrial ecosystems, the initial conditions of the carbon pools (e.g., soil organic matter and carbon in plant organs in the vegetation) could be a cause for the difference in the magnitude of the GPP.

4.3.3 PFT phenology and its variability

ET

This section describes the results of the investigation on the mean and the standard deviation of the yearly evolution of ET across PFTs and data sources (Figure 4.4a, c, e, g). We will analyze the ET mean and standard deviation for each PFT sequentially. On average, the annual evolution of ET for $CLM5_{grid}$ and $CLM5_{PFT}$ compares well to the ICOS measurements, as already hinted by the good correlation values in the previous section. They also capture the observed seasonal transitions between low winter ET and high summer ET well. Except for CRO sites, $CLM5_{grid}$ and $CLM5_{PFT}$ ET are slightly lower than the ICOS observations throughout the year but especially in summer (mean PBIAS of −13.08 % and −18.70 %, respectively; see Table B.4). ERA5L and GLASS overestimate ET at sites of all PFTs, most predominantly in the ENF and DBF sites and during summer (mean PBIAS of +28.64 % and +18.25 %, respectively). The magnitude of variation across sites within each PFT (Figure 4.4b, d, f, h) is captured well, generally showing smaller variations at DBF and CRO sites and larger variations at ENF and GRA. Some specific aspects of this variation across sites are captured best by $CLM5_{PFT}$. The bimodality of the intra-station variation at GRA sites is seen across the year (Figure 4.4f), and the peak variability across stations at CRO sites is seen in the second half of the year (Figure 4.4h). This exhibits the ability of $CLM5_{PFT}$ to differentiate ET between stations and the PFTs

better than $CLM5_{grid}$ and the other models. The GLASS ET variability across stations compares remarkably well to the observed across ENF at DBF sites (Figure 4.4b and d).

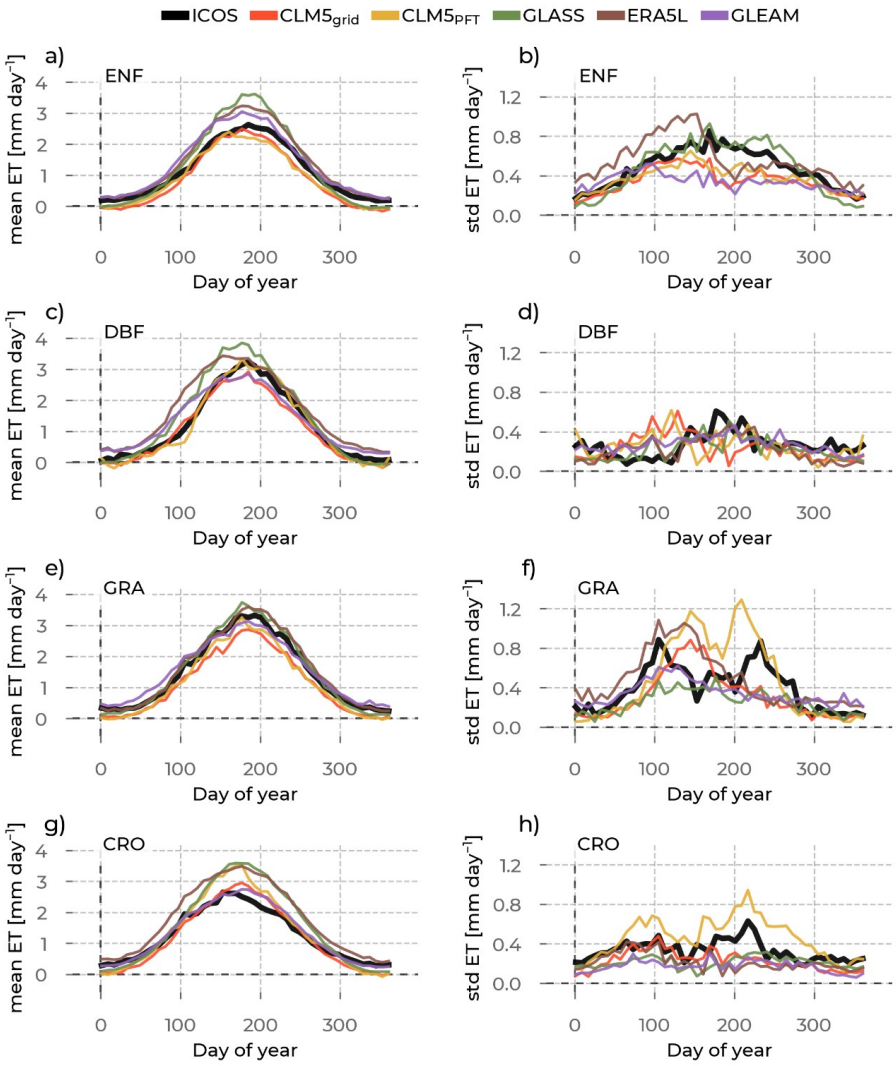

Figure 4.4: In the left column are the yearly evapotranspiration (ET) evolutions averaged across stations belonging to one plant functional type (rows: Evergreen Needleleaf Forest (ENF), Deciduous Broadleaf Forest (DBF), Grasslands (GRA), and Croplands (CRO)) and across the years (available years vary per station, see Table B.1). We differentiate the data source by color (Integrated Carbon Observation System (ICOS) observations: black, Community Land Model v5 ($CLM5$), $CLM5_{grid}$: red, $CLM5_{PFT}$: yellow, Global Land Surface Satellite (GLASS): green, European Center for Medium-Range Weather Forecasting Reanalysis 5 – Land ($ERA5L$): brown, Global Land Evaporation Amsterdam Model (GLEAM): purple). The

corresponding standard deviations across the sites and across the years are plotted in the right column to measure the spread around this mean.

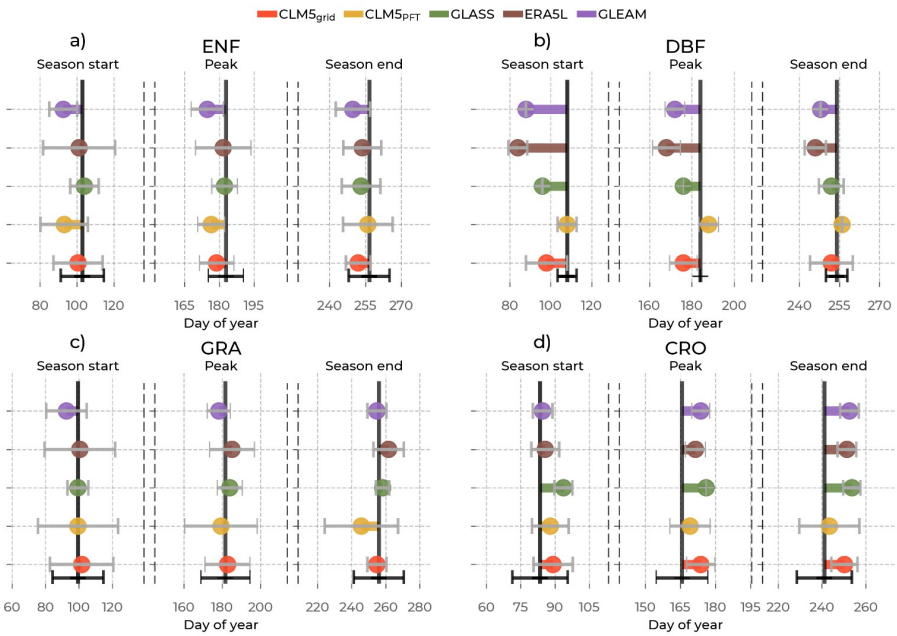

Figure 4.5: Mean shifts in ET phenological events (the start of the growing season, peak, and the end of the growing season) between the Integrated Carbon Observation System (ICOS) observations (solid black line) and the models (by color: Community Land Model v5 (CLM5), $CLM5_{grid}$: red, $CLM5_{PFT}$: yellow, Global Land Surface Satellite (GLASS): green, European Center for Medium-Range Weather Forecasts Reanalysis 5 Land (ERA5L): brown, Global Land Evaporation Amsterdam Model (GLEAM): purple), among sites belonging to one plant functional type: Evergreen Needleleaf Forest (ENF), Deciduous Broadleaf Forest (DBF), Grasslands (GRA), and Croplands (CRO). On the x-axis is the day of the year of the event. Error bars in grey correspond to the standard deviation of the day of the event in the models across sites of one plant functional type, and the error bars in black correspond to the standard deviation across the respective observations.

Figure 4.5 reveals the shift in the timings of key phenological events based on ET (growing season start, summer peak, and growing season end) between each model and the ICOS observations. Generally, for ENF and DBF sites (Figure 4.5a, b), all models show the earlier occurrence, and at CRO (Figure 4.5d), they show a later occurrence of these phenological events than the measurements. $CLM5_{PFT}$ has the mean timing of the events within the standard deviation of the ICOS timing across all PFTs. However, it shows a substantial variability, larger than observed in the event timings across GRA sites. Similarly, GLASS and $CLM5_{grid}$ show close approximations to the observed timings but simulate all these events significantly earlier at DBF sites and significantly later at CRO sites, with little variation in the timings across sites. The ERA5L and GLEAM data exhibit a much

earlier growing season start (24 and 20 d earlier) and summer peak (16 and 12 d earlier, respectively) than observed by ICOS at GRA sites.

GPP

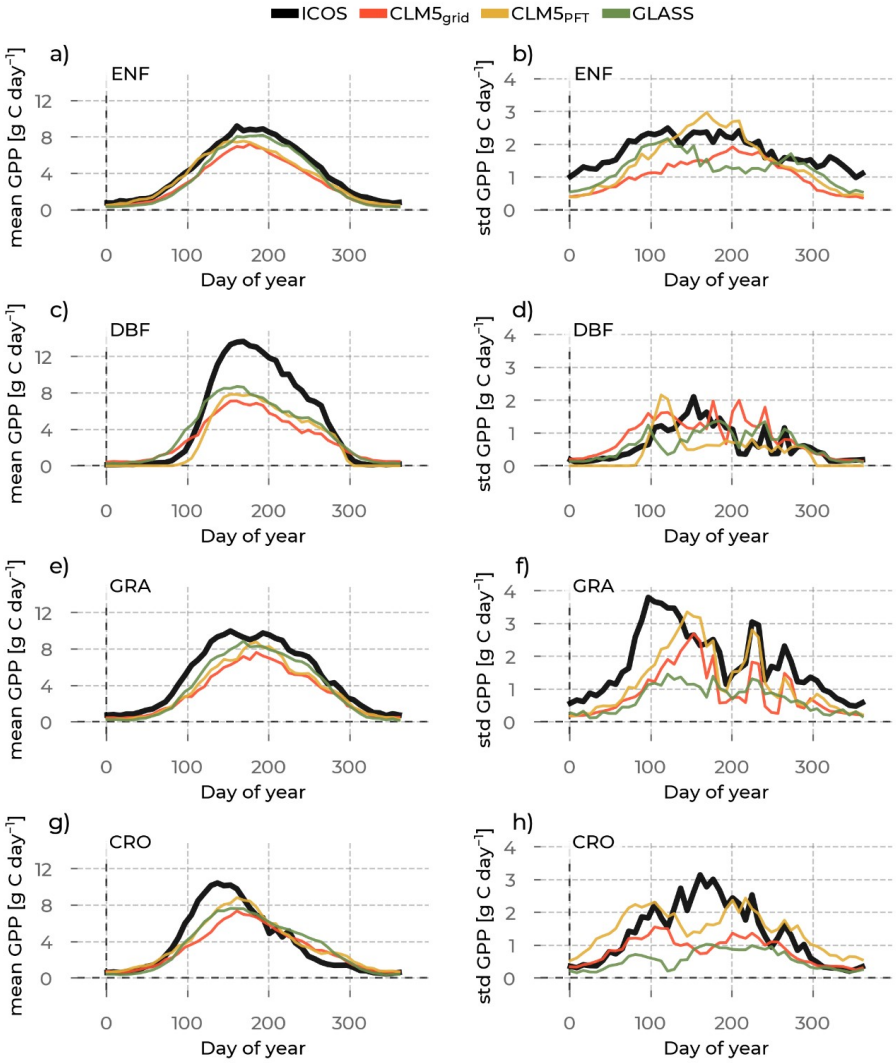

Figure 4.6: In the left column are the yearly Gross Primary Production (GPP) evolutions averaged across stations belonging to one plant functional type (rows: Evergreen Needleleaf Forest (ENF), Deciduous Broadleaf Forest (DBF), Grasslands (GRA), and Croplands (CRO)) and across the years (available years vary per station; see Table B.1). We differentiate the data source by color (Integrated Carbon Observation System (ICOS) observations: black, Community Land Model v5 (CLM5), $CLM5_{grid}$: red, $CLM5_{PFT}$: yellow, Global Land Surface Satellite (GLASS): green). The corresponding standard deviations across the sites and across the years are plotted in the right column to measure the spread around this mean.

The GPP values of all PFTs show a summer peak and a low period in winter (Figure 4.6). The negative values present in the ICOS measurements are caused by the processing of the measurements by ICOS and are, therefore, not represented by CLM5 or GLASS. Again, a general underestimation of observed GPP is shown across all PFTs (Figure 4.6a, c, e, g), particularly during the summer months from all models. $CLM5_{PFT}$ shows a larger GPP than $CLM5_{grid}$ and, therefore, has a lower systematic bias (mean PBIAS across PFTs of −19.61 % and −27.65 %; see Table B.5). GLASS GPP is closer to the ICOS GPP at ENF, DBF, and GRA and has the lowest mean PBIAS across PFTs of −16.67. The most substantial underestimations are at DBF during summer (Figure 4.6c), where $CLM5_{grid}$ and $CLM5_{PFT}$ have a PBIAS of −38.88 % and −43.76 %, and GLASS −24.52 %. The GPP variability across sites is, similar to ET, the lowest at DBF sites. Notably, GLASS remote-sensing GPP underestimates the variability among sites of one PFT substantially throughout the year at GRA and CRO sites (Figure 4.6f, h). The observed variability dynamics across the year, e.g., the bimodality at GRA sites (Figure 4.6f) that was also visible for ET, is captured best by $CLM5_{PFT}$. However, not all models capture the behavior of CRO GPP inter-site variability (Figure 4.6h). This supports the suspicion of the influence of management and missing processes in CRO in the models, possibly concerning the timings of planting, fertilizing, and harvesting the crops as the cause of these mismatches. The overall negative systematic bias in the models points at potentially missing sensitivities to or lower levels of, e.g., atmospheric CO_2 and vapour pressure deficit (VPD) that have been recently found to increase the water use efficiency and carbon assimilation (Friedlingstein et al., 2023; Poppe Terán et al., 2023).

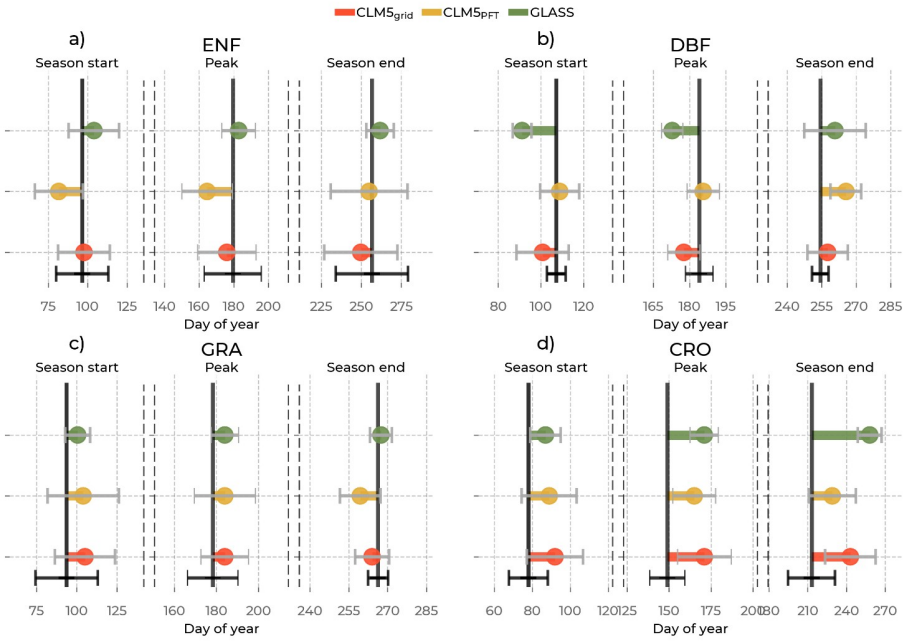

Figure 4.7: Mean shifts in GPP phenological events (the start of the growing season, peak, and the end of the growing season) between the Integrated Carbon Observation System (ICOS) observations (solid black line) and the models (by color: Community Land Model v5 (CLM5), $CLM5_{grid}$: red, $CLM5_{PFT}$: yellow, Global Land Surface Satellite (GLASS): green), among sites belonging to one plant functional type: Evergreen Needleleaf Forest (ENF), Deciduous Broadleaf Forest (DBF), Grasslands (GRA), and Croplands (CRO). On the x-axis is the day of the year of the event. Error bars in grey correspond to the standard deviation of the day of the event in the models across sites of one plant functional type, and the error bars in black correspond to the standard deviation of the respective observations.

Shifts in phenological events between the observations and the models are already noticeable in Figure 4.6 but are quantified and visualized in detail in Figure 4.7. $CLM5_{PFT}$ and $CLM5_{grid}$ predominantly simulate the timing of these events within the standard deviation across ICOS stations for each PFT. In the GLASS GPP data, the events are shifted further from the measurements, most notably at DBF sites (16 d earlier growing season start and 11 d earlier summer peak) and at CRO sites (22 d belated peak and 45 d belated end of the growing season). Generally, in both CLM5 scales, the shifts to the ICOS observations were the largest in CRO. Similar to the ET event timings, $CLM5_{PFT}$ shows the largest variation in these timings among the models, especially at GRA sites, and also considerable differences in the timing of the growing season end of ENF sites. These findings confirm the ability of $CLM5_{PFT}$ to approximate PFT-specific variation in ecosystem processes, but the contrasting results of the model performance indices will be further reviewed in section 4.4.

4.3.4 Statistical distributions

ET

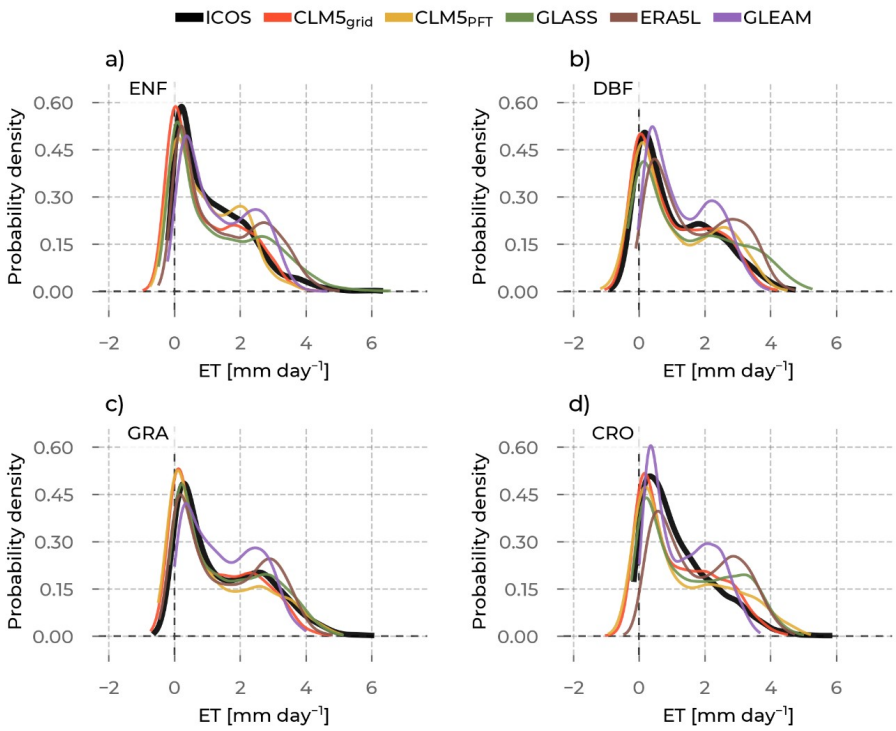

Figure 4.8: The probability density curves for all evapotranspiration (ET) values from stations belonging to the selected plant functional types: Evergreen Needleleaf Forest (ENF), Deciduous Broadleaf Forest (DBF), Grasslands (GRA), and Croplands (CRO). The data source differs by color (Integrated Carbon Observation System (ICOS) observations: black, Community Land Model v5 (CLM5), $CLM5_{grid}$: red, $CLM5_{PFT}$: yellow, Global Land Surface Satellite (GLASS): green, European Center for Medium-Range Weather Forecasts Reanalysis 5 Land ($ERA5L$): brown, Global Land Evaporation Amsterdam Model (GLEAM): purple).

In this section, we describe the results of the statistical distributions of ET in the model and the observations for each PFT. Then, we give more details on the moments of these distributions and how the models compare to the observations. Generally, the models approximate well the shape of the distributions (Figure 4.8), with a pronounced peak in the occurrence of positive ET values close to 0 that represent low winter values across all PFTs and, moreover, the slowly decreasing frequency of values towards the high ET summer values, which is more variable among the models. The variability in the summer peak magnitude (see section 4.3.3) among stations of the same PFT causes the ICOS and CLM5 ET distributions to have only a slightly pronounced second mode at the high summer ET values. On the other hand, the ERA5L and GLEAM ET distributions

show a very pronounced second mode at the higher ET values for each PFT. This hints at the lower variability in the summer peak magnitude among these stations, which misrepresents the observed high variation in ICOS.

The moments of these distributions give more insights into their specific characteristics. Furthermore, differences in moments between the observations and the models can yield important information on potential misrepresentations (Figure 4.9). For example, a differing mean between ICOS and a model points to a general shift in the distribution, specifically its center of mass. Therefore, we confirm a shift in ET distributions of ERA5L, GLASS, and GLEAM towards higher values for all PFTs in reference to ICOS. $CLM5_{grid}$ and $CLM5_{PFT}$ have lower means, except for $CLM5_{PFT}$ at CRO. The second moment, the variance, informs us about the variability in values. Notably, GLEAM data underestimate, and GLASS data overestimate, the observed variability in ET at all PFTs. $CLM5_{PFT}$ has a broad range of variability across PFTs, which corresponds well with ICOS observations, while $CLM5_{grid}$ and the other models show a very similar level of variability independent of the PFT. All models agree with the observed positive sign of the skewness (indicating a longer right tail of the distribution) for all PFTs. And while all the models simulate a platykurtic (negative excess kurtosis and pronounced relative tail) characteristic of the distributions across PFTs, ICOS shows a leptokurtic (positive excess kurtosis, less pronounced tails, and more pronounced peak) behavior at ENF and CRO sites. Furthermore, the variation in the reach model's skewnesses and kurtoses (y-axis ranges for each color in Figure 4.9c and d) across the PFTs is considerably lower than the observed ranges (corresponding x-axis ranges). Altogether, these findings showcase the ability of $CLM5_{PFT}$ to model intra- and inter-PFT ET variance better than the other considered models, on the one hand, but also showcase the shortcomings of all the considered models in representing the variation in the extreme ends of the ET distributions across all PFTs on the other hand.

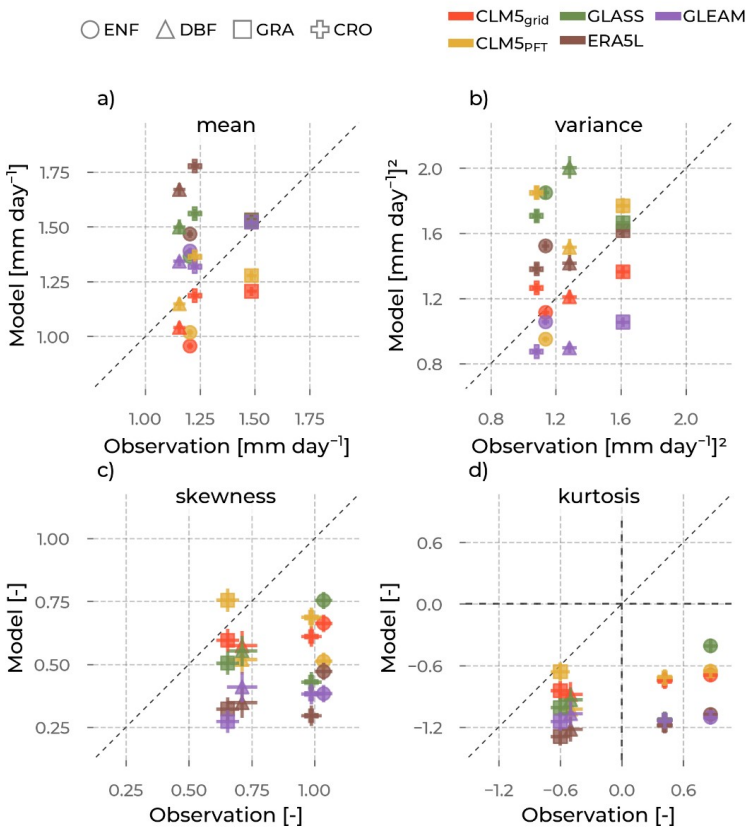

Figure 4.9: The mean (a), variance (b), skewness (c), and excess kurtosis (d) of the evapotranspiration (ET) distributions (visualized in Figure 4.8) from the models (y-axis, colors: Community Land Model v5 (CLM5), $CLM5_{grid}$: red, $CLM5_{PFT}$: yellow, Global Land Surface Satellite (GLASS): green, European Center for Medium-Range Weather Forecasts Reanalysis 5 Land ($ERA5L$): brown, Global Land Evaporation Amsterdam Model (GLEAM): purple), as opposed to the corresponding values from observations (x-axis) aggregated for each plant functional type (marker type): Evergreen Needleleaf Forest (ENF), Deciduous Broadleaf Forest (DBF), Grasslands (GRA), Croplands (CRO). The error bars are the standard errors of the respective moment, depending on the sample size.

The moments of these distributions give more insights into their specific characteristics. Furthermore, differences in moments between the observations and the models can yield important information on potential misrepresentations (Figure 4.9). For example, a differing mean between ICOS and a model points to a general shift in the distribution, specifically its center of mass. Therefore, we confirm a shift in ET distributions of $ERA5L$, GLASS, and GLEAM towards higher values for all PFTs in reference to ICOS. $CLM5_{grid}$ and $CLM5_{PFT}$ have lower means, except for $CLM5_{PFT}$ at CRO. The second moment, the variance, informs us about the variability in values. Notably, GLEAM data underestimate, and GLASS data overestimate, the observed variability in ET at all PFTs. $CLM5_{PFT}$ has

a broad range of variability across PFTs, which corresponds well with ICOS observations, while $CLM5_{grid}$ and the other models show a very similar level of variability independent of the PFT. All models agree with the observed positive sign of the skewness (indicating a longer right tail of the distribution) for all PFTs. And while all the models simulate a platykurtic (negative excess kurtosis and pronounced relative tail) characteristic of the distributions across PFTs, ICOS shows a leptokurtic (positive excess kurtosis, less pronounced tails, and more pronounced peak) behavior at ENF and CRO sites. Furthermore, the variation in the reach model's skewnesses and kurtoses (y-axis ranges for each color in Figure 4.9c and d) across the PFTs is considerably lower than the observed ranges (corresponding x-axis ranges). Altogether, these findings showcase the ability of $CLM5_{PFT}$ to model intra- and inter-PFT ET variance better than the other considered models, on the one hand, but also showcase the shortcomings of all the considered models in representing the variation in the extreme ends of the ET distributions across all PFTs on the other hand.

GPP

We continue to delineate the results of the same analyses for the GPP distributions and their moments (Figure 4.10). The frequency peaks at the low GPP values, which correspond to the base winter GPP, are overestimated by all models at ENF, DBF, and GRA. This could partly be explained by negative GPP values in the ICOS data, which the models do not represent. By definition, there is no negative GPP. However, these negative values are given through the uncertainty range of the NEE partitioning method and are retained in the analysis to preserve the partitioning distribution (Pastorello et al., 2020; Reichstein et al., 2012). This is probably related to underestimating the observed winter GPP in ENF and GRA sites seen in Figure 4.6a and e. Another striking finding is the missing occurrence of the highest observed GPP values in the models at all PFTs, but most noticeable at DBF sites, where the upper-half range of GPP values (>12 g C d^{-1}) is not represented in any model. The overrepresented mid-range GPP values and the partly pronounced second modes in the mid-range GPP values across PFTs are possibly caused by the low summer peaks and low variability across sites (see Figure 4.6).

The models show lower GPP means than the ICOS measurements for all PFTs in Figure 4.11a. Similarly, for all models across all PFTs, the underestimated GPP variance indicates a lower spread of the PFT distributions than in ICOS. While models agree on the positive skewness of the GPP distribution (skewed to the left), the largest skewness at CRO sites is not well represented by all the models.

Finally, similar to the findings with ET kurtosis, the models fail to distinguish the distinct leptokurtic characteristics (tails that are less heavy) of the GPP distribution of CRO sites compared to the other PFTs, as seen in the observations. Across PFTs and for all models, the ranges spanned by the intra-PFT distribution moments are smaller than those observed. Most strikingly, the GPP variance range across PFTs, which is, among the models, the largest for $CLM5_{PFT}$ (between 8 and 12 g C d^{-1}), is much smaller than for ICOS (11 to 27 g C d^{-1}). This suggests the models do not simulate GPP differently enough between the PFT groupings. Thus, model development and parameter optimization studies that aim to improve these representations should focus on enhancing the variability in DBF.

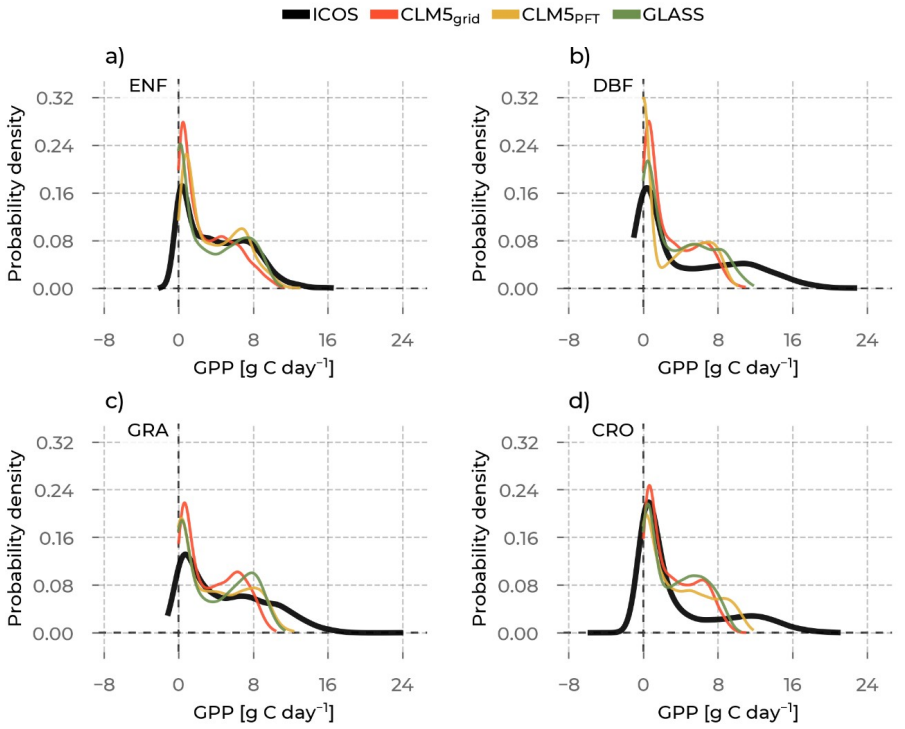

Figure 4.10: The probability density curves for all Gross Primary Production (GPP) values from stations belonging to the selected plant functional types are shown: Evergreen Needleleaf Forest (ENF), Deciduous Broadleaf Forest (DBF), Grasslands (GRA), Croplands (CRO). The data source differs by color (Integrated Carbon Observation System (ICOS) observations: black, Community Land Model v5 (CLM5), $CLM5_{grid}$: red, $CLM5_{PFT}$: yellow, Global Land Surface Satellite (GLASS): green).

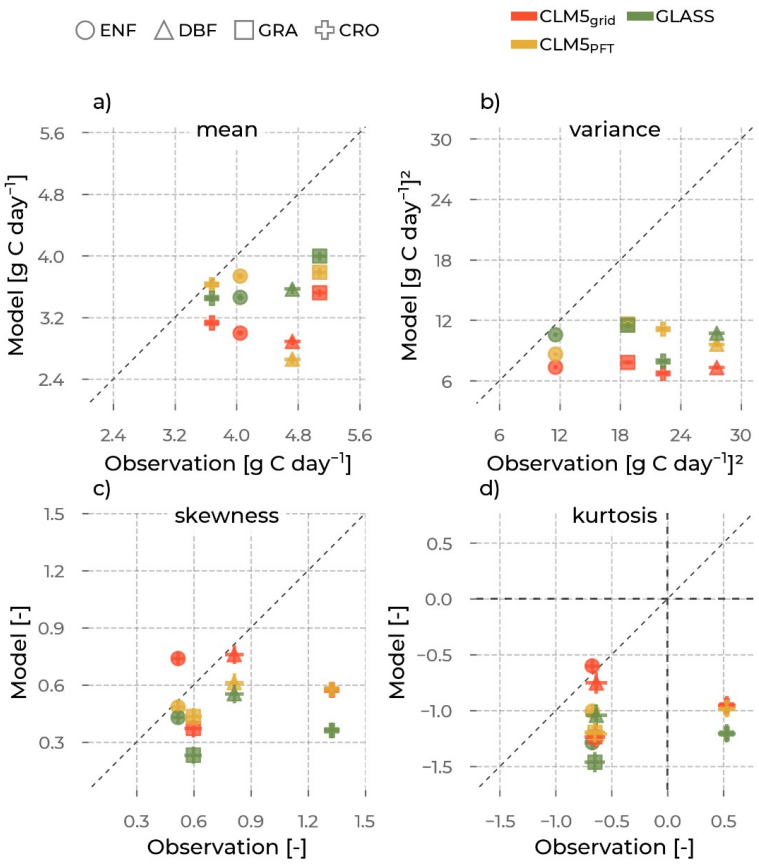

Figure 4.11: The mean (a), variance (b), skewness (c), and excess kurtosis (d) of the gross primary production (GPP) distributions (visualized in Figure 4.10) from the models (y-axis, colors: Community Land Model v5 (CLM5), $CLM5_{grid}$: red, $CLM5_{PFT}$: yellow, Global Land Surface Satellite (GLASS): green), as opposed to the corresponding values from observations (x-axis) aggregated for each plant functional type (marker type): Evergreen Needleleaf Forest (ENF), Deciduous Broadleaf Forest (DBF), Grasslands (GRA), Croplands (CRO). The error bars are the standard errors of the respective moment, depending on the sample size.

4.3.5 The inter-site similarity of PFT-groups

To support the interpretations of our findings, we quantify the similarity of ET and GPP across sites of the same PFT and compare the differences between the models and the observations. In this section, we analyze the mean RMSD of each PFT per ET and GPP data sources. A low RMSD indicates that the stations corresponding to one PFT are similar, while a high RMSD hints at a greater diversity within the PFT. By comparing the mean RMSD per PFT for ET and GPP across data sources, we can evaluate how much diversity is captured in the data of a particular PFT in the observations and models. The standard deviation

of the RMSD for each PFT gives information on the spread of the inter-site RMSDs within the PFT group around that mean.

Figure 4.12 shows that $CLM5_{grid}$ and GLEAM have lower ET time series differences between the corresponding sites for all PFTs than ICOS. CLM_{PFT} has a lower mean RMSD than $CLM5_{grid}$ among ENF and DBF sites. Both $CLM5_{PFT}$ and $CLM5_{grid}$ underestimate the observed diversity of ET at ENF and DBF sites. Interestingly, the variation in ERA5L and GLASS ET time series for ENF is higher than observed, and they also show the most significant variation in RMSD. Meanwhile, the DBF mean RMSD of all models is lower than that of ICOS. $CLM5_{PFT}$ shows a higher diversity of ET between GRA sites and CRO sites than $CLM5_{grid}$. The $CLM5_{PFT}$ surpasses the observed mean RMSD for the GRA PFT, highlighting the potential to simulate GRA sites variably. All other models underestimate it slightly ($CLM5_{grid}$, ERA5L) or in a more pronounced manner (GLASS and GLEAM). Particularly at CRO sites, the ET RMSD of $CLM5_{PFT}$ is substantially higher than the other models and at a similar level to ICOS observations. In contrast, all other models show significantly lower mean RMSDs there. Generally, a higher ET RMSD mean in a PFT group comes with a higher spread (higher standard deviation) for all data sources. The RMSD in ET between stations is lower for $CLM5_{grid}$ and GLEAM than for ICOS for all PFTs.

Figure 4.13 shows that for GPP, the models generally have a lower mean RMSD than ICOS across stations for all PFTs, except for $CLM5_{grid}$ at DBF. $CLM5_{PFT}$ has a more diversely simulated ET across ENF, GRA, and CRO sites than $CLM5_{grid}$. Interestingly, the observed magnitude of the RMSD is lowest for DBF and highest for CRO and has a more extensive range across PFTs than the models. For example, the RMSDs of ICOS data differ by approximately 1.3 $g\,C\,d^{-1}$ between GRA and CRO, while $CLM5_{grid}$, $CLM5_{PFT}$, and GLASS indicate similar RMSDs for those PFTs. Especially $CLM5_{grid}$ shows a constant within-PFT variability in around 1.5 $g\,C\,d^{-1}$ independent of the PFT. Higher mean GPP RMSD values also come with a higher standard deviation. These results hint at a complex relationship of variability representation within the PFTs. The higher RMSE values of $CLM5_{PFT}$ in the general model performance analysis (section 4.3.2) suggest that the variation across sites of one PFT seen here does not directly translate to better model performance. Apart from the magnitude of the variability, its accurate and proportionate timing is pivotal for enhanced model performance.

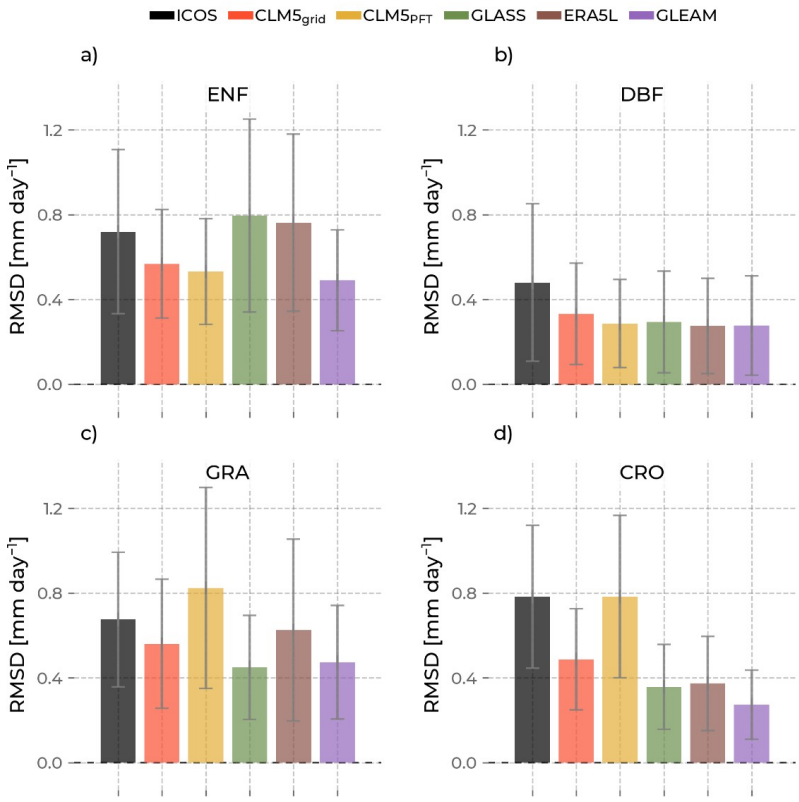

Figure 4.12: The bars indicate the mean of the root mean square difference (RMSD) of evapotranspiration calculated for sites with the same plant functional type. The error bars are their standard deviation. Low values indicate high similarity between the sites, and high values show high dissimilarity. The color of the bars differentiates the data source (Integrated Carbon Observation System (ICOS): black, Community Land Model v5 (CLM5), $CLM5_{grid}$: red, $CLM5_{PFT}$: yellow, Global Land Surface Satellite (GLASS): green, European Center for Medium-Range Weather Forecasts Reanalysis 5 Land ($ERA5L$): brown, Global Land Evaporation Amsterdam Model (GLEAM): purple).

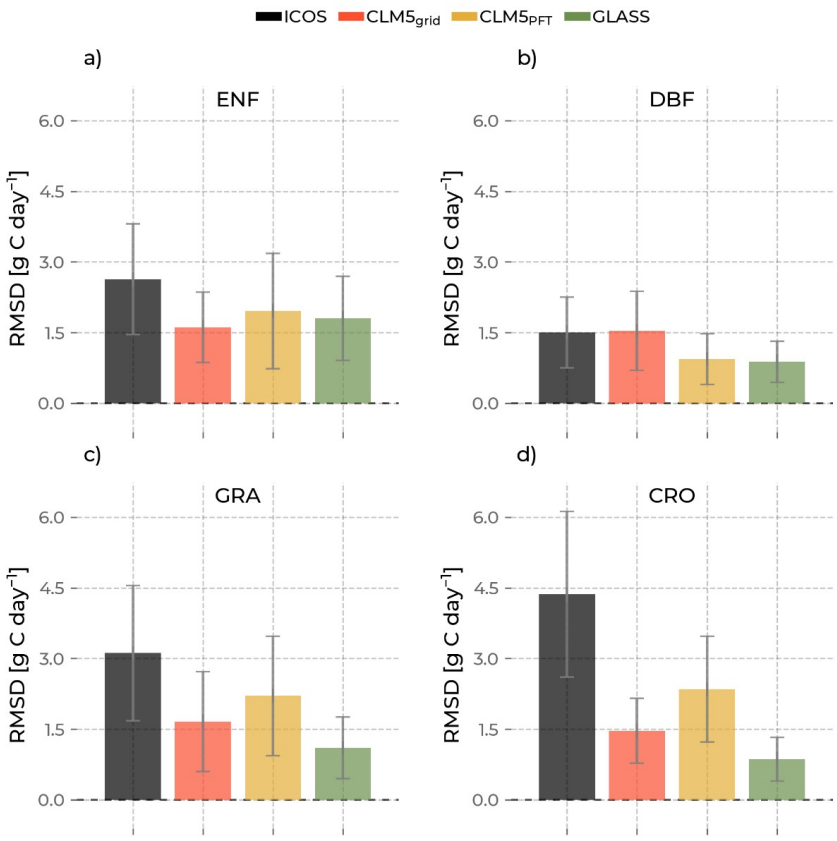

Figure 4.13: The bars indicate the mean of the root mean square difference (RMSD) of gross primary production calculated for sites with the same plant functional type. The error bars are their standard deviation. Low values indicate high similarity between the sites, and high values show high dissimilarity. The color of the bars differentiates the data source (Integrated Carbon Observation System: black, Community Land Model v5 (CLM5), $CLM5_{grid}$: red, $CLM5_{PFT}$: yellow, Global Land Surface Satellite (GLASS): green).

4.4 Discussion

Our results show that $CLM5_{grid}$ and $CLM5_{PFT}$ approximate the ET observations from ICOS better than GLASS remote-sensing and ERA5L reanalysis but worse than GLEAM reanalysis. Moreover, especially for $CLM5_{PFT}$, the systematic error in simulating ET is lower than all other evaluated data sets. For GPP, we found that $CLM5_{grid}$ and $CLM5_{PFT}$ performed worse than GLASS data, indicated by a larger PBIAS and larger RMSE. Surprisingly, $CLM5_{PFT}$ generally had a higher RMSE than $CLM5_{grid}$ but, at the same time, a lower PBIAS. Averaged ET and GPP phenologies were relatively well simulated but exhibited underestimations across all PFTs, especially in DBF, compared to ICOS measurements. $CLM5_{PFT}$ better captured the PFT-specific mean and standard deviation of the ET and GPP

annual dynamics than $CLM5_{grid}$ and reanalyses and remote-sensing data. The GPP and ET distributions analysis showed underestimations of their observed variability for all models, namely $CLM5_{grid}$, $CLM5_{PFT}$, GLASS, ERA5L, and GLEAM. Last, we found that for most PFTs, the modeled and remotely sensed data were too similar between stations of the same PFT group compared to the ICOS observations.

4.4.1 Uncertainty

Observations

Notably, the EC measurements carry uncertainties that might affect the results of this study, especially related to the systematic errors in the simulations. For instance, EC measurements neglect the energy from large eddies. To check for possible inconsistencies, we evaluated the energy-balance-corrected ET (ET_{corr}) from the ICOS sites (Pastorello et al., 2020). This methodology assumes a constant Bowen ratio to close the energy imbalance. Simulated ET underestimates ET_{corr} to a greater degree than the non-corrected ICOS ET (Figure B.1 and Figure B.2), suggesting a higher systematic error than in the analysis of non-corrected ET. Besides that, we discovered the same patterns with the corrected ET, concluding that the energy balance error did not introduce significant bias to our results and the interpretations. Furthermore, GPP is not directly measured but partitioned from NEE. The NEE partitioning method has an underlying uncertainty stemming from potentially unfulfilled assumptions that propagate to the GPP and ER variables in the ICOS data. So, we also ensured that our results remained consistent by evaluating the non-partitioned NEE and the ER variables (Figure B.3, Figure B.4, Figure B.5, and Figure B.6). We discovered a substantial underestimation and missing variability in NEE and ER across PFTs in CLM5, confirming the systematic underestimation in our analysis of GPP. While we believe that our analyses have followed meticulous approaches to ensure robust results by applying the ICOS quality flags and comparing these additional variables, many studies still emphasized the biases arising from a shifting footprint with varying wind direction and wind speed and the energy balance correction method assuming a constant Bowen ratio (Chu et al., 2021; Eshonkulov et al., 2019; Jung et al., 2020). Therefore, we encourage developing and using novel and more accurate energy-balance-closure methods (W. Zhang et al., 2024). Furthermore, dropping bad-quality gap-filled data from the ET and GPP time series might introduce a bias that underrepresents periods of low-friction velocity and atmospheric inversion conditions. Last, based on the geographical distribution of the ICOS station network, the results might misrepresent southern

and eastern Europe and semi-arid and arid hydro-climates (Figure 4.1; also read Ohnemus et al., 2024). Those factors might have influenced the diversity of ET and GPP values and the ranges of their distributions.

Forcing

Importantly, discrepancies between the COSMO Reanalysis used to force the European CLM5, and the station observations might introduce deviation into our analyses that could hamper interpretations of our results regarding the model functionality. While the high-resolution forcing data already include information from observations through data assimilation, particular locations and conditions might be less well represented than others, and a resulting bias in the meteorological variables would propagate to the simulation of ET and GPP. However, data assimilation approaches minimize the systematic error in the atmospheric model to the observations. Furthermore, the probability and potential influence of including a bias from the forcing of a single location is lowered by considering multiple sites in the performance and statistics of the PFTs. Nevertheless, we assessed the meteorological variables from the COSMO Reanalysis 6 (temperature, shortwave incoming radiation, precipitation, and relative humidity) with the ICOS station data to scrutinize potential errors arising from the forcing. We used the same approach for the GPP and ET evaluation (Figure B.7 – Figure B.14). We discovered that the forcing variables' average yearly dynamics and distributions represent the ICOS observations well. More minor yet notable misrepresentations include underestimations of shortwave downward radiation and precipitation in summer and relative humidity over GRA and CRO sites throughout the year compared to the measurements. This could explain some of our analyses' ET and GPP underestimations by CLM5. Notably, the mean and variance across the PFTs and their ranking are represented reasonably well for all forcing variables compared to our results with GPP and ET. Furthermore, the skewness and excess kurtosis of the forcing temperature and shortwave downward radiation compare well to the ones from ICOS, indicating well-matching distributions between the COSMO Reanalysis 6 and the observations. However, in particular, the higher-degree moments of the distribution are not well simulated for precipitation and relative humidity. These characteristics of the distributions affect the CLM5 simulations of GPP and ET and might have influenced our results. Further considerations, including ensemble simulations with perturbed forcings, are required to capture the uncertainty introduced into CLM5 fully, but this is beyond the scope of this study.

Static information and initial conditions

The static surface information, including the soil texture, elevation, aspect, land unit, and PFT distributions, affect the simulation of ET and GPP in CLM5. The soil texture composition will define how water is stored and conducted in the soil, contributing to the evaporation from the soil, an essential ET component. Furthermore, the soil texture will influence root water uptake if vegetation is present in the soil column, indirectly impacting plants' transpiration, another critical ET component. Furthermore, ET is regulated by the available energy, which is determined by how the canopy, the elevation, and the aspect of that location influence the incoming radiation. Especially the diversity between these input variables across the locations of the ICOS stations might have played an essential role in the simulation of the PFT-specific ET and GPP distributions.

Last, particularly for $CLM5_{grid}$, GLASS, GLEAM, and ERA5L, the distribution of PFTs across the domain and in the grid cells corresponding to the ICOS stations define the equations and parameters that will be used for the calculation of ET and GPP. Consequently, if the grid cells corresponding to ICOS stations are dominated by PFTs that do not comply with the stations' footprints, the simulations of specific PFTs in the model are negatively affected. Importantly, this does not apply to $CLM5_{PFT}$ because we could select the data that belong to the adequate PFT. Therefore, interpretations of our results relating directly to vegetation functions implemented in CLM5 are here primarily focusing on the $CLM5_{PFT}$ data.

The initial conditions of the carbon cycle, most notably the size of the soil and vegetation carbon pools, are another source of uncertainty. Essentially, our spin-up and production simulations were restricted to the years where the high-resolution forcing was available (1995–2018). The spin-up simulations, therefore, recycle atmospheric forcings for a substantial period, which we also use in the production simulations. Hence, the production simulations adopted the equilibrium state (incoming carbon equals outgoing carbon) required to conclude the spin-up. However, in natural conditions, there was no carbon equilibrium in the simulated years. Instead, the carbon cycle experiences dynamic changes, such as long-term trends resulting from changing environmental conditions. Many European ecosystems exhibited a net carbon uptake, thus acting as a carbon sink (Pilli et al., 2017; Winkler et al., 2023), and were measured in ICOS accordingly. The negative long-term mean NEE indicates carbon sources, evident across all PFTs in the EC observations (Figure B.4a). On the other hand, the simulations show a NEE close to zero for all PFTs, directly showing the effect of

the equilibrium state of the land surface in the model. The results of DBF, which is the most significant carbon sink in the ICOS data and simultaneously shows the largest GPP underestimations by CLM5, underline a potentially important role of the carbon equilibrium in our results. Future work will conduct a more comprehensive spin-up under conditions closer to a real-world carbon equilibrium (the 1950s or earlier) and a transition run before the production simulations to capture the dynamic trends of the land surface processes. Possibly, the bias in the EC measurements towards conditions with low-friction velocity and atmospheric inversion might also cause overestimations of GPP and the resulting carbon sink in ICOS.

4.4.2 PFT-specific evaluation

While $CLM5_{PFT}$ showed a smaller systematic error than CLM_{grid} for most PFT compared to the observations (lower absolute PBIAS), the ability to approximate the observation time series is worse (higher RMSE). A shifting sign in the bias of the $CLM5_{PFT}$ data explains these counterintuitive results. The presence of both positive and negative bias (in time and across stations) cancels out and yields an overall low PBIAS. In summary, we find in the evaluation that the ET time series of CLM_{PFT} are not closer to observations than $CLM5_{grid}$ for any PFT, but $CLM5_{PFT}$ generally approximates the ET sum over time better than $CLM5_{grid}$ for ENF, DBF, and CRO. However, it is also clear that, on average, the phenology of $CLM5_{PFT}$ is closer to the observed than $CLM5_{grid}$, for instance, for both ET and GPP at DBF and GRA sites. Furthermore, the timings of the phenological events in $CLM5_{PFT}$ are most often closer to the observed than in $CLM5_{grid}$. Importantly, critical PFT-specific characteristics, like the timing of DBF's steep spring GPP increase, are only captured by $CLM5_{PFT}$ and the inter-site variability in ET and GPP throughout a standard year. This discrepancy between the evaluation metrics and the vegetation phenology suggests that $CLM5_{PFT}$ could better capture the PFT-specific variability that ICOS observes. However, this variability is modeled in a way that did not contribute to a low RMSE that is, for instance, shifted in time or space, so the averaged PFT-specific comparisons (the phenology and the distribution moments) compare better with ICOS than $CLM5_{grid}$. Further evidence of this explanation is that $CLM5_{PFT}$ generally captures more variability (higher ET and GPP standard deviation across sites throughout the year for ENF, GRA, and CRO and higher variance for each PFT). This ability to capture more variability than the other models, closer to the observed variability, can improve the represented variability in $CLM5_{PFT}$ if the suitable variation can be modeled at the right time and location. This spatiotemporal

discrepancy of simulated and observed GPP and ET variability could potentially be solved with optimized PFT parameters (Baker et al., 2022; Birch et al., 2021; Cheng et al., 2021; Dagon et al., 2020; M. Deng et al., 2021; Fisher et al., 2019).

Several past studies also indicated the underestimation of ET and GPP in CLM5 compared to observations (Birch et al., 2021; Boas et al., 2023; Cheng et al., 2021; Strebel et al., 2023), which we confirm in this study. Parameter improvements could also alleviate these general underestimations of GPP and ET across PFTs, especially during summer (Dagon et al., 2020). However, optimal parameters might vary from site to site (Lin et al., 2015), even if they have the same PFT. Thus, CLM5 and, more generally, LSMs that implement plant traits as parameters on the PFT level cannot capture this intrinsic PFT variability resulting from these traits. Although optimized parameters might still reduce the bias on the continental level, a more comprehensive approach to the spatiotemporal variability in plant traits might improve regional simulations drastically (L. D. L. Anderegg et al., 2022; Kattge et al., 2011; Van Bodegom et al., 2014).

Given the hydraulic role of vegetation leaves in controlling transpiration, there is a tight relationship between ET, GPP, and LAI. In CLM5–BGC, the assimilated carbon by GPP gets further partitioned to respiration and the carbon storage in the plant organs, i.e., leaves, roots, and stems. Furthermore, the leaf carbon then controls the development and state of the vegetation leaves and, thus, the LAI. On the other hand, LAI controls GPP by determining the upscaling factors from leaf photosynthesis to the canopy, thereby driving canopy conductance. Unfortunately, no large-scale LAI in situ measurements and no $CLM5_{PFT}$ simulated LAI are available, and comparisons between $CLM5_{grid}$ LAI and reanalysis or remote-sensing LAI suffer from known biases in the latter and yield no further context for our evaluation based on ground truth information. We adhered to an LAI evaluation of CLM5 with sparse but systematic ICOS measurements, ERA5L reanalysis, and GLASS based on MODIS (Figure B.15). Notably, the ICOS LAI measurements are only available for 2 years of the study period (2017 to 2018) and are limited to ENF and CRO sites. Additionally, LAI measurements' expensive and time-intensive nature restricts the time resolution to a few yearly measurement points. As a result, the data points for comparison are few, and the uncertainties are larger (noticeable larger error bars in Figure B.15). Another caveat is the potential mismatch of the land surface representation between the EC tower footprint (ET and GPP measurements) and the area covered by the LAI measurement campaigns. However, some key findings from this analysis are still robust. For example, all models overestimate LAI at ENF and

CRO sites (Figure B.15a), contrasting the results of GPP and ET. The variance in ENF sites is much more significant in GLASS and ERA5L than in $CLM5_{grid}$, which is closest to the observations. The higher-order moments are more uncertain because of the small number of data points. The contrasting results, especially between the LAI and GPP PFT level averages, suggest that processes and parameters connecting the assimilated carbon to the leaf area, depending on the environmental conditions, must be revisited. However, we make an even stronger case for systematic, long-term, and high-resolution LAI in situ measurements (for example, using drones; Bates et al., 2021), which would support a more robust and diverse evaluation of the simulations of this essential variable.

4.4.3 Inter-site similarity of PFT groups

For all models ($CLM5_{grid}$, $CLM5_{PFT}$, ERA5L, GLASS, and GLEAM), the distributions of ET and GPP across PFTs are very similar, which is not the case for the observations. This is especially true for their variances (i.e., their spread around the mean) but also notable for the means, skewnesses, and kurtoses. We expected $CLM5_{PFT}$ to show more significant variability than $CLM5_{grid}$ and the other grid scale models because the aggregated mixed-PFT data of the grid cell would homogenize the variables and cancel out some of the variability. While $CLM5_{PFT}$ shows a more extensive range of variation in ET and GPP across PFTs than $CLM5_{grid}$, ERA5L, GLASS, and GLEAM, it still vastly underestimates the observed range of variance by ICOS, especially for GPP (Figure 4.9 and Figure 4.11).

The mean RMSD across sites of the same PFT indicates that ET across sites can be as different in CLM_{PFT} for GRA and CRO as in the observations (Figure 4.12). However, the ET differences across sites with the same PFT were underestimated at ENF and DBF. GPP differences across sites with the same PFTs were underestimated for all PFTs (Figure 4.13). This suggests that the missed variance could mainly stem from missed PFT internal inter-site differences or unresolved differences in site-specific abiotic conditions (e.g., soil depth and texture). Possibly, this could not be improved through optimization of PFT-specific parameters, as these sites would still share the same set of parameters. An enhanced concept of functional types in vegetation, focusing on the spatiotemporal variability in observed plant traits, could better facilitate improvements that raise the simulated ET and GPP variance in space and time.

4.4.4 Data requirements

As outlined above, beyond parameter optimizations, a comprehensive implementation of functional ecosystem diversity could significantly improve the LSM simulation outputs regarding multiple aspects of their distributions. This could introduce a state-of-the-art understanding of vegetation function into LSMs, which is essential to evaluate different theories of plant trait evolution and their effect on current and future energy, water, and carbon cycles.

In that light, we encourage sites to co-locate research infrastructures (Futter et al., 2023), like ICOS and the integrated European Long-Term Ecosystem Research Infrastructure (eLTER RI). Thereby, sites cover additional observation spheres like biodiversity (e.g., functional diversity of plants) and socio-ecology (through forest and crop management and driving land use change) and establish a strong base for studies to increase the understanding of the whole system (Baatz et al., 2018; Mirtl et al., 2018, 2021; Ohnemus et al., 2024). Furthermore, this would promote large-scale observations needed to introduce more trait variability into LSMs. Last, combining LSMs and these holistic observations by data assimilation, going beyond decoupled modeling efforts (Bloom et al., 2020) and resulting in an ecosystem reanalysis (Baatz et al., 2021), would provide essential, explicit and accurate data on the carbon cycle, which are currently unavailable.

4.4.5 Distribution moments and droughts

Investigating the influence of drought on the analyses, or generally the ability of the models to simulate drought and the vegetation response, is complex due to the differences in drought response functionality. For instance, plant water stress might occur due to different magnitudes of water deficit in the soil on different aggregation timescales and with a variable lag to the water deficit. A future study will investigate the PFT-scale drought responses from the model and how the drought propagates through the ecohydrological sphere and compare it to observations. However, drought frequency, duration, and severity affect the shapes of the distribution of the precipitation and, eventually, the ecosystem processes. Thus, we briefly discuss possible insights into their drought responses.

Importantly, the skewness and excess kurtosis moments, which inform us about the characteristics of the distribution tails (relativity between the tails and the general tailed aspect, respectively) of precipitation (Guo, 2022), as well as vegetation states and function (Cooley et al., 2022; Kanavi et al., 2020; C. Liu et al., 2022), are influenced by dry conditions, depending on their frequency,

duration, and severity. We found a low variability in the skewness and excess kurtosis of the precipitation used to force our CLM5 simulations (Figure B.10c and d), specifically a significantly lower skewness and excess kurtosis at ENF and DBF sites. A lower positive skewness than the observations means that the distribution is less skewed towards lower values, and a lower positive excess kurtosis than the observations indicates generally larger tails. A possible interpretation of these differences in the distribution moments is that the atmospheric forcings show more frequent, longer, and more severe extreme precipitation events, while the ICOS measurements are more concentrated around their mean. While the propagation of these extreme events could be complex and non-linear, we generally found the same results (lower skewness and smaller absolute excess kurtosis) for the simulated distributions of ET and GPP for almost all models and PFTs (Figure 4.9c–d and Figure 4.11c–d), suggesting a more direct relationship. However, because of the possible non-linearity and the influence of other factors, the detailed relationship between these findings and the ability of CLM5 to simulate ecosystem drought responses must be examined in future studies. In any case, the missing accuracy in representing higher distribution moments in the atmospheric forcings and in land surface models must be considered in studies using these to investigate drought.

4.5 Conclusions

We evaluated the simulated evapotranspiration (ET) and gross primary production (GPP) from a 3 km resolved Community Land Model v5 (CLM5) set up over the European CORDEX domain. We differentiated the model outputs between the grid scale ($CLM5_{grid}$) and the plant-functional-type scale ($CLM5_{PFT}$) and compared them with ICOS station data as ground truth data. Furthermore, we compared with ET and GPP from remote-sensing-derived data from the Global Land Surface Satellite (GLASS) and reanalysis products such as the European Centre for Medium-Range Weather Forecast Reanalysis 5 – Land (ERA5L) and the Global Land Evaporation Amsterdam Model (GLEAM). $CLM5_{grid}$ and $CLM5_{PFT}$ exhibited promising skills in approximating the observations and often performed better than ERA5L, GLASS, and GLEAM. $CLM5_{PFT}$ showed a lower systematic bias (lower percent bias) but approximated the ICOS observations in a generally worse manner (larger root mean square error) than $CLM5_{grid}$ (Figure 4.2, Figure 4.3, Table B.4, and Table B.5). ET and GPP were systematically underestimated across all PFTs throughout the year for both model scales. Especially during summer at DBF sites, GPP was substantially

lower for $CLM5_{PFT}$ and $CLM5_{grid}$ than for ICOS observations (Figure 4.4 and Figure 4.6).

Essentially, $CLM5_{PFT}$ and, to a greater degree, $CLM5_{grid}$, ERA5L, GLEAM, and GLASS showed a lower spatiotemporal variability in ET and GPP than the measurements exhibited by a lower range of all the modeled ET and GPP distribution moments across PFTs than in ICOS. This smaller range and a lower root mean square difference between sites of one PFT group suggests that $CLM5_{grid}$ and, more surprisingly, $CLM5_{PFT}$ simulate GPP and ET more similarly across PFTs than the ICOS measurements.

Future studies should investigate whether optimizing parameters in $CLM5_{PFT}$ with observation data increases the diversity of ET and GPP values or whether this is a structurally induced bias. This work provides essential insights for studies that aim to find optimized parameters and meaningful context for analyses of more specific ET and GPP dynamics using the evaluated data.

5 The drought response of European ecosystem processes via multiple components of the hydrological cycle

This chapter is based on the manuscript:

Poppe Terán, C., Naz, B.S., Belleflamme, A., Rahmati, M., Vereecken, H., Hendricks Franssen, H.-J., 2025. The drought response of European ecosystem processes via multiple components of the hydrological cycle.

5.1 Introduction

Readily available water is required for human life and well-being: societies depend on water for domestic and industrial use, as well as agricultural food and fiber production (M. A. Ali & Kamraju, 2023). Furthermore, natural ecosystems need a sufficient water supply for their functioning and to continuously provide ecosystem services, such as carbon storage on the land surface, habitat for a diverse flora and fauna, and clean and breathable air (Schröter et al., 2019), which have additional significant implications for society. While available water resources vary in magnitude, time, and space, ecosystems and cultures have adapted to the local conditions. However, a water deficit beyond the normal variability they locally adapted to can invoke irreversible changes to the ecosystem's structure and performance (Clark et al., 2016; Graf et al., 2020; Jiang et al., 2013; W. Li et al., 2023; Poppe Terán et al., 2023; Rohde et al., 2024) and threaten human lives and livelihoods (European Commission. Joint Research Centre., 2020; Rusca et al., 2022; WMO, 2021; Zscheischler et al., 2020).

These significant water deficits – a.k.a. droughts – are predominantly categorized by the Earth System compartment (atmosphere, surface, subsurface) where they occur. For example, much drought research has focused on precipitation, runoff, and soil moisture, indicating meteorological, hydrological, and agricultural drought, respectively. These drought indicators measure the deficit statistically but do not comprehensively account for the systematic differences in water demand among societies and ecosystems. For instance, significantly lower than regular soil moisture in a region with a very humid hydro-climate will likely not inhibit vegetation responses or cause a domestic water supply shortage unless sustained for a considerable period, unlike droughts in more arid hydro-climates,

where ecosystems tightly depend on the little available water and are immediately affected by small deficits. Additionally, ecosystems' structure and type of vegetation (e.g., plant species composition) will control the consequences of a particular water shortage on their processes and functioning (framing ecological droughts (Bradford et al., 2020; Crausbay et al., 2017; Slette et al., 2019)) through, e.g., root structure resulting from eco-evolutionary principles. This leads to a highly complex process controlling the drought impacts on vegetation, even on the local scale (Harrison et al., 2021; Hoek Van Dijke et al., 2022; Joshi et al., 2022; Stocker et al., 2023; Teuling et al., 2010).

More specifically, terrestrial natural and managed ecosystems depend on the availability of water for photosynthesis, in which plants assimilate carbon from the atmosphere for growth and metabolism, binding it to the land surface (Friedlingstein et al., 2023; Whitmarsh & Govindjee, 1999; Wohlfahrt & Gu, 2015). This flux is the most considerable carbon flux between the atmosphere and the terrestrial surface, and understanding its variability and drivers is essential to quantifying greenhouse gas emission budgets and climate change mitigation strategies (Friedlingstein et al., 2023; IPCC, 2023b; C. G. Jones et al., 2024). Photosynthesis is coupled with water availability through plant water management strategies: Stomata are partly closed to reduce transpiration during low soil water content or high atmospheric water demand, inhibiting the carbon influx to the land surface. This is a widely applied ecosystem function to save water, but along with other ecosystem traits, its timing varies significantly in time and space (Joshi et al., 2022; Short Gianotti et al., 2024; Stocker et al., 2023). Consequently, drought impacts and the emerging carbon cycle variability are influenced locally by the heterogeneity of the water deficit itself, site characteristics, such as soil and vegetation patterns, and legacy effects of preceding seasonal climatological anomalies (Bastos et al., 2020; Bevacqua et al., 2024). However, droughts and their impacts are clustered as discrete events with a quantifiable regional and temporal extent. For a holistic, functional understanding of droughts, their variation, and the implications for water security and the carbon cycle, systematic approaches that discretely distinguish between these spatiotemporal events are required (Brunner & Stahl, 2023; Cammalleri et al., 2020, 2021; Cammalleri & Toreti, 2023; Lloyd-Hughes, 2012; Tallaksen & Lanen, 2024).

The emerging dimensions of droughts, when accounting for their impacts, are their propagation over time, space, and through compartments of the Earth System (such as from the atmosphere to the soil, rivers, and vegetation). The structure of the propagation cascade and the propagation time scale depend on

local ecosystem properties that define the connectivity and damping factors between these compartments, and the drought severity and impacts (Crausbay et al., 2020; Entekhabi, 2023). Therefore, droughts are a multivariate and time-scale-sensitive problem.

Especially in Europe, where droughts are already more frequent and more severe than in the 20th century (Manning et al., 2019; Markonis et al., 2021; Rakovec et al., 2022) – a trend that is expected to continue (Lehner et al., 2017; Suarez-Gutierrez et al., 2023) – an accurate characterization of the heterogeneity of drought impacts is essential. Recent studies have shown how local and continental-scale gross primary productivity and evapotranspiration were affected during years of drought (Bastos et al., 2020; Ciais et al., 2005; Graf et al., 2020; Smith et al., 2020; Thompson et al., 2020; Van Der Woude et al., 2023), but have left open questions regarding the drivers of differing drought responses across Europe. Furthermore, the effect of different methodologies for identifying droughts (e.g., by using deficits of various hydrological variables on different time scales) makes formulating a holistic and systematic paradigm of European ecosystem drought responses particularly challenging.

Large-scale analyses are necessary to gain a general understanding of drought responses of ecosystem processes. While observation networks like the Integrated Carbon Observation System (ICOS (Heiskanen et al., 2022)) or the upcoming Integrated European Long-Term Ecosystem, critical zone, and socio-ecological Research Infrastructure (eLTER RI (Mirtl, 2010)) offer large-scale and ground-truth data, their geographical coverage is inconsistent. It is even geologically, ecologically, and climatologically biased (Ohnemus et al., 2024). Further, many required vegetation and hydrological states are only available in coarse temporal resolution. Regional land-surface model simulations offer the opportunity to assess ecosystem responses to drought on the continental scale, with consistent spatiotemporal coverage for many states and fluxes of the terrestrial water, carbon, and energy cycles.

Here, we use long-term (1995 – 2018, 24 years) simulations of the Community Land Model version 5 (D. M. Lawrence et al., 2019) (CLM5) at 3-kilometer resolution over the European Coordinated Regional Climate Downscaling Experiment (Giorgi et al., 2009) (CORDEX) domain to analyze the characteristics of droughts. We define discrete drought events by applying a novel generalized clustering algorithm (Cammalleri & Toreti, 2023) to the simulated standardized precipitation, runoff, soil moisture, and vapor pressure deficits on 1-monthly, 3-

monthly, 6-monthly, and 12-monthly aggregation time scales. This study presents

1. The most significant drought events in Europe based on the different variables and time scales.
2. Statistics on these drought events (e.g., the variation of their spatiotemporal extent and propagation speed) and their temporal trends over the study period.
3. The impact of drought events on gross primary production, transpiration, vegetation water stress, and the influence of drought types and aggregation time scales on those.

Consequently, this study leads the way towards more holistic and systematic approaches when accounting for drought impacts on ecosystem processes by improving the understanding of the influence of drought types and aggregation time scales on the droughts' characteristics and their effects on ecosystems.

5.2 Methods

5.2.1 Setup of the European CLM5

The Community Land Model version 5 (CLM5) (D. M. Lawrence et al., 2018, 2019) is one of the most used land component models of Earth System Models globally. It resolves the energy and water states and fluxes (and carbon and nitrogen if the biogeochemistry module is activated) in each soil column and for each plant functional type (PFT) within each grid cell masked as a terrestrial surface in the study domain. PFTs are distinguished by leaf habit (evergreen or deciduous), morphology (needle and broad leaves, grass, and shrubs), and bioclimate (boreal, temperate, and tropical). Further, PFTs that are in the same soil column (i.e., in the exact location or grid cell) compete for water. Importantly, crops are in a separate soil column from natural vegetation and are either rainfed or irrigated when the soil moisture falls below a specific threshold.

The European CLM5 setup simulates the European CORDEX domain (Giorgi et al., 2009), and has a curvilinear structure and consistent grid cell spacing. The chosen resolution is 3 km (0.0275°), which agrees with previous work done with CLM over Europe (Naz et al., 2019, 2020; Poppe Terán et al., 2023; Poppe Terán, Naz, Vereecken, et al., 2025) and results in 1544 × 1592 grid cells, including the ocean cells masked during the simulation. The standalone CLM5 simulations were forced by the Consortium for Small-Scale Modelling (COSMO) Reanalysis

6 (Bollmeyer et al., 2015; Wahl et al., 2017). This is the publicly available atmospheric data set with the finest resolution (6 km), and we downscaled it to the 3 km CLM5 resolution. over the European CORDEX domain. This high resolution of the atmospheric model had better approximations of observed seasonal precipitation intensities than coarser resolved simulations (Bollmeyer et al., 2015; Prein et al., 2016). This will lead to a better representation of hydrology on and below the land surface and, therefore, meteorological and hydrological droughts. The land surface input data was created using tools from the CLM5 repository, including land use (Hurtt et al., 2020), soil texture (IGBP, 2000), slope and elevation (Earth Resources Observation And Science (EROS) Center, 2017), and maps of PFTs (P. J. Lawrence & Chase, 2007).

The biogeochemistry (BGC) module of CLM5, which was turned on in our simulations, requires a spin-up simulation process to create initial conditions of carbon and nitrogen pools and fluxes. This process approximates the systemic equilibrium state of these fluxes and pools from arbitrary initial conditions. The primary global equilibrium condition is that the carbon pools at 97% of the grid cells are steady (i.e., no significant change or trend in the evolution of the carbon pool sizes). Further details on the model setup and spin-up conditions are described in (Poppe Terán, Naz, Vereecken, et al., 2025). We used the equilibrium conditions determined by the spin-up as initial conditions for the simulations from 1995 to 2018, which we analyzed in this study.

The raw simulation outputs were resampled to 8-daily means (to fit the temporal resolution of remote sensing observations used in the evaluation (Poppe Terán, Naz, Vereecken, et al., 2025)). We calculated the vapor pressure deficit from the air temperature and air humidity according to the atmospheric forcing (R. G. Allen, 2000). Finally, to calculate the rootzone soil moisture, we first calculated the root fraction in each layer for each present PFT (D. M. Lawrence et al., 2018).

$$r_i = \left(\beta^{z_{h,i-1} \times 100} - \beta^{z_{h,i} \times 100} \right) \tag{5.1}$$

Where r [dimensionless] is the resulting root fraction for a given PFT, i [dimensionless] is the soil layer index, β [dimensionless] is a PFT-specific parameter, and $z_{h,i}$ [m] is the depth from the surface to the interface between the layers i and $i+1$. These PFT-specific root fractions are then weighted by the land unit's area share covered by this PFT. Then, the resulting weighted root fractions for each layer serve as a weight to calculate the soil moisture level so that the

layers with a larger root fraction contribute more significantly than those with a smaller root fraction.

Stomatal conductance (g_s) [µmol m^{-2} s^{-1}] is the inverse of the stomatal resistance (r_s) and is calculated with the Medlyn model (Medlyn et al., 2011):

$$g_s = \frac{1}{r_s} = g_0 + 1.6\left(1 + \frac{g_1}{\sqrt{VPD}}\right)\frac{A}{c_s} \tag{5.2}$$

Where g_o and g_1 are model parameters. g_o [µmol m^{-2} s^{-1}] is fixed, and g_1 [dimensionless] is calibrated to each PFT. *VPD* [kPa] is the vapor pressure deficit, A [µmol CO_2 m^{-2} s^{-1}] is photosynthesis, and c_s [Pa] is the CO_2 partial pressure at the leaf surface relative to the atmospheric pressure.

The resulting transpiration flux is then determined by:

$$T_r = \frac{e_s - e_i}{r_s} \tag{5.3}$$

Where e_s [Pa] is the water vapor pressure at the leaf surface, and e_i [Pa] is the water vapor pressure resulting from the leaf temperature.

5.2.2 Standardized drought indices

The standardized indices were calculated using an adjusted algorithm for the standardized precipitation index (SPI) (McKee et al., 1993, 1995). The calculation is done individually for each grid cell. We first deseasonalize each variable's time series. Then, we calculate a rolling sum series based on the time window given by each aggregation period (31 days, 92 days, 183 days, and 365 days). Notably, the selected variables differ in their probability distributions, and these distributions differ across the study domain. So, to facilitate a generalized method that we apply to the whole European study domain for calculating the standardized index for all variables, we flexibly approximate each variable's probability density function and the cumulative distribution function with a Gaussian kernel density estimator on the rolling sum series. Each corresponding value in the processed series in the normalized cumulative distribution constitutes the drought index value. The corresponding points of the normal cumulative distribution at those percent points constitute the drought index series.

Finally, we have a data set with drought indices for precipitation, vapor pressure deficit, rootzone soil moisture, surface runoff, and groundwater for each terrestrial grid cell in the European 3-km grid from 1995 until 2018.

5.2.3 Clustering drought events

To quantify the spatiotemporal extent of droughts on an event basis, we leverage a generalized 3-dimensional algorithm (Cammalleri & Toreti, 2023) that clusters drought points (i.e., where a given drought index indicates a water deficit) and labels each drought point with an event identifier. The algorithm uses Density-Based Spatial Clustering of Applications with Noise (DBSCAN) (Ester et al., 1996), which determines core samples in high-density regions and expands clusters around them. DBSCAN is not limited to clusters of spherical shape and does not require the number of clusters to be found, such as the k-means clustering algorithm. However, two parameters are needed to define how core samples will be found (the search window and the required density within it). In our case, the samples are the spatiotemporal locations of the drought points. Significantly, we will weigh the samples by their drought index value so that the distance between drought points and non-drought points is additionally scaled (Cammalleri et al., 2016):

$$w = \frac{1}{1 + \left(\frac{k}{s}\right)^{e}} \tag{5.4}$$

Where w is the weight, k is a parameter that sets the center of the logistic curve, s is the drought index, and e is the steepness of that curve. Furthermore, this logistic scaling method gives smoother, more inclusive, and generalizable transitions of drought events, as points that would not have been included in the event with more rigid drought definitions (e.g., the drought index must be lower than -1) could be included and considered affected by this drought if the density around it is accordingly high. The algorithm then basically consists of three steps for each variable:

1. Spatial, 2-dimensional clustering of the maps of the weighted drought index maps at each 8-daily time step;
2. Filtering of minor droughts: Droughts that are smaller than a given threshold are discarded so that large 3-dimensional clusters do not overextend through the incorporation of these tiny events;
3. Spatiotemporal, 3-dimensional clustering of the weighted drought index data cubes over the 1995 – 2018 study period.

In each clustering process, we only use the spatial and time coordinates as features and introduce the weights as sample weights into DBSCAN, which is computationally more efficient than introducing the drought indices as an additional dimension.

Besides the drought indices data set, we have another 3-dimensional data set for the variables precipitation, vapor pressure deficit, rootzone soil moisture, and groundwater, with labels at each point that specify whether the point at a given time is experiencing a drought and, if this is the case, the label of the specific event. Table 5.1 shows the parameters used in the clustering algorithm in this study (Cammalleri & Toreti, 2023).

Table 5.1: Parameter used in the three steps of the three-dimensional clustering algorithm, in the weighting process (k and e), clustering process (l and p), for scaling time distance relative to space distances (t), and for filtering less significant clusters (a). For more information, please refer to Cammalleri & Toreti, 2023.

PARAMETER	MEANING AND UNITS	VALUE
k	Center of the logistic weighing function [-].	-1.4
e	Steepness of the logistic weighing function [-].	6
l	Window size (in grid cells) when determining the density around a point [-].	3
p	Share of present drought points in the window between the minimum (2) and the maximum (depending on the dimensions, see steps 1 and 3 above): $\frac{1}{window\ \ number\ \ of\ \ dimensions}$ [-].	0.1
t	Space-time scaling factor [-].	1.0
a	The minimum area for the drought events filter in step 2 above [km²].	30000

5.2.4 Drought event properties

Each drought event has a unique ID, prescribed by the clustering algorithm, which groups the points in space and time that delimit the drought's extent. To determine the properties (or characteristics) of a drought event, we mask the drought indices dataset to the points that are labeled with that drought's ID and continue the calculations only including this drought's spatiotemporal extent and weighted anomalies (see Equation (5.4)). The start and end dates correspond to the time stamps of the drought label's first and last occurrences along the time dimension. The difference between the time stamps constitutes the duration of the drought event, here in days. The drought area, during its activity, is calculated as follows.

$$A_{i,t} = \sum_{\Omega} a_{x,i,t} \tag{5.5}$$

$A_{i,t}$ is the total area of drought i at time t over the model domain Ω, and $a_{x,i,t}$ is the area of a grid cell corresponding to drought i at time t and location x. Notably, the droughts also differ in severity. Thus, we also determine the integrated drought

index by weighting each grid cell area by the weighted drought index (see Equation (5.4)).

$$I_{i,t} = \sum_{\Omega} a_{x,i,t} \; s_{x,i,t} \tag{5.6}$$

$I_{i,t}$ results as the integrated drought index $s_{x,i,t}$ is the drought index at location x, for event i and at time t.

The integrated area (in the text called the drought event size) and the total integrated drought index (in the text called the severity) for an event i is the sum of $A_{i,t}$ and $I_{i,t}$ across time t. The average rate of change across time of the $I_{i,t}$, and $A_{i,t}$ series indicates the drought index propagation speed and spatiotemporal propagation speed of the respective event i. Lastly, the centroid coordinates of the drought are defined as follows (Cammalleri et al., 2016; J. Zhang, Zhang, Yu, & Yu, 2024).

$$X_{i,t} Y_{i,t} = \frac{\sum x_{x,i,t} \; y_{x,i,t} \; w_{x,i,t}}{\sum w_{x,i,t}} \tag{5.7}$$

Here, $X_{i,t}$ and $Y_{i,t}$ are the coordinates of the centroid of the drought event i at time t, yielding a time series of centroid coordinates as long as the drought persists. Furthermore, $x_{x,i,t}$ and $y_{x,i,t}$ are the grid cell x's coordinates from the event i at time t and $w_{x,i,t}$ is the weighted drought index of grid cell x from drought event i at time t (see Equation (5.4)).

5.2.5 Drought impacts on ecosystem processes

We define ecosystem processes' drought response as the local anomaly during drought conditions, referring to the local mean during non-drought periods. Furthermore, the response only includes significant values, i.e., values higher than the variable's local standard deviation during non-drought periods.

$$X_{d,t,x} = X_{t,x} - \overline{X_{n,x}} \tag{5.8}$$

Where $X_{d,t,x}$ is the drought response at time t and location x for variable X, presumed that a drought event is identified at that location and time. To omit regions of low vegetation activity, such as deserts, we exclude regions with a negligible standard deviation from the distributions used in the analysis.

5.3 Results

5.3.1 The most severe drought events from 1995 – 2018

In Figure 5.1, we showcase the ability of our drought event identification method by presenting each variable's most severe drought event, i.e., the event with the most considerable spatiotemporal extent weighted by its total standardized anomaly. The results in Figure 5.1 refer to events based on the 6-monthly (183 days) aggregation period (t_{agg}); outcomes based on the other t_{agg} are in Figure C.1–Figure C.3. In this main section, we focus on the 6-monthly t_{agg} due to the close correlation and covariation with ecosystem processes found by previous studies. However, the results of the other t_{agg} agree with the presented findings in this section unless stated otherwise. A more detailed analysis of the critical t_{agg} of drought indices and their impact on ecosystem processes on the event scale is recommended for future studies, given that complex spatiotemporal interactions of climate and land surface processes affect and change these responses even in the same site across different events (Baez-Villanueva et al., 2024; Bastos et al., 2020; Martínez-de La Torre & Miguez-Macho, 2019).

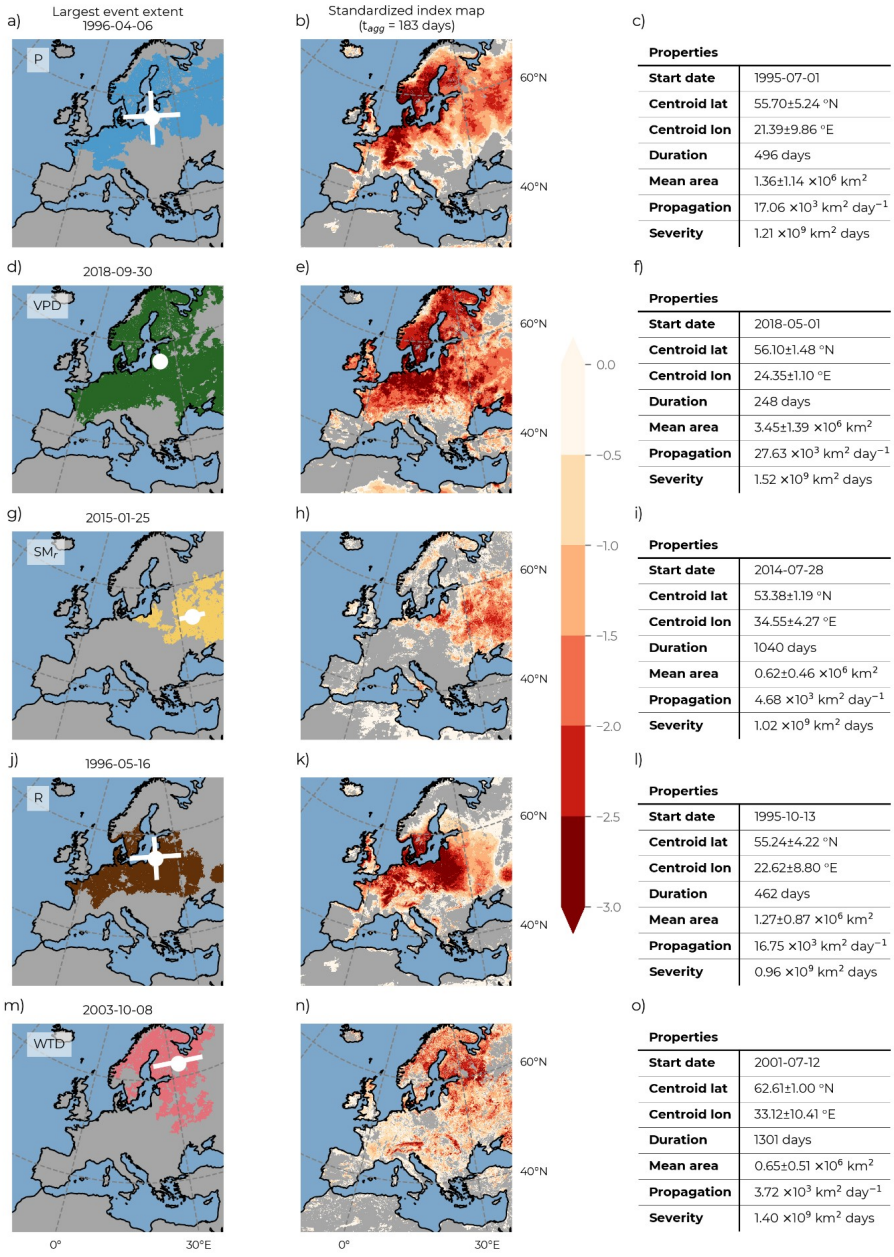

Properties	
Start date	1995-07-01
Centroid lat	55.70±5.24 °N
Centroid lon	21.39±9.86 °E
Duration	496 days
Mean area	1.36±1.14 ×10^6 km^2
Propagation	17.06 ×10^3 km^2 day^{-1}
Severity	1.21 ×10^9 km^2 days

Properties	
Start date	2018-05-01
Centroid lat	56.10±1.48 °N
Centroid lon	24.35±1.10 °E
Duration	248 days
Mean area	3.45±1.39 ×10^6 km^2
Propagation	27.63 ×10^3 km^2 day^{-1}
Severity	1.52 ×10^9 km^2 days

Properties	
Start date	2014-07-28
Centroid lat	53.38±1.19 °N
Centroid lon	34.55±4.27 °E
Duration	1040 days
Mean area	0.62±0.46 ×10^6 km^2
Propagation	4.68 ×10^3 km^2 day^{-1}
Severity	1.02 ×10^9 km^2 days

Properties	
Start date	1995-10-13
Centroid lat	55.24±4.22 °N
Centroid lon	22.62±8.80 °E
Duration	462 days
Mean area	1.27±0.87 ×10^6 km^2
Propagation	16.75 ×10^3 km^2 day^{-1}
Severity	0.96 ×10^9 km^2 days

Properties	
Start date	2001-07-12
Centroid lat	62.61±1.00 °N
Centroid lon	33.12±10.41 °E
Duration	1301 days
Mean area	0.65±0.51 ×10^6 km^2
Propagation	3.72 ×10^3 km^2 day^{-1}
Severity	1.40 ×10^9 km^2 days

Figure 5.1: For each hydrological variable, per row, precipitation (P), vapor pressure deficit (VPD), runoff (R), and groundwater (per water table depth, WTD), these are insights into the largest detected event cluster for the 6-monthly (183 days) aggregation period. The maps on the left show the maximum extent of the event, and in the center, maps with the drought indices at the corresponding point in time. On the right, the tables list the properties of the selected largest event cluster.

Comparing the cluster extents with the drought index maps (first vs. second column of Figure 5.1), it is evident that the clustering algorithm yielded good results and quantified the spatially distributed and clustered drought data points to one event. While the temporal dimension of these events could not be depicted in the maps, the start date, duration (event property table in the third column of Figure 5.1), and the date of the largest event extent (title of the cluster map, first column of Figure 5.1) are also listed. The location of the centroid and the standard deviation of its coordinates give insights into the event origin and the variability of the spatial expansion and movement of the event cluster (black circles and error lines in the event extent maps in the left column of Figure 5.1). For example, the most significant rootzone soil moisture (SM_r) drought event (Figure 5.1g) predominantly varied in longitude direction, pointing to a predominantly longitudinal spatial propagation or cluster movement along that axis.

Notably, the most significant events of all variables are predominantly located in the East of the study domain. This is likely due to the geographical distribution of land area across the domain: Where there is more continuous land area, drought events connect better and faster, are likely bigger, and have, thus, a more significant severity. Events of terrestrial variables, such as soil moisture or runoff, are more affected by this bias than atmospheric variables, such as precipitation and vapor pressure deficit, where anomaly patterns are connected aloft. This is evident in the large events connecting precipitation (P) and vapor pressure deficit (VPD) drought indices across Eastern Europe, Central Europe, and Scandinavia in Figure 5.1a and d, as opposed to the more compact SM_r, runoff (R), and groundwater (WTD) events in Figure 5.1g, j and m.

We identified four periods when large-scale droughts with high severity (drought index integrated over spatiotemporal extent) occurred over Europe: at the beginning of the study period in 1996, 2002/2003, 2015, and at the end of the study period, 2018. While the aggregation periods yielded some differences in the dates of their most prominent events, they all agreed that the largest soil moisture drought event occurred in 2015. Climatic drivers and the connectivity of the hydrological compartments lead to multivariate propagation of anomalies and these shared periods of large-scale droughts across variables. However, apart from that, the ranking of these drought events, even at their largest scale, differs by variable (showing different dates of the most significant drought event across the different variables per t_{agg}) and by t_{agg} (showing different dates of the most significant drought event across the different t_{agg} per variable). This further strengthens our rationale for a holistic, time-scale sensitive perspective on the propagation of water scarcity in ecosystems.

Connected areas where the anomalies are not as significant as around them were successfully excluded from the shown event clusters (e.g., large swaths of the Balkans and central Europe in the most considerable groundwater drought (per water table depth, WTD, see Figure 5.1m and n) and not directly connected areas of anomalies are also secluded events (e.g., the VPD drought event in the British Isles from the large-scale event on the European mainland, Figure 5.1d and e). Separated blobs that are still labeled as part of the large-scale event (e.g., a solitary part of the runoff drought that is part of the extensive R event in the easternmost part of our study domain in Figure 5.1j and k) are connected through the time dimension. Through the drought's spatial propagation and movement, they were or will be attached at another point in time and are both part of the continuous 3-dimensional event cluster.

The parameters of the clustering method influence the connectivity between single clusters in space and between time steps, hence controlling the total number of clusters and their sizes. However, the chosen clustering parameters remained constant throughout the study. While this means that the uncertainty in cluster sizes persisted, this effect was consistent across variables and aggregation period scales.

Essentially, we also observe systematic effects of t_{agg} on the properties of the clusters. Logically, the event duration, the mean area, and the severity increase with increasing t_{agg} because events with shorter aggregation periods are inherently more dynamic (Baez-Villanueva et al., 2024). Essentially, t_{agg} determines the length of the rolling window for which the sum is calculated, so, logically, single values of an index with a small t_{agg} will have a smaller influence on the aggregate's overall value than longer t_{agg}. Hence, drought indices of a smaller t_{agg} are more dynamic than those of a larger t_{agg}. These effects may play out differently on the selected variables and on each property of the drought events. In the next section, we will present statistics on the event properties across all identified events (not only the largest) and investigate the effects of t_{agg} on their distribution.

5.3.2 Atmospheric droughts are becoming increasingly severe

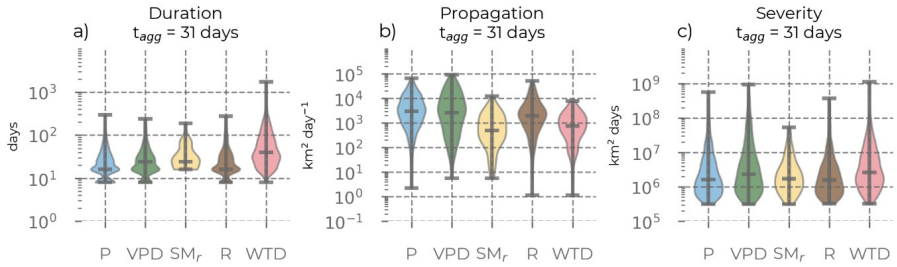

Figure 5.2: The violin plots characterize the distribution of key event properties (y-axis) across all identified precipitation (P), vapor pressure deficit (VPD), rootzone soil moisture (SM_r), runoff (R), and groundwater (per water table depth, WTD) drought events (x-axis) of 6-monthly (183 days) aggregation period.

In Figure 5.2, the distributions of key event properties of all events and for each variable are displayed in boxplots. Generally, the larger the duration, propagation, and severity median across the events, the more extensive the distribution spread and the upper quartile range of the duration, propagation, and severity distributions, indicating a non-linear relationship towards a higher likelihood of quickly propagating, long-term, spatially extensive, or very severe drought events. Essentially, the severity can be approximated by a simple fitted power law (Cammalleri et al., 2023) ($a \times b^{duration}$), which we confirm works well for the different variables and aggregation periods (Figure C.4). However, especially for large-scale droughts, the fitted power relationship becomes more uncertain, somewhat underestimating the sizes of the most prominent droughts related to their duration. This indicates a tendency for the most severe droughts to propagate in space rather than time, irrespective of the hydrological compartment or aggregation period.

Drought events in the hydrological compartments of the subsurface, i.e., SM_r and WTD, show distribution characteristics of their duration, propagation, and severity properties distinct to the distributions of P, VPD, and R. Subsurface droughts – on average – last longer compared to surface and atmospheric droughts (Figure 5.2a), they propagate more slowly in space (Figure 5.2b), and they have a greater severity (Figure 5.2c) than droughts in the more dynamic above-surface hydrological compartments. This is consistent across events of different t_{agg} (see Figure C.5– Figure C.7). Conversely, meteorological and atmospheric droughts (P and VPD drought events) persist on average the shortest and propagate the most rapidly over space.

Further, in Figure 5.3, the distributions of the drought properties of the different t_{agg} are compared. The scale and distances between the t_{agg} categories are not linear (irregular and exponential scaling from 31 to 92, 183, and 365 days, and the presence of the enormous drought events, essentially lying outside the 95% percentile, increase non-linearly with t_{agg}; see Figure 5.3). Nevertheless, the indicated linear regressions of medians of event properties and t_{agg} showcase this relationship simplistically.

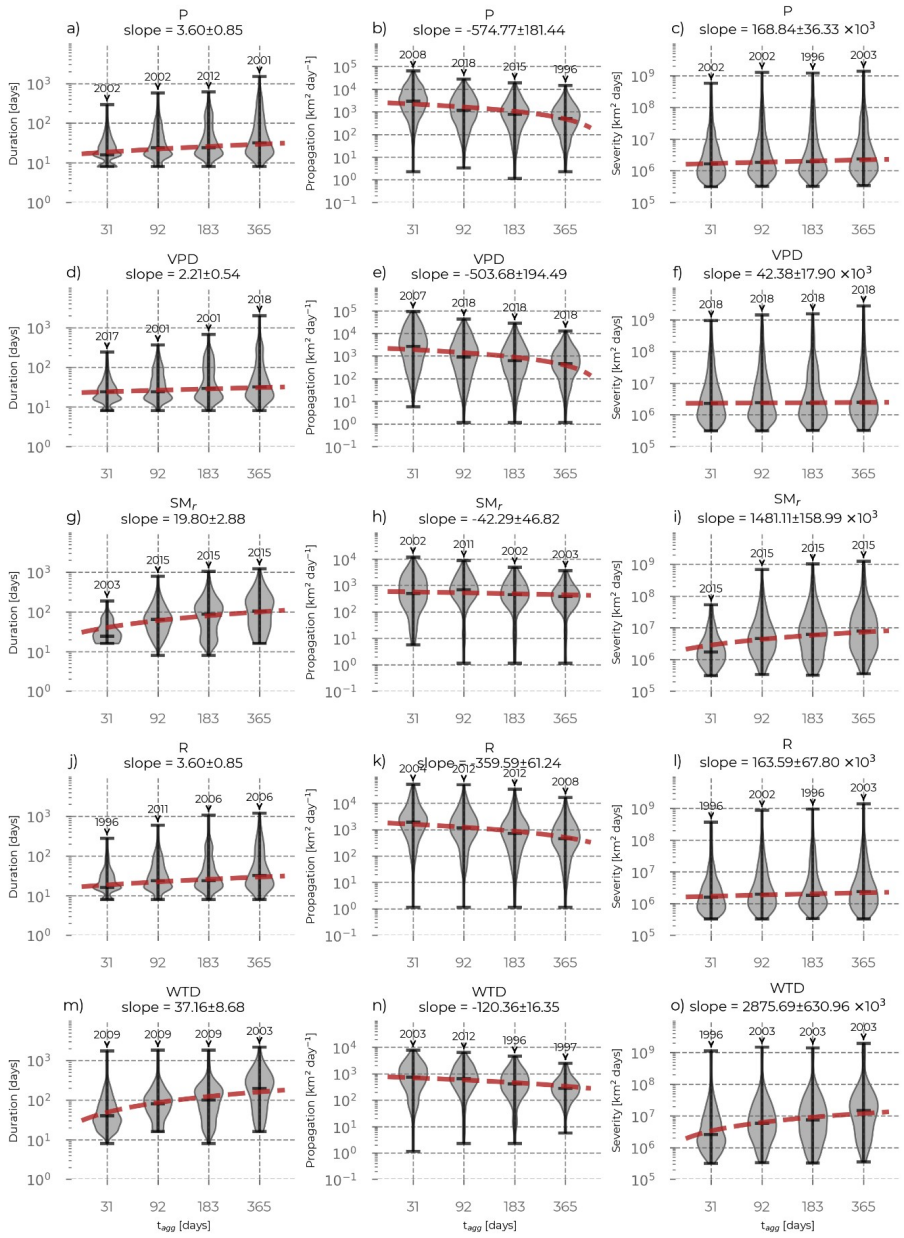

Figure 5.3: Each violin plot depicts the distribution of drought event properties (y-axis, in logarithmic scale. Left column: duration, center column: propagation speed, right column: severity) for each of the drought index variables precipitation (P), vapor pressure deficit (VPD), rootzone soil moisture (SM_r), surface runoff (R), and groundwater (per water table depth, WTD) and each drought deficit aggregation period (t_{agg}: 31days, 92 days, 183 days, 365 days corresponding to monthly, 3-monthly, 6-monthly and yearly). The red dashed line is a simple linear regression (here curved in the linear-logarithmic plane) of the medians, exemplifying the effect of increasing t_{agg} on the drought event properties.

The severity of atmospheric droughts (VPD) increases with increasing t_{agg}, indicating a greater importance of small-scale aggregation times for atmospheric droughts than other drought types. This is due to a positive relationship of t_{agg} on the drought event severity (the lower t_{agg}, the lower the median severity) of P, R, SM_r, and WTD droughts, which is not present for VPD (Figure 5.3c, f, i, l, and o). Thus, in the median, the severity of atmospheric drought events is independent of the t_{agg} of the drought index. However, the likelihood of large-scale events increases towards greater t_{agg}, and these vast events have to be considered more carefully when accounting for their implications on ecosystems and societies.

All drought indices show increasing event durations with increasing t_{agg} (Figure 5.3a, d, g, j, and m), the most substantial dependency being soil moisture and groundwater droughts (SM_r and WTD, Figure 5.3j and m), indicating more prolonged droughts for extended aggregation periods. All variables show decreasing propagation speed with increasing t_{agg} (Figure 5.3b, e, h, k, and n). Again, larger t_{agg} for SM_r and WTD drought indices facilitated a more significant severity, while the other variables show indifference. While the medians seem well approximated by the linear regression, the maxima often appear to follow a non-linear interrelation (e.g., the maxima of total groundwater drought event duration; Figure 5.3m). The most notable drought events (the most temporally extensive, fastest propagating, and most severe, outside of the 1.5×interquartile range region) are approximately exponentially larger than most other events, producing distributions with a long tail – we chose to display these distributions on a logarithmic scale. For a better view of the interquartile ranges and the uncertainty of the linear regression of the medians, please look at Figure C.8.

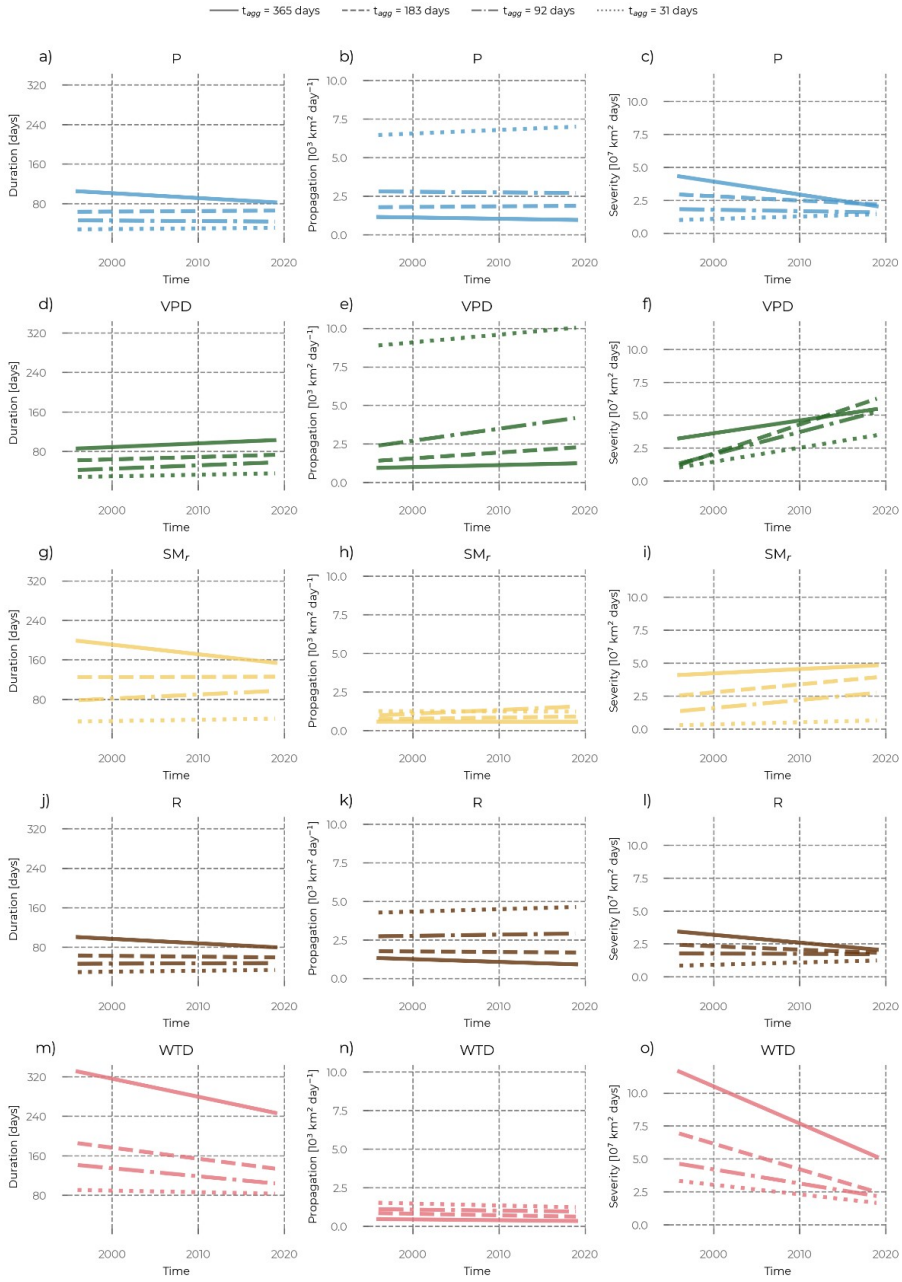

Figure 5.4: Temporal trends of the drought event properties (see y-axis label) for precipitation (P), vapor pressure deficit (VPD), runoff (R), and groundwater (per water table depth, WTD) and per aggregation period (line style, see legend). For all trend plots including their uncertainty, see Figure C.9 - Figure C 12. Further, the exact interception and slope values, including their uncertainty, are given in Table C.1.

Recent studies have indicated that drought properties, such as their severity, are continuously affected by the changing climate and environment, thus exhibiting temporal trends (Cammalleri et al., 2020; Hoek Van Dijke et al., 2022; Lloyd -Hughes & Saunders, 2002; Manning et al., 2019; Slette et al., 2019). We leverage our drought event dataset to relate each drought property to the drought centroid date and calculate the resulting trends. These trends are depicted in Figure 5.4. Notably, the trends of a specific variable are not necessarily consistent across different t_{agg}. For example, the severity of precipitation droughts (Figure 5.4 c) shows a predominant decreasing trend in the study period for t_{agg}=365 days but a slight increase for t_{agg}=31 days. Furthermore, the duration of rootzone soil moisture droughts of t_{agg}=92 days has increased, while for t_{agg}=365 days, it has decreased. Figure C.9 - Figure C 12 and Table C.1 compare the trends and related uncertainties of all the aggregation periods per variable and selected property.

Most strikingly, our results suggest increasing severity ($0.22 \pm 0.11 \times 10^7$ km^2 days year^{-1}) and propagation speed ($0.08 \pm 0.04 \times 10^3$ km^2 day^{-1} year^{-1}) of atmospheric droughts, likely related to increasing air temperatures and associated lower relative humidities, possibly enhanced by changes in atmospheric dynamics (e.g., the positioning of high and low air pressure systems, and the occurrence of atmospheric blockage). Notably, groundwater droughts became shorter (-1.63 ± 1.47 days year^{-1}) and less severe ($-0.28 \pm 0.38 \times 10^7$ km^2 days year^{-1}) during our study period, although with more considerable uncertainties.

The limited study period and very large or small drought events coincidentally occurring at the end or the beginning of the study period could bias the trend estimates. Further, more complex temporal relationships, e.g., non-linear trends and shifting trend signals, can attenuate the significance of these linear temporal correlations.

5.3.3 Complex patterns of ecosystem drought responses

In most drought research, only the magnitude of the water deficit in a particular hydrological compartment primarily characterizes drought events. However, these drought definitions fall short of describing the impacts on ecosystem fitness, services, and human livelihoods. The following results focus on establishing systematic relationships between the water deficits and ecosystem responses.

Figure 5.5: Maps of mean responses of transpiration (T_r) to soil moisture (SM_r, top row) and vapor pressure deficit (VPD, second row) drought events with different aggregation periods (31, 92, 183, and 365 days). The maps in the last row depict the mean T_r response during compound events, i.e., where droughts defined by soil moisture and droughts defined by vapor pressure deficit at impactful aggregation times co-occur.

In Figure 5.5, transpiration (T_r) responses to SM_r and VPD drought events show distinct geographical patterns. Furthermore, substantial differences exist between the T_r response and the drought index aggregation period (t_{agg}). Please refer to Figure C.13 and Figure C.14 for soil evaporation (E_s) and downregulation factor (β) responses. The patterns of GPP responses are almost identical to those of T_r and are depicted in Figure C.15

For the shortest aggregation period, SM_r droughts are not evenly distributed across the continent, exhibiting gaps where no events of this type occurred (Figure 5.5a). This hints at inhibited compatibility of the relatively inert hydrological compartment in the root-zone soil with short aggregation times. Moderate aggregation times (92 and 183 days) identify SM_r events that evoke the most widespread negative T_r responses, predominantly in Central Europe (Figure 5.5b and c). On the other hand, wet regions like the Alps and Scandinavia have generally increased T_r during soil moisture droughts independent of t_{agg}. More arid regions (check Figure C.16), where ecosystem processes are limited by water availability and the magnitude of mean T_r is lower (e.g., Spain and Turkey), show limited T_r responses. Patterns of T_r response along aridity gradients are also present for VPD droughts (Figure 5.5e – h). However, the reactions are

extensively positive for the shorter t_{agg} across most Central, Eastern, and Northern Europe (Figure 5.5e and f), and negative responses are only present in the longer t_{agg} and smaller magnitudes (Figure 5.5g and h). The same observation counts for E_s responses, supporting the interpretation that possible confounding factors (e.g., correlation between VPD and atmospheric pressure and incoming radiation) and demand-controlled evapotranspiration, rather than supply shortages and plant water management through stomatal conductance, determine drought responses at these temporal scales. However, the confounding factors cancel out when these droughts persist over extended periods. On top of that, the initial T_r increases deplete the soil moisture in the root zone and could potentially negatively impact T_r, E_s, and GPP in the long term.

Notably, the current understanding of drivers of transpiration and photosynthesis variability implemented in CLM5 makes it clear that they depend on multivariate states even during droughts. The carbon and moisture gradients between the atmosphere and the plants' leaves, among other factors, influence the stomatal conductance, determining the magnitude of vegetation transpiration and carbon uptake. Thus, both a dry atmosphere and a dry soil directly influence ecosystem processes. Even plants applying conservative water management strategies to maximize their carbon input reduce their stomatal conductance when persistent droughts co-occur in these crucial compartments. Thus, we also analyze T_r's drought response when ecosystems face soil and vapor pressure droughts, overlaying drought events of t_{agg} that correspond to the most widespread negative response. These compound drought events co-occur almost universally with negative T_r (Figure 5.5i – l) and GPP (Figure C.15) anomalies. Exceptions are the very humid regions where the relative anomalies do not necessarily mean a water limitation for the ecosystem processes (Norway's west coast and the Alpes) and landscapes dominated by grasslands (e.g., parts of Turkey, see Figure C.17 for a map of the dominating plant functional type in the European CLM5 model setup), demonstrating the ability to regulate the water use efficiency effectively during droughts (Poppe Terán et al., 2023).

Figure 5.6 shows the distribution of the drought responses for T_r, E_s, and β. The findings from Figure 5.5 are reflected in Figure 5.6a – c: T_r shows mainly negative responses to SM_r droughts, more dominantly in the short to medium t_{agg}, positive responses during VPD events of short time scales, increasingly negative responses during VPD events for long time scales, and uniform negative responses during compound drought events.

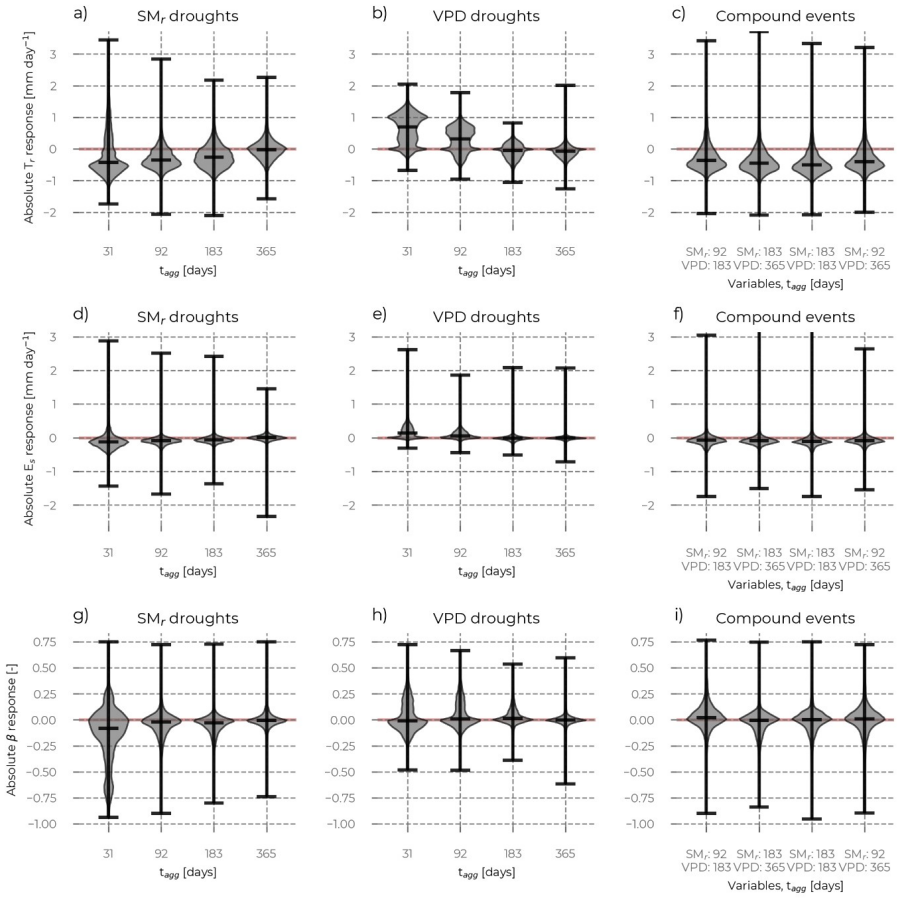

Figure 5.6: Distributions of the transpiration (T_r, top row), soil evaporation (E_s, middle row), and transpiration attenuation factor (β, bottom row) response to root-level soil moisture (SM_r) drought events (left column) and to vapor pressure deficit (VPD) drought events (center column), based on different aggregation times (t_{agg}, x-axes) of the respective drought index. The responses in the right column are based on compound T_r and VPD drought events of impactful t_{agg}.

On top of that, Figure 5.6d – f shows the distributions of soil evaporation (E_s) response to droughts. E_s responses are in the median of smaller magnitude than T_r responses, but have equally long tails. This results from geographical patterns of E_s drought responses across Europe (e.g., the north-south gradient, see Figure C.16). Again, the aggregation periods determine the signal of the E_s response to SM_r and VPD droughts. Still, compound events have a predominantly negative impact on E_s. However, the large upper tails mirror E_s's very local yet considerable positive reactions to compound events on the Iberian Peninsula, Norway, and around the Black Sea (Figure C.13).

The β factor indicates attenuation of stomatal conductance due to insufficient soil moisture (Figure 5.6g – i), where β=1 means no moisture limitation. The contrasting responses of β to drought events showcase the limitation of standardized indices in drought identification. Identified soil moisture droughts do not directly correlate with water limitations for ecosystem processes. We find the most potent responses in Eastern Europe: β reacts negatively during SM_r droughts and positively during VPD droughts (Figure C.14). Interestingly, Southern Europe exhibits widespread negative responses during all SM_r, VPD, and compound events, characterizing the β responses along an aridity gradient in Europe. Notably, across other regions, or more generally, β drought responses do not show a universal signal during compound drought events, questioning a direct relationship between vegetation water potential and the identified drought events in this study.

5.4 Discussion

This study's findings must be interpreted in the context of the underlying uncertainties. These uncertainties primarily originate from input data uncertainty, model bias, clustering fuzziness, and conceptual shortcomings.

The Consortium for Small-Scale Modelling Reanalysis 6 (COSMO-REA6) atmospheric data used as forcing for the European CLM_5 showed better performance than coarser reanalysis products in simulating precipitation intensities (Bollmeyer et al., 2015; Wahl et al., 2017). Some research evaluating the COSMO-REA6 as a forcing for hydrological modelling applications shows limited added value compared to coarser reanalysis forcings (e.g., European Center for Medium-Range Weather Forecast Reanalysis 5, ERA5) when simulating precipitation-runoff propagation (Alexopoulos et al., 2023), but it is expected to be more beneficial with spatially distributed models than single-location models. The precipitation, temperature, and humidity values that are essential to calculate the drought indices in this study were found to compare well in terms of seasonality, magnitude, and variability to in situ observations across Europe (Poppe Terán, Naz, Vereecken, et al., 2025). A recent study found that COSMO-REA6 captures extreme events significantly better than other state-of-the-art atmospheric data sets, albeit limited to only Germany (Hammoudeh et al., 2025). We conclude that on the continental scale applied in this study, the chosen atmospheric forcing does not introduce substantial uncertainty to the identified clusters, especially the most significant events. Future work can use multiple atmospheric model outputs as forcing, perturb the forcing data, and use

ensemble simulations to scrutinize the effect of this uncertainty on the drought event properties and impact in more detail. Apart from atmospheric forcing inputs, e.g., the use of high-resolution soil texture data could improve the representation of soil moisture and vegetation water limitation in the European CLM5 setup (Oloruntoba et al., 2025).

Importantly, we evaluated the performance of key ecosystem processes from the same European CLM5 simulations used here with in situ observation data from a European station network in a previous study (Poppe Terán, Naz, Vereecken, et al., 2025). Most vegetation types systematically underestimate the magnitude of carbon uptake, most strikingly deciduous broadleaf forests across Europe. Furthermore, CLM5 exhibited significant shortcomings in simulating the variability in water and carbon cycles. In more detail, the simulated variance of evapotranspiration (ET) and GPP is significantly underestimated, with missed variability towards larger values during summer. Thus, the upper tails of the simulated ET and GPP distributions are shorter and lighter than the observed, which may have implications for the simulated responses to extreme events in this study. Further comparisons, specifically of the drought response from the European CLM5 with extensive observations, are required to find the specific uncertainty related to drought conditions. Regions on the Iberian Peninsula and the Nile Delta have a prevalent crop PFT that introduces irrigation (See Figure C.17). The irrigation routine introduces water into the soil columns of these PFT whenever a critical soil moisture level drops below a threshold. Thus, while droughts will be identified, the drought responses are expected to be insignificant because the drought indices are relative to these local irrigated conditions.

Over the last decade, droughts have been increasingly mapped as spatiotemporal events, with the World Meteorological Organization calling for labelled event clusters and discrete, event-specific results (WMO, 2015). This concept has predominantly been used to identify precipitation drought events and analyze their properties (Cammalleri et al., 2023; Cammalleri & Toreti, 2023; J. Zhang, Zhang, Yu, & Yu, 2024; Zhu et al., 2024). Few studies expanded the approach to different hydrological compartments (Di Nunno & Granata, 2023; K. Feng et al., 2023; J. Zhang, Zhang, Yu, Yu, et al., 2024) and few have connected these drought events to vegetation responses (Pei et al., 2023; Weng et al., 2023). Diverse methods that cluster droughts to spatiotemporal events have been deployed and published. For this large-scale study, it was essential not to be limited to a parameter defining the number of drought events. Further, our study benefited from a generalizable method, i.e., the same was applicable across scales and variables (Cammalleri et al., 2023). The identified drought events were reasonably assessed to agree with

events from previous literature (with a focus on the most significant meteorological drought events in 1996, 2002-2003, 2010, 2015, and 2018) (Cammalleri et al., 2023). The size–duration power relationship across drought events found in previous studies for precipitation droughts is also valid for our data (Cammalleri et al., 2023) (Figure C.4). However, soil moisture, vapor pressure deficit, runoff, and groundwater events are scarcely defined spatiotemporally in previous literature, and, hence, we cannot confirm the agreement with actual recorded events. Furthermore, while the clustering method is flexible, it also allows exploring different parameterization sets depending on the hydrological variable and the aggregation time. While we argue that our parameter choice remains reasonable throughout, clusters identified by different parameters may change the distribution of drought event properties significantly, as, e.g., the inclusion of drought points at the cluster extremities and the exclusion of events below a threshold area are controlled by parameters and can influence these distributions substantially. Additional studies analyzing the uncertainty of the cluster properties based on different clustering parameter sets would help confine the fuzziness of the event definitions. We hypothesize that the identified trends of the drought properties are sound despite the fuzziness of the event constraints, as these are driven primarily by hydro-meteorological trends and the aggregation period of the drought index. Significant limitations of the identified trends remain: The inclusion of 24 years falls short of a climatological period defined as 30 years by the WMO (WMO, 1989), and the occurrence of extensive extreme events in the beginning (1995/1996) and at the end of the study period (2018) affects the determined trend slope. It is crucial to conduct these analyses based on climatological slices of more extended simulations, including earlier years (e.g., from 1990), and expand the simulations to the future using climate scenarios as forcing.

While this study's account for different drought time scales includes multiple aggregation periods of the drought index and yields insights on the effect of varying water deficit aggregations, this approach leaves several open questions. Firstly, depending on the hydro-meteorological conditions and local characteristics, the time scale of water deficits that are of interest to ecosystem process anomalies may vary, i.e., T_r in one region might show significant responses for events of one t_{agg}, but also another t_{agg} under another circumstance. Therefore, we recommend further distinguishing the ecosystem processes drought responses not only per pixel, but also per event, to systematically distill the interrelations of water deficits, aggregation times, climate, and local traits. Additionally, using a more granular and extended array of aggregation periods

may yield more explicit results on the effect of t_{agg} on the drought event properties and the impact on ecosystems. The application of aggregation times gives us an understanding of how the selected processes respond to droughts as events. However, in CLM5, the vegetation functions are regulated by the plant's real-time matric potentials; thus, for a more mechanistic understanding of the drought responses, non-aggregated anomalies may yield more notable responses.

While this study focuses on the overall distribution of drought event properties, analyzing the most significant drought events is of greater importance and practical significance for monitoring societal impacts and predicting optimal water management strategies and agricultural practices. These massive events correspond to most other events non-linearly in terms of their sizes and severity. They might exhibit property trends that differ from the entire sample size. On the other hand, due to the sizeable spatiotemporal extent, these events might cause very heterogeneous responses, given that a more diverse land surface and PFT distribution across the event extent is expected. We recommend further in-depth studies on the most significant drought events, focusing on their impact on ecosystem services.

Our results exemplified the application of these multi-scale, multi-variable drought event data by analyzing the drought responses of ecosystems. This highlights the complex relationships between water deficits in different hydrological compartments and vegetation processes. Some of these response gradients seem to agree with aridity gradients across Europe (e.g., T_r responses to VPD droughts), and other response patterns correspond to PFT distribution maps (e.g., GPP responses to SM_r droughts). These responses, irrespective of the drought type, are modulated in magnitude and even sign by the aggregation period used to determine the drought index. Further, contrasting responses of β, which directly indicate stomatal conductance attenuation to water shortages, to SM_r, VPD, and compound drought events, exhibit the spurious link between the locally relative definition of drought events and their actual importance and impact. These divergent responses have been found throughout recent literature. Our findings, however, especially the contrasting reactions of β, suggest that these reactions are not necessarily responses to water limitation, but more complex interactions to phenomena co-occurring with drought events. We experimentally calculated drought indices based on β Figure C.18), and identified events in the same manner as with the hydrological variables to analyze the respective T_r responses. The positive T_r responses in Northern Europe and the Alps correspond well with areas of significantly low mean rooting depth and low mean β (Figure C.19 and Figure C.20), showcasing how vegetation in humid

regions is limited in their processes due to limited access to water in deeper soil layers. The β factor is a relatively fuzzy definition of water limitation: Here, the used CLM5 output is the daily minimum of the attenuation factor. Plants in regions with high precipitation often have shallow roots because water frequently passes through the surface soil layers, thus making deeper roots obsolete. However, during non-rainy periods, these layers will be emptied quickly by percolation and root water uptake, and the daily minimum β will reach relatively low values. As a result, deviations of the daily minimum β in these regions may not be as informative about general water limitations of ecosystems as in other areas, and the most practical drought indicator for ecosystem processes demands further work and considerations of these local dynamics.

Crucially, implementing the plant hydraulic stress (PHS) module improved the functionality of vegetation drought responses in CLM5 over previous versions (Kennedy et al., 2019). In this, the vegetation water stress is simulated by water potentials from the soil to the leaf, which may attenuate the transpiration and adjust the mean depth of soil water extraction by roots. While there is uncertainty related to the coupling of the Medlyn g_s model with PHS, further implications for our study are, e.g., the simplified root water definition (the mean root water uptake depth is not adjusted through time but is assumed to be the depth of the centroid of the root system), and potentially overestimated compensatory extraction of soil water during dry conditions. More generally, vegetation in CLM5 is limited spatiotemporally in its diversity: The relatively coarse concept of plant functional types, e.g., does not allow for functional added values for diverse forests as opposed to single-PFT forests, which were found to have significantly higher drought resilience (W. R. L. Anderegg et al., 2018; Moreno et al., 2024; Rohde et al., 2024). Furthermore, the spatiotemporal constraints of PFT distributions (i.e., static sets of parameters) do not adjust for functional vegetation acclimation to a drying environment or even ecosystem transformations based on eco-evolutionary principles toward a practical optimum (L. D. L. Anderegg et al., 2022; Hähn et al., 2024; Kinzinger et al., 2023; Van Bodegom et al., 2012).

A more detailed consideration of regional functional dependencies of drought properties and impacts with the hydro-climate and the present PFTs may shed further light on the complex responses we found in this study. Another complicating circumstance is that a certain level of water limitation is the norm for many ecosystems, and conceptualizing a relative level, by which water limitation is actually harmful, remains elusive. Further ecological modelling approaches are needed to project water limitations and affected ecosystem

processes to persistent impacts on ecosystem health and evocation of ecosystem transformations, and comprehensively introduce these into land surface models.

5.5 Conclusions

In this work, we presented analyses of drought events based on simulations with a high-resolution setup of the Community Land Model version 5 over the European continent. A generizable, three-dimensional clustering algorithm was applied to identify spatiotemporally explicit drought events based on drought indices of various aggregation periods calculated from multiple meteorological and hydrological variables. The algorithm identified the significant massive drought events of 1996, 2002-2003, 2015, and 2018, which agree with previous literature.

Our findings show that, on average, drought events involving dynamic variables, such as precipitation and vapor pressure deficit, propagate faster but last shorter than events involving more inert variables, such as soil moisture and groundwater. Further, the aggregation period affected the distributions of the drought event properties: more extended aggregation periods brought more durable and more severe droughts, which propagated more slowly. Those effects were less apparent for vapor pressure deficit droughts. The drought properties exhibited temporal trends, with increasing severity of vapor pressure deficit droughts ($0.22 \pm 0.11 \times 10^7$ km^2 days year^{-1}) and decreasing severity of groundwater droughts ($-0.28 \pm 0.38 \times 10^7$ km^2 days year^{-1}).

Finally, we identified the responses of ecosystem processes (transpiration, gross primary production, and water stress). Our results exhibit complex patterns of these responses, with magnitude variations and even differences in sign across Europe. Importantly, regional differences match PFT distributions and aridity gradients. The PFTs control the drought impacts through parametric regulations of stomatal conductance and root depth distributions. This work is the first to identify droughts in multiple hydrological compartments across various time scales and contextualize their properties and relevance for ecosystem processes.

These results are essential to understanding droughts as event-scale phenomena and present a holistic approach to projecting their impacts on ecosystem processes.

6 Synthesis and conclusions

Climate change and increasing drought frequency and severity threaten the stability of ecosystem processes, with grave implications for human livelihoods through inhibited ecosystem services. More specifically, it is crucial to quantify ecosystem processes variability, particularly for water and agricultural management applications. For that, a continuous research-guided development of land-surface models is indispensable.

The following sections will synthesize the outcomes of the individual research works in Chapters 3, 4, and 5, by cutting across the connected findings and discussing related interactions and overarching controlling factors. Additionally, promising research questions that would carry the results of this research project forward will be proposed.

6.1 Emerging patterns of terrestrial ecosystem process variability in Europe

The constituent studies of this thesis are large-scale analyses of data on spatiotemporal ecosystem processes. Independently, using different data sources, they found how ET, GPP, and WUE vary in the long term with the changing climate, how they respond to droughts locally, and how these local signals form geographical patterns on the European continent. Further, there are apparent gradients of ecosystem drought responses and drivers along hydroclimates and PFTs.

The geographical regions featuring the most striking results in this research project are: Central Europe, Eastern Europe, Southern Europe, the Alps, and Scandinavia. It is important to emphasize that these emerging geographical patterns result from a physical template of the climate and local factors on the land surface that modulate these signals. These factors are interconnected, e.g., hydroclimate and PFT response gradients, as climate is a primary determinant of the arising ecosystem types. However, many local features, such as microclimate, soil characteristics, extreme events, and disturbance, further influence which PFTs can establish. Consequently, an area with a similar hydroclimate can have a wide range of present PFTs, and the same PFT can be sustained across a range of hydroclimates. In any case, the vegetation's physiology and the resulting plant traits have evolved to the local conditions.

Central and Eastern Europe frequently show uniform trends and responses of ecosystem processes. The presented studies show largely negative EWUE and TWUE trends in Central and Eastern Europe, where EWUE and TWUE also responds negatively to droughts. In these regions, water use predominantly controls WUE variability, but less so during droughts. Concurrently, the most significant large-scale drought events appear mostly in Central and Eastern Europe. This highlights the importance of these regions' drought responses, as their impacts scale across the extensive area and duration of the events, anticipating significant losses of ecosystem services with economic implications. Chapter 5 shows that vapor pressure and soil moisture drought events in impactful aggregation periods, which negatively affect GPP and ET, are increasing in severity in Europe. In this light, urgent considerations on agricultural and water resource management adaptations and measures to increase drought resilience of natural ecosystems are required in Central and Eastern Europe. A more refined analysis of the trends of drought properties, which points out drought property trends for individual European subregions, would provide essential background information for this concern. Research infrastructures must improve the present network design and expand standardized observations to the Eastern European region, which is underrepresented geographically in currently available situ observation data sets (Ohnemus et al., 2024).

While EWUE and TWUE increased in Scandinavia, the detected drought responses and the high sensitivity to water use are similar to Central and Eastern European regions. GPP prevailed as the primary driver of EWUE and TWUE variability along the Norwegian coastline. GPP and T_r responses to vapor pressure, soil moisture, and compound drought events are extensively positive. There are similar features of trends and drought responses in the Alps region. These collated results show a spurious relationship between drought events from hydrological variables and actual vegetation water stress. Further, there are positive drought responses in these very humid hydroclimates for T_r and GPP, but not for EWUE and TWUE. The vegetation likely exploited increased energy availability and sufficient soil water during drought periods to increase productivity in these humid regions. While this does not hint at imminent risk to ecosystem function in Scandinavia and the Alps, increasing severity of atmospheric droughts might slowly deplete soil moisture reserves in the long term. Studies analyzing the drought responses to long-term change in climate change conditions could provide further insights on this issue, using the holistic drought approach presented in Chapter 5. Further model developments

improving the representation of the steep ecohydrological gradients are expected to improve the simulation of vegetation water availability and management, especially in mountainous regions like the Alps.

The isohydric-anisohydric continuum characterizes the plant capacity to adjust stomatal conductance and vegetation water potential in response to dry conditions. Isohydric ecosystems adapt the stomatal conductance quickly to retain a constant water potential and save water in dry conditions. In contrast, anisohydric ecosystems maintain a constant level of stomatal conductance and carbon uptake even during dry conditions. PFTs are generally not a good predictor of isohydricity. Except for evergreen needleleaf forests, which are more isohydric ecosystems, and face a greater mortality risk than anisohydric species under climate change scenarios, because extended stomatal closure to save water finally starves the ecosystem of carbon, with detrimental effects on metabolism, particularly defense mechanisms against pests and diseases (Y. Liu et al., 2017; Meinzer et al., 2017; F. Wang et al., 2024). Specifically in Central, Eastern, and Northern Europe, where this PFT is abundant, the increasing drought severity trends might initiate an ecological negative spiral, with potentially widespread transformational impacts. In the evaluation study, ET and GPP from CLM5 at evergreen needleleaf forest sites compared well to ICOS observations, in terms of the phenology and the yearly cycle. Further research on PFT-specific drought responses in CLM5 across Europe, also using future climate scenarios, might be crucial to disentangle the climate change and drought-related risk of these ecosystems. Additionally, analyzing the shifts of phenological dates in future climates could provide important insights, given that recent changes in growing season length are driven by atmospheric dryness (Rahmati et al., 2023), and the reported increasing vapor pressure drought severity.

In the remote-sensing-based study in Chapter 3, grasslands in humid hydroclimates showed a relatively small, negative EWUE and TWUE drought response, and in semi-arid hydroclimates, a small positive EWUE and TWUE drought response. Also in CLM5 simulations over Europe, there is a functional distinction between the grasslands present in Norway and the Alps, showing negative drought responses (C_3 arctic grasslands PFT) and the grasslands in Turkey showing positive drought responses (C_3 grasslands), with a lower parameterized intrinsic leaf-level WUE for the C_3 arctic grasslands.

However, grassland-related PFT-specific analysis differs between the presented studies: the land cover on the Norwegian coast is categorized as tundra in Chapter 3, and as grasslands in Chapters 4 and 5 (all land cover and PFT data used are

based on MODIS remote sensing, but a different land cover and PFT classification system was employed in Chapter 3 compared to the CLM5 input used in Chapters 4 and 5). The evaluation study, Chapter 4, finds that the grassland PFT-scale ET shows higher RSME and lower correlation values than GLASS remote sensing, and GLEAM and ERA5-Land reanalyses when evaluated locally against ICOS. Further, CLM5 underestimated the summer ET and GPP at grassland stations. However, only grasslands in semi-humid, humid, and very humid hydroclimates were considered. Hence, it does not provide a performance indication of grasslands in semi-arid regions.

In most of semi-arid Southern Europe, EWUE and TWUE increased. Incidentally, drought responses in this region are primarily positive. The widespread, prevalent T_r control of TWUE here, combined with increased GPP control during droughts, indicates an effective regulation of water and carbon conductance by the vegetation. However, generally lower water availability combined with increased atmospheric dryness could drive this region quickly to conditions that put even well-adapted ecosystems at risk. Essentially, Southern Europe also has a more arid hydroclimate than Central and Eastern Eurpe, and different dominant PFTs, such as grasslands and evergreen broadleaf forests, which functionally explains the difference in the emerging patterns from the rest of the continent. These areas with semi-arid hydroclimate experienced disproportionate decreases of T_r and GPP, resulting in increased WUE during droughts. This outlines modulations towards a more efficient water use to save water in semi-arid areas, which is unnecessary in very humid areas, where the relative definition of droughts likely does not indicate water shortages for ecosystem processes, and ecosystems do not need to adapt

These patterns show a continent at an ecohydrological tipping point: Southern European regions leverage adaptive strategies for resilience. At the same time, Central and Eastern Europe's ecosystems already face systemic risks. Moreover, increasing drought frequency and severity will be a critical development across the continent.

6.2 Recommendations for research infrastructures

Locally observed data is invaluable for evaluating model performance, developing new process models, and creating high-level data products by merging these data into model simulations. The presented studies show that the current network design of European research infrastructures exhibits a significant bias that

inhibits the detection of ecological change hotspots and a thorough evaluation of the continental modeling results.

For example, the ICOS station network does not cover the Eastern European region. However, the simulated significant WUE trends and widespread negative drought responses of ecosystem processes in Eastern Europe outline a potential hotspot of ecosystems at risk, which could not be evaluated or verified with ground truth data. Further, Southern and Northern Europe are also underrepresented in terms of station density when compared to Central Europe. Particularly, the non-forested areas, such as shrubs and grasslands, are less well represented in the network, which makes it difficult to assess and improve the general model performance, and evaluate our findings in these regions. These regions experience significant pressure from land use change and climate change, and are found to be underrepresented in the eLTER RI (Ohnemus et al., 2025).

These geographical biases were confirmed in a separate study, analyzing additional ecological and climatological dimensions across the eLTER RI network, which largely overlaps with the ICOS RI network (Ohnemus et al., 2024). Additionally, croplands were found to be underrepresented. Furthermore, a consistent coverage of observed variables across the stations and the spheres is of significant importance to facilitate a Whole System Analysis framework (WAILS), which entails studies across the atmosphere, sociosphere, biosphere, hydrosphere, and geosphere (Mirtl et al., 2021), and across plant, landscape and regional scales. Further, the co-location of research infrastructures (e.g., eLTER and ICOS) at a set of sites can help achieve these holistic and harmonized data sets (Futter et al., 2023) for interdisciplinary studies. A practical, straightforward example of leveraging data from co-located RIs and different scales would be using plant traits and biodiversity data to constrain ecosystem model parameters while assimilating carbon and water fluxes from ICOS, to create accurate and consistent predictions of ecosystem processes across the continent. For example, eLTER biosphere data can inform on species traits to determine PFT parameters, while ET and GPP states could be updated using assimilation of ICOS EC measurements.

On the basis of work presented in this thesis and other work (Futter et al., 2023; Ohnemus et al., 2024, 2025; Poppe Terán, Naz, Strebel, et al., 2025), three main recommendations are outlined for future environmental RI development in Europe:

1. Homogenized, curated, comprehensive datasets from plant to ecosystem scale enable a straightforward, efficient, continental-scale analysis.

2. Compilation of observation data across spheres and scales, to facilitate a holistic analysis of as much of the present functional diversity as possible.
3. Continuous integration of continental-scale modelling to identify hotspots of environmental change, and the potential for RI network design extensions.

6.3 Improving and extending the European CLM5

While land surface models are already a vital tool to approximate ecosystem processes consistently and on a large scale, improvements of the input data and methods to make the simulations more accurate will always be required. Specifically, the evaluation study in Chapter 4 yielded important insights on the flaws in the current setup of the European CLM5. The following sections outline changes in the input data, the model structure, and the model setup that would elevate the simulations of ecosystem processes with the European CLM5.

Various studies have reported the sensitivity of land surface models, in particular CLM5, to input data (Post et al., 2018; Fisher et al., 2019; Song et al., 2020; Oloruntoba et al., 2025). The appropriate choice of input data is essential to facilitate consistent and accurate simulations of ecosystem processes. For distributed simulations over regions, continents, and the whole globe, the resolution of the land surface static input information and the atmospheric forcing matter, as they represent the heterogeneity of the land surface better and allow for, e.g., better resolved land surface fluxes and soil water flows and more accurate responses to extreme conditions (Prein et al., 2016; Wahl et al., 2017; Naz et al., 2019). Further, the novelty and precision of the raw data (e.g., remote sensing data) and processing method (e.g., land cover and PFT classification method) are essential factors when choosing the input. In more detail, more novel data is of higher interest in terms of innovation potential. However, it must also be beneficial in terms of data accuracy compared to older data sets.

Replacement of the atmospheric forcings, land cover, and soil texture data would be a promising improvement to the European CLM5. The atmospheric forcing that was used, the COSMO Reanalysis 6, still has the highest spatial resolution (6 km) among atmospheric data over the European CORDEX domain (Wahl et al., 2017). However, the limited period (1995 to August 2019) and the lack of updates (its boundary conditions are based on the ERA Interim reanalysis, and the successor, ERA5, has already been available since 2018) are significant disadvantages. Running CLM5 with statistically downscaled ERA5 data has the disadvantage of the relatively coarse resolution, and, as a result,

misrepresentation of e.g., convective rainfall events (Prein et al., 2016). However, it is heavily evaluated by the scientific community. Furthermore, it provides data over an extensive period from 1940 until present, which offers the opportunity to implement a more comprehensive spin-up procedure.

The static input data, soil texture, land cover, and PFT distribution significantly impact how well the European CLM5 represents the actual conditions (P. J. Lawrence & Chase, 2007; Fisher & Koven, 2020; Longo et al., 2019; L. Li et al., 2022). Studies have shown improvements in the simulation of hydrological processes when introducing high-resolution soil texture and PFT maps, often in combinations with meteorological forcing datasets (Fatichi et al., 2020; X. Li et al., 2024; Malle et al., 2024). For example, the SoilGrids soil texture data at 250m resolution (Hengl et al., 2017) simulates water cycle components over Africa similarly in comparison to the coarser, default FAO soil texture input (IGBP, 2000), with only a small influence of the applied upscaling method (Oloruntoba et al., 2025). The land cover and the corresponding PFT distribution changed rapidly in recent decades, so an up-to-date land cover representation for models is a promising improvement opportunity (Hurtt et al., 2020). Notably, while using higher-resolution, alternative PFT distributions would improve the representation of land surface heterogeneity, these might not be compatible with the default set of PFT parameters in CLM5, thus misrepresenting the carefully calibrated vegetation functionality distribution. Hence, concurrently to updating PFT maps over Europe, PFT parameter optimization efforts have to be considered.

Another interesting improvement to the European CLM5 model would include spatially resolved atmospheric CO_2 concentrations, given that the local concentrations can vary substantially, depending on the distance and magnitude of emission locations and wind conditions. The atmospheric CO_2 concentration co-determines the carbon gradient between the canopy and the leaf, influencing the overall carbon uptake, leaf carbon, and area, as well as evapotranspiration. Especially in areas close to dominant carbon emitters, these local concentrations could differ substantially from the global mean. Until now, this was impossible, especially over large study domains, because data on CO_2 emissions from the land surface were scarce. However, recent developments in sensing and modelling of carbon emissions (Dou et al., 2022; Z. Liu et al., 2020, 2024; Z. Wu et al., 2024), combined with high-resolution atmospheric models, could provide essential, gridded CO_2 concentration information to force the carbon cycle in CLM5 over Europe. All in all, studies analyzing the effect of different atmospheric forcings and different soil and vegetation inputs, and replacement with the most

appropriate, should be carried out regularly to maintain a state-of-the-art continental model that serves for research and scientific services.

A spin-up procedure is necessary to create adequate initial conditions for the terrestrial carbon pools in CLM5. In practice, around 10 years of atmospheric data is cycled to force the carbon cycle simulations until a steady state is reached. This omits the systematic trend biases in the production simulations, which occur when the BGC model approximates the steady state from arbitrary conditions. This is because any simulation of carbon pools and fluxes starting from non-steady conditions will converge towards to the equilibrium state. However, a steady state in the terrestrial ecosystems is a conceptual pitfall: Global and local pressures, such as land use and land cover change and also climate change, drive long-term trends in ecosystem processes, and cannot be assumed to be in steady state. Instead, they are transitioning to another steady state. Additionally, the conditions defining the possible steady states change with the climate. To include these trends observed in contemporary ecosystems (e.g., carbon sources and sinks transformations), it is critical to integrate these long-term trends in the production simulations, instead of running the BGC model in continuous steady state. For that, a spin-up should be carried out for a period when ecosystems were close to an actual equilibrium, which should be before climatic changes were strong transformational factors. Thus, the availability of atmospheric forcing data for the past centuries is essential. Further aspects of land use and land cover change, such as deforestation, and human management (such as wood harvest), should also be considered.

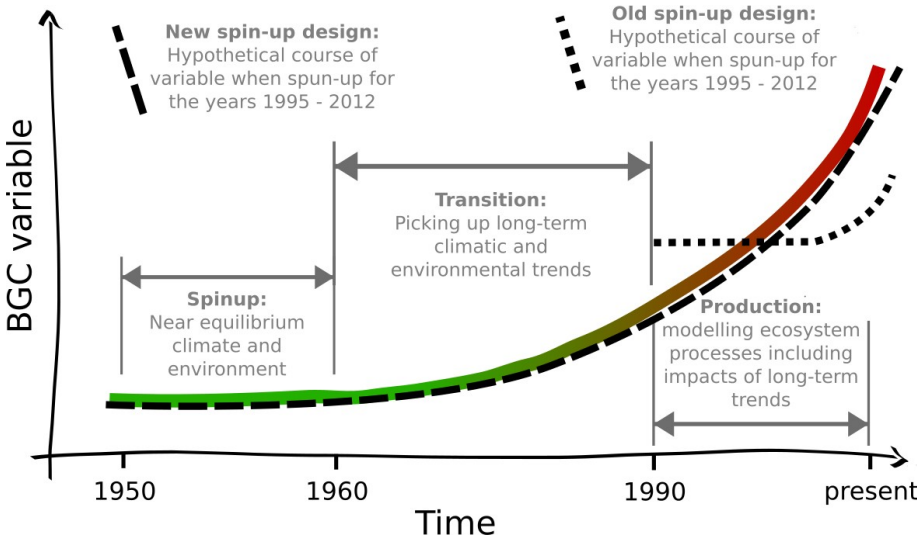

Figure Synthesis and conclusions.7: Schematic of an updated spin-up design. On the y-axis is the value of an arbitrary biogeochemistry (BGC) variable experiencing a trend over time (x-axis). The dashed line shows the qualitative evolution of the simulated variable with the new spin-up design. The dotted line is the qualitative evolution of the variable of the old spin-up design. Adopted from Poppe Terán, Naz, Strebel, et al., 2025.

A more comprehensive concept for the spin-up involves, three steps:

1. A long-term spin-up with atmospheric forcing close to steady-state in the past conditions. In this phase, the steady state of the carbon pools and fluxes is approximated.
2. A transition simulation that follows the trends and transitions after the spin-up. During this simulation, the climatic changes will drive long-term trends in the carbon cycle, so that sources and sinks can emerge, and the transitioning states are well represented.
3. A production simulation after the transition period, where the trends are well-represented and carbon states and pools follow the naturally occurring long-term changes, including land use and land cover change scenarios.

However, any long-term BGC spin-up over high-resolution and large-scale domains will be computationally expensive, as it takes over 1000 years until a steady state is reached for most of the included pixels. Exploring methods that approximate the steady states of carbon pools more efficiently than the traditional method is worthwhile. For example, machine learning algorithms that can approximate the carbon states based on the present local information and climate (Sun et al., 2023), reduce computational costs by up to 80%. Or advanced

semi-analytical spin-up methods that need one order of magnitude less computational effort than the traditional method (Liao et al., 2023). These methods are still in development and are not easily transferable across grids, domains, and simulation setups. In the future, they will play a critical role in advancing research in carbon cycle modelling, as large-scale experiments will become easier to implement and more accessible to researchers with limited access to high-performance computing infrastructures.

Chapter 4 outlines the ability of CLM5 to simulate ecosystem processes, particularly ET and GPP over Europe. Concurrently, it discovered limitations when compared to ICOS observations. The following section proposes specific developments to improve the representation of ecosystem processes in the model structure and setup designs with the European CLM5 that could offer valuable services.

Functional distinction of the vegetation in CLM5, and any other land surface model, is done by discretizing the vegetated land surface into PFTs. Then, each PFT follows a set of equations with a given set of parameters to calculate the PFT-scale processes. Thus, the models assume a convergence of ecosystem functioning for each PFT group. However, PFTs as fitting functional types were questioned mainly because they do not systematically cover the multidimensional space of plant traits (Harrison et al., 2021; Van Bodegom et al., 2014). For example, the parametrization of water-use efficiency in the Medlyn stomatal conductance model (g_1 parameter) is implemented on the PFT level in CLM5, but it is found to vary substantially within one PFT across its spatial extent and even in time (Lin et al., 2015; Medlyn et al., 2011). Further, hydraulic plant trait parameters do not converge significantly across PFTs, resulting in spurious parametrization of drought sensitivity (such as the maximum conductance, k_{max}, and the water potential at 50% conductance loss, p_{50}) (Y. Liu et al., 2017; Meinzer et al., 2017; F. Wang et al., 2024).

The PFT concept has recently been widely proven to be outdated because it does not sufficiently explain the variance of global ecosystem processes (Cranko Page et al., 2024). Alternatively, trait-based modelling encompasses a continuous functional space for local and time-variable parameters (Kattge et al., 2011). However, there is limited information to constrain these parameters across large areas of the terrestrial surface, and the spatial convergence of these plant traits suggests that a functional grouping is possible and a sensible approach, as it requires less distributed trait data and would be more computationally efficient. Implementing a local parameter distribution in CLM5 (by resolving functional

types locally rather than globally), and combining it with local trait and processes measurements from a distributed European RI would be an intriguing start to investigate where and how ecosystem functioning converges, and what this implies for optimal functional groupings of vegetation in land surface models. In the best case, this approach could overarch from plant to stand and ecosystem levels, so that multi-scale measurements can be implemented and the simulations would allow for analyses and interpretations across all these scales. In practice, this would help compare outputs from the CLM5 model to observations from different scales and interpret the resulting outputs for scale-based scientific inference. This goes beyond additional subgrid functionality that is developed for future-generation land surface models, such as hillslope tiles, microclimate, and soil nutrients (Arboleda Obando et al., 2022; Hes et al., 2024; M. Jones et al., 2023; Longo et al., 2019; Swenson et al., 2019).

In any case, any introduction of new processes must carefully consider on which scale it is applied, and whether the interactions with other processes introduce biases. There is considerable uncertainty in land surface models, which stems from inadequately coupling processes across scales that rely on incompatible assumptions. For example, the Medlyn stomatal conductance model optimizes the carbon gain per water loss, while recently introduced plant hydraulic models, which are tightly coupled with stomatal conductance, prioritize water transport safety by simulating embolism resistance thresholds. The resulting feedback of the inconsistent coupling of these models is not well studied (Kennedy et al., 2019). Efforts are underway to unify the water and carbon economics within plants across species (Joshi et al., 2022). However, it must still be scaled based on trait distributions and adapted to PFT (or novel distinctions of plant functionality). These efforts will be instrumental in analyzing comprehensive drought responses from models across many ecosystems.

Lastly, there are ample opportunities to project the impact of climate change on ecosystem processes using CLM5 and future climate scenarios or storyline simulations. Specifically, the impacts of increasing frequency and severity of extreme events over the European continent are intriguing to analyze. Data from climate projections can be derived using emission scenarios, such as the Coupled Model Intercomparison Project (CMIP), and can be downscaled and used as forcing. Alternatively, storyline scenarios extrapolate current conditions to hypothetical future conditions, e.g., projecting how the terrestrial system functions change in a +2K warmer future (Klimiuk et al., 2025; Martin et al., 2025). Further, it is essential to consider different agricultural adaptations and forest management strategies in future climate conditions by implementing, e.g.,

new crop routines (Boas et al., 2021; Dombrowski et al., 2024) and crop types depending on the expected climate in the growing season in the European CLM5. Importantly, introducing comprehensive irrigation, and other human water abstractions, into the European CLM5 could provide insights into the human influence on droughts, especially in future scenarios (Wanders & Wada, 2015).

6.4 Integration of models and observations

Together with continuous improvements to the European CLM5 model outlined in Chapter 6.3, a tight integration of remote and in situ observations into the model promises accurate information on the states of the European ecosystem processes in the present and future. The following section highlights the potential to fuse observation data into the European CLM5 model.

Prior parameter optimization might be necessary for accurate predictions, especially for future climate projections. Notably, developing an emulator of, e.g., the CLM5 drought response of ecosystem processes might be helpful and efficient for highly computation-intensive iterative parameter optimization methods, such as Markov Chain Monte Carlo approaches (Keetz et al., 2024), focusing on sensitive parameters driving ET and GPP variation (Eloundou et al., 2025). Notably, these methods would infer a static value, which contradicts its variation due to, e.g., vegetation acclimation. However, this is required to implement as a PFT parameter in CLM5, which best approximates the observations of the respective ecosystem processes. However, this approach does not consider mid-term and long-term vegetation adaptations, e.g., acclimation to new climatic conditions, which would alter the vegetation trait and result in a time-variable PFT parameter. A comprehensive approach constrained by observed plant traits that formulates PFT parameters as a function of the changing climate and environment has not yet been implemented.

Reanalyses are the gold standard for analyzing Earth System variables. They are invaluable because they use information from measurement distributions and errors, as well as model errors, to update model states. As a result, they extend the scarce available observations in a spatiotemporal consistent manner, yielding gapless time series of the state-of-the-art understanding of the terrestrial system with physical consistency (Baatz et al., 2021). There are several available reanalysis products for the land surface, e.g., the Carbon Data Model Framework (CARDAMOM) (Bloom & Williams, 2015). However, a comprehensive reanalysis summarizing the water and carbon cycle by jointly assimilating hydrological and ecological variables remains challenging. The large-scale in situ observations

from the atmospheric, hydrological, and biological spheres offered by continental research infrastructures, such as ICOS and eLTER, bring an excellent opportunity to include ground truth data when creating a European ecosystem reanalysis. Further, remotely sensed information provides spatially extensive data to complement the in situ RIs. For example, soil moisture from the European Space Agency Climate Change Initiative (ESACCI) (Dorigo et al., 2017) was used to update land surface states of CLM3.5 over Europe in a study by Naz et al., 2020. Other studies assimilating remotely sensed soil moisture into land surface models also achieved an improved characterization of soil moisture, but did not improve other hydrological variables, like runoff and evapotranspiration (Lu et al., 2020; Naz et al., 2019; Strebel et al., 2023; H. Zhao et al., 2025). Multivariate assimilation of hydrological and vegetation-related observations (e.g., remotely sensed leaf area index) could improve the simulated ecosystem more comprehensively. Further, total water storage from the Gravity Recovery and Climate Experiment (GRACE) (Landerer & Swenson, 2012) and LAI from the Moderate Resolution Imaging Spectroradiometer (MODIS) (Myneni et al., 2015) can be used in the assimilation. The coupling of CLM5 and the Parallel Data Assimilation Framework (PDAF) offers an excellent opportunity to fuse observations and the European CLM5 using different assimilation techniques (Strebel et al., 2022).

Bibliography

Adams, J. (2022). Climate_indices, an open source Python library providing reference implementations of commonly used climate indices [Computer software]. https://github.com/monocongo/climate_indices

Adams, M. A., Buckley, T. N., & Turnbull, T. L. (2020). Diminishing CO_2-driven gains in water-use efficiency of global forests. Nature Climate Change, 10(5), 466–471. https://doi.org/10.1038/s41558-020-0747-7

Alexopoulos, M. J., Müller-Thomy, H., Nistahl, P., Šraj, M., & Bezak, N. (2023). Validation of precipitation reanalysis products for rainfall-runoff modelling in Slovenia. Hydrology and Earth System Sciences, 27(13), 2559–2578. https://doi.org/10.5194/hess-27-2559-2023

Ali, A. A., Xu, C., Rogers, A., Fisher, R. A., Wullschleger, S. D., Massoud, E. C., Vrugt, J. A., Muss, J. D., McDowell, N. G., Fisher, J. B., Reich, P. B., & Wilson, C. J. (2016). A global scale mechanistic model of photosynthetic capacity (LUNA V1.0). Geoscientific Model Development, 9(2), 587–606. https://doi.org/10.5194/gmd-9-587-2016

Ali, M. A., & Kamraju, M. (2023). Natural resources and society: Understanding the complex relationship between humans and the environment. Springer.

Allen, R. G. (Ed.). (2000). Crop evapotranspiration: Guidelines for computing crop water requirements (repr). Food and Agriculture Organization of the United Nations.

Allen, R., Pereira, L., Raes, D., & Smith, M. (1998). FAO Irrigation and drainage paper No. 56. Rome: Food and Agriculture Organization of the United Nations, 56, 26–40.

Anderegg, L. D. L., Griffith, D. M., Cavender-Bares, J., Riley, W. J., Berry, J. A., Dawson, T. E., & Still, C. J. (2022). Representing plant diversity in land models: An evolutionary approach to make "Functional Types" more functional. Global Change Biology, 28(8), 2541–2554. https://doi.org/10.1111/gcb.16040

Anderegg, W. R. L., Konings, A. G., Trugman, A. T., Yu, K., Bowling, D. R., Gabbitas, R., Karp, D. S., Pacala, S., Sperry, J. S., Sulman, B. N., & Zenes, N. (2018). Hydraulic diversity of forests regulates ecosystem resilience during drought. Nature, 561(7724), 538–541. https://doi.org/10.1038/s41586-018-0539-7

Andreadis, K. M., Clark, E. A., Wood, A. W., Hamlet, A. F., & Lettenmaier, D. P. (2005). Twentieth-Century Drought in the Conterminous United States. Journal of Hydrometeorology, 6(6), 985–1001. https://doi.org/10.1175/JHM450.1

Arboleda Obando, P. F., Ducharne, A., Cheruy, F., Jost, A., Ghattas, J., Colin, J., & Nous, C. (2022). Influence of Hillslope Flow on Hydroclimatic Evolution Under Climate Change. Earth's Future, 10(9), e2021EF002613. https://doi.org/10.1029/2021EF002613

Arrhenius, S. (1896). On the influence of carbonic acid in the air upon the temperature of the ground. The London, Edinburgh, and Dublin Philosophical Magazine and Journal of Science, 41(251), 237–276. https://doi.org/10.1080/14786449608620846

Aubinet, M., Vesala, T., & Papale, D. (Eds.). (2012). Eddy covariance: A practical guide to measurement and data analysis. Springer.

Baatz, R., Hendricks Franssen, H. J., Euskirchen, E., Sihi, D., Dietze, M., Ciavatta, S., Fennel, K., Beck, H., De Lannoy, G., Pauwels, V. R. N., Raiho, A., Montzka, C., Williams, M., Mishra, U., Poppe, C., Zacharias, S., Lausch, A., Samaniego, L., Van Looy, K., … Vereecken, H. (2021). Reanalysis in Earth System Science: Toward Terrestrial Ecosystem Reanalysis. Reviews of Geophysics, 59(3). https://doi.org/10.1029/2020RG000715

Baatz, R., Sullivan, P. L., Li, L., Weintraub, S. R., Loescher, H. W., Mirtl, M., Groffman, P. M., Wall, D. H., Young, M., White, T., Wen, H., Zacharias, S., Kühn, I., Tang, J., Gaillardet, J., Braud, I., Flores, A. N., Kumar, P., Lin, H., … Van Looy, K. (2018). Steering operational synergies in terrestrial observation networks: Opportunity for advancing Earth system dynamics modellingB6. Earth System Dynamics, 9(2), 593–609. https://doi.org/10.5194/esd-9-593-2018

Baez-Villanueva, O. M., Zambrano-Bigiarini, M., Miralles, D. G., Beck, H. E., Siegmund, J. F., Alvarez-Garreton, C., Verbist, K., Garreaud, R., Boisier, J. P., & Galleguillos, M. (2024). On the timescale of drought indices for monitoring streamflow drought considering catchment hydrological regimes. Hydrology and Earth System Sciences, 28(6), 1415–1439. https://doi.org/10.5194/hess-28-1415-2024

Bai, Y., Zha, T., Bourque, C. P.-A., Jia, X., Ma, J., Liu, P., Yang, R., Li, C., Du, T., & Wu, Y. (2020). Variation in ecosystem water use efficiency along a southwest-to-northeast aridity gradient in China. Ecological Indicators, 110, 105932. https://doi.org/10.1016/j.ecolind.2019.105932

Baker, E., Harper, A. B., Williamson, D., & Challenor, P. (2022). Emulation of high-resolution land surface models using sparse Gaussian processes with application to JULES. Geoscientific Model Development, 15(5), 1913–1929. https://doi.org/10.5194/gmd-15-1913-2022

Bakke, S. J., Ionita, M., & Tallaksen, L. M. (2023). Recent European drying and its link to prevailing large-scale atmospheric patterns. Scientific Reports, 13(1), 21921. https://doi.org/10.1038/s41598-023-48861-4

Bastos, A., Ciais, P., Friedlingstein, P., Sitch, S., Pongratz, J., Fan, L., Wigneron, J. P., Weber, U., Reichstein, M., Fu, Z., Anthoni, P., Arneth, A., Haverd, V., Jain, A. K., Joetzjer, E., Knauer, J., Lienert, S., Loughran, T., McGuire, P. C., … Zaehle, S. (2020). Direct and seasonal legacy effects of the 2018 heat wave and drought on European ecosystem productivity. Science Advances, 6(24), eaba2724. https://doi.org/10.1126/sciadv.aba2724

Bates, J. S., Montzka, C., Schmidt, M., & Jonard, F. (2021). Estimating Canopy Density Parameters Time-Series for Winter Wheat Using UAS Mounted LiDAR. Remote Sensing, 13(4), 710. https://doi.org/10.3390/rs13040710

Beer, C., Ciais, P., Reichstein, M., Baldocchi, D., Law, B. E., Papale, D., Soussana, J.-F., Ammann, C., Buchmann, N., Frank, D., Gianelle, D., Janssens, I. A., Knohl, A., Köstner, B., Moors, E., Roupsard, O., Verbeeck, H., Vesala, T., Williams, C. A., & Wohlfahrt, G. (2009). Temporal and among-site variability of inherent water use efficiency at the ecosystem level. Global Biogeochemical Cycles, 23(2), n/a-n/a. https://doi.org/10.1029/2008GB003233

Beer, C., Reichstein, M., Tomelleri, E., Ciais, P., Jung, M., Carvalhais, N., Rodenbeck, C., Arain, M. A., Baldocchi, D., Bonan, G. B., Bondeau, A., Cescatti, A., Lasslop, G., Lindroth, A., Lomas, M., Luyssaert, S., Margolis, H., Oleson, K. W., Roupsard, O., … Papale, D. (2010). Terrestrial Gross Carbon Dioxide Uptake: Global Distribution and Covariation with Climate. Science, 329(5993), 834–838. https://doi.org/10.1126/science.1184984

Belleflamme, A., Goergen, K., Wagner, N., Kollet, S., Bathiany, S., El Zohbi, J., Rechid, D., Vanderborght, J., & Vereecken, H. (2023). Hydrological forecasting at impact scale: The integrated ParFlow hydrological model at 0.6 km for climate resilient water resource management over Germany. Frontiers in Water, 5, 1183642. https://doi.org/10.3389/frwa.2023.1183642

Belmecheri, S., Maxwell, R. S., Taylor, A. H., Davis, K. J., Guerrieri, R., Moore, D. J. P., & Rayback, S. A. (2021). Precipitation alters the CO_2 effect on water-use

efficiency of temperate forests. Global Change Biology, 27(8), 1560–1571. https://doi.org/10.1111/gcb.15491

Bevacqua, E., Rakovec, O., Schumacher, D. L., Kumar, R., Thober, S., Samaniego, L., Seneviratne, S. I., & Zscheischler, J. (2024). Direct and lagged climate change effects intensified the 2022 European drought. Nature Geoscience. https://doi.org/10.1038/s41561-024-01559-2

Birch, L., Schwalm, C. R., Natali, S., Lombardozzi, D., Keppel-Aleks, G., Watts, J., Lin, X., Zona, D., Oechel, W., Sachs, T., Black, T. A., & Rogers, B. M. (2021). Addressing biases in Arctic–boreal carbon cycling in the Community Land Model Version 5. Geoscientific Model Development, 14(6), 3361–3382. https://doi.org/10.5194/gmd-14-3361-2021

Bloom, A. A., Bowman, K. W., Liu, J., Konings, A. G., Worden, J. R., Parazoo, N. C., Meyer, V., Reager, J. T., Worden, H. M., Jiang, Z., Quetin, G. R., Smallman, T. L., Exbrayat, J.-F., Yin, Y., Saatchi, S. S., Williams, M., & Schimel, D. S. (2020). Lagged effects regulate the inter-annual variability of the tropical carbon balance. Biogeosciences, 17(24), 6393–6422. https://doi.org/10.5194/bg-17-6393-2020

Bloom, A. A., & Williams, M. (2015). Constraining ecosystem carbon dynamics in a data-limited world: Integrating ecological "common sense" in a model–data fusion framework. Biogeosciences, 12(5), 1299–1315. https://doi.org/10.5194/bg-12-1299-2015

Boas, T., Bogena, H., Grünwald, T., Heinesch, B., Ryu, D., Schmidt, M., Vereecken, H., Western, A., & Hendricks Franssen, H.-J. (2021). Improving the representation of cropland sites in the Community Land Model (CLM) version 5.0. Geoscientific Model Development, 14(1), 573–601. https://doi.org/10.5194/gmd-14-573-2021

Boas, T., Bogena, H. R., Ryu, D., Vereecken, H., Western, A., & Hendricks Franssen, H.-J. (2023). Seasonal soil moisture and crop yield prediction with fifth-generation seasonal forecasting system (SEAS5) long-range meteorological forecasts in a land surface modelling approach. Hydrology and Earth System Sciences, 27(16), 3143–3167. https://doi.org/10.5194/hess-27-3143-2023

Bollmeyer, C., Keller, J. D., Ohlwein, C., Wahl, S., Crewell, S., Friederichs, P., Hense, A., Keune, J., Kneifel, S., Pscheidt, I., Redl, S., & Steinke, S. (2015). Towards a high-resolution regional reanalysis for the European CORDEX domain: High-Resolution Regional Reanalysis for the European CORDEX

Domain. Quarterly Journal of the Royal Meteorological Society, 141(686), 1–15. https://doi.org/10.1002/qj.2486

Bonan, G. B. (2019). Climate change and terrestrial ecosystem modeling. Cambridge University Press.

Bonan, G. B., Lawrence, P. J., Oleson, K. W., Levis, S., Jung, M., Reichstein, M., Lawrence, D. M., & Swenson, S. C. (2011). Improving canopy processes in the Community Land Model version 4 (CLM4) using global flux fields empirically inferred from FLUXNET data. Journal of Geophysical Research, 116(G2), G02014. https://doi.org/10.1029/2010JG001593

Bonan, G. B., Levis, S., Kergoat, L., & Oleson, K. W. (2002). Landscapes as patches of plant functional types: An integrating concept for climate and ecosystem models: PLANT FUNCTIONAL TYPES AND CLIMATE MODELS. Global Biogeochemical Cycles, 16(2), 5-1-5–23. https://doi.org/10.1029/2000GB001360

Bonan, G. B., Williams, M., Fisher, R. A., & Oleson, K. W. (2014). Modeling stomatal conductance in the earth system: Linking leaf water-use efficiency and water transport along the soil–plant–atmosphere continuum. Geoscientific Model Development, 7(5), 2193–2222. https://doi.org/10.5194/gmd-7-2193-2014

Bradford, J. B., Schlaepfer, D. R., Lauenroth, W. K., & Palmquist, K. A. (2020). Robust ecological drought projections for drylands in the 21st century. Global Change Biology, 26(7), 3906–3919. https://doi.org/10.1111/gcb.15075

Brönnimann, S., Stucki, P., Franke, J., Valler, V., Brugnara, Y., Hand, R., Slivinski, L. C., Compo, G. P., Sardeshmukh, P. D., Lang, M., & Schaefli, B. (2022). Influence of warming and atmospheric circulation changes on multidecadal European flood variability. Climate of the Past, 18(4), 919–933. https://doi.org/10.5194/cp-18-919-2022

Brunner, M. I., & Stahl, K. (2023). Temporal hydrological drought clustering varies with climate and land-surface processes. Environmental Research Letters, 18(3), 034011. https://doi.org/10.1088/1748-9326/acb8ca

Budyko, M. I. (with Miller, D. H.). (1974). Climate and life. Academic Press.

Cai, W., & Prentice, I. C. (2020). Recent trends in gross primary production and their drivers: Analysis and modelling at flux-site and global scales. Environmental Research Letters, 15(12), 124050. https://doi.org/10.1088/1748-9326/abc64e

Caldararu, S., Purves, D. W., & Smith, M. J. (2015). The effect of using the plant functional type paradigm on a data-constrained global phenology model

[Preprint]. Biogeochemistry: Modelling, Terrestrial. https://doi.org/10.5194/bgd-12-16847-2015

Callejas Moncaleano, D. C., Pande, S., & Rietveld, L. (2021). Water Use Efficiency: A Review of Contextual and Behavioral Factors. Frontiers in Water, 3, 685650. https://doi.org/10.3389/frwa.2021.685650

Cammalleri, C., Acosta Navarro, J. C., Bavera, D., Diaz, V., Di Ciollo, C., Maetens, W., Magni, D., Masante, D., Spinoni, J., & Toreti, A. (2023). An event-oriented database of meteorological droughts in Europe based on spatio-temporal clustering. Scientific Reports, 13(1), 3145. https://doi.org/10.1038/s41598-023-30153-6

Cammalleri, C., Arias-Muñoz, C., Barbosa, P., De Jager, A., Magni, D., Masante, D., Mazzeschi, M., McCormick, N., Naumann, G., Spinoni, J., & Vogt, J. (2021). A revision of the Combined Drought Indicator (CDI) used in the European Drought Observatory (EDO). Natural Hazards and Earth System Sciences, 21(2), 481–495. https://doi.org/10.5194/nhess-21-481-2021

Cammalleri, C., Micale, F., & Vogt, J. (2016). A novel soil moisture-based drought severity index (DSI) combining water deficit magnitude and frequency. Hydrological Processes, 30(2), 289–301. https://doi.org/10.1002/hyp.10578

Cammalleri, C., Naumann, G., Mentaschi, L., Bisselink, B., Gelati, E., De Roo, A., & Feyen, L. (2020). Diverging hydrological drought traits over Europe with global warming. Hydrology and Earth System Sciences, 24(12), 5919–5935. https://doi.org/10.5194/hess-24-5919-2020

Cammalleri, C., & Toreti, A. (2023). A Generalized Density-Based Algorithm for the Spatiotemporal Tracking of Drought Events. Journal of Hydrometeorology, 24(3), 537–548. https://doi.org/10.1175/JHM-D-22-0115.1

Cheng, Y., Huang, M., Zhu, B., Bisht, G., Zhou, T., Liu, Y., Song, F., & He, X. (2021). Validation of the Community Land Model Version 5 Over the Contiguous United States (CONUS) Using In Situ and Remote Sensing Data Sets. Journal of Geophysical Research: Atmospheres, 126(5), e2020JD033539. https://doi.org/10.1029/2020JD033539

Christiansen, E., Waring, R. H., & Berryman, A. A. (1987). Resistance of conifers to bark beetle attack: Searching for general relationships. Forest Ecology and Management, 22(1–2), 89–106. https://doi.org/10.1016/0378-1127(87)90098-3

Chu, H., Luo, X., Ouyang, Z., Chan, W. S., Dengel, S., Biraud, S. C., Torn, M. S., Metzger, S., Kumar, J., Arain, M. A., Arkebauer, T. J., Baldocchi, D., Bernacchi, C., Billesbach, D., Black, T. A., Blanken, P. D., Bohrer, G., Bracho, R., Brown, S.,

… Zona, D. (2021). Representativeness of Eddy-Covariance flux footprints for areas surrounding AmeriFlux sites. Agricultural and Forest Meteorology, 301–302, 108350. https://doi.org/10.1016/j.agrformet.2021.108350

Ciais, P., Reichstein, M., Viovy, N., Granier, A., Ogée, J., Allard, V., Aubinet, M., Buchmann, N., Bernhofer, C., Carrara, A., Chevallier, F., Noblet, N. D., Friend, A. D., Friedlingstein, P., Grünwald, T., Heinesch, B., Keronen, P., Knohl, A., Krinner, G., … Valentini, R. (2005). Europe-wide reduction in primary productivity caused by the heat and drought in 2003. Nature, 437(7058), 529–533. https://doi.org/10.1038/nature03972

Clapeyron, M. C. (1834). Mémoire sur la puissance motrice de la chaleur. Journal de l'École Polytechnique, 23, 153–190.

Clark, J. S., Iverson, L., Woodall, C. W., Allen, C. D., Bell, D. M., Bragg, D. C., D'Amato, A. W., Davis, F. W., Hersh, M. H., Ibanez, I., Jackson, S. T., Matthews, S., Pederson, N., Peters, M., Schwartz, M. W., Waring, K. M., & Zimmermann, N. E. (2016). The impacts of increasing drought on forest dynamics, structure, and biodiversity in the United States. Global Change Biology, 22(7), 2329–2352. https://doi.org/10.1111/gcb.13160

Clausius, R. (1850). Über die bewegende kraft der Wärme und die Gesetze, welche sich daraus für die Wärmelehre selbst ableiten lassen. Annalen Der Physik, 155(4), 500–524.

Condon, L. E., Atchley, A. L., & Maxwell, R. M. (2020). Evapotranspiration depletes groundwater under warming over the contiguous United States. Nature Communications, 11(1), 873. https://doi.org/10.1038/s41467-020-14688-0

Cooley, S. S., Fisher, J. B., & Goldsmith, G. R. (2022). Convergence in water use efficiency within plant functional types across contrasting climates. Nature Plants. https://doi.org/10.1038/s41477-022-01131-z

Copernicus Climate Change Service. (2019). ERA5-Land hourly data from 2001 to present [Dataset]. ECMWF. https://doi.org/10.24381/CDS.E2161BAC

Cowan, I. R., & Farquhar, G. D. (1977). Stomatal function in relation to leaf metabolism and environment. Symposia of the Society for Experimental Biology, 31, 471–505.

Cranko Page, J., Abramowitz, G., De Kauwe, Martin. G., & Pitman, A. J. (2024). Are Plant Functional Types Fit for Purpose? Geophysical Research Letters, 51(1), e2023GL104962. https://doi.org/10.1029/2023GL104962

Crausbay, S. D., Betancourt, J., Bradford, J., Cartwright, J., Dennison, W. C., Dunham, J., Enquist, C. A. F., Frazier, A. G., Hall, K. R., Littell, J. S., Luce, C. H., Palmer, R., Ramirez, A. R., Rangwala, I., Thompson, L., Walsh, B. M., & Carter, S. (2020). Unfamiliar Territory: Emerging Themes for Ecological Drought Research and Management. One Earth, 3(3), 337–353. https://doi.org/10.1016/j.oneear.2020.08.019

Crausbay, S. D., Ramirez, A. R., Carter, S. L., Cross, M. S., Hall, K. R., Bathke, D. J., Betancourt, J. L., Colt, S., Cravens, A. E., Dalton, M. S., Dunham, J. B., Hay, L. E., Hayes, M. J., McEvoy, J., McNutt, C. A., Moritz, M. A., Nislow, K. H., Raheem, N., & Sanford, T. (2017). Defining Ecological Drought for the Twenty-First Century. Bulletin of the American Meteorological Society, 98(12), 2543–2550. https://doi.org/10.1175/BAMS-D-16-0292.1

Crutzen, P. J. (2016). Geology of Mankind. In P. J. Crutzen & H. G. Brauch (Eds.), Paul J. Crutzen: A Pioneer on Atmospheric Chemistry and Climate Change in the Anthropocene (pp. 211–215). Springer International Publishing. https://doi.org/10.1007/978-3-319-27460-7_10

Dagon, K., Sanderson, B. M., Fisher, R. A., & Lawrence, D. M. (2020). A machine learning approach to emulation and biophysical parameter estimation with the Community Land Model, version 5. Advances in Statistical Climatology, Meteorology and Oceanography, 6(2), 223–244. https://doi.org/10.5194/ascmo-6-223-2020

Darcy, H. (1856). Les fontaines publiques de la ville de Dijon: Exposition et application des principes {\`a} suivre et des formules {\`a} employer dans les questions de distribution d'eau (Vol. 1). Victor Dalmont.

Davies-Barnard, T., Meyerholt, J., Zaehle, S., Friedlingstein, P., Brovkin, V., Fan, Y., Fisher, R. A., Jones, C. D., Lee, H., Peano, D., Smith, B., Wårlind, D., & Wiltshire, A. J. (2020). Nitrogen cycling in CMIP6 land surface models: Progress and limitations. Biogeosciences, 17(20), 5129–5148. https://doi.org/10.5194/bg-17-5129-2020

De Pue, J., Wieneke, S., Bastos, A., Barrios, J. M., Liu, L., Ciais, P., Arboleda, A., Hamdi, R., Maleki, M., Maignan, F., Gellens-Meulenberghs, F., Janssens, I., & Balzarolo, M. (2023). Temporal variability of observed and simulated gross primary productivity, modulated by vegetation state and hydrometeorological drivers [Preprint]. Biogeochemistry: Modelling, Terrestrial. https://doi.org/10.5194/egusphere-2023-994

Dekker, S. C., Groenendijk, M., Booth, B. B. B., Huntingford, C., & Cox, P. M. (2016). Spatial and temporal variations in plant water-use efficiency inferred from tree-ring, eddy covariance and atmospheric observations. Earth System Dynamics, 7(2), 525–533. https://doi.org/10.5194/esd-7-525-2016

Deng, M., Meng, X., Lu, Y., Li, Z., Zhao, L., Hu, Z., Chen, H., Shang, L., Wang, S., & Li, Q. (2021). Impact and Sensitivity Analysis of Soil Water and Heat Transfer Parameterizations in Community Land Surface Model on the Tibetan Plateau. Journal of Advances in Modeling Earth Systems, 13(9). https://doi.org/10.1029/2021MS002670

Deng, Z., Chen, J., Wang, S., Li, T., Huang, K., Gu, P., Peng, H., & Chen, Z. (2025). Response of Vegetation Photosynthesis to the 2022 Drought in Yangtze River Basin by Diurnal Orbiting Carbon Observatory-2/3 Satellite Observations. Journal of Remote Sensing, 5, 0445. https://doi.org/10.34133/remotesensing.0445

Di Nunno, F., & Granata, F. (2023). Spatio-temporal analysis of drought in Southern Italy: A combined clustering-forecasting approach based on SPEI index and artificial intelligence algorithms. Stochastic Environmental Research and Risk Assessment, 37(6), 2349–2375. https://doi.org/10.1007/s00477-023-02390-8

Dingman, S. L., & Dingman, S. L. (2015). Physical hydrology (Third edition). Waveland Press, Inc.

Dombrowski, O., Brogi, C., Hendricks Franssen, H. -J., Pisinaras, V., Panagopoulos, A., Swenson, S., & Bogena, H. (2024). Land Surface Modeling as a Tool to Explore Sustainable Irrigation Practices in Mediterranean Fruit Orchards. Water Resources Research, 60(7), e2023WR036139. https://doi.org/10.1029/2023WR036139

Dorigo, W., Wagner, W., Albergel, C., Albrecht, F., Balsamo, G., Brocca, L., Chung, D., Ertl, M., Forkel, M., Gruber, A., Haas, E., Hamer, P. D., Hirschi, M., Ikonen, J., De Jeu, R., Kidd, R., Lahoz, W., Liu, Y. Y., Miralles, D., … Lecomte, P. (2017). ESA CCI Soil Moisture for improved Earth system understanding: State-of-the art and future directions. Remote Sensing of Environment, 203, 185–215. https://doi.org/10.1016/j.rse.2017.07.001

Dou, X., Wang, Y., Ciais, P., Chevallier, F., Davis, S. J., Crippa, M., Janssens-Maenhout, G., Guizzardi, D., Solazzo, E., Yan, F., Huo, D., Zheng, B., Zhu, B., Cui, D., Ke, P., Sun, T., Wang, H., Zhang, Q., Gentine, P., … Liu, Z. (2022). Near-real-time global gridded daily CO_2 emissions. The Innovation, 3(1), 100182. https://doi.org/10.1016/j.xinn.2021.100182

Drought 2018 Team, & ICOS Ecosystem Thematic Centre. (2020). Drought-2018 ecosystem eddy covariance flux product for 52 stations in FLUXNET-Archive format [Collection of FLUXNET product ZIP archives]. https://doi.org/10.18160/YVR0-4898

Earth Resources Observation And Science (EROS) Center. (2017). Global Topographic 30 Arc-Second Hydrologic Digital Elevation Model 1 km [Tiff]. U.S. Geological Survey. https://doi.org/10.5066/F77P8WN0

Ehleringer, J. R., Hall, A. E., & Farquhar, G. D. (1993). Introduction: Water Use in Relation to Productivity. In Stable Isotopes and Plant Carbon-water Relations (pp. 3–8). Elsevier. https://doi.org/10.1016/B978-0-08-091801-3.50007-6

Eloundou, F. B., Strebel, L., Naz, B. S., Teran, C. P., Vereecken, H., & Franssen, H.-J. H. (2025). Disentangling Sources of Uncertainty in CLM5 Model Predictions: Water, Energy, and Carbon Fluxes at European Observation Sites. Preprints. https://doi.org/10.22541/essoar.174526373.38206874/v1

Entekhabi, D. (2023). Propagation in the Drought Cascade: Observational Analysis Over the Continental US. Water Resources Research, e2022WR032608. https://doi.org/10.1029/2022WR032608

Eshonkulov, R., Poyda, A., Ingwersen, J., Wizemann, H.-D., Weber, T. K. D., Kremer, P., Högy, P., Pulatov, A., & Streck, T. (2019). Evaluating multi-year, multi-site data on the energy balance closure of eddy-covariance flux measurements at cropland sites in southwestern Germany. Biogeosciences, 16(2), 521–540. https://doi.org/10.5194/bg-16-521-2019

Ester, M., Kriegel, H.-P., Sander, J., & Xu, X. (1996). A Density-Based Algorithm for Discovering Clusters in Large Spatial Databases with Noise. Proceedings of the 2nd International Conference on Knowledge Discovery and Data Mining, 226–231.

European Commission. Joint Research Centre. (2020). Global warming and drought impacts in the EU: JRC PESETA IV project : Task 7. Publications Office. https://data.europa.eu/doi/10.2760/597045

Farquhar, G. D., von Caemmerer, S., & Berry, J. A. (1980). A biochemical model of photosynthetic CO_2 assimilation in leaves of C_3 species. Planta, 149(1), 78–90. https://doi.org/10.1007/BF00386231

Fatichi, S., Or, D., Walko, R., Vereecken, H., Young, M. H., Ghezzehei, T. A., Hengl, T., Kollet, S., Agam, N., & Avissar, R. (2020). Soil structure is an important

omission in Earth System Models. Nature Communications, 11(1), 522. https://doi.org/10.1038/s41467-020-14411-z

Feng, K., Yan, Z., Li, Y., Wang, F., Zhang, Z., Su, X., Wu, H., Zhang, G., & Wang, Y. (2023). Spatio-temporal dynamic evaluation of agricultural drought based on a three-dimensional identification method in Northwest China. Agricultural Water Management, 284, 108325. https://doi.org/10.1016/j.agwat.2023.108325

Feng, X., Ackerly, D. D., Dawson, T. E., Manzoni, S., Skelton, R. P., Vico, G., & Thompson, S. E. (2018). The ecohydrological context of drought and classification of plant responses. Ecology Letters, 21(11), 1723–1736. https://doi.org/10.1111/ele.13139

Fernández-Martínez, M., Sardans, J., Chevallier, F., Ciais, P., Obersteiner, M., Vicca, S., Canadell, J. G., Bastos, A., Friedlingstein, P., Sitch, S., Piao, S. L., Janssens, I. A., & Peñuelas, J. (2019). Global trends in carbon sinks and their relationships with CO_2 and temperature. Nature Climate Change, 9(1), 73–79. https://doi.org/10.1038/s41558-018-0367-7

Feynman, R. P. (2011). The Feynman lectures on physics. Volume 1: Mainly mechanics, radiation, and heat (The new millennium edition, paperback first published). Basic Books.

Fisher, R. A., & Koven, C. D. (2020). Perspectives on the Future of Land Surface Models and the Challenges of Representing Complex Terrestrial Systems. Journal of Advances in Modeling Earth Systems, 12(4). https://doi.org/10.1029/2018MS001453

Fisher, R. A., Wieder, W. R., Sanderson, B. M., Koven, C. D., Oleson, K. W., Xu, C., Fisher, J. B., Shi, M., Walker, A. P., & Lawrence, D. M. (2019). Parametric Controls on Vegetation Responses to Biogeochemical Forcing in the CLM5. Journal of Advances in Modeling Earth Systems, 11(9), 2879–2895. https://doi.org/10.1029/2019MS001609

Folke, C., Kofinas, G. P., & Chapin, F. S. (Eds.). (2009). Principles of Ecosystem Stewardship: Resilience-Based Natural Resource Management in a Changing World. Springer New York. https://doi.org/10.1007/978-0-387-73033-2

Foote, E. (1856). Circumstances affecting the Heat of the Sun's Rays. The American Journal of Science and Arts, 72, 382–383.

Frank, D. C., Poulter, B., Saurer, M., Esper, J., Huntingford, C., Helle, G., Treydte, K., Zimmermann, N. E., Schleser, G. H., Ahlström, A., Ciais, P., Friedlingstein, P., Levis, S., Lomas, M., Sitch, S., Viovy, N., Andreu-Hayles, L., Bednarz, Z.,

Berninger, F., … Weigl, M. (2015). Water-use efficiency and transpiration across European forests during the Anthropocene. Nature Climate Change, 5(6), 579–583. https://doi.org/10.1038/nclimate2614

Franklin, O., Harrison, S. P., Dewar, R., Farrior, C. E., Brännström, Å., Dieckmann, U., Pietsch, S., Falster, D., Cramer, W., Loreau, M., Wang, H., Mäkelä, A., Rebel, K. T., Meron, E., Schymanski, S. J., Rovenskaya, E., Stocker, B. D., Zaehle, S., Manzoni, S., … Prentice, I. C. (2020). Organizing principles for vegetation dynamics. Nature Plants, 6(5), 444–453. https://doi.org/10.1038/s41477-020-0655-x

Friedlingstein, P., Jones, M. W., O'Sullivan, M., Andrew, R. M., Bakker, D. C. E., Hauck, J., Le Quéré, C., Peters, G. P., Peters, W., Pongratz, J., Sitch, S., Canadell, J. G., Ciais, P., Jackson, R. B., Alin, S. R., Anthoni, P., Bates, N. R., Becker, M., Bellouin, N., … Zeng, J. (2022). Global Carbon Budget 2021. Earth System Science Data, 14(4), 1917–2005. https://doi.org/10.5194/essd-14-1917-2022

Friedlingstein, P., O'Sullivan, M., Jones, M. W., Andrew, R. M., Bakker, D. C. E., Hauck, J., Landschützer, P., Le Quéré, C., Luijkx, I. T., Peters, G. P., Peters, W., Pongratz, J., Schwingshackl, C., Sitch, S., Canadell, J. G., Ciais, P., Jackson, R. B., Alin, S. R., Anthoni, P., … Zheng, B. (2023). Global Carbon Budget 2023. Earth System Science Data, 15(12), 5301–5369. https://doi.org/10.5194/essd-15-5301-2023

Fu, Z., Ciais, P., Makowski, D., Bastos, A., Stoy, P. C., Ibrom, A., Knohl, A., Migliavacca, M., Cuntz, M., Šigut, L., Peichl, M., Loustau, D., El-Madany, T. S., Buchmann, N., Gharun, M., Janssens, I., Markwitz, C., Grünwald, T., Rebmann, C., … Wigneron, J. (2021). Uncovering the critical soil moisture thresholds of plant water stress for European ecosystems. Global Change Biology, gcb.16050. https://doi.org/10.1111/gcb.16050

Fu, Z., Ciais, P., Prentice, I. C., Gentine, P., Makowski, D., Bastos, A., Luo, X., Green, J. K., Stoy, P. C., Yang, H., & Hajima, T. (2022). Atmospheric dryness reduces photosynthesis along a large range of soil water deficits. Nature Communications, 13(1), 989. https://doi.org/10.1038/s41467-022-28652-7

Fu, Z., Ciais, P., Wigneron, J.-P., Gentine, P., Feldman, A. F., Makowski, D., Viovy, N., Kemanian, A. R., Goll, D. S., Stoy, P. C., Prentice, I. C., Yakir, D., Liu, L., Ma, H., Li, X., Huang, Y., Yu, K., Zhu, P., Li, X., … Smith, W. K. (2024). Global critical soil moisture thresholds of plant water stress. Nature Communications, 15(1), 4826. https://doi.org/10.1038/s41467-024-49244-7

Futter, M. N., Dirnböck, T., Forsius, M., Bäck, J. K., Cools, N., Diaz-Pines, E., Dick, J., Gaube, V., Gillespie, L. M., Högbom, L., Laudon, H., Mirtl, M., Nikolaidis, N., Poppe Terán, C., Skiba, U., Vereecken, H., Villock, H., Weldon, J., Wohner, C., & Alam, S. A. (2023). Leveraging research infrastructure co-location to evaluate constraints on terrestrial carbon cycling in northern European forests. Ambio. https://doi.org/10.1007/s13280-023-01930-4

Giorgi, F., Jones, C., & Asrar, G. R. (2009). Addressing Climate Information Needs at the Regional Level: The CORDEX Framework. World Meteorological Organization Bulletin, 58(3), 175–183.

Gong, X. Y., Ma, W. T., Yu, Y. Z., Fang, K., Yang, Y., Tcherkez, G., & Adams, M. A. (2022). Overestimated gains in water-use efficiency by global forests. Global Change Biology, 28(16), 4923–4934. https://doi.org/10.1111/gcb.16221

Graf, A., Klosterhalfen, A., Arriga, N., Bernhofer, C., Bogena, H., Bornet, F., Brüggemann, N., Brümmer, C., Buchmann, N., Chi, J., Chipeaux, C., Cremonese, E., Cuntz, M., Dušek, J., El-Madany, T. S., Fares, S., Fischer, M., Foltýnová, L., Gharun, M., … Vereecken, H. (2020). Altered energy partitioning across terrestrial ecosystems in the European drought year 2018. Philosophical Transactions of the Royal Society B: Biological Sciences, 375(1810), 20190524. https://doi.org/10.1098/rstb.2019.0524

Graf, A., Wohlfahrt, G., Aranda-Barranco, S., Arriga, N., Brümmer, C., Ceschia, E., Ciais, P., Desai, A. R., Di Lonardo, S., Gharun, M., Grünwald, T., Hörtnagl, L., Kasak, K., Klosterhalfen, A., Knohl, A., Kowalska, N., Leuchner, M., Lindroth, A., Mauder, M., … Vereecken, H. (2023). Joint optimization of land carbon uptake and albedo can help achieve moderate instantaneous and long-term cooling effects. Communications Earth & Environment, 4(1), 298. https://doi.org/10.1038/s43247-023-00958-4

Green, C., & Byrne, K. A. (2004). Biomass: Impact on Carbon Cycle and Greenhouse Gas Emissions. In Encyclopedia of Energy (pp. 223–236). Elsevier. https://doi.org/10.1016/B0-12-176480-X/00418-6

Green, J. K., Zhang, Y., Luo, X., & Keenan, T. F. (2024). Systematic Underestimation of Canopy Conductance Sensitivity to Drought by Earth System Models. AGU Advances, 5(1), e2023AV001026. https://doi.org/10.1029/2023AV001026

Gu, C., Tang, Q., Zhu, G., Ma, J., Gu, C., Zhang, K., Sun, S., Yu, Q., & Niu, S. (2021). Discrepant responses between evapotranspiration- and transpiration-based ecosystem water use efficiency to interannual precipitation fluctuations.

Agricultural and Forest Meteorology, 303, 108385. https://doi.org/10.1016/j.agrformet.2021.108385

Guan, Y., Gu, X., Slater, L. J., Li, X., Li, J., Wang, L., Tang, X., Kong, D., & Zhang, X. (2024). Human-induced intensification of terrestrial water cycle in dry regions of the globe. Npj Climate and Atmospheric Science, 7(1), 45. https://doi.org/10.1038/s41612-024-00590-9

Guerrieri, R., Belmecheri, S., Ollinger, S. V., Asbjornsen, H., Jennings, K., Xiao, J., Stocker, B. D., Martin, M., Hollinger, D. Y., Bracho-Garrillo, R., Clark, K., Dore, S., Kolb, T., Munger, J. W., Novick, K., & Richardson, A. D. (2019). Disentangling the role of photosynthesis and stomatal conductance on rising forest water-use efficiency. Proceedings of the National Academy of Sciences, 116(34), 16909–16914. https://doi.org/10.1073/pnas.1905912116

Guo, T. (2022). Extreme Precipitation Strongly Impacts the Interaction of Skewness and Kurtosis of Annual Precipitation Distribution on the Qinghai–Tibetan Plateau. Atmosphere, 13(11), 1857. https://doi.org/10.3390/atmos13111857

Hähn, G. J. A., Damasceno, G., Alvarez-Davila, E., Aubin, I., Bauters, M., Bergmeier, E., Biurrun, I., Bjorkman, A. D., Bonari, G., Botta-Dukát, Z., Campos, J. A., Čarni, A., Chytrý, M., Ćušterevska, R., De Gasper, A. L., De Sanctis, M., Dengler, J., Dolezal, J., El-Sheikh, M. A., … Bruelheide, H. (2024). Global decoupling of functional and phylogenetic diversity in plant communities. Nature Ecology & Evolution. https://doi.org/10.1038/s41559-024-02589-0

Hammoudeh, S., Goergen, K., Belleflamme, A., Giles, J. A., Trömel, S., & Kollet, S. (2025). Evaluating precipitation products for water resources hydrologic modeling over Germany. Frontiers in Earth Science, 13, 1548557. https://doi.org/10.3389/feart.2025.1548557

Hansen, J., Ruedy, R., Sato, M., & Lo, K. (2010). GLOBAL SURFACE TEMPERATURE CHANGE. Reviews of Geophysics, 48(4), RG4004. https://doi.org/10.1029/2010RG000345

Harding, B., Tremblay, C., & Cousineau, D. (2014). Standard errors: A review and evaluation of standard error estimators using Monte Carlo simulations. The Quantitative Methods for Psychology, 10(2), 107–123. https://doi.org/10.20982/tqmp.10.2.p107

Harrison, S. P., Cramer, W., Franklin, O., Prentice, I. C., Wang, H., Brännström, Å., Boer, H., Dieckmann, U., Joshi, J., Keenan, T. F., Lavergne, A., Manzoni, S., Mengoli, G., Morfopoulos, C., Peñuelas, J., Pietsch, S., Rebel, K. T., Ryu, Y.,

Smith, N. G., … Wright, I. J. (2021). Eco-evolutionary optimality as a means to improve vegetation and land-surface models. New Phytologist, 231(6), 2125–2141. https://doi.org/10.1111/nph.17558

Hartick, C., Furusho-Percot, C., Clark, M. P., & Kollet, S. (2022). An Interannual Drought Feedback Loop Affects the Surface Energy Balance and Cloud Properties. Geophysical Research Letters, 49(22), e2022GL100924. https://doi.org/10.1029/2022GL100924

Hatfield, J. L., & Dold, C. (2019). Water-Use Efficiency: Advances and Challenges in a Changing Climate. Frontiers in Plant Science, 10, 103. https://doi.org/10.3389/fpls.2019.00103

Heiskanen, J., Brümmer, C., Buchmann, N., Calfapietra, C., Chen, H., Gielen, B., Gkritzalis, T., Hammer, S., Hartman, S., Herbst, M., Janssens, I. A., Jordan, A., Juurola, E., Karstens, U., Kasurinen, V., Kruijt, B., Lankreijer, H., Levin, I., Linderson, M.-L., … Kutsch, W. (2022). The Integrated Carbon Observation System in Europe. Bulletin of the American Meteorological Society, 103(3), E855–E872. https://doi.org/10.1175/BAMS-D-19-0364.1

Hengl, T., Mendes De Jesus, J., Heuvelink, G. B. M., Ruiperez Gonzalez, M., Kilibarda, M., Blagotić, A., Shangguan, W., Wright, M. N., Geng, X., Bauer-Marschallinger, B., Guevara, M. A., Vargas, R., MacMillan, R. A., Batjes, N. H., Leenaars, J. G. B., Ribeiro, E., Wheeler, I., Mantel, S., & Kempen, B. (2017). SoilGrids250m: Global gridded soil information based on machine learning. PLOS ONE, 12(2), e0169748. https://doi.org/10.1371/journal.pone.0169748

Hes, G., Vanderkelen, I., Fisher, R., Chave, J., Ogée, J., & L Davin, E. (2024). Projecting future forest microclimate using a land surface model. Environmental Research Letters, 19(2), 024030. https://doi.org/10.1088/1748-9326/ad1f04

Hoek Van Dijke, A. J., Herold, M., Mallick, K., Benedict, I., Machwitz, M., Schlerf, M., Pranindita, A., Theeuwen, J. J. E., Bastin, J.-F., & Teuling, A. J. (2022). Shifts in regional water availability due to global tree restoration. Nature Geoscience, 15(5), 363–368. https://doi.org/10.1038/s41561-022-00935-0

Huang, L., He, B., Han, L., Liu, J., Wang, H., & Chen, Z. (2017). A global examination of the response of ecosystem water-use efficiency to drought based on MODIS data. Science of The Total Environment, 601–602, 1097–1107. https://doi.org/10.1016/j.scitotenv.2017.05.084

Huang, M., Piao, S., Sun, Y., Ciais, P., Cheng, L., Mao, J., Poulter, B., Shi, X., Zeng, Z., & Wang, Y. (2015). Change in terrestrial ecosystem water-use efficiency

over the last three decades. Global Change Biology, 21(6), 2366–2378. https://doi.org/10.1111/gcb.12873

Huang, M., Piao, S., Zeng, Z., Peng, S., Ciais, P., Cheng, L., Mao, J., Poulter, B., Shi, X., Yao, Y., Yang, H., & Wang, Y. (2016). Seasonal responses of terrestrial ecosystem water-use efficiency to climate change. Global Change Biology, 22(6), 2165–2177. https://doi.org/10.1111/gcb.13180

Huang, M., Zhai, P., & Piao, S. (2021). Divergent responses of ecosystem water use efficiency to drought timing over Northern Eurasia. Environmental Research Letters, 16(4), 045016. https://doi.org/10.1088/1748-9326/abf0d1

Hurtt, G. C., Chini, L., Sahajpal, R., Frolking, S., Bodirsky, B. L., Calvin, K., Doelman, J. C., Fisk, J., Fujimori, S., Klein Goldewijk, K., Hasegawa, T., Havlik, P., Heinimann, A., Humpenöder, F., Jungclaus, J., Kaplan, J. O., Kennedy, J., Krisztin, T., Lawrence, D., … Zhang, X. (2020). Harmonization of global land use change and management for the period 850–2100 (LUH_2) for CMIP6. Geoscientific Model Development, 13(11), 5425–5464. https://doi.org/10.5194/gmd-13-5425-2020

Hussain, Md., & Mahmud, I. (2019). pyMannKendall: A python package for non parametric Mann Kendall family of trend tests. Journal of Open Source Software, 4(39), 1556. https://doi.org/10.21105/joss.01556

IGBP. (2000). Global Soil Data Task (IGBP-DIS, ISO-image of CD). PANGAEA. https://doi.org/10.1594/PANGAEA.869912

Ionita, M., Nagavciuc, V., Scholz, P., & Dima, M. (2022). Long-term drought intensification over Europe driven by the weakening trend of the Atlantic Meridional Overturning Circulation. Journal of Hydrology: Regional Studies, 42, 101176. https://doi.org/10.1016/j.ejrh.2022.101176

IPCC. (2023a). Climate Change 2021 – The Physical Science Basis: Working Group I Contribution to the Sixth Assessment Report of the Intergovernmental Panel on Climate Change (1st ed.). Cambridge University Press. https://doi.org/10.1017/9781009157896

IPCC (Ed.). (2023b). Climate Change 2022 - Mitigation of Climate Change: Working Group III Contribution to the Sixth Assessment Report of the Intergovernmental Panel on Climate Change (1st ed.). Cambridge University Press. https://doi.org/10.1017/9781009157926

Jafari, M., Tavili, A., Panahi, F., Zandi Esfahan, E., & Ghorbani, M. (2018). Reclamation of Arid Lands. Springer International Publishing. https://doi.org/10.1007/978-3-319-54828-9

Jiang, X., Rauscher, S. A., Ringler, T. D., Lawrence, D. M., Williams, A. P., Allen, C. D., Steiner, A. L., Cai, D. M., & McDowell, N. G. (2013). Projected Future Changes in Vegetation in Western North America in the Twenty-First Century. Journal of Climate, 26(11), 3671–3687. https://doi.org/10.1175/JCLI-D-12-00430.1

Jones, C. G., Adloff, F., Booth, B. B. B., Cox, P. M., Eyring, V., Friedlingstein, P., Frieler, K., Hewitt, H. T., Jeffery, H. A., Joussaume, S., Koenigk, T., Lawrence, B. N., O'Rourke, E., Roberts, M. J., Sanderson, B. M., Séférian, R., Somot, S., Vidale, P. L., Van Vuuren, D., … Zaehle, S. (2024). Bringing it all together: Science priorities for improved understanding of Earth system change and to support international climate policy. Earth System Dynamics, 15(5), 1319–1351. https://doi.org/10.5194/esd-15-1319-2024

Jones, M., Swenson, S. C., Sebestyen, S. D., Dymond, S., & Feng, X. (2023). Representing Peatland Heterogeneity in CLM5.0 Using Subgrid Hillslope Methods. 2023, H11G-1342. https://ui.adsabs.harvard.edu/abs/2023AGUFM.H11G1342J

Joshi, J., Stocker, B. D., Hofhansl, F., Zhou, S., Dieckmann, U., & Prentice, I. C. (2022). Towards a unified theory of plant photosynthesis and hydraulics. Nature Plants. https://doi.org/10.1038/s41477-022-01244-5

Jung, M., Reichstein, M., Ciais, P., Seneviratne, S. I., Sheffield, J., Goulden, M. L., Bonan, G., Cescatti, A., Chen, J., de Jeu, R., Dolman, A. J., Eugster, W., Gerten, D., Gianelle, D., Gobron, N., Heinke, J., Kimball, J., Law, B. E., Montagnani, L., … Zhang, K. (2010). Recent decline in the global land evapotranspiration trend due to limited moisture supply. Nature, 467(7318), 951–954. https://doi.org/10.1038/nature09396

Jung, M., Schwalm, C., Migliavacca, M., Walther, S., Camps-Valls, G., Koirala, S., Anthoni, P., Besnard, S., Bodesheim, P., Carvalhais, N., Chevallier, F., Gans, F., Goll, D. S., Haverd, V., Köhler, P., Ichii, K., Jain, A. K., Liu, J., Lombardozzi, D., … Reichstein, M. (2020). Scaling carbon fluxes from eddy covariance sites to globe: Synthesis and evaluation of the FLUXCOM approach. Biogeosciences, 17(5), 1343–1365. https://doi.org/10.5194/bg-17-1343-2020

Kanavi, M. S. P., Somu, G., Marappa, N., & Prakash, K. (2020). Studies on skewness and kurtosis of quantitative traits in green gram germplasm accessions

[Vigna radiata (L.)] under drought condition. Journal of Pharmacognosy and Phytochemistry, 9(2), 501–509.

Kattge, J., Díaz, S., Lavorel, S., Prentice, I. C., Leadley, P., Bönisch, G., Garnier, E., Westoby, M., Reich, P. B., Wright, I. J., Cornelissen, J. H. C., Violle, C., Harrison, S. P., Van Bodegom, P. M., Reichstein, M., Enquist, B. J., Soudzilovskaia, N. A., Ackerly, D. D., Anand, M., … Wirth, C. (2011). TRY - a global database of plant traits: TRY - A GLOBAL DATABASE OF PLANT TRAITS. Global Change Biology, 17(9), 2905–2935. https://doi.org/10.1111/j.1365-2486.2011.02451.x

Kautz, L.-A., Martius, O., Pfahl, S., Pinto, J. G., Ramos, A. M., Sousa, P. M., & Woollings, T. (2022). Atmospheric blocking and weather extremes over the Euro-Atlantic sector – a review. Weather and Climate Dynamics, 3(1), 305–336. https://doi.org/10.5194/wcd-3-305-2022

Keenan, T. F., Hollinger, D. Y., Bohrer, G., Dragoni, D., Munger, J. W., Schmid, H. P., & Richardson, A. D. (2013). Increase in forest water-use efficiency as atmospheric carbon dioxide concentrations rise. Nature, 499(7458), 324–327. https://doi.org/10.1038/nature12291

Keenan, T. F., & Williams, C. A. (2018). The Terrestrial Carbon Sink. Annual Review of Environment and Resources, 43(1), 219–243. https://doi.org/10.1146/annurev-environ-102017-030204

Keetz, L. T., Aalstad, K., Fisher, R. A., Teran, C. P., Naz, B. S., Pirk, N., Yilmaz, Y., & Skarpaas, O. (2024). Inferring parameters in a complex land surface model by combining data assimilation and machine learning. Preprints. https://doi.org/10.22541/essoar.172070530.05098424/v1

Keith, D. A., Ferrer-Paris, J. R., Nicholson, E., Bishop, M. J., Polidoro, B. A., Ramirez-Llodra, E., Tozer, M. G., Nel, J. L., Mac Nally, R., Gregr, E. J., Watermeyer, K. E., Essl, F., Faber-Langendoen, D., Franklin, J., Lehmann, C. E. R., Etter, A., Roux, D. J., Stark, J. S., Rowland, J. A., … Kingsford, R. T. (2022). A function-based typology for Earth's ecosystems. Nature. https://doi.org/10.1038/s41586-022-05318-4

Kennedy, D., Swenson, S., Oleson, K. W., Lawrence, D. M., Fisher, R., Lola Da Costa, A. C., & Gentine, P. (2019). Implementing Plant Hydraulics in the Community Land Model, Version 5. Journal of Advances in Modeling Earth Systems, 11(2), 485–513. https://doi.org/10.1029/2018MS001500

Kinzinger, L., Mach, J., Haberstroh, S., Schindler, Z., Frey, J., Dubbert, M., Seeger, S., Seifert, T., Weiler, M., Orlowski, N., & Werner, C. (2023). Interaction between Beech and Spruce trees in temperate forests affects water use, root water uptake pattern and canopy structure. Tree Physiology, tpad144. https://doi.org/10.1093/treephys/tpad144

Klimiuk, T., Ludwig, P., Sanchez-Benitez, A., Goessling, H. F., Braesicke, P., & Pinto, J. G. (2025). The European summer heatwave of 2019 – a regional storyline perspective. Earth System Dynamics, 16(1), 239–255. https://doi.org/10.5194/esd-16-239-2025

Knauer, J., Cuntz, M., Smith, B., Canadell, J. G., Medlyn, B. E., Bennett, A. C., Caldararu, S., & Haverd, V. (2023). Higher global gross primary productivity under future climate with more advanced representations of photosynthesis. Science Advances, 9(46), eadh9444. https://doi.org/10.1126/sciadv.adh9444

Konings, A. G., & Gentine, P. (2017). Global variations in ecosystem-scale isohydricity. Global Change Biology, 23(2), 891–905. https://doi.org/10.1111/gcb.13389

Krich, C., Mahecha, M. D., Migliavacca, M., De Kauwe, M. G., Griebel, A., Runge, J., & Miralles, D. G. (2022). Decoupling between ecosystem photosynthesis and transpiration: A last resort against overheating. Environmental Research Letters, 17(4), 044013. https://doi.org/10.1088/1748-9326/ac583e

Krich, C., Runge, J., Miralles, D. G., Migliavacca, M., Perez-Priego, O., El-Madany, T., Carrara, A., & Mahecha, M. D. (2020). Estimating causal networks in biosphere–atmosphere interaction with the PCMCI approach. Biogeosciences, 17(4), 1033–1061. https://doi.org/10.5194/bg-17-1033-2020

Kühn, N., Tovar, C., Carretero, J., Vandvik, V., Enquist, B. J., & Willis, K. J. (2021). Globally important plant functional traits for coping with climate change. Frontiers of Biogeography, 13(4), e53774. https://doi.org/10.21425/F5FBG53774

Kumar, S. V., M. Mocko, D., Wang, S., Peters-Lidard, C. D., & Borak, J. (2019). Assimilation of Remotely Sensed Leaf Area Index into the Noah-MP Land Surface Model: Impacts on Water and Carbon Fluxes and States over the Continental United States. Journal of Hydrometeorology, 20(7), 1359–1377. https://doi.org/10.1175/JHM-D-18-0237.1

Lacis, A. A., Schmidt, G. A., Rind, D., & Ruedy, R. A. (2010). Atmospheric CO_2: Principal Control Knob Governing Earth's Temperature. Science, 330(6002), 356–359. https://doi.org/10.1126/science.1190653

Landerer, F. W., & Swenson, S. C. (2012). Accuracy of scaled GRACE terrestrial water storage estimates. Water Resources Research, 48(4), 2011WR011453. https://doi.org/10.1029/2011WR011453

Lavergne, A., Graven, H., De Kauwe, M. G., Keenan, T. F., Medlyn, B. E., & Prentice, I. C. (2019). Observed and modelled historical trends in the water-use efficiency of plants and ecosystems. Global Change Biology, 25(7), 2242–2257. https://doi.org/10.1111/gcb.14634

Lawrence, D. M., Fisher, R. A., Koven, C. D., Oleson, K. W., Swenson, S. C., Bonan, G., Collier, N., Ghimire, B., Kampenhout, L., Kennedy, D., Kluzek, E., Lawrence, P. J., Li, F., Li, H., Lombardozzi, D., Riley, W. J., Sacks, W. J., Shi, M., Vertenstein, M., … Zeng, X. (2019). The Community Land Model Version 5: Description of New Features, Benchmarking, and Impact of Forcing Uncertainty. Journal of Advances in Modeling Earth Systems, 11(12), 4245–4287. https://doi.org/10.1029/2018MS001583

Lawrence, D. M., Fisher, R., Koven, C., Oleson, K., Swenson, S., Mariana Vertenstein, Ben Andre, Gordon Bonan, Bardan Ghimire, Leo van Kampenhout, Daniel Kennedy, Erik Kluzek, Ryan Knox, Peter Lawrence, Fang Li, Hongyi Li, Danica Lombardozzi, Yaqiong Lu, Justin Perket, … Xubin Zeng. (2018, February). CLM5 Documentation (Technical Note). NCAR. https://www2.cesm.ucar.edu/models/cesm2/land/CLM50_Tech_Note.pdf

Lawrence, P. J., & Chase, T. N. (2007). Representing a new MODIS consistent land surface in the Community Land Model (CLM 3.0). Journal of Geophysical Research, 112(G1), G01023. https://doi.org/10.1029/2006JG000168

Lehner, F., Coats, S., Stocker, T. F., Pendergrass, A. G., Sanderson, B. M., Raible, C. C., & Smerdon, J. E. (2017). Projected drought risk in 1.5°C and 2°C warmer climates. Geophysical Research Letters, 44(14), 7419–7428. https://doi.org/10.1002/2017GL074117

Li, L., Bisht, G., & Leung, L. R. (2022). Spatial heterogeneity effects on land surface modeling of water and energy partitioning. Geoscientific Model Development, 15(14), 5489–5510. https://doi.org/10.5194/gmd-15-5489-2022

Li, N., Xiao, J., Bai, R., Wang, J., Wu, L., Gao, W., Li, W., Chen, M., & Li, Q. (2023). Preseason sunshine duration determines the start of growing season of natural rubber forests. International Journal of Applied Earth Observation and Geoinformation, 124, 103513. https://doi.org/10.1016/j.jag.2023.103513

Li, W., Migliavacca, M., Forkel, M., Denissen, J. M. C., Reichstein, M., Yang, H., Duveiller, G., Weber, U., & Orth, R. (2022). Widespread increasing vegetation sensitivity to soil moisture. Nature Communications, 13(1), 3959. https://doi.org/10.1038/s41467-022-31667-9

Li, W., Pacheco-Labrador, J., Migliavacca, M., Miralles, D., Hoek Van Dijke, A., Reichstein, M., Forkel, M., Zhang, W., Frankenberg, C., Panwar, A., Zhang, Q., Weber, U., Gentine, P., & Orth, R. (2023). Widespread and complex drought effects on vegetation physiology inferred from space. Nature Communications, 14(1), 4640. https://doi.org/10.1038/s41467-023-40226-9

Li, X., Carrillo, C. M., Ault, T., Richardson, A. D., Friedl, M. A., & Frolking, S. (2024). Evaluation of Leaf Phenology of Different Vegetation Types From Local to Hemispheric Scale in CLM. Journal of Geophysical Research: Biogeosciences, 129(10), e2024JG008261. https://doi.org/10.1029/2024JG008261

Lian, X., Piao, S., Li, L. Z. X., Li, Y., Huntingford, C., Ciais, P., Cescatti, A., Janssens, I. A., Peñuelas, J., Buermann, W., Chen, A., Li, X., Myneni, R. B., Wang, X., Wang, Y., Yang, Y., Zeng, Z., Zhang, Y., & McVicar, T. R. (2020). Summer soil drying exacerbated by earlier spring greening of northern vegetation. Science Advances, 6(1), eaax0255. https://doi.org/10.1126/sciadv.aax0255

Liang, S., Cheng, J., Jia, K., Jiang, B., Liu, Q., Xiao, Z., Yao, Y., Yuan, W., Zhang, X., Zhao, X., & Zhou, J. (2021). The Global Land Surface Satellite (GLASS) Product Suite. Bulletin of the American Meteorological Society, 102(2), E323–E337. https://doi.org/10.1175/BAMS-D-18-0341.1

Liao, C., Lu, X., Huang, Y., Tao, F., Lawrence, D. M., Koven, C. D., Oleson, K. W., Wieder, W. R., Kluzek, E., Huang, X., & Luo, Y. (2023). Matrix Approach to Accelerate Spin-Up of CLM5. Journal of Advances in Modeling Earth Systems, 15(8), e2023MS003625. https://doi.org/10.1029/2023MS003625

Lin, Y.-S., Medlyn, B. E., Duursma, R. A., Prentice, I. C., Wang, H., Baig, S., Eamus, D., De Dios, V. R., Mitchell, P., Ellsworth, D. S., De Beeck, M. O., Wallin, G., Uddling, J., Tarvainen, L., Linderson, M.-L., Cernusak, L. A., Nippert, J. B., Ocheltree, T. W., Tissue, D. T., … Wingate, L. (2015). Optimal stomatal behaviour around the world. Nature Climate Change, 5(5), 459–464. https://doi.org/10.1038/nclimate2550

Liu, C., Sack, L., Li, Y., & He, N. (2022). Contrasting adaptation and optimization of stomatal traits across communities at continental scale. Journal of Experimental Botany, 73(18), 6405–6416. https://doi.org/10.1093/jxb/erac266

Liu, J., You, Y., Li, J., Sitch, S., Gu, X., Nabel, J. E. M. S., Lombardozzi, D., Luo, M., Feng, X., Arneth, A., Jain, A. K., Friedlingstein, P., Tian, H., Poulter, B., & Kong, D. (2021). Response of global land evapotranspiration to climate change, elevated CO_2, and land use change. Agricultural and Forest Meteorology, 311, 108663. https://doi.org/10.1016/j.agrformet.2021.108663

Liu, X., Feng, X., & Fu, B. (2020). Changes in global terrestrial ecosystem water use efficiency are closely related to soil moisture. Science of The Total Environment, 698, 134165. https://doi.org/10.1016/j.scitotenv.2019.134165

Liu, Y., Parolari, A. J., Kumar, M., Huang, C.-W., Katul, G. G., & Porporato, A. (2017). Increasing atmospheric humidity and CO_2 concentration alleviate forest mortality risk. Proceedings of the National Academy of Sciences, 114(37), 9918–9923. https://doi.org/10.1073/pnas.1704811114

Liu, Z., Ciais, P., Deng, Z., Davis, S. J., Zheng, B., Wang, Y., Cui, D., Zhu, B., Dou, X., Ke, P., Sun, T., Guo, R., Zhong, H., Boucher, O., Bréon, F.-M., Lu, C., Guo, R., Xue, J., Boucher, E., … Chevallier, F. (2020). Carbon Monitor, a near-real-time daily dataset of global CO_2 emission from fossil fuel and cement production. Scientific Data, 7(1), 392. https://doi.org/10.1038/s41597-020-00708-7

Liu, Z., Deng, Z., Davis, S. J., & Ciais, P. (2024). Global carbon emissions in 2023. Nature Reviews Earth & Environment. https://doi.org/10.1038/s43017-024-00532-2

Lloyd-Hughes, B. (2012). A spatio-temporal structure-based approach to drought characterisation. International Journal of Climatology, 32(3), 406–418. https://doi.org/10.1002/joc.2280

Lloyd-Hughes, B., & Saunders, M. A. (2002). A drought climatology for Europe. International Journal of Climatology, 22(13), 1571–1592. https://doi.org/10.1002/joc.846

Loaiciga, H. A., Valdes, J. B., Vogel, R., Garvey, J., & Schwarz, H. (1996). Global warming and the hydrologic cycle. Journal of Hydrology, 174(1–2), 83–127. https://doi.org/10.1016/0022-1694(95)02753-X

Lombardozzi, D. L., Bonan, G. B., Smith, N. G., Dukes, J. S., & Fisher, R. A. (2015). Temperature acclimation of photosynthesis and respiration: A key uncertainty in the carbon cycle-climate feedback. Geophysical Research Letters, 42(20), 8624–8631. https://doi.org/10.1002/2015gl065934

Longo, M., Knox, R. G., Medvigy, D. M., Levine, N. M., Dietze, M. C., Kim, Y., Swann, A. L. S., Zhang, K., Rollinson, C. R., Bras, R. L., Wofsy, S. C., & Moorcroft, P. R. (2019). The biophysics, ecology, and biogeochemistry of functionally diverse,

vertically and horizontally heterogeneous ecosystems: The Ecosystem Demography model, version 2.2 – Part 1: Model description. Geoscientific Model Development, 12(10), 4309–4346. https://doi.org/10.5194/gmd-12-4309-2019

Lu, Y., Steele-Dunne, S. C., & De Lannoy, G. J. M. (2020). Improving Soil Moisture and Surface Turbulent Heat Flux Estimates by Assimilation of SMAP Brightness Temperatures or Soil Moisture Retrievals and GOES Land Surface Temperature Retrievals. Journal of Hydrometeorology, 21(2), 183–203. https://doi.org/10.1175/JHM-D-19-0130.1

Ma, H., & Liang, S. (2022). Development of the GLASS 250-m leaf area index product (version 6) from MODIS data using the bidirectional LSTM deep learning model. Remote Sensing of Environment, 273, 112985. https://doi.org/10.1016/j.rse.2022.112985

Malle, J. T., Mazzotti, G., Karger, D. N., & Jonas, T. (2024). Regionally optimized high-resolution input datasets enhance the representation of snow cover in CLM5. Earth System Dynamics, 15(4), 1073–1115. https://doi.org/10.5194/esd-15-1073-2024

Manning, C., Widmann, M., Bevacqua, E., Van Loon, A. F., Maraun, D., & Vrac, M. (2019). Increased probability of compound long-duration dry and hot events in Europe during summer (1950–2013). Environmental Research Letters, 14(9), 094006. https://doi.org/10.1088/1748-9326/ab23bf

Marchand, W., Girardin, M. P., Hartmann, H., Depardieu, C., Isabel, N., Gauthier, S., Boucher, É., & Bergeron, Y. (2020). Strong overestimation of water -use efficiency responses to rising CO_2 in tree-ring studies. Global Change Biology, 26(8), 4538–4558. https://doi.org/10.1111/gcb.15166

Markonis, Y., Kumar, R., Hanel, M., Rakovec, O., Máca, P., & AghaKouchak, A. (2021). The rise of compound warm-season droughts in Europe. Science Advances, 7(6), eabb9668. https://doi.org/10.1126/sciadv.abb9668

Martens, B., Miralles, D. G., Lievens, H., van der Schalie, R., de Jeu, R. A. M., Fernández-Prieto, D., Beck, H. E., Dorigo, W. A., & Verhoest, N. E. C. (2017). GLEAM v3: Satellite-based land evaporation and root-zone soil moisture. Geoscientific Model Development, 10(5), 1903–1925. https://doi.org/10.5194/gmd-10-1903-2017

Martin, L., Smerald, A., Kiese, R., Klimiuk, T., Ludwig, P., Sanchéz-Benítez, A., Goessling, H., & Scheer, C. (2025). The vulnerability of European agricultural

areas to anthesis heat stress increases with climate change. Environmental Research: Food Systems, 2(2), 025002. https://doi.org/10.1088/2976-601X/adb03d

Martínez-de La Torre, A., & Miguez-Macho, G. (2019). Groundwater influence on soil moisture memory and land–atmosphere fluxes in the Iberian Peninsula. Hydrology and Earth System Sciences, 23(12), 4909–4932. https://doi.org/10.5194/hess-23-4909-2019

Mastrotheodoros, T., Pappas, C., Molnar, P., Burlando, P., Keenan, T. F., Gentine, P., Gough, C. M., & Fatichi, S. (2017). Linking plant functional trait plasticity and the large increase in forest water use efficiency. Journal of Geophysical Research: Biogeosciences, 122(9), 2393–2408. https://doi.org/10.1002/2017JG003890

Mathias, J. M., & Thomas, R. B. (2021). Global tree intrinsic water use efficiency is enhanced by increased atmospheric CO_2 and modulated by climate and plant functional types. Proceedings of the National Academy of Sciences, 118(7), e2014286118. https://doi.org/10.1073/pnas.2014286118

Maxwell, R. M., Condon, L. E., Kollet, S. J., Maher, K., Haggerty, R., & Forrester, M. M. (2016). The imprint of climate and geology on the residence times of groundwater. Geophysical Research Letters, 43(2), 701–708. https://doi.org/10.1002/2015GL066916

McColl, K. A., Roderick, M. L., Berg, A., & Scheff, J. (2022). The terrestrial water cycle in a warming world. Nature Climate Change, 12(7), 604–606. https://doi.org/10.1038/s41558-022-01412-7

McKee, T. B., Doesken, N. J., & Kleist, J. (1993). THE RELATIONSHIP OF DROUGHT FREQUENCY AND DURATION TO TIME SCALES. 8. https://doi.org/6

McKee, T. B., Doesken, N. J., & Kleist, J. (1995). Drought Monitoring with Multiple Time Scales. Applied Climatology, 233–236.

Medlyn, B. E., De Kauwe, M. G., Lin, Y., Knauer, J., Duursma, R. A., Williams, C. A., Arneth, A., Clement, R., Isaac, P., Limousin, J., Linderson, M., Meir, P., Martin-StPaul, N., & Wingate, L. (2017). How do leaf and ecosystem measures of water-use efficiency compare? New Phytologist, 216(3), 758–770. https://doi.org/10.1111/nph.14626

Medlyn, B. E., Duursma, R. A., Eamus, D., Ellsworth, D. S., Prentice, I. C., Barton, C. V. M., Crous, K. Y., De Angelis, P., Freeman, M., & Wingate, L. (2011). Reconciling the optimal and empirical approaches to modelling stomatal conductance: RECONCILING OPTIMAL AND EMPIRICAL STOMATAL

MODELS. Global Change Biology, 17(6), 2134–2144. https://doi.org/10.1111/j.1365-2486.2010.02375.x

Meinzer, F. C., Smith, D. D., Woodruff, D. R., Marias, D. E., McCulloh, K. A., Howard, A. R., & Magedman, A. L. (2017). Stomatal kinetics and photosynthetic gas exchange along a continuum of isohydric to anisohydric regulation of plant water status. Plant, Cell & Environment, 40(8), 1618–1628. https://doi.org/10.1111/pce.12970

Migliavacca, M., Musavi, T., Mahecha, M. D., Nelson, J. A., Knauer, J., Baldocchi, D. D., Perez-Priego, O., Christiansen, R., Peters, J., Anderson, K., Bahn, M., Black, T. A., Blanken, P. D., Bonal, D., Buchmann, N., Caldararu, S., Carrara, A., Carvalhais, N., Cescatti, A., … Reichstein, M. (2021). The three major axes of terrestrial ecosystem function. Nature. https://doi.org/10.1038/s41586-021-03939-9

Mirtl, M. (2010). Introducing the Next Generation of Ecosystem Research in Europe: LTER-Europe's Multi-Functional and Multi-Scale Approach. In Long-Term Ecological Research (pp. 75–93). Springer Netherlands. https://doi.org/10.1007/978-90-481-8782-9_6

Mirtl, M., Kuhn, I., Montheith, D., Bäck, J., Orenstein, D., Provenzale, A., Zacharias, S., Haase, P., & Shachak, M. (2021). Whole System Approach for in-situ research on Life Supporting Systems in the Anthropocene (WAILS) [Other]. pico. https://doi.org/10.5194/egusphere-egu21-16425

Mirtl, M., T. Borer, E., Djukic, I., Forsius, M., Haubold, H., Hugo, W., Jourdan, J., Lindenmayer, D., McDowell, W. H., Muraoka, H., Orenstein, D. E., Pauw, J. C., Peterseil, J., Shibata, H., Wohner, C., Yu, X., & Haase, P. (2018). Genesis, goals and achievements of Long-Term Ecological Research at the global scale: A critical review of ILTER and future directions. Science of The Total Environment, 626, 1439–1462. https://doi.org/10.1016/j.scitotenv.2017.12.001

Monin, A. S., & Obukhov, A. M. (1954). Basic laws of turbulent mixing in the surface layer of the atmosphere. Tr. Akad. Nauk SSSR Geophiz. Inst., 24(151), 163–187.

Moreno, M., Simioni, G., Cochard, H., Doussan, C., Guillemot, J., Decarsin, R., Fernandez-Conradi, P., Dupuy, J.-L., Trueba, S., Pimont, F., Ruffault, J., Jean, F., Marloie, O., & Martin-StPaul, N. K. (2024). Isohydricity and hydraulic isolation explain reduced hydraulic failure risk in an experimental tree species mixture. Plant Physiology, 195(4), 2668–2682. https://doi.org/10.1093/plphys/kiae239

Myneni, R., Knyazikhin, Y., & Park, T. (2015). MYD15A2H MODIS/Aqua Leaf Area Index/FPAR 8-Day L4 Global 500m SIN Grid V006 [Dataset]. NASA Land Processes Distributed Active Archive Center. https://doi.org/10.5067/MODIS/MYD15A2H.006

Naumann, G., Cammalleri, C., Mentaschi, L., & Feyen, L. (2021). Increased economic drought impacts in Europe with anthropogenic warming. Nature Climate Change, 11(6), 485–491. https://doi.org/10.1038/s41558-021-01044-3

Naz, B. S., Kao, S.-C., Ashfaq, M., Rastogi, D., Mei, R., & Bowling, L. C. (2016). Regional hydrologic response to climate change in the conterminous United States using high-resolution hydroclimate simulations. Global and Planetary Change, 143, 100–117. https://doi.org/10.1016/j.gloplacha.2016.06.003

Naz, B. S., Kollet, S., Franssen, H.-J. H., Montzka, C., & Kurtz, W. (2020). A 3 km spatially and temporally consistent European daily soil moisture reanalysis from 2000 to 2015. Scientific Data, 7(1), 111. https://doi.org/10.1038/s41597-020-0450-6

Naz, B. S., Kurtz, W., Montzka, C., Sharples, W., Goergen, K., Keune, J., Gao, H., Springer, A., Hendricks Franssen, H.-J., & Kollet, S. (2019). Improving soil moisture and runoff simulations at 3 km over Europe using land surface data assimilation. Hydrology and Earth System Sciences, 23(1), 277–301. https://doi.org/10.5194/hess-23-277-2019

Nelson, J. A., Pérez-Priego, O., Zhou, S., Poyatos, R., Zhang, Y., Blanken, P. D., Gimeno, T. E., Wohlfahrt, G., Desai, A. R., Gioli, B., Limousin, J., Bonal, D., Paul-Limoges, E., Scott, R. L., Varlagin, A., Fuchs, K., Montagnani, L., Wolf, S., Delpierre, N., … Jung, M. (2020). Ecosystem transpiration and evaporation: Insights from three water flux partitioning methods across FLUXNET sites. Global Change Biology, 26(12), 6916–6930. https://doi.org/10.1111/gcb.15314

Niu, G., Yang, Z., Dickinson, R. E., & Gulden, L. E. (2005). A simple TOPMODEL-based runoff parameterization (SIMTOP) for use in global climate models. Journal of Geophysical Research: Atmospheres, 110(D21), 2005JD006111. https://doi.org/10.1029/2005JD006111

Novick, K. A., Ficklin, D. L., Stoy, P. C., Williams, C. A., Bohrer, G., Oishi, A. C., Papuga, S. A., Blanken, P. D., Noormets, A., Sulman, B. N., Scott, R. L., Wang, L., & Phillips, R. P. (2016). The increasing importance of atmospheric demand for ecosystem water and carbon fluxes. Nature Climate Change, 6(11), 1023–1027. https://doi.org/10.1038/nclimate3114

Novick, K. A., Konings, A. G., & Gentine, P. (2019). Beyond soil water potential: An expanded view on isohydricity including land–atmosphere interactions and phenology. Plant, Cell & Environment, 42(6), 1802–1815. https://doi.org/10.1111/pce.13517

Ohnemus, T., Dirnböck, T., Bäck, J., Gaube, V., Kühn, I., Mirtl, M., Mollenhauer, H., Vereecken, H., & Zacharias, S. (2025). Fitness for future: eLTER RI's representation of climate and land use change. Ecological Indicators, 171, 113159. https://doi.org/10.1016/j.ecolind.2025.113159

Ohnemus, T., Zacharias, S., Dirnböck, T., Bäck, J., Brack, W., Forsius, M., Mallast, U., Nikolaidis, N. P., Peterseil, J., Piscart, C., Pando, F., Poppe Terán, C., & Mirtl, M. (2024). The eLTER research infrastructure: Current design and coverage of environmental and socio-ecological gradients. Environmental and Sustainability Indicators, 23, 100456. https://doi.org/10.1016/j.indic.2024.100456

Oki, T., & Kanae, S. (2006). Global Hydrological Cycles and World Water Resources. Science, 313(5790), 1068–1072. https://doi.org/10.1126/science.1128845

Oloruntoba, B., Kollet, S., Montzka, C., Vereecken, H., & Hendricks Franssen, H.-J. (2025). High-resolution land surface modelling over Africa: The role of uncertain soil properties in combination with forcing temporal resolution. Hydrology and Earth System Sciences, 29(6), 1659–1683. https://doi.org/10.5194/hess-29-1659-2025

Pastorello, G., Trotta, C., Canfora, E., Chu, H., Christianson, D., Cheah, Y.-W., Poindexter, C., Chen, J., Elbashandy, A., Humphrey, M., Isaac, P., Polidori, D., Reichstein, M., Ribeca, A., van Ingen, C., Vuichard, N., Zhang, L., Amiro, B., Ammann, C., … Papale, D. (2020). The FLUXNET2015 dataset and the ONEFlux processing pipeline for eddy covariance data. Scientific Data, 7(1), 225. https://doi.org/10.1038/s41597-020-0534-3

Pei, W., Hao, L., Fu, Q., Ren, Y., & Li, T. (2023). Study on Agricultural Drought Risk Assessment Based on Information Entropy and a Cluster Projection Pursuit Model. Water Resources Management, 37(2), 619–638. https://doi.org/10.1007/s11269-022-03391-y

Peng, J., Tang, J., Xie, S., Wang, Y., Liao, J., Chen, C., Sun, C., Mao, J., Zhou, Q., & Niu, S. (2024). Evidence for the acclimation of ecosystem photosynthesis to soil moisture. Nature Communications, 15(1), 9795. https://doi.org/10.1038/s41467-024-54156-7

Peñuelas, J., Canadell, J. G., & Ogaya, R. (2011). Increased water-use efficiency during the 20th century did not translate into enhanced tree growth: Tree growth in the 20th century. Global Ecology and Biogeography, 20(4), 597–608. https://doi.org/10.1111/j.1466-8238.2010.00608.x

Penuelas, J., Fernández-Martínez, M., Vallicrosa, H., Maspons, J., Zuccarini, P., Carnicer, J., Sanders, T. G. M., Krüger, I., Obersteiner, M., Janssens, I. A., Ciais, P., & Sardans, J. (2020). Increasing atmospheric CO_2 concentrations correlate with declining nutritional status of European forests. Communications Biology, 3(1), 125. https://doi.org/10.1038/s42003-020-0839-y

Peters, W., Velde, I. R. van der, Schaik, E. van, Miller, J. B., Ciais, P., Duarte, H. F., Laan-Luijkx, I. T. van der, Molen, M. K. van der, Scholze, M., Schaefer, K., Vidale, P. L., Verhoef, A., W\aarlind, D., Zhu, D., Tans, P. P., Vaughn, B., & White, J. W. C. (2018). Increased water-use efficiency and reduced CO_2 uptake by plants during droughts at a continental scale. Nature Geoscience, 11(10), 744–748. https://doi.org/10.1038/s41561-018-0212-7

Pilli, R., Grassi, G., Kurz, W. A., Fiorese, G., & Cescatti, A. (2017). The European forest sector: Past and future carbon budget and fluxes under different management scenarios. Biogeosciences, 14(9), 2387–2405. https://doi.org/10.5194/bg-14-2387-2017

Poppe Terán, C., Naz, B. S., Graf, A., Qu, Y., Hendricks Franssen, H.-J., Baatz, R., Ciais, P., & Vereecken, H. (2023). Rising water-use efficiency in European grasslands is driven by increased primary production. Communications Earth & Environment, 4(1), 95. https://doi.org/10.1038/s43247-023-00757-x

Poppe Terán, C., Naz, B. S., Vereecken, H., Baatz, R., Fisher, R. A., & Hendricks Franssen, H.-J. (2025). Systematic underestimation of type-specific ecosystem process variability in the Community Land Model v5 over Europe. Geoscientific Model Development, 18(2), 287–317. https://doi.org/10.5194/gmd-18-287-2025

Poppe Terán, C., Naz, B., Strebel, L., Belleflamme, A., Hendricks-Franssen, H.-J., & Vereecken, H. (2025). eLTER PLUS Deliverable D9.3—A report detailing the pan-European continental scale terrestrial ecosystem model. https://doi.org/10.5281/ZENODO.14898628

Post, H., Hendricks Franssen, H.-J., Han, X., Baatz, R., Montzka, C., Schmidt, M., & Vereecken, H. (2018). Evaluation and uncertainty analysis of regional-scale CLM4.5 net carbon flux estimates. Biogeosciences, 15(1), 187–208. https://doi.org/10.5194/bg-15-187-2018

Povey, A. C., & Grainger, R. G. (2015). Known and unknown unknowns: Uncertainty estimation in satellite remote sensing. Atmospheric Measurement Techniques, 8(11), 4699–4718. https://doi.org/10.5194/amt-8-4699-2015

Poyatos, R., Granda, V., Flo, V., Molowny-Horas, R., Steppe, K., Mencuccini, M., & Martínez-Vilalta, J. (2020). SAPFLUXNET: A global database of sap flow measurements (Version 0.1.5) [Dataset]. Zenodo. https://doi.org/10.5281/ZENODO.3971689

Prein, A. F., Gobiet, A., Truhetz, H., Keuler, K., Goergen, K., Teichmann, C., Fox Maule, C., van Meijgaard, E., Déqué, M., Nikulin, G., Vautard, R., Colette, A., Kjellström, E., & Jacob, D. (2016). Precipitation in the EURO-CORDEX $ $0.11^{\circ }$$ 0 . 11 ∘ and $$0.44^{\circ }$$ 0 . 44 ∘ simulations: High resolution, high benefits? Climate Dynamics, 46(1–2), 383–412. https://doi.org/10.1007/s00382-015-2589-y

Rahmati, M., Graf, A., Poppe Terán, C., Amelung, W., Dorigo, W., Franssen, H.-J. H., Montzka, C., Or, D., Sprenger, M., Vanderborght, J., Verhoest, N. E. C., & Vereecken, H. (2023). Continuous increase in evaporative demand shortened the growing season of European ecosystems in the last decade. Communications Earth & Environment, 4(1), 236. https://doi.org/10.1038/s43247-023-00890-7

Rakovec, O., Samaniego, L., Hari, V., Markonis, Y., Moravec, V., Thober, S., Hanel, M., & Kumar, R. (2022). The 2018–2020 Multi-Year Drought Sets a New Benchmark in Europe. Earth's Future, 10(3), e2021EF002394. https://doi.org/10.1029/2021EF002394

Reich, P. B. (2010). The Carbon Dioxide Exchange. Science, 329(5993), 774–775. https://doi.org/10.1126/science.1194353

Reichstein, M., Stoy, P. C., Desai, A. R., Lasslop, G., & Richardson, A. D. (2012). Partitioning of Net Fluxes. In M. Aubinet, T. Vesala, & D. Papale (Eds.), Eddy Covariance (pp. 263–289). Springer Netherlands. https://doi.org/10.1007/978-94-007-2351-1_9

Richards, L. A. (1931). CAPILLARY CONDUCTION OF LIQUIDS THROUGH POROUS MEDIUMS. Physics, 1(5), 318–333. https://doi.org/10.1063/1.1745010

Rohde, M. M., Stella, J. C., Singer, M. B., Roberts, D. A., Caylor, K. K., & Albano, C. M. (2024). Establishing ecological thresholds and targets for groundwater management. Nature Water. https://doi.org/10.1038/s44221-024-00221-w

Rousi, E., Kornhuber, K., Beobide-Arsuaga, G., Luo, F., & Coumou, D. (2022). Accelerated western European heatwave trends linked to more-persistent double

jets over Eurasia. Nature Communications, 13(1), 3851. https://doi.org/10.1038/s41467-022-31432-y

Runge, J. (2020). Discovering contemporaneous and lagged causal relations in autocorrelated nonlinear time series datasets. Proceedings of the 36th Conference on Uncertainty in Artificial Intelligence. UAI 2020, Toronto. http://auai.org/uai2020/proceedings/579_main_paper.pdf

Runge, J., Bathiany, S., Bollt, E., Camps-Valls, G., Coumou, D., Deyle, E., Glymour, C., Kretschmer, M., Mahecha, M. D., Muñoz-Marí, J., van Nes, E. H., Peters, J., Quax, R., Reichstein, M., Scheffer, M., Schölkopf, B., Spirtes, P., Sugihara, G., Sun, J., … Zscheischler, J. (2019). Inferring causation from time series in Earth system sciences. Nature Communications, 10(1), 2553. https://doi.org/10.1038/s41467-019-10105-3

Rusca, M., Savelli, E., Di Baldassarre, G., Biza, A., & Messori, G. (2022). Unprecedented droughts are expected to exacerbate urban inequalities in Southern Africa. Nature Climate Change. https://doi.org/10.1038/s41558-022-01546-8

Sade, N., Gebremedhin, A., & Moshelion, M. (2012). Risk-taking plants: Anisohydric behavior as a stress-resistance trait. Plant Signaling & Behavior, 7(7), 767–770. https://doi.org/10.4161/psb.20505

Samaniego, L., Thober, S., Kumar, R., Wanders, N., Rakovec, O., Pan, M., Zink, M., Sheffield, J., Wood, E. F., & Marx, A. (2018). Anthropogenic warming exacerbates European soil moisture droughts. Nature Climate Change, 8(5), 421–426. https://doi.org/10.1038/s41558-018-0138-5

Schröter, M., Bonn, A., Klotz, S., Seppelt, R., & Baessler, C. (Eds.). (2019). Atlas of Ecosystem Services: Drivers, Risks, and Societal Responses. Springer International Publishing. https://doi.org/10.1007/978-3-319-96229-0

Schuldt, B., Buras, A., Arend, M., Vitasse, Y., Beierkuhnlein, C., Damm, A., Gharun, M., Grams, T. E. E., Hauck, M., Hajek, P., Hartmann, H., Hiltbrunner, E., Hoch, G., Holloway-Phillips, M., Körner, C., Larysch, E., Lübbe, T., Nelson, D. B., Rammig, A., … Kahmen, A. (2020). A first assessment of the impact of the extreme 2018 summer drought on Central European forests. Basic and Applied Ecology, 45, 86–103. https://doi.org/10.1016/j.baae.2020.04.003

Scott, D. W. (1992). Multivariate Density Estimation: Theory, Practice, and Visualization (1st ed.). Wiley. https://doi.org/10.1002/9780470316849

Sellers, P. J. (1985). Canopy reflectance, photosynthesis and transpiration. International Journal of Remote Sensing, 6(8), 1335–1372. https://doi.org/10.1080/01431168508948283

Sevanto, S., Mcdowell, N. G., Dickman, L. T., Pangle, R., & Pockman, W. T. (2014). How do trees die? A test of the hydraulic failure and carbon starvation hypotheses. Plant, Cell & Environment, 37(1), 153–161. https://doi.org/10.1111/pce.12141

Short Gianotti, D. J., McColl, K. A., Feldman, A. F., Xu, X., & Entekhabi, D. (2024). Two sub-annual timescales and coupling modes for terrestrial water and carbon cycles. Global Change Biology, 30(8), e17463. https://doi.org/10.1111/gcb.17463

Sitch, S., Friedlingstein, P., Gruber, N., Jones, S. D., Murray-Tortarolo, G., Ahlström, A., Doney, S. C., Graven, H., Heinze, C., Huntingford, C., Levis, S., Levy, P. E., Lomas, M., Poulter, B., Viovy, N., Zaehle, S., Zeng, N., Arneth, A., Bonan, G., … Myneni, R. (2015). Recent trends and drivers of regional sources and sinks of carbon dioxide. Biogeosciences, 12(3), 653–679. https://doi.org/10.5194/bg-12-653-2015

Slette, I. J., Post, A. K., Awad, M., Even, T., Punzalan, A., Williams, S., Smith, M. D., & Knapp, A. K. (2019). How ecologists define drought, and why we should do better. Global Change Biology, 25(10), 3193–3200. https://doi.org/10.1111/gcb.14747

Smith, N. E., Kooijmans, L. M. J., Koren, G., van Schaik, E., van der Woude, A. M., Wanders, N., Ramonet, M., Xueref-Remy, I., Siebicke, L., Manca, G., Brümmer, C., Baker, I. T., Haynes, K. D., Luijkx, I. T., & Peters, W. (2020). Spring enhancement and summer reduction in carbon uptake during the 2018 drought in northwestern Europe. Philosophical Transactions of the Royal Society B: Biological Sciences, 375(1810), 20190509. https://doi.org/10.1098/rstb.2019.0509

Solomon, A. M., & Shugart, H. H. (Eds.). (1993). Vegetation dynamics & global change. Chapman & Hall ; IIASA].

Song, J., Miller, G. R., Cahill, A. T., Aparecido, L. M. T., & Moore, G. W. (2020). Modeling land surface processes over a mountainous rainforest in Costa Rica using CLM4.5 and CLM5. Geoscientific Model Development, 13(11), 5147–5173. https://doi.org/10.5194/gmd-13-5147-2020

Stocker, B. D., Tumber-Dávila, S. J., Konings, A. G., Anderson, M. C., Hain, C., & Jackson, R. B. (2023). Global patterns of water storage in the rooting zones of vegetation. Nature Geoscience, 16(3), 250–256. https://doi.org/10.1038/s41561-023-01125-2

Strebel, L., Bogena, H. R., Vereecken, H., & Hendricks Franssen, H.-J. (2022). Coupling the Community Land Model version 5.0 to the parallel data assimilation framework PDAF: Description and applications. Geoscientific Model Development, 15(2), 395–411. https://doi.org/10.5194/gmd-15-395-2022

Strebel, L., Bogena, H., Vereecken, H., Andreasen, M., Aranda, S., & Hendricks Franssen, H.-J. (2023). Evapotranspiration prediction for European forest sites does not improve with assimilation of in-situ soil water content data [Preprint]. Vadose Zone Hydrology/Modelling approaches. https://doi.org/10.5194/egusphere-2023-366

Suarez-Gutierrez, L., Müller, W. A., & Marotzke, J. (2023). Extreme heat and drought typical of an end-of-century climate could occur over Europe soon and repeatedly. Communications Earth & Environment, 4(1), 415. https://doi.org/10.1038/s43247-023-01075-y

Sun, Y., Goll, D. S., Huang, Y., Ciais, P., Wang, Y., Bastrikov, V., & Wang, Y. (2023). Machine learning for accelerating process-based computation of land biogeochemical cycles. Global Change Biology, 29(11), 3221–3234. https://doi.org/10.1111/gcb.16623

Swenson, S. C., Clark, M., Fan, Y., Lawrence, D. M., & Perket, J. (2019). Representing Intrahillslope Lateral Subsurface Flow in the Community Land Model. Journal of Advances in Modeling Earth Systems, 11(12), 4044–4065. https://doi.org/10.1029/2019MS001833

Tallaksen, L. M., & Lanen, H. A. J. van (Eds.). (2024). Hydrological drought: Processes and estimation methods for streamflow and groundwater (Second ed). Elsevier.

Tang, X., Li, H., Desai, A. R., Nagy, Z., Luo, J., Kolb, T. E., Olioso, A., Xu, X., Yao, L., Kutsch, W., Pilegaard, K., Köstner, B., & Ammann, C. (2015). How is water-use efficiency of terrestrial ecosystems distributed and changing on Earth? Scientific Reports, 4(1), 7483. https://doi.org/10.1038/srep07483

Terrer, C., Phillips, R. P., Hungate, B. A., Rosende, J., Pett-Ridge, J., Craig, M. E., van Groenigen, K. J., Keenan, T. F., Sulman, B. N., Stocker, B. D., Reich, P. B., Pellegrini, A. F. A., Pendall, E., Zhang, H., Evans, R. D., Carrillo, Y., Fisher, J. B., Van Sundert, K., Vicca, S., & Jackson, R. B. (2021). A trade-off between plant and soil carbon storage under elevated CO_2. Nature, 591(7851), 599–603. https://doi.org/10.1038/s41586-021-03306-8

Teuling, A. J., Seneviratne, S. I., Stöckli, R., Reichstein, M., Moors, E., Ciais, P., Luyssaert, S., Van Den Hurk, B., Ammann, C., Bernhofer, C., Dellwik, E., Gianelle, D., Gielen, B., Grünwald, T., Klumpp, K., Montagnani, L., Moureaux, C., Sottocornola, M., & Wohlfahrt, G. (2010). Contrasting response of European forest and grassland energy exchange to heatwaves. Nature Geoscience, 3(10), 722–727. https://doi.org/10.1038/ngeo950

Thompson, R. L., Broquet, G., Gerbig, C., Koch, T., Lang, M., Monteil, G., Munassar, S., Nickless, A., Scholze, M., Ramonet, M., Karstens, U., Schaik, E. van, Wu, Z., & Rödenbeck, C. (2020). Changes in net ecosystem exchange over Europe during the 2018 drought based on atmospheric observations. Philosophical Transactions of the Royal Society B: Biological Sciences, 375(1810), 20190512. https://doi.org/10.1098/rstb.2019.0512

Trenberth, K. E., Fasullo, J. T., & Kiehl, J. (2009). Earth's Global Energy Budget. Bulletin of the American Meteorological Society, 90(3), 311–324. https://doi.org/10.1175/2008BAMS2634.1

Tyndall, J. (1873). Heat, considered as a mode of motion. Appleton.

Ukkola, A. M., De Kauwe, M. G., Pitman, A. J., Best, M. J., Abramowitz, G., Haverd, V., Decker, M., & Haughton, N. (2016). Land surface models systematically overestimate the intensity, duration and magnitude of seasonal-scale evaporative droughts. Environmental Research Letters, 11(10), 104012. https://doi.org/10.1088/1748-9326/11/10/104012

Umair, M., Kim, D., & Choi, M. (2020). Impact of climate, rising atmospheric carbon dioxide, and other environmental factors on water-use efficiency at multiple land cover types. Scientific Reports, 10(1), 11644. https://doi.org/10.1038/s41598-020-68472-7

Van Bodegom, P. M., Douma, J. C., & Verheijen, L. M. (2014). A fully traits-based approach to modeling global vegetation distribution. Proceedings of the National Academy of Sciences, 111(38), 13733–13738. https://doi.org/10.1073/pnas.1304551110

Van Bodegom, P. M., Douma, J. C., Witte, J. P. M., Ordoñez, J. C., Bartholomeus, R. P., & Aerts, R. (2012). Going beyond limitations of plant functional types when predicting global ecosystem-atmosphere fluxes: Exploring the merits of traits-based approaches: Merits of traits-based vegetation modelling. Global Ecology and Biogeography, 21(6), 625–636. https://doi.org/10.1111/j.1466-8238.2011.00717.x

Van Der Woude, A. M., Peters, W., Joetzjer, E., Lafont, S., Koren, G., Ciais, P., Ramonet, M., Xu, Y., Bastos, A., Botía, S., Sitch, S., De Kok, R., Kneuer, T.,

Kubistin, D., Jacotot, A., Loubet, B., Herig-Coimbra, P.-H., Loustau, D., & Luijkx, I. T. (2023). Temperature extremes of 2022 reduced carbon uptake by forests in Europe. Nature Communications, 14(1), 6218. https://doi.org/10.1038/s41467-023-41851-0

Vautard, R., Cattiaux, J., Happé, T., Singh, J., Bonnet, R., Cassou, C., Coumou, D., D'Andrea, F., Faranda, D., Fischer, E., Ribes, A., Sippel, S., & Yiou, P. (2023). Heat extremes in Western Europe increasing faster than simulated due to atmospheric circulation trends. Nature Communications, 14(1), 6803. https://doi.org/10.1038/s41467-023-42143-3

Verdin, K. L., & Greenlee, S. K. (1996). Development of continental scale digital elevation models and extraction of hydrographic features. Third International Conference/Workshop on Integrating GIS and Environmental Modeling, Santa Fe, New Mexico.

Vicente-Serrano, S. M., Domínguez-Castro, F., Beguería, S., El Kenawy, A., Gimeno-Sotelo, L., Franquesa, M., Azorin-Molina, C., Andres-Martin, M., & Halifa-Marín, A. (2025). Atmospheric drought indices in future projections. Nature Water. https://doi.org/10.1038/s44221-025-00416-9

Wahl, S., Bollmeyer, C., Crewell, S., Figura, C., Friederichs, P., Hense, A., Keller, J. D., & Ohlwein, C. (2017). A novel convective-scale regional reanalysis COSMO-REA2: Improving the representation of precipitation. Meteorologische Zeitschrift, 26(4), 345–361. https://doi.org/10.1127/metz/2017/0824

Wanders, N., & Wada, Y. (2015). Human and climate impacts on the 21st century hydrological drought. Journal of Hydrology, 526, 208–220. https://doi.org/10.1016/j.jhydrol.2014.10.047

Wang, F., Zhang, J., Fonti, P., Sun, Q., Wang, Y., Zhang, F., Wang, Y., Yang, J., & Gou, X. (2024). Effects of site aridity and species on stand transpiration in high-elevation dryland ecosystems. Journal of Hydrology, 630, 130662. https://doi.org/10.1016/j.jhydrol.2024.130662

Wang, G., Gertner, G. Z., Fang, S., & Anderson, A. B. (2005). A Methodology for Spatial Uncertainty Analysis Of Remote Sensing and GIS Products. Photogrammetric Engineering & Remote Sensing, 71(12), 1423–1432. https://doi.org/10.14358/PERS.71.12.1423

Wang, M., Chen, Y., Wu, X., & Bai, Y. (2018). Forest-Type-Dependent Water Use Efficiency Trends Across the Northern Hemisphere. Geophysical Research Letters, 45(16), 8283–8293. https://doi.org/10.1029/2018GL079093

Wang, M., Ding, Z., Wu, C., Song, L., Ma, M., Yu, P., Lu, B., & Tang, X. (2021). Divergent responses of ecosystem water-use efficiency to extreme seasonal droughts in Southwest China. Science of The Total Environment, 760, 143427. https://doi.org/10.1016/j.scitotenv.2020.143427

Warm Winter 2020 Team & ICOS Ecosystem Thematic Centre. (2022). Warm Winter 2020 ecosystem eddy covariance flux product for 73 stations in FLUXNET-Archive format—Release 2022-1 (Version 1.0) [Collection of FLUXNET product ZIP archives]. ICOS Carbon Portal. https://doi.org/10.18160/2G60-ZHAK

Weng, Z., Niu, J., Guan, H., & Kang, S. (2023). Three-dimensional linkage between meteorological drought and vegetation drought across China. Science of The Total Environment, 859, 160300. https://doi.org/10.1016/j.scitotenv.2022.160300

Whitcraft, A. K., Becker-Reshef, I., & Justice, C. O. (2015). Agricultural growing season calendars derived from MODIS surface reflectance. International Journal of Digital Earth, 8(3), 173–197. https://doi.org/10.1080/17538947.2014.894147

Whitmarsh, J. & Govindjee. (1999). The Photosynthetic Process. In G. S. Singhal, G. Renger, S. K. Sopory, K.-D. Irrgang, & Govindjee (Eds.), Concepts in Photobiology (pp. 11–51). Springer Netherlands. https://doi.org/10.1007/978-94-011-4832-0_2

Winkler, K., Yang, H., Ganzenmüller, R., Fuchs, R., Ceccherini, G., Duveiller, G., Grassi, G., Pongratz, J., Bastos, A., Shvidenko, A., Araza, A., Herold, M., Wigneron, J.-P., & Ciais, P. (2023). Changes in land use and management led to a decline in Eastern Europe's terrestrial carbon sink. Communications Earth & Environment, 4(1), 237. https://doi.org/10.1038/s43247-023-00893-4

WMO. (1989). Calculation of Monthly and Annual 30-year standard normals. In CALCULATION OF MONTHLY AND ANNUAL 30-YEAR STANDARD NORMALS.

WMO. (2015). Seventeenth World Meteorological Congress: Abridged final report with resolutions : Geneva, 25 May-12 June 2015. World Meteorological Organization. https://library.wmo.int/idurl/4/54771

WMO. (2021). WMO ATLAS OF MORTALITY AND ECONOMIC LOSSES FROM WEATHER, CLIMATE AND WATER EXTREMES (No. 1267). https://library.wmo.int/records/item/57564-wmo-atlas-of-mortality-and-economic-losses-from-weather-climate-and-water-extremes-1970-2019

WMO. (2025, January 10). WMO confirms 2024 as warmest year on record at about 1.55°C above pre-industrial level. World Meteorological Organization.

https://wmo.int/news/media-centre/wmo-confirms-2024-warmest-year-record-about-155degc-above-pre-industrial-level

Wohlfahrt, G., & Gu, L. (2015). The many meanings of gross photosynthesis and their implication for photosynthesis research from leaf to globe. Plant, Cell & Environment, 38(12), 2500–2507. https://doi.org/10.1111/pce.12569

Wohner, C., Ohnemus, T., Zacharias, S., Mollenhauer, H., Ellis, E. C., Klug, H., Shibata, H., & Mirtl, M. (2021). Assessing the biogeographical and socio-ecological representativeness of the ILTER site network. Ecological Indicators, 127, 107785. https://doi.org/10.1016/j.ecolind.2021.107785

Wood, E. F., Roundy, J. K., Troy, T. J., van Beek, L. P. H., Bierkens, M. F. P., Blyth, E., de Roo, A., Döll, P., Ek, M., Famiglietti, J., Gochis, D., van de Giesen, N., Houser, P., Jaffé, P. R., Kollet, S., Lehner, B., Lettenmaier, D. P., Peters-Lidard, C., Sivapalan, M., … Whitehead, P. (2011). Hyperresolution global land surface modeling: Meeting a grand challenge for monitoring Earth's terrestrial water: OPINION. Water Resources Research, 47(5). https://doi.org/10.1029/2010WR010090

Wozniak, M. C., Bonan, G. B., Keppel-Aleks, G., & Steiner, A. L. (2020). Influence of Vertical Heterogeneities in the Canopy Microenvironment on Interannual Variability of Carbon Uptake in Temperate Deciduous Forests. Journal of Geophysical Research: Biogeosciences, 125(8), e2020JG005658. https://doi.org/10.1029/2020JG005658

Wright, I. J., Reich, P. B., Westoby, M., Ackerly, D. D., Baruch, Z., Bongers, F., Cavender-Bares, J., Chapin, T., Cornelissen, J. H. C., Diemer, M., Flexas, J., Garnier, E., Groom, P. K., Gulias, J., Hikosaka, K., Lamont, B. B., Lee, T., Lee, W., Lusk, C., … Villar, R. (2004). The worldwide leaf economics spectrum. Nature, 428(6985), 821–827. https://doi.org/10.1038/nature02403

Wu, H., Fu, C., Wu, H., & Zhang, L. (2020). Plant Hydraulic Stress Strategy Improves Model Predictions of the Response of Gross Primary Productivity to Drought Across China. Journal of Geophysical Research: Atmospheres, 125(24), e2020JD033476. https://doi.org/10.1029/2020JD033476

Wu, Z., Vermeulen, A., Sawa, Y., Karstens, U., Peters, W., De Kok, R., Lan, X., Nagai, Y., Ogi, A., & Tarasova, O. (2024). Investigating the differences in calculating global mean surface CO_2 abundance: The impact of analysis methodologies and site selection. Atmospheric Chemistry and Physics, 24(2), 1249–1264. https://doi.org/10.5194/acp-24-1249-2024

Xia, L., Wang, F., Mu, X., Jin, K., Sun, W., Gao, P., & Zhao, G. (2015). Water use efficiency of net primary production in global terrestrial ecosystems. Journal of Earth System Science, 124(5), 921–931. https://doi.org/10.1007/s12040-015-0587-4

Xie, X., Li, A., Tan, J., Lei, G., Jin, H., & Zhang, Z. (2020). Uncertainty analysis of multiple global GPP datasets in characterizing the lagged effect of drought on photosynthesis. Ecological Indicators, 113, 106224. https://doi.org/10.1016/j.ecolind.2020.106224

Xu, Z., Jiang, Y., Jia, B., & Zhou, G. (2016). Elevated-CO_2 Response of Stomata and Its Dependence on Environmental Factors. Frontiers in Plant Science, 7. https://doi.org/10.3389/fpls.2016.00657

Yang, F., Kumar, A., Schlesinger, M. E., & Wang, W. (2003). Intensity of Hydrological Cycles in Warmer Climates. Journal of Climate, 16(14), 2419–2423. https://doi.org/10.1175/2779.1

Yang, Y., Bi, M., Nie, Z., Jiang, H., Liu, X., Fang, X., & Brodribb, T. J. (2021). Evolution of stomatal closure to optimize water-use efficiency in response to dehydration in ferns and seed plants. New Phytologist, 230(5), 2001–2010. https://doi.org/10.1111/nph.17278

Yang, Y., Guan, H., Batelaan, O., McVicar, T. R., Long, D., Piao, S., Liang, W., Liu, B., Jin, Z., & Simmons, C. T. (2016). Contrasting responses of water use efficiency to drought across global terrestrial ecosystems. Scientific Reports, 6(1). https://doi.org/10.1038/srep23284

Zaitchik, B. F., Rodell, M., Biasutti, M., & Seneviratne, S. I. (2023). Wetting and drying trends under climate change. Nature Water, 1(6), 502–513. https://doi.org/10.1038/s44221-023-00073-w

Zhang, J., Zhang, M., Yu, J., Yu, Y., Jiang, F., & Yu, R. (2024). Identifying and characterizing short-term drought with rapid onset based on the SAPEI in the Yangtze River basin. Journal of Hydrology: Regional Studies, 51, 101629. https://doi.org/10.1016/j.ejrh.2023.101629

Zhang, J., Zhang, M., Yu, Y., & Yu, R. (2024). An innovative method integrating run theory and DBSCAN for complete three-dimensional drought structures. Science of The Total Environment, 926, 171901. https://doi.org/10.1016/j.scitotenv.2024.171901

Zhang, L., Ning, F., Bai, X., Zeng, X., & He, C. (2023). Performance evaluation of CLM5.0 in simulating liquid soil water in high mountainous area, Northwest

China. Journal of Mountain Science, 20(7), 1865–1883. https://doi.org/10.1007/s11629-022-7803-x

Zhang, L., Xiao, J., Zheng, Y., Li, S., & Zhou, Y. (2020). Increased carbon uptake and water use efficiency in global semi-arid ecosystems. Environmental Research Letters, 15(3), 034022. https://doi.org/10.1088/1748-9326/ab68ec

Zhang, Q., Ficklin, D. L., Manzoni, S., Wang, L., Way, D., Phillips, R. P., & Novick, K. A. (2019). Response of ecosystem intrinsic water use efficiency and gross primary productivity to rising vapor pressure deficit. Environmental Research Letters, 14(7), 074023. https://doi.org/10.1088/1748-9326/ab2603

Zhang, W., Luo, M., Gao, S., Chen, W., Hari, V., & Khouakhi, A. (2021). Compound Hydrometeorological Extremes: Drivers, Mechanisms and Methods. Frontiers in Earth Science, 9, 673495. https://doi.org/10.3389/feart.2021.673495

Zhang, W., Nelson, J. A., Miralles, D. G., Mauder, M., Migliavacca, M., Poyatos, R., Reichstein, M., & Jung, M. (2024). A New Post-Hoc Method to Reduce the Energy Imbalance in Eddy Covariance Measurements. Geophysical Research Letters, 51(2), e2023GL107084. https://doi.org/10.1029/2023GL107084

Zhang, Y., Keenan, T. F., & Zhou, S. (2021). Exacerbated drought impacts on global ecosystems due to structural overshoot. Nature Ecology & Evolution. https://doi.org/10.1038/s41559-021-01551-8

Zhao, H., Montzka, C., Keller, J., Li, F., Vereecken, H., & Franssen, H.-J. H. (2025). How does assimilating SMAP soil moisture improve characterization of the terrestrial water cycle in an integrated land surface-subsurface model? Preprints. https://doi.org/10.22541/essoar.174349969.95856958/v1

Zhao, J., Feng, H., Xu, T., Xiao, J., Guerrieri, R., Liu, S., Wu, X., He, X., & He, X. (2021). Physiological and environmental control on ecosystem water use efficiency in response to drought across the northern hemisphere. Science of The Total Environment, 758, 143599. https://doi.org/10.1016/j.scitotenv.2020.143599

Zhao, M., A, G., Liu, Y., & Konings, A. G. (2022). Evapotranspiration frequently increases during droughts. Nature Climate Change, 12(11), 1024–1030. https://doi.org/10.1038/s41558-022-01505-3

Zheng, Y., Shen, R., Wang, Y., Li, X., Liu, S., Liang, S., Chen, J. M., Ju, W., Zhang, L., & Yuan, W. (2020). Improved estimate of global gross primary production for reproducing its long-term variation, 1982–2017. Earth System Science Data, 12(4), 2725–2746. https://doi.org/10.5194/essd-12-2725-2020

Zhu, Z., Duan, W., Zou, S., Zeng, Z., Chen, Y., Feng, M., Qin, J., & Liu, Y. (2024). Spatiotemporal characteristics of meteorological drought events in 34 major global river basins during 1901–2021. Science of The Total Environment, 921, 170913. https://doi.org/10.1016/j.scitotenv.2024.170913

Zscheischler, J., Martius, O., Westra, S., Bevacqua, E., Raymond, C., Horton, R. M., Van Den Hurk, B., AghaKouchak, A., Jézéquel, A., Mahecha, M. D., Maraun, D., Ramos, A. M., Ridder, N. N., Thiery, W., & Vignotto, E. (2020). A typology of compound weather and climate events. Nature Reviews Earth & Environment, 1(7), 333–347. https://doi.org/10.1038/s43017-020-0060-z

A Appendix to: Rising water-use efficiency in European grasslands is driven by increased primary production

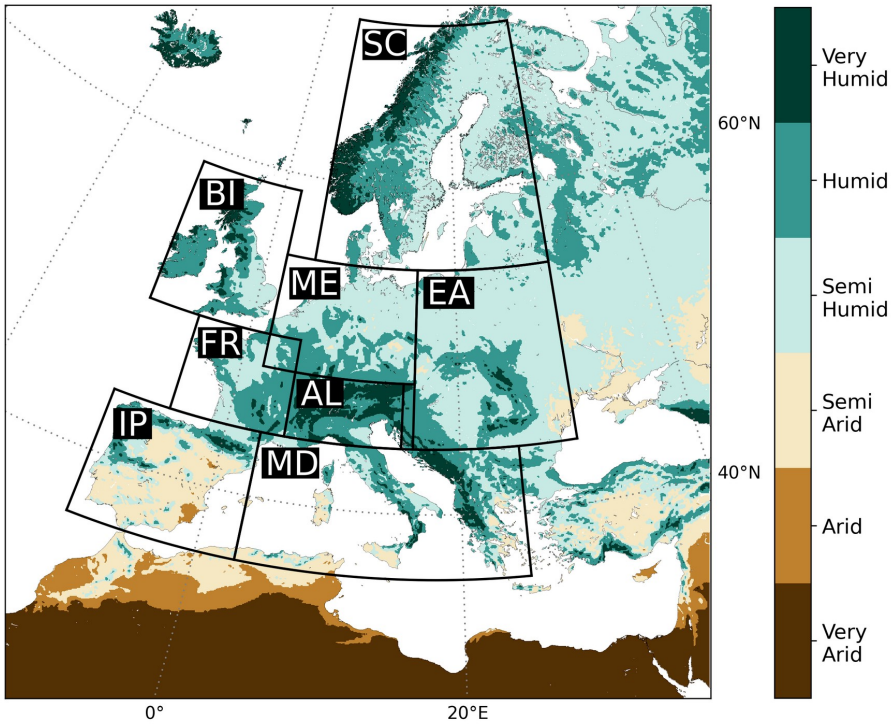

Figure A.1: Hydro-climates (colormap, defined by annual precipitation thresholds, see Table A.1) and PRUDENCE regions (Giorgi et al., 2009; Jafari et al., 2018). IP: Iberian Peninsula, MD: Mediterranean, FR: France, AL: Alps, EA: Eastern Europe, BI: British Islands, ME: Mid / Central Europe, SC: Scandinavia.

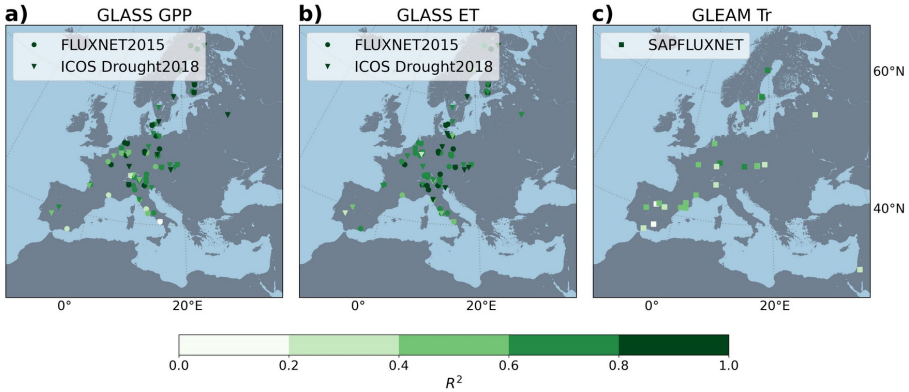

Figure A.2: Distribution of FLUXNET (circles), ICOS (triangles) and SAPFLUXNET (squares) stations. The colors of the markers indicate the coefficient of determination R^2 (colormap) for gross primary production (GPP)(a), evapotranspiration (ET)(b) and transpiration (T_r)(c).

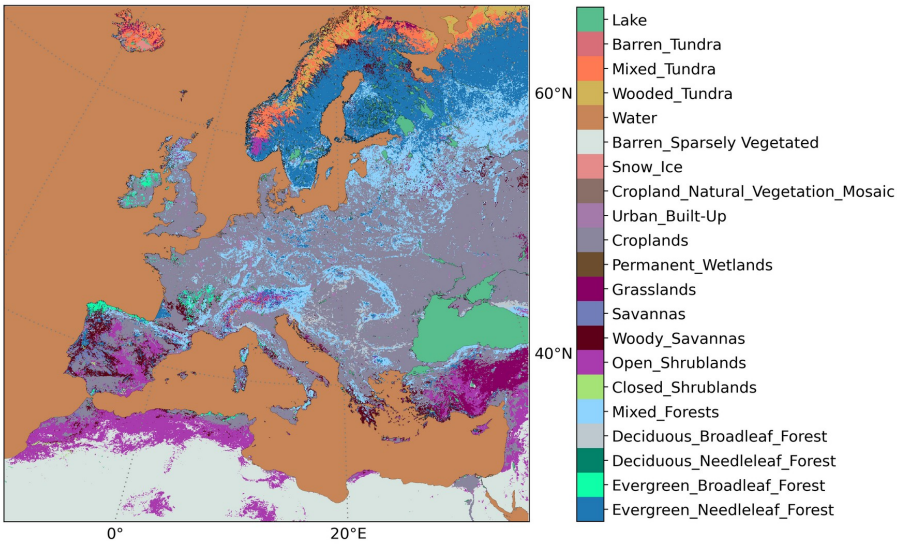

Figure A.3: Land cover over the study domain from IGBP-modified MODIS 20 land-use categories.

Table A.1: Hydro-climates and defined annual precipitation (P_a) thresholds.

Hydro-climate	**Annual precipitation (P_a) thresholds [mm]**
Very humid	$P_a \geq 1200$
Humid	$700 \leq P_a < 1200$
Semi humid	$500 \leq P_a < 700$
Semi arid	$250 \leq P_a < 500$
Arid	$100 \leq P_a < 250$
Very arid	$P_a < 100$

Table A.2: Drought categories by thresholds of a drought index (SXI). These thresholds were applied to both SPI and SSI values to determine the severity of the drought as used in Figure 3.3 of the main article.

Drought Category	**Drought Index (SXI) Threshold**
Extreme dry	$SXI < -2$
Very dry	$-2 \leq SXI < -1.5$
Moderate dry	$-1.5 \leq SXI < -1$
Normal	$-1 \leq SXI < 1$
Moderate wet	$1 \leq SXI < 2$
Very wet	$1.5 \leq SXI < 2$
Extreme wet	$SXI \geq 2$

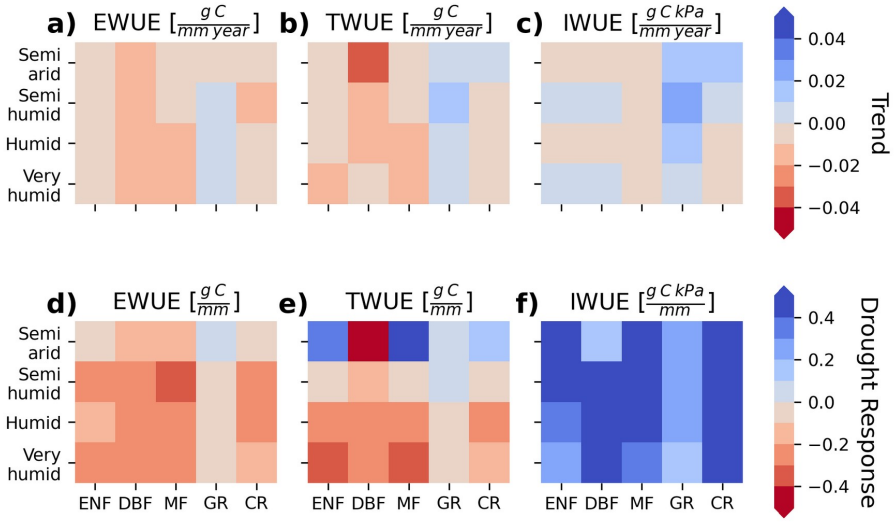

Figure A.4: The median trend (a, b, c) and median drought response (d, e, f) aggregated over grid cells along land cover (x-axes, ENF = Evergreen Needleleaf Forest, DBF = Deciduous Broadleaf Forest, MF = Mixed Forest, GR = Grasslands, C = Croplands) and hydro-climates (y-axes).

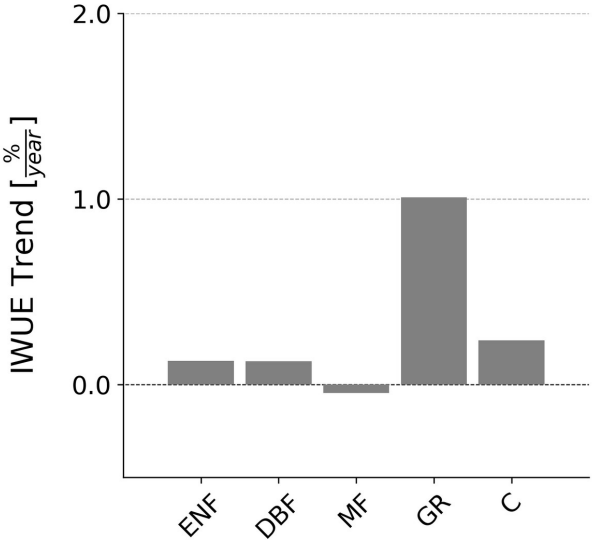

Figure A.5: The median relative trend slope from the grid cell wise Mann-Kendall trend analysis from grid cells with corresponding dominant land cover (ENF = Evergreen Needleleaf Forest, DBF = Deciduous Broadleaf Forest, MF = Mixed Forest, GR = Grasslands, C = Croplands). The median relative trends is calculated by the median slope of those grid cells divided by the median intercept.

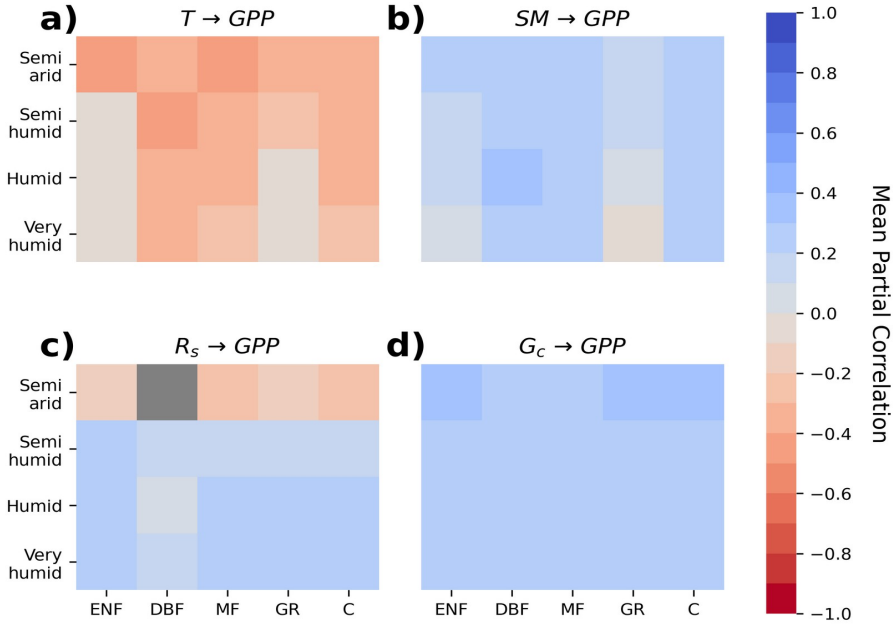

Figure A.6: Mean partial correlations (colormap) at detected directed links from the PCMCI+ analysis between temperature (T), soil moisture (SM), shortwave incoming radiation (R_s) and canopy conductance (G_c) to gross primary production (GPP) aggregated over land cover (x-axes, ENF = Evergreen Needleleaf Forest, DBF = Deciduous Broadleaf Forest, MF = Mixed Forest, GR = Grasslands, C = Croplands) and hydroclimates (y-axes).

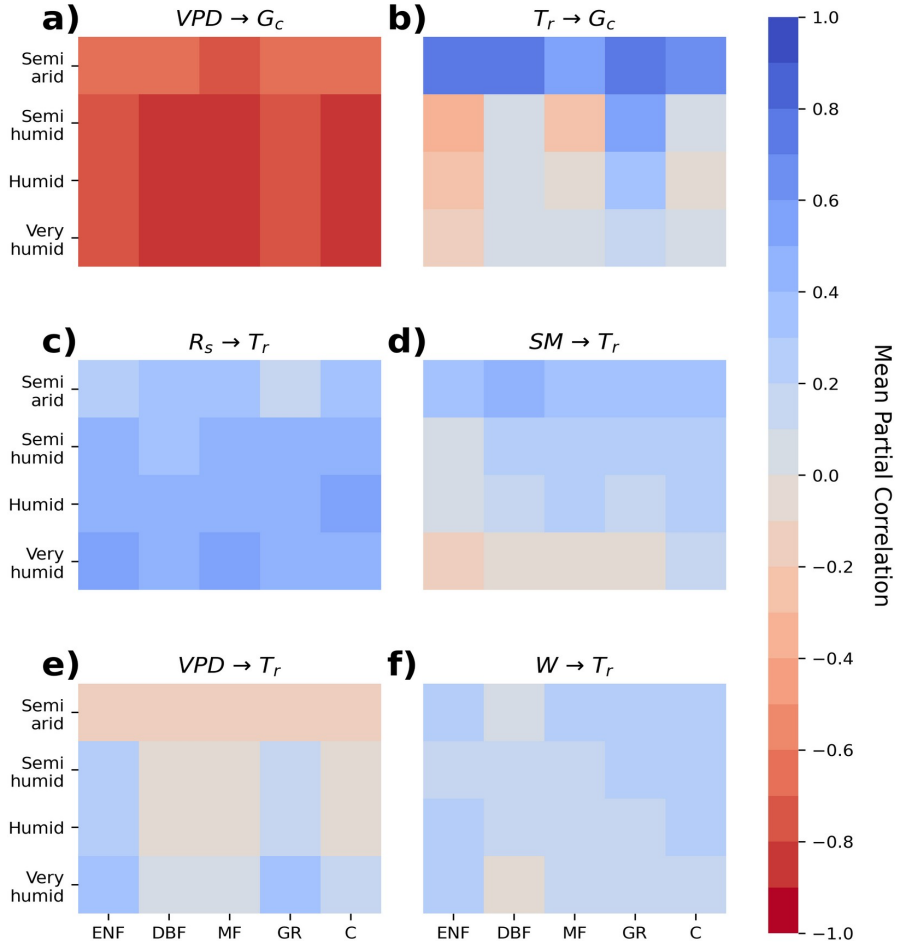

Figure A.7: Mean partial correlations (colormap) at detected directed links from the PCMCI+ analysis between vapour pressure deficit (VPD) and transpiration (T_r) to canopy conductance (G_c) and incoming shortwave radiation (R_s), soil moisture (SM), VPD, and wind speed (W) to T_r aggregated over land cover (x-axes, ENF =Evergreen Needleleaf Forest, DBF = Deciduous Broadleaf Forest, MF = Mixed Forest, GR = Grasslands, C = Croplands) and hydro-climates (y-axes).

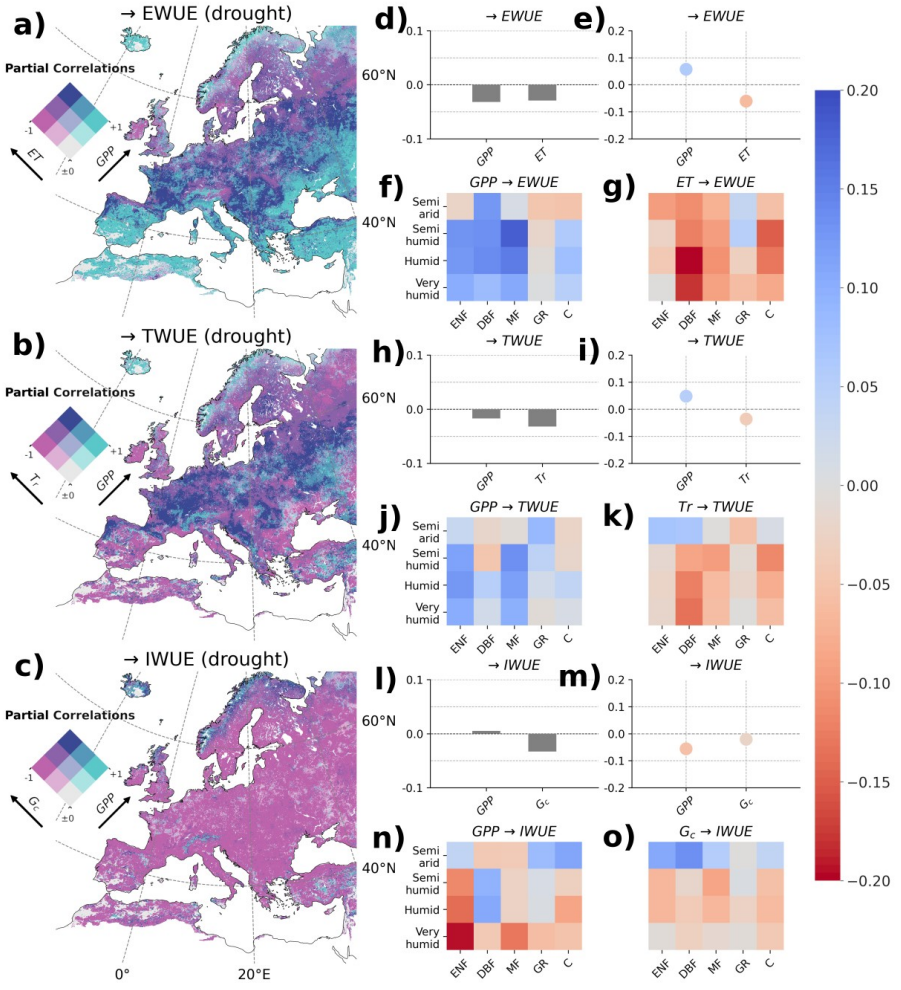

Figure A.8: Here we show partial correlations of GPP versus ET to EWUE (a), GPP versus transpiration (T_r) to TWUE (b) and GPP versus canopy conductance (G_c) to IWUE (c) from the PCMCI+ analysis similarly to Figure 3.4 in the main article but only for drought periods. Green colors show a stronger link between GPP and WUE variability, and pink colors a stronger link between water-use and WUE, while gray shows low correlations and dark purple strong correlations of both. On the right side, we show the change of relative area change with directed links between non-drought and drought periods (d, h, l) and the respective change of mean partial correlations (circle) across the continent (e, i, m). Lastly, we aggregate the change in partial correlations during droughts of those links (f, g, j, k, n, o) over land cover (x-axes, ENF =Evergreen Needleleaf Forest, DBF = Deciduous Broadleaf Forest, MF = Mixed Forest, GR = Grasslands, C = Croplands) and hydro-climates (y-axes) see Methods for a more detailed description.

Table.A.3: FLUXNET2015 site data availability information and coefficient of determination (R^2) with the interpolated GLASS gross primary production (GPP) and evapotranspiration (ET).

Site Code	Latitude	Longitude	Start Year	End Year	N Years	R^2 - GPP	R^2 - ET
AT-Neu	47.12	11.32	2002	2012	11	0.65	0.73
BE-Bra	51.3076	4.5198	1996	2014	19	0.7969	0.7498
BE-Lon	50.5516	4.7462	2004	2014	11	0.4158	0.6768
BE-Vie	50.3049	5.9981	1996	2014	19	0.8259	0.7544
CH-Cha	47.2102	8.4104	2005	2014	10	0.5779	0.8279
CH-Dav	46.8153	9.8559	1997	2014	18	0.6405	0.5675
CH-Fru	47.1158	8.5378	2005	2014	10	0.7134	0.7406
CH-Lae	47.4783	8.3644	2004	2014	11	0.725	0.7836
CH-Oe1	47.2858	7.7319	2002	2008	7	0.5537	0.7991
CH-Oe2	47.2864	7.7338	2004	2014	11	0.372	0.7057
CZ-BK1	49.5021	18.5369	2004	2014	11	0.7039	0.6453
CZ-BK2	49.4944	18.5429	2004	2012	9	0.7047	0.6735
CZ-wet	49.0247	14.7704	2006	2014	9	0.777	0.8101
DE-Akm	53.8662	13.6834	2009	2014	6	0.7967	0.833
DE-Geb	51.0997	10.9146	2001	2014	14	0.5494	0.7468
DE-Gri	50.95	13.5126	2004	2014	11	0.7394	0.7693
DE-Hai	51.0792	10.4522	2000	2012	13	0.8139	0.8466
DE-Kli	50.8931	13.5224	2004	2014	11	0.5183	0.6573
DE-Lkb	49.0996	13.3047	2009	2013	5	0.5941	0.7711
DE-Lnf	51.3282	10.3678	2002	2012	11	0.8058	0.8037
DE-Obe	50.7867	13.7213	2008	2014	7	0.7338	0.7647
DE-RuR	50.6219	6.3041	2011	2014	4	0.7825	0.8995
DE-RuS	50.8659	6.4471	2011	2014	4	0.6267	0.8024
DE-Seh	50.8706	6.4497	2007	2010	4	0.5818	0.7269
DE-SfN	47.8064	11.3275	2012	2014	3	0.749	0.8758

DE-Spw	51.8923	14.0337	2010	2014	5	0.8777	0.84
DE-Tha	50.9626	13.5652	1996	2014	19	0.8457	0.7349
DE-Zrk	53.8759	12.889	2013	2014	2	0.8265	0.8869
DK-Eng	55.6905	12.1918	2005	2008	4	0.7097	0.8365
DK-Sor	55.4859	11.6446	1996	2014	19	0.9202	0.858
ES-LgS	37.0979	-2.9658	2007	2009	3	0.2269	0.602
FI-Hyy	61.8474	24.2948	1996	2014	19	0.9093	0.8344
FI-Jok	60.8986	23.5135	2000	2003	4	0.6497	0.7566
FI-Let	60.6418	23.9595	2009	2012	4	0.8718	0.8641
FI-Lom	67.9972	24.2092	2007	2009	3	0.8537	0.7982
FI-Sod	67.3624	26.6386	2001	2014	14	0.8103	0.8082
FR-Fon	48.4764	2.7801	2005	2014	10	0.8276	0.8583
FR-Gri	48.8442	1.9519	2004	2014	11	0.4655	0.6215
FR-LBr	44.7171	-0.7693	1996	2008	13	0.6657	0.662
FR-Pue	43.7413	3.5957	2000	2014	15	0.3914	0.4659
IT-BCi	40.5238	14.9574	2004	2014	11	0.0259	0.51
IT-CA1	42.3804	12.0266	2011	2014	4	0.6549	0.6857
IT-CA2	42.3772	12.026	2011	2014	4	0.3282	0.3121
IT-CA3	42.38	12.0222	2011	2014	4	0.4748	0.7485
IT-Col	41.8494	13.5881	1996	2014	19	0.6799	0.7071
IT-Cp2	41.7043	12.3573	2012	2014	3	0.5305	0.7626
IT-Cpz	41.7053	12.3761	1997	2009	13	0.4681	0.6185
IT-Isp	45.8126	8.6336	2013	2014	2	0.742	0.8319
IT-La2	45.9542	11.2853	2000	2002	3	0.7812	0.6949
IT-Lav	45.9562	11.2813	2003	2014	12	0.7602	0.7545
IT-MBo	46.0147	11.0458	2003	2013	11	0.8252	0.8322
IT-PT1	45.2009	9.061	2002	2004	3	0.7463	0.8603
IT-Ren	46.5869	11.4337	1998	2013	16	0.7666	0.7354

IT-Ro1	42.4081	11.93	2000	2008	9	0.5296	0.7576
IT-Ro2	42.3903	11.9209	2002	2012	11	0.3693	0.7277
IT-SR2	43.732	10.2909	2013	2014	2	0.7706	0.8171
IT-SRo	43.7279	10.2844	1999	2012	14	0.5607	0.4291
IT-Tor	45.8444	7.5781	2008	2014	7	0.8306	0.825
NL-Hor	52.2404	5.0713	2004	2011	8	0.8252	0.6789
NL-Loo	52.1666	5.7436	1996	2014	19	0.8552	0.698
∑ 60					∑ 569	Ø 0.67	Ø 0.74

Table A.4: ICOS Drought2018 site data availability information and coefficient of determination (R^2) with the interpolated GLASS gross primary production (GPP) and evapotranspiration (ET).

Site Code	**Latitude**	**Longitude**	**Start Year**	**End Year**	**N Years**	**R^2 - GPP**	**R^2 - ET**
BE-Bra	51.31	4.52	1996	2018	23	0.79	0.75
BE-Lon	50.5516	4.7462	2004	2018	15	0.4188	0.6574
BE-Vie	50.3049	5.9981	1996	2018	23	0.8295	0.7542
CH-Aws	46.5832	9.7904	2010	2018	9	0.6327	0.4476
CH-Cha	47.2102	8.4104	2005	2018	14	0.5837	0.8275
CH-Dav	46.8153	9.8559	1997	2018	22	0.5372	0.6758
CH-Fru	47.1158	8.5378	2005	2018	14	0.6628	0.7174
CH-Lae	47.4783	8.3644	2004	2018	15	0.4655	0.7584
CH-Oe2	47.2864	7.7338	2004	2018	15	0.359	0.6998
CZ-BK1	49.5021	18.5369	2004	2018	15	0.7139	0.6301
CZ-Lnz	48.6816	16.9464	2015	2018	4	0.8997	0.877
CZ-RAJ	49.4437	16.6965	2012	2018	7	0.7669	0.7075
CZ-Stn	49.036	17.9699	2010	2018	9	0.7893	0.8051
CZ-wet	49.0247	14.7704	2006	2018	13	0.7835	0.8295
DE-Akm	53.8662	13.6834	2009	2018	10	0.747	0.5106

DE-Geb	51.0997	10.9146	2001	2018	18	0.5273	0.7345
DE-Gri	50.95	13.5126	2004	2018	15	0.6702	0.7809
DE-Hai	51.0792	10.4522	2000	2018	19	0.802	0.8093
DE-HoH	52.0853	11.2192	2015	2018	4	0.7152	0.806
DE-Hte	54.2103	12.1761	2009	2018	10	0.6624	0.821
DE-Hzd	50.9638	13.4898	2010	2018	9	0.6875	0.7165
DE-Kli	50.8931	13.5224	2004	2018	15	0.4974	0.6684
DE-Obe	50.7867	13.7213	2008	2018	11	0.7272	0.6545
DE-RuR	50.6219	6.3041	2011	2018	8	0.755	0.8054
DE-RuS	50.8659	6.4471	2011	2018	8	0.4853	0.7272
DE-RuW	50.5049	6.331	2010	2018	9	0.5919	0.3929
DE-Tha	50.9626	13.5652	1996	2018	23	0.8262	0.7107
DK-Sor	55.4859	11.6446	1996	2018	23	0.9105	0.8605
ES-Abr	38.7018	-6.7859	2015	2018	4	0.4522	0.2721
ES-LM1	39.9427	-5.7787	2014	2018	5	0.561	0.545
ES-LM2	39.9346	-5.7759	2014	2018	5	0.6123	0.5113
FI-Hyy	61.8474	24.2948	1996	2018	23	0.9104	0.8369
FI-Let	60.6418	23.9595	2009	2018	10	0.8119	0.7951
FI-Sii	61.8327	24.1929	2016	2018	3	0.8426	0.7666
FI-Var	67.7549	29.61	2016	2018	3	0.8327	0.8588
FR-Bil	44.4937	-0.9561	2014	2018	5	0.5664	0.6605
FR-EM2	49.8721	3.0207	2017	2018	2	0.53	0.773
FR-Hes	48.6741	7.0647	2014	2018	5	0.8491	0.7584
IT-BCi	40.5238	14.9574	2004	2018	15	0.0172	0.4715
IT-Cp2	41.7043	12.3573	2012	2018	7	0.5443	0.5834
IT-Lsn	45.7405	12.7503	2016	2018	3	0.7726	0.8336
IT-SR2	43.732	10.2909	2013	2018	6	0.7066	0.8293
IT-Tor	45.8444	7.5781	2008	2018	11	0.8221	0.7769

NL-Loo	52.1666	5.7436	1996	2018	23	0.8503	0.6938
RU-Fy2	56.4476	32.9019	2015	2018	4	0.849	0.7957
RU-Fyo	56.4615	32.9221	1998	2018	21	0.8575	0.7646
SE-Deg	64.182	19.5565	2001	2018	18	0.8362	0.7623
SE-Htm	56.0976	13.419	2015	2018	4	0.8045	0.77
SE-Lnn	58.3406	13.1018	2014	2018	5	0.6429	0.6703
SE-Nor	60.0865	17.4795	2014	2018	5	0.8721	0.8426
SE-Ros	64.1725	19.738	2014	2018	5	0.8834	0.7261
SE-Svb	64.2561	19.7745	2014	2018	5	0.8847	0.5192
∑ 52					∑ 577	Ø 0.70	Ø 0.71

Table A.5: SAPFLUXNET sites used in this study and further information as well as R^2 s of transpiration upscaled from sap flux with correspondent data from interpolated GLEAM and ERA5-Land.

Site Code	**Latitude**	**Longitude**	**Start Year**	**End Year**	**N Years**	**R^2 -GLEAM**	**R^2 - ERA5L**
CZE_BIK	49.49	18.53	2015	2016	1	0.31	0.3
CZE_BIL_BIL	49.25	16.69	2014	2017	3	0.38	0.37
CZE_KRT_KRT	49.32	16.75	2013	2017	4	0.55	0.57
CZE_LIZ_LES	49.07	13.68	2007	2009	2	0.63	0.57
CZE_SOB_SOB	49.25	16.69	2013	2017	4	0.3	0.33
CZE_UTE_BEE	49.28	16.65	2013	2017	4	0.59	0.58
CZE_UTE_BNA	49.28	16.65	2013	2017	4	0.58	0.56
CZE_UTE_BPO	49.28	16.65	2013	2017	4	0.53	0.48
CZE_UTE_SPR	49.28	16.65	2013	2017	4	0.43	0.27
DEU_MER_BEE_NON	49.27	7.81	2009	2012	3	0.28	0.21
DEU_MER_BEE_THI	49.27	7.81	2012	2015	3	0.53	0.52
DEU_MER_DOU_NON	49.27	7.81	2009	2012	3	0.42	0.37
DEU_MER_DOU_THI	49.27	7.81	2012	2015	3	0.57	0.59

DEU_MER_MIX_NON	49.27	7.81	2009	2012	3	0.53	0.37
DEU_MER_MIX_THI	49.27	7.81	2012	2015	3	0.62	0.62
ESP_ALT_ARM	40.78	−2.33	2009	2014	5	0.56	0.51
ESP_ALT_HUE	40.79	−2.29	2009	2013	4	0.45	0.35
ESP_ALT_TRI	40.8	−2.23	2008	2015	7	0.27	0.21
ESP_CAN	41.43	2.07	2011	2012	1	0.47	0.45
ESP_GUA_VAL	40.9	-4.03	2011	2013	2	0.02	0.21
ESP_LAH_COM	37.74	-3.38	2011	2013	2	0.11	0.46
ESP_LAS	28.31	-16.57	2008	2009	1	0.14	0.02
ESP_MAJ_MAI	39.94	-5.77	2015	2018	3	0.49	0.43
ESP_MAJ_NOR_LM1	39.94	-5.77	2015	2018	3	0.56	0.57
ESP_MON_SIE_NAT	41.12	-3.5	2010	2014	4	0.4	0.49
ESP_RON_PIL	36.69	-5.02	2011	2013	2	0	0.25
ESP_TIL_MIX	41.33	1.01	2010	2013	3	0.51	0.28
ESP_TIL_OAK	41.33	1.01	2010	2011	1	0.48	0.24
ESP_TIL_PIN	41.33	1.01	2010	2011	1	0.4	0.11
ESP_VAL_BAR	42.2	1.82	2003	2005	2	0.31	0.24
ESP_VAL_SOR	42.2	1.81	2003	2005	2	0.51	0.49
ESP_YUN_C1	36.72	-4.97	2009	2014	5	0.26	0.26
ESP_YUN_C2	36.72	-4.97	2011	2014	3	0.52	0.63
ESP_YUN_T1_THI	36.72	-4.97	2010	2014	4	0.42	0.47
ESP_YUN_T3_THI	36.72	-4.97	2009	2014	5	0.33	0.4
FRA_FON	48.48	2.78	2005	2014	9	0.45	0.37
FRA_HES_HE1_NON	48.67	7.06	1997	1999	2	0.35	0.32
FRA_HES_HE2_NON	48.67	7.06	2000	2006	6	0.34	0.3
FRA_PUE	43.74	3.6	1999	2015	16	0.56	0.5
ISR_YAT_YAT	31.35	35.05	2009	2015	6	0.32	0.21
ITA_TOR	45.82	7.56	2015	2016	1	0.38	0.52

NLD_LOO	52.17	5.74	2011	2015	4	0.58	0.48
RUS_FYO	56.46	32.92	1998	2004	6	0.27	0.22
SWE_NOR_ST1_AF1	60.09	17.48	2009	2010	1	0.31	0.41
SWE_NOR_ST1_AF2	60.09	17.48	2009	2010	1	0.6	0.58
SWE_NOR_ST1_BEF	60.09	17.48	2007	2009	2	0.01	0.03
SWE_NOR_ST2	60.09	17.48	2001	2002	1	0.35	0.26
SWE_NOR_ST3	60.09	17.48	2002	2008	6	0.36	0.28
SWE_NOR_ST4_AFT	60.08	17.48	1999	2001	2	0.57	0.52
SWE_NOR_ST5_REF	60.08	17.48	1998	2001	3	0.47	0.44
SWE_SKO_MIN	58.36	12.15	2014	2015	1	0.53	0.43
SWE_SKY_38Y	60.13	17.84	2001	2003	2	0.46	0.31
SWE_SKY_68Y	60.1	17.83	2001	2003	2	0.65	0.54
SWE_SVA_MIX_NON	64.26	19.77	2016	2017	1	0.71	0.66
∑ 54					∑ 180	Ø 0.42	Ø 0.39

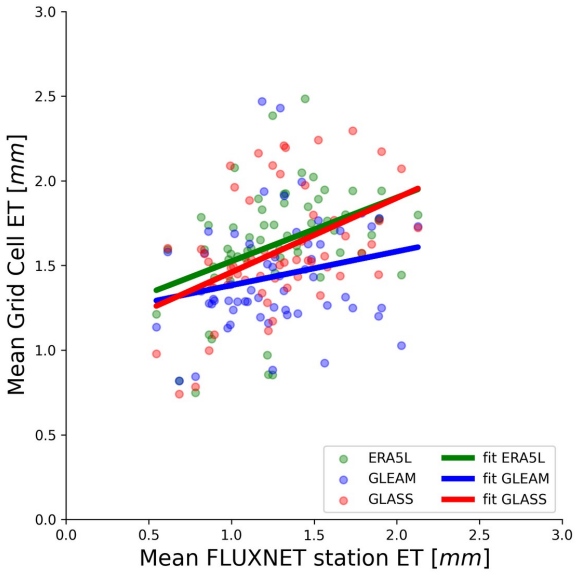

Figure A.9: Comparison of mean evapotranspiration (ET) values from FLUXNET2015 stations in the domain (see Table.A.3) and the mean of the corresponding grid cell of ERA5-Land (ERA5L, green markers), GLEAM (blue markers), and GLASS (red markers) ET. The solid lines correspond to a linear regression fit with a least squares method.

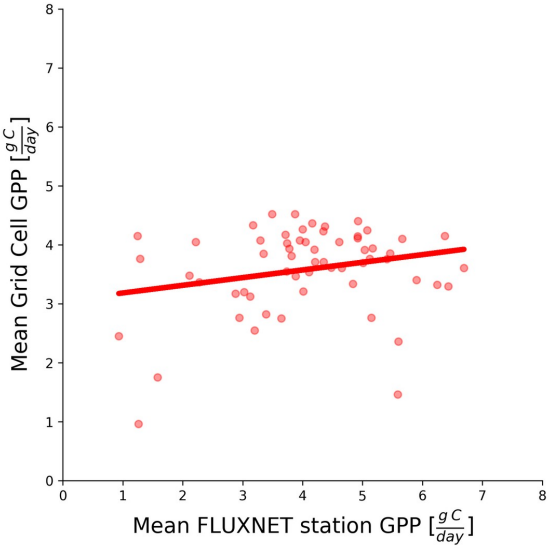

Figure A.10: Comparison of mean gross primary production (GPP) values from FLUXNET2015 stations in the domain (see Table.A.3) and the mean of the corresponding grid cell GLASS GPP. The solid line corresponds to a linear regression with least squares method

Figure A.11: A network with physically possible and plausible links between the included variables in the PCMCI+ analysis in this work controlled through its selected_links parameter. PCMCI+ will therefore just test shown links for significant causality and yield the final causal network as a subset of this. The included links allow for differences in causal networks between hydro-climates and land cover.

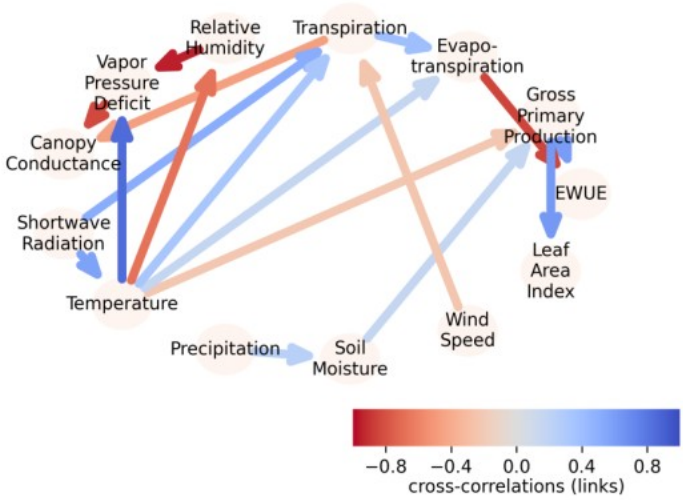

Figure A.12: Exemplary output of PCMCI+ for the grid cell corresponding to the ICOS site Wüstebach (DE-RuW). The algorithm tested the possible links from the total possible network from Figure A.11 for significant causal relationships and yielded the output as a subset of it with corresponding link strengths (cross-correlations). Auto-correlations where not tested in this network.

B Appendix to: Systematic underestimation of type-specific ecosystem process variability in CLM5 over Europe

Table B.1: A list of ICOS stations, their land cover, coordinates, years of data availability for our study period (1995 – 2018), the coordinates of the corresponding grid cell of the 3 km European Coordinated Regional Climate Downscaling Experiment (CORDEX) grid used in our simulations, and the number of 8-daily data points available for the analyses for evapotranspiration (ET) and gross primary production (GPP). Note that stations that do not belong to the plant functional types (PFT) of evergreen needleleaf forest (ENF), deciduous broadleaf forest (DBF), grasslands (GRA), and croplands (CRO) were omitted, and some included sites did not have data corresponding with the study period, thus having a count of 0 data points. See Section 4.2.2. The indicated PFT is the predominant PFT in the footprint of the ICOS eddy covariance towers. Stations, where the land cover was not directly indicated in the metadata sites were also left out in our analyses.

ID	country	PFT	lat	lon	years	lat (cell)	lon (cell)	N (ET)	N (GPP)
BE-Bra	Belgium	ENF	51.31	4.52	1996 – 2018	51.29	4.51	608	670
BE-Dor	Belgium	GRA	50.31	4.97	2011 – 2018	50.31	4.96	0	270
BE-Lcr	Belgium	DBF	51.11	3.85		51.10	3.85	0	0
BE-Lon	Belgium	CRO	50.55	4.75	2004 – 2018	50.57	4.76	519	476
CH-Cha	Switzerland	GRA	47.21	8.41	2005 – 2018	47.21	8.43	423	459
CH-Dav	Switzerland	ENF	46.82	9.86	1997 – 2018	46.80	9.84	578	866
CH-Fru	Switzerland	GRA	47.12	8.54	2005 – 2018	47.11	8.53	284	447
CH-Oe2	Switzerland	CRO	47.29	7.73	2004 – 2018	47.28	7.72	0	592
CZ-BK1	Czech Republic	ENF	49.50	18.54	2004 – 2018	49.50	18.54	146	389
CZ-Lnz	Czech Republic	DBF	48.68	16.95	2015 – 2018	48.67	16.95	0	145
DE-Geb	Germany	CRO	51.10	10.91	2001 – 2020	51.10	10.93	824	638
DE-Gri	Germany	GRA	50.95	13.51	2001 – 2018	50.95	13.49	673	492
DE-Hai	Germany	DBF	51.08	10.45	2000 – 2018	51.07	10.45	813	548
DE-HoH	Germany	DBF	52.09	11.22	2015 – 2018	52.09	11.23	184	113
DE-Kli	Germany	CRO	50.89	13.52	2004 – 2018	50.90	13.54	481	450
DE-RuR	Germany	GRA	50.62	6.30	2011 – 2018	50.62	6.28	336	309
DE-RuS	Germany	CRO	50.87	6.45	2011 – 2018	50.86	6.44	285	224
DE-RuW	Germany	ENF	50.50	6.33	2012 – 2018	50.51	6.31	0	125
DE-Tha	Germany	ENF	50.96	13.57	1996 – 2018	50.96	13.58	1012	888
DK-Gds	Denmark	ENF	56.07	9.33		56.07	9.34	0	0
DK-Sor	Denmark	DBF	55.49	11.64	1996 – 2018	55.48	11.65	437	882
FI-Hyy	Finland	ENF	61.85	24.29	1996 – 2018	61.86	24.29	435	812
FI-Ken	Finland	ENF	67.99	24.24	2018	67.99	24.23	0	18
FI-Let	Finland	ENF	60.64	23.96	2009 – 2018	60.63	23.96	412	254

FI-Var	Finland	ENF	67.75	29.61	2016 – 2018	67.76	29.63	135	133
FR-Aur	France	CRO	43.55	1.11	2005 – 2018	43.54	1.12	470	483
FR-Bil	France	ENF	44.49	-0.96	2014 – 2020	44.50	-0.98	203	144
FR-FBn	France	ENF	43.24	5.68	2008 – 2018	43.25	5.69	0	358
FR-Fon	France	DBF	48.48	2.78	2005 – 2018	48.47	2.80	0	566
FR-Gri	France	CRO	48.84	1.95	2004 – 2018	48.86	1.95	563	313
FR-Hes	France	DBF	48.67	7.06	2014 – 2018	48.67	7.05	229	219
FR-Lam	France	CRO	43.50	1.24	2005 – 2018	43.51	1.25	548	431
FR-Tou	France	GRA	43.57	1.37	2018	43.58	1.38	46	28
IT-BFt	Italy	DBF	45.20	10.74		45.21	10.75	0	0
IT-MBo	Italy	GRA	46.01	11.05	2003 – 2018	46.00	11.04	616	582
IT-Ren	Italy	ENF	46.59	11.43	1999 – 2018	46.58	11.44	531	525
IT-SR2	Italy	ENF	43.73	10.29	2013 – 2018	43.74	10.31	255	214
IT-Tor	Italy	GRA	45.84	7.58	2008 – 2018	45.85	7.57	481	251
RU-Fy2	Russia	ENF	56.45	32.90	2015 – 2018	56.46	32.89	156	138
SE-Htm	Sweden	ENF	56.10	13.42	2015 – 2018	56.10	13.42	177	152
SE-Nor	Sweden	ENF	60.09	17.48	2014 – 2018	60.09	17.50	229	181
SE-Svb	Sweden	ENF	64.26	19.77	2014 – 2018	64.26	19.77	161	109

Table B.2: The root mean square error (RMSE) and percent bias (PBIAS) for model evapotranspiration (ET) in relation to the Integrated Carbon Observation System (ICOS) observations. Stations from ICOS that did not belong to plant functional types (PFTs) of evergreen needleleaf forest (ENF), broadleaf deciduous forest (DBF), croplands (CRO), or grasslands (GRA) or did not have overlapping periods were omitted. See Section 4.2.4. For the amount of data points per station used for the calculations, see Table B.1.

	ET RMSE [mm day^{-1}]					**ET PBIAS [%]**				
	$CLM5_{gri_d}$	**$CLM5_{PF_T}$**	**ERA5 L**	**GLAS S**	**GLEA M**	**$CLM5_{gri_d}$**	**$CLM5_{PF_T}$**	**ERA5 L**	**GLAS S**	**GLEA M**
BE-Bra	0.54	0.51	1.12	1.1	0.65	20.53	22.4	103.3	86.1	53.95
BE-Lon	0.67	0.99	0.82	0.91	0.49	12.76	24.31	66.69	43.88	19.71
CH-Cha	0.8	0.85	0.59	0.54	0.56	-33.03	-21.19	-13.73	-10.68	-8.47
CH-Dav	1.2	0.95	0.91	1.35	0.85	-51.08	-33.29	-54.41	-32.38	-27.66
CH-Fru	0.62	0.85	0.52	0.62	0.62	-23.73	-8.69	-6.68	-5.21	7.17
CZ-BK1	0.48	0.54	0.76	0.57	0.52	-23.06	-26.04	29.54	19.72	25.78
DE-Geb	0.51	0.82	0.7	0.85	0.48	-7.61	-5.35	64.26	40.08	14.93
DE-Gri	0.48	0.77	0.57	0.55	0.36	2.45	11.15	33.24	20.49	9.14
DE-Hai	0.49	0.6	0.73	0.76	0.52	2.64	8.99	58.52	46.6	31.18
DE-HoH	0.69	0.65	0.6	0.58	0.66	-28.06	-16.86	-1.62	-10.44	-24.37
DE-Kli	0.69	1	0.79	0.74	0.63	6.77	19.04	38.9	27.7	21.78

DE-RuR	0.39	0.76	0.6	0.54	0.45	-17.86	5.37	28.01	9.89	17.22
DE-RuS	0.78	0.97	0.68	0.55	0.68	-32.8	-31.45	7.9	-12.81	-24.98
DE-Tha	0.62	0.5	0.72	0.71	0.48	0.59	-0.52	39.68	20.84	13.92
DK-Sor	0.6	0.6	0.57	0.66	0.5	-26.29	-14.98	42.64	20.57	2.18
FI-Hyy	0.5	0.51	0.49	0.41	0.62	-35.58	-27.65	20.64	11.27	41.7
FI-Let	0.68	0.65	0.63	0.8	0.73	-31.77	-21.53	51.02	11.16	40.21
FI-Var	0.37	0.49	0.73	0.48	0.6	-30.13	-9.59	67.09	58.22	84.39
FR-Aur	0.85	1.19	1.1	1.05	0.78	5.44	45.08	52.04	37.1	16.89
FR-Bil	0.67	0.92	1.46	0.72	0.67	-25.5	-28.35	24.98	48.24	24.47
FR-Gri	0.77	1.01	0.9	0.85	0.58	-1.63	0.98	44.94	30.06	3.86
FR-Hes	0.58	0.67	0.83	0.86	0.72	0.19	13.09	51.71	35.65	36.79
FR-Lam	0.86	1.09	0.97	1.01	0.79	-6.76	20.9	31.79	17.15	-1.53
FR-Tou	0.69	0.89	0.86	1.04	0.49	-36.01	-45.95	60.87	30.99	17.48
IT-MBo	0.55	0.84	0.5	0.49	0.72	-2.29	-17.01	8.99	6.24	16.68
IT-Ren	0.85	0.81	0.74	0.72	0.76	-23.81	-3.55	-9.57	-15.41	2.18
IT-SR2	0.89	1.53	0.73	0.76	0.8	-34.1	-60.81	28.98	3.25	-23.83
IT-Tor	0.91	1.01	0.6	0.78	0.75	-45.19	-48.2	-38.59	-10.22	-28.59
RU-Fy2	0.4	0.51	0.65	0.69	0.7	-4.43	-16.31	52.09	26.21	54.79
SE-Htm	0.45	0.45	1.19	0.88	0.9	-7.31	-3.36	72.78	61.52	79.05
SE-Nor	0.36	0.37	0.66	0.58	0.59	-14.29	-4.12	47.2	22.25	46.44
SE-Svb	0.45	0.64	0.55	0.35	0.56	-18.82	-0.66	16.38	16.8	35.55

Table B.3: The root mean square error (RMSE) and percent bias (PBIAS) for model gross primary production (GPP) in relation to the Integrated Carbon Observation System (ICOS) observations. Stations from ICOS that did not belong to the plant functional types (PFTs) of evergreen needleleaf forest (ENF), deciduous broadleaf forest (DBF), croplands (CRO), or grasslands (GRA) or did not have overlapping periods were omitted. See Section 4.2.4. For the amount of data points per station used for the calculations, see Table B.1.

	GPP RMSE [g C day^{-1}]			GPP PBIAS [%]		
	$CLM5_{grid}$	**$CLM5_{PFT}$**	**GLASS**	**$CLM5_{grid}$**	**$CLM5_{PFT}$**	**GLASS**
BE-Bra	2.29	1.69	1.3	-35.36	0.58	4.7
BE-Dor	3.19	3.39	2.74	-41.69	-40.3	-35.11
BE-Lon	4.31	4.31	3.98	-18.21	-8.23	-11.32
CH-Cha	4.61	3.94	4.29	-50.9	-38.52	-47.17
CH-Dav	2.4	2.13	2.13	-16.93	31.37	-25.57
CH-Fru	3.6	2.84	2.62	-40.1	-23.16	-23.97
CH-Oe2	3.75	3.95	3.53	-10.8	-12.63	2.72
CZ-BK1	2.79	2.31	1.95	-37.05	-22.83	-20.65
CZ-Lnz	4.64	3.44	2.9	-62.06	-49.31	-28.91
DE-Geb	3.63	4.32	2.98	-35.96	-40.43	-1.84
DE-Gri	2.61	2.68	2.02	-21.19	-11.94	-9.65
DE-Hai	2.83	2.59	1.7	-34.83	-42.5	-1.51
DE-HoH	2.94	2.51	3.04	-30.53	-40.55	-27.82
DE-Kli	3.5	3.66	3.15	1.74	2.04	-2.73
DE-RuR	2.4	2.39	2	-26.99	-10.45	-19.5
DE-RuS	4.74	5.05	4.34	-43.49	-45.67	-34.68
DE-RuW	2.63	2.61	2.14	-32.13	-27.64	-23.88
DE-Tha	1.87	1.48	1.29	-28.99	-3.95	-19.27

Table B.4: The evapotranspiration (ET) root mean square error (RMSE) indicates the general model approximations and the percent bias (PBIAS), demonstrating systematic bias of the models (Community Land Model v5 (CLM_5) on grid-scale (CLM_{5grid}), CLM_5 on PFT scale (CLM_{5PFT}), from the European Center of Medium-Range Weather Forecasts Renalysis 5 Land (ERA_5-Land), the Global Land Surface Satellite (GLASS), and the Global Land Evaporation Amsterdam Model (GLEAM)) to the observations. Each value corresponds to a group of stations representing the same plant functional type (PFT; Evergreen Needleleaf Forest (ENF), Deciduous Broadleaf Forest (DBF), Grasslands (GRA), and Croplands (CRO)). The amount of data points (N) for each PFT is also indicated.

	PFT	**N**	**$CLM5_{grid}$**	**$CLM5_{PFT}$**	**ERA5L**	**GLASS**	**GLEAM**
RMSE [mm day^{-1}]	**ENF**	5038	0.71	0.72	0.84	0.83	0.67
	DBF	1663	0.56	0.62	0.73	0.70	0.56
	GRA	2859	0.65	0.85	0.60	0.57	0.59
	CRO	3690	0.72	1.00	0.88	0.86	0.63
	mean	3285	0.66	0.80	0.76	0.74	0.61
PBIAS	**ENF**	5038	-20.57	-15.42	21.86	13.32	15.43

[%]	**DBF**	1663	-9.90	-0.54	44.55	29.74	16.24
	GRA	2859	-18.62	-13.94	3.14	2.63	2.41
	CRO	3690	-3.24	11.20	44.99	27.30	7.58
	mean	3285	-13.08	-4.68	28.64	18.25	10.42

Table B.5: The gross primary production (GPP) root mean square error (RMSE) indicates the general model approximation and the percent bias (PBIAS), demonstrating systematic bias of the models (Community Land Model v5 ($CLM5$) on grid-scale ($CLM5_{grid}$), $CLM5$ on PFT scale ($CLM5_{PFT}$), from the European Center of Medium-Range Weather Forecasts Renalysis 5 Land ($ERA5$-Land), the Global Land Surface Satellite (GLASS), and the Global Land Evaporation Amsterdam Model (GLEAM)) to the observations. Each value corresponds to a group of stations representing the same plant functional type (PFT: Evergreen Needleleaf Forest (ENF), Deciduous Broadleaf Forest (DBF), Grasslands (GRA), and Croplands (CRO)). The amount of data points (N) for each PFT is also indicated.

	PFT	N	$CLM5_{grid}$	$CLM5_{PFT}$	GLASS
RMSE [g C day^{-1}]	ENF	5976	2.25	2.44	1.75
	DBF	2473	3.71	3.35	2.81
	GRA	2838	3.14	3.01	2.63
	CRO	3607	3.85	4.21	3.55
	mean	3723.5	3.24	3.25	2.69
PBIAS [%]	ENF	5976	-26.00	-7.7	-14.53
	DBF	2473	-38.88	-43.76	-24.51
	GRA	2838	-30.73	-25.5	-21.34
	CRO	3607	-14.99	-1.48	-6.29
	mean	3723.5	-27.65	-19.61	-16.67

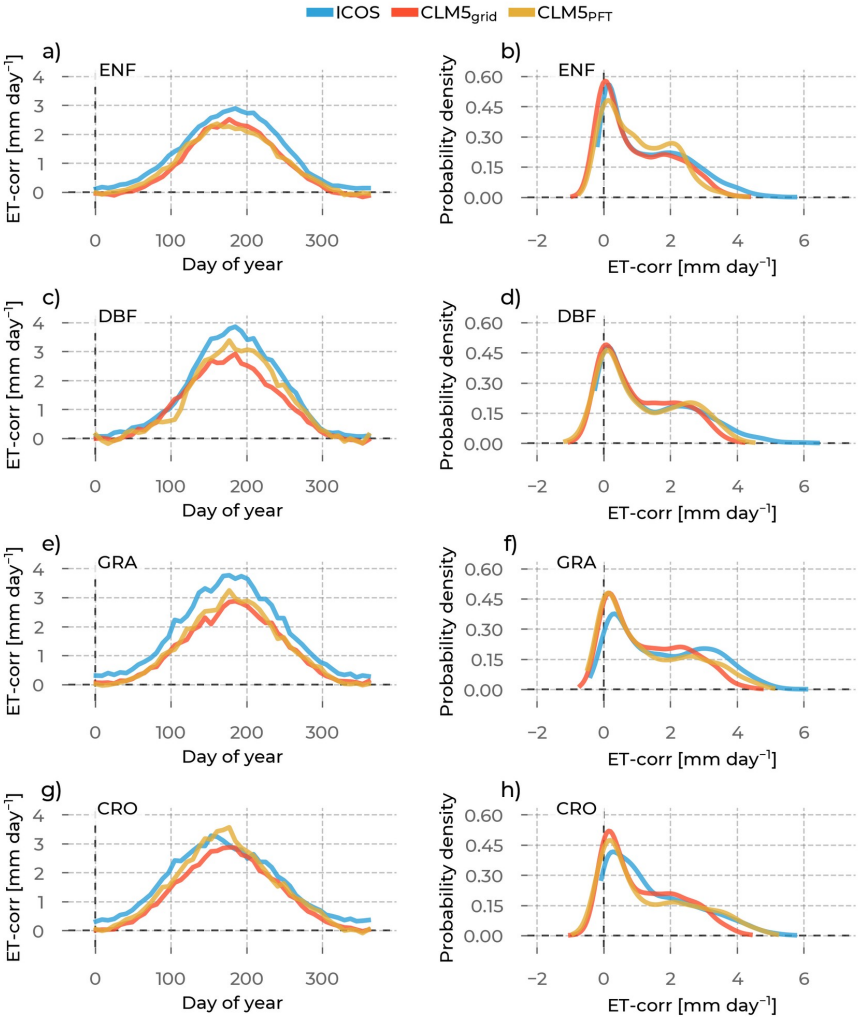

Figure B.1: In the left column are the yearly energy balance corrected evapotranspiration (ET-corr) evolutions averaged across stations belonging to one PFT (rows). We differentiate the data source by color (ICOS observations: blue, $CLM5_{grid}$: red, $CLM5_{PFT}$: yellow, GLASS: green, ERA5L: brown, GLEAM: purple). The probability density curves for all ET-corr values from stations belonging to the selected PFT are in the right column. Each row shows these plots for one PFT: Evergreen Needleleaf Forest (ENF), Deciduous Broadleaf Forest (DBF), Grasslands (GRA), and Croplands (CRO).

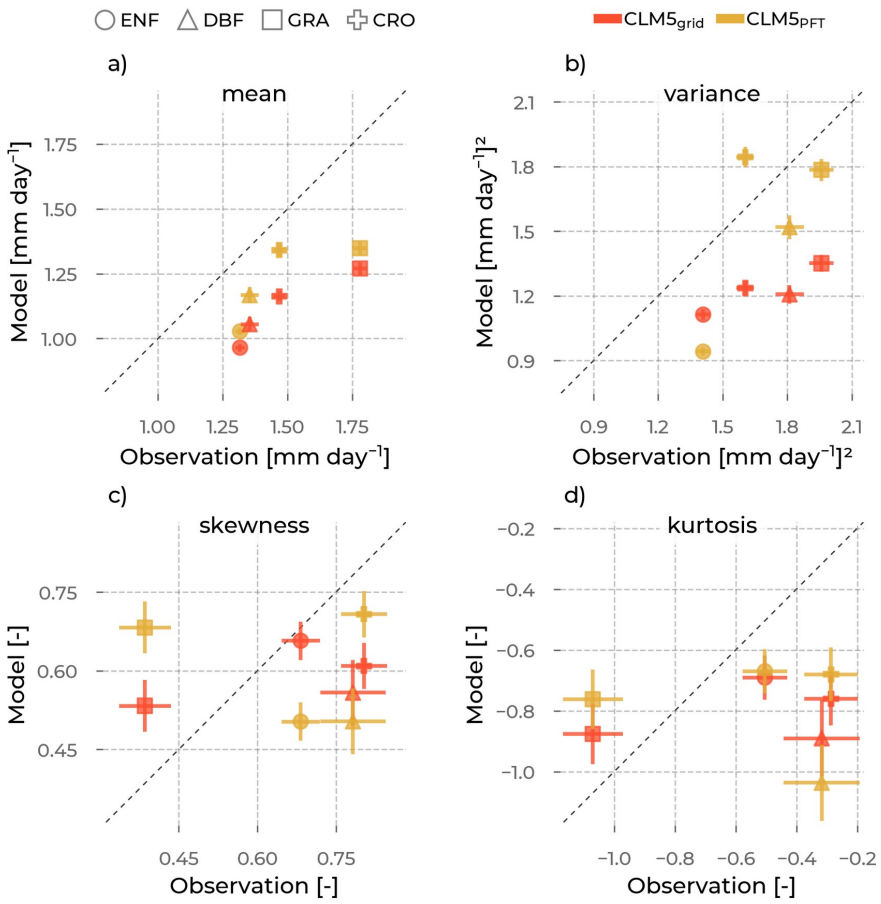

Figure B.2: The mean (a), variance (b), skewness (c), and excess kurtosis (d) of the ET-corr distributions (visualized in Figure B.1) from the models (color, y-axis), as opposed to the corresponding values from observations (x-axis) aggregated for each PFT (marker type): Evergreen Needleleaf Forest (ENF), Deciduous Broadleaf Forest (DBF), Grasslands (GRA), Croplands (CRO). The error bars are the standard errors of the respective moment, depending on the sample size.

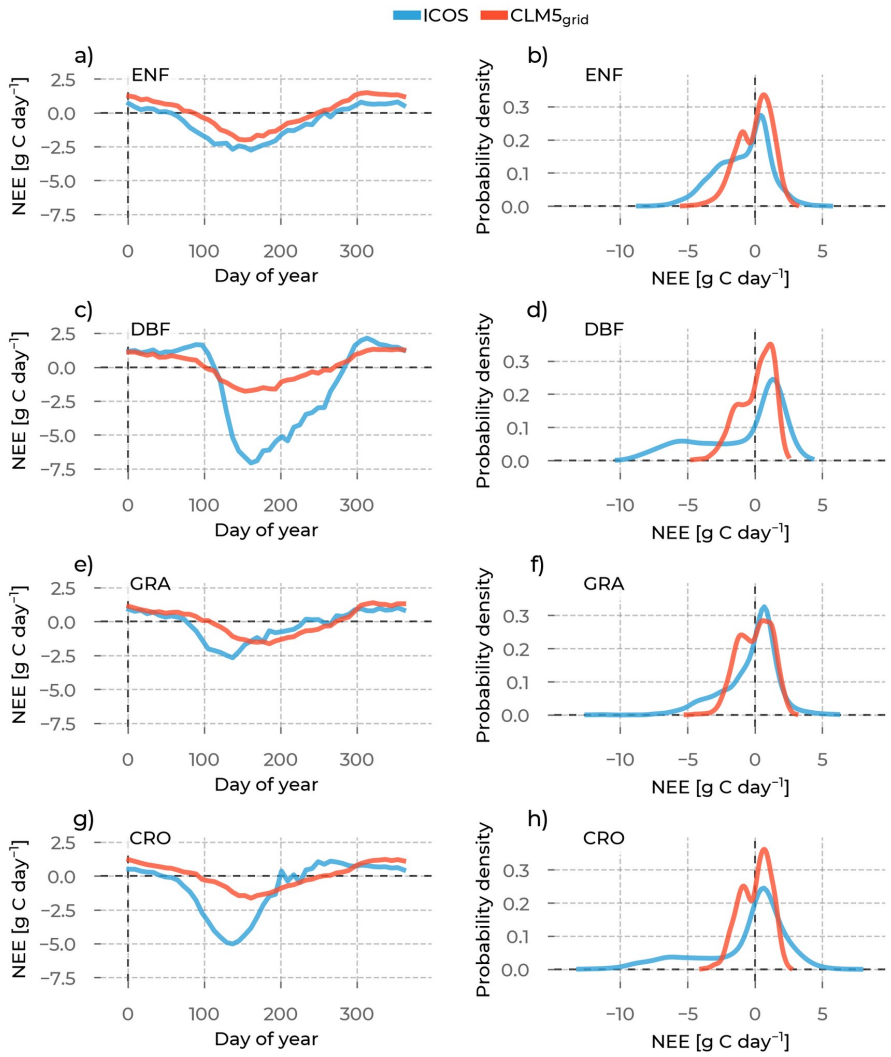

Figure B.3: In the left column are the yearly net ecosystem exchange (NEE) evolutions averaged across stations belonging to one PFT (rows). We differentiate the data source by color (ICOS observations: blue, $CLM5_{grid}$: red, $CLM5_{PFT}$: yellow, GLASS: green, $ERA5L$: brown, GLEAM: purple). The probability density curves for all NEE values from stations belonging to the selected PFT are in the right column. Each row shows these plots for one PFT: Evergreen Needleleaf Forest (ENF), Deciduous Broadleaf Forest (DBF), Grasslands (GRA), and Croplands (CRO).

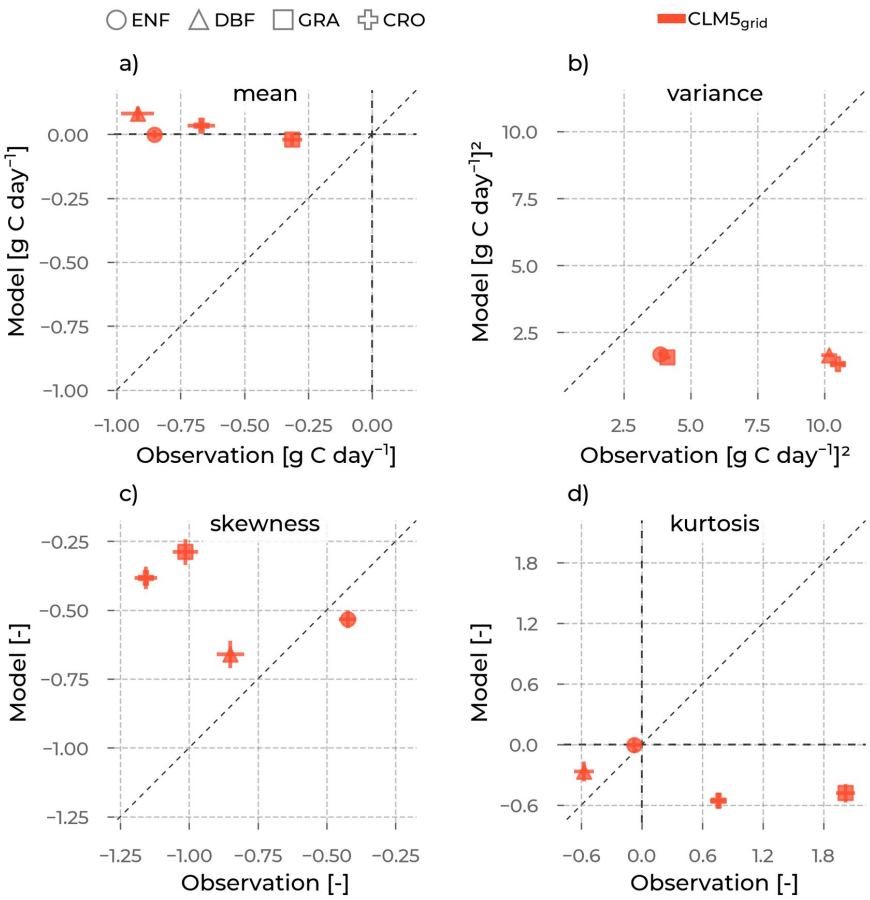

Figure B.4: The mean (a), variance (b), skewness (c), and excess kurtosis (d) of the NEE distributions (visualized in Figure B.3) from the models (color, y-axis), as opposed to the corresponding values from observations (x-axis) aggregated for each PFT (marker type): Evergreen Needleleaf Forest (ENF), Deciduous Broadleaf Forest (DBF), Grasslands (GRA), Croplands (CRO). The error bars are the standard errors of the respective moment, depending on the sample size.

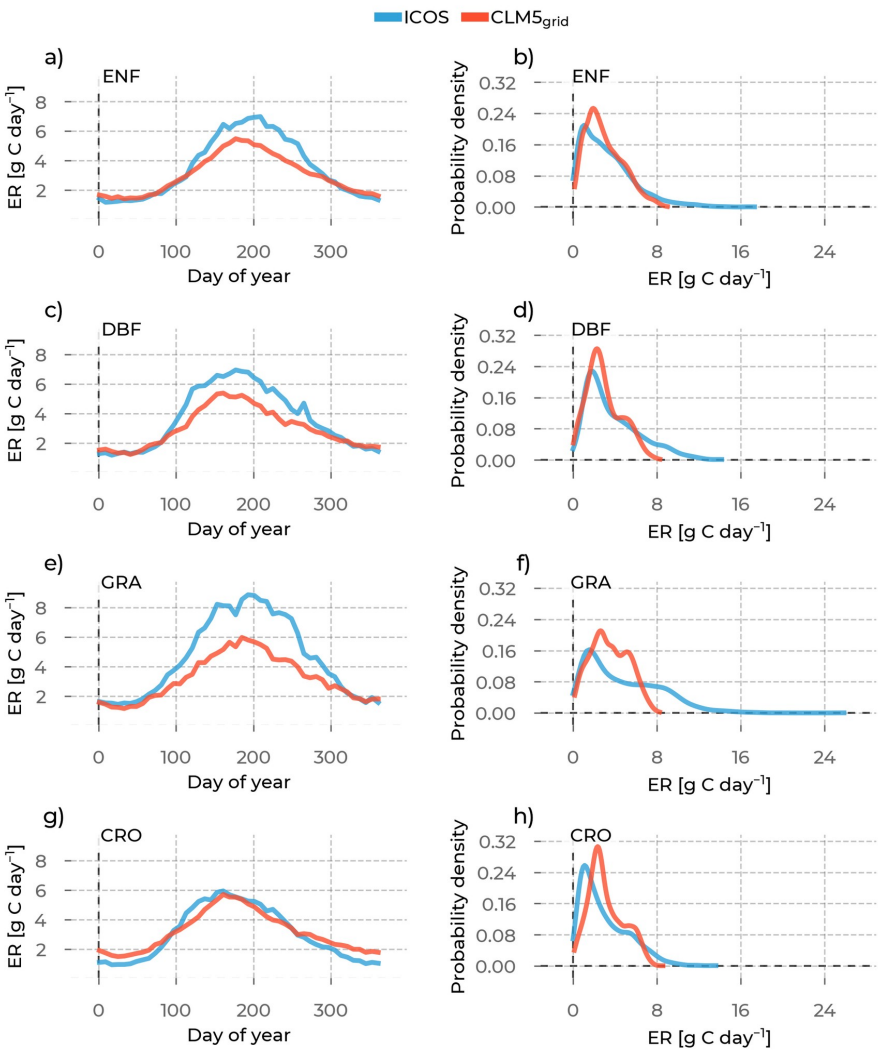

Figure B.5: In the left column are the yearly ecosystem respiration (ER) evolutions averaged across stations belonging to one PFT (rows). We differentiate the data source by color (ICOS observations: blue, $CLM5_{grid}$: red, $CLM5_{PFT}$: yellow, GLASS: green, $ERA5L$: brown, GLEAM: purple). The probability density curves for all ER values from stations belonging to the selected PFT are in the right column. Each row shows these plots for one PFT: Evergreen Needleleaf Forest (ENF), Deciduous Broadleaf Forest (DBF), Grasslands (GRA), and Croplands (CRO).

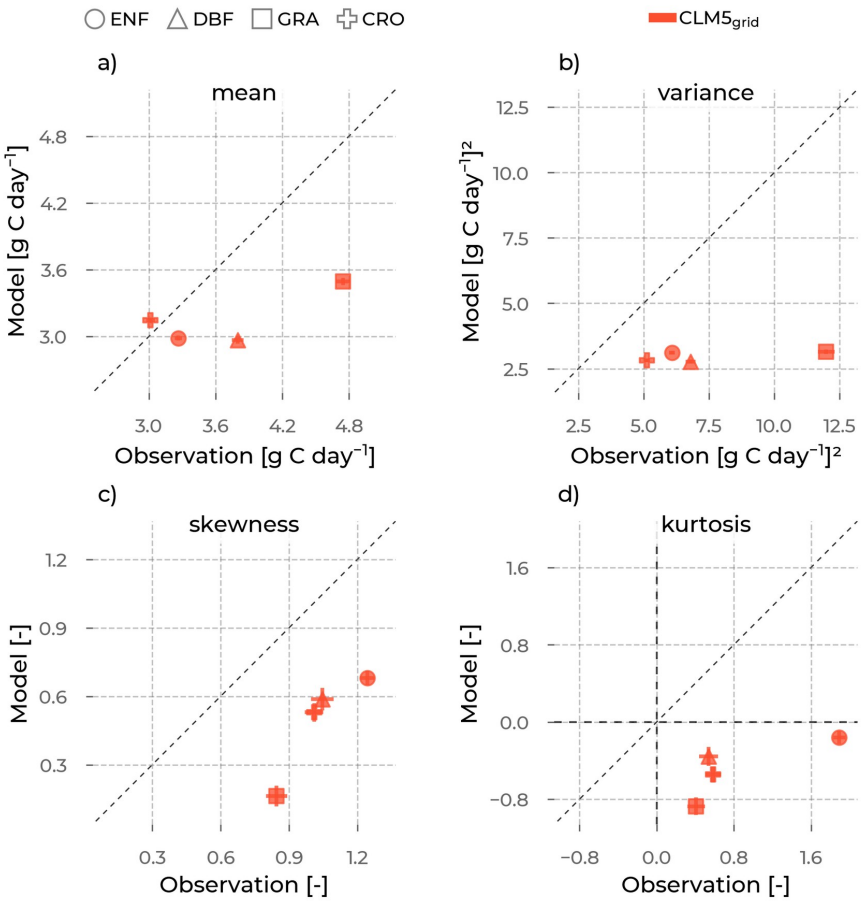

Figure B.6: The mean (a), variance (b), skewness (c), and excess kurtosis (d) of the ER distributions (visualized in Figure B.5) from the models (color, y-axis), as opposed to the corresponding values from observations (x-axis) aggregated for each PFT (marker type): Evergreen Needleleaf Forest (ENF), Deciduous Broadleaf Forest (DBF), Grasslands (GRA), Croplands (CRO). The error bars are the standard errors of the respective moment, depending on the sample size.

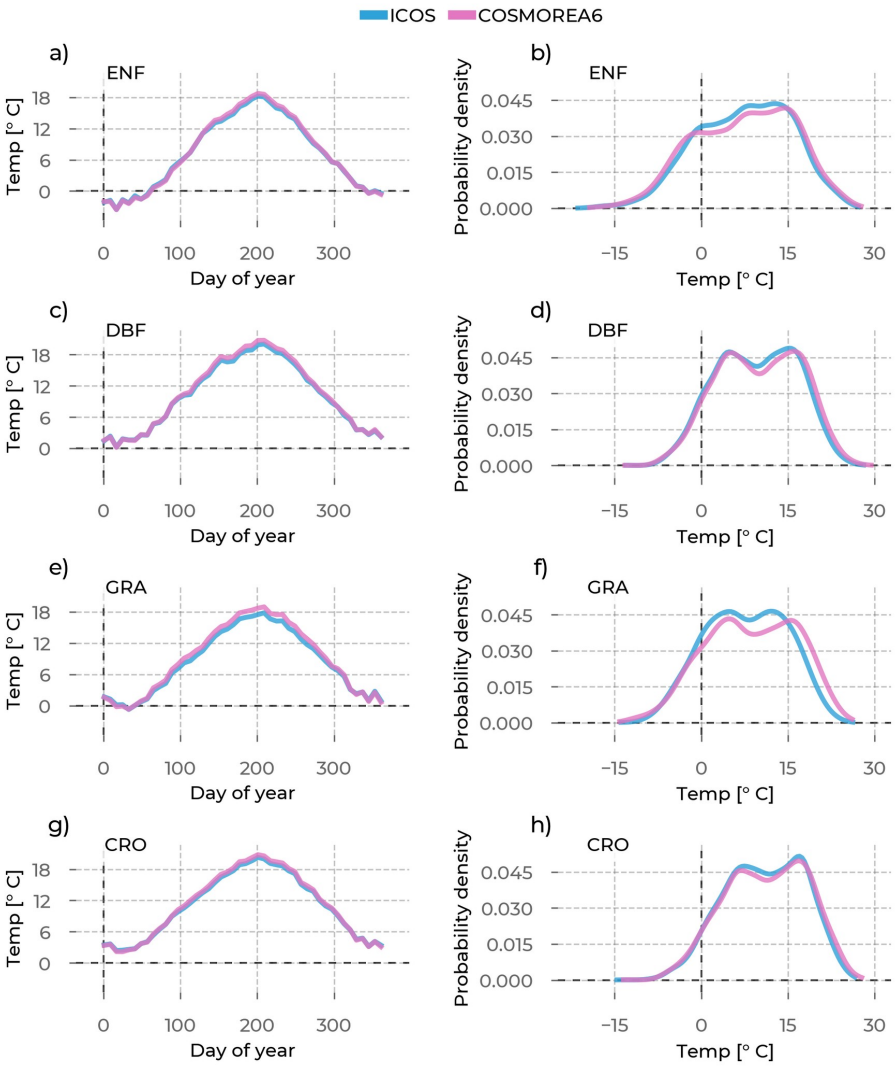

Figure B.7: In the left column are the yearly Temperature (Temp) evolutions averaged across stations belonging to one PFT (rows). We differentiate the data source by color (ICOS observations: blue, $CLM5_{grid}$: red, $CLM5_{PFT}$: yellow, GLASS: green, ERA5L: brown, GLEAM: purple). The probability density curves for all Temp values from stations belonging to the selected PFT are in the right column. Each row shows these plots for one PFT: Evergreen Needleleaf Forest (ENF), Deciduous Broadleaf Forest (DBF), Grasslands (GRA), and Croplands (CRO).

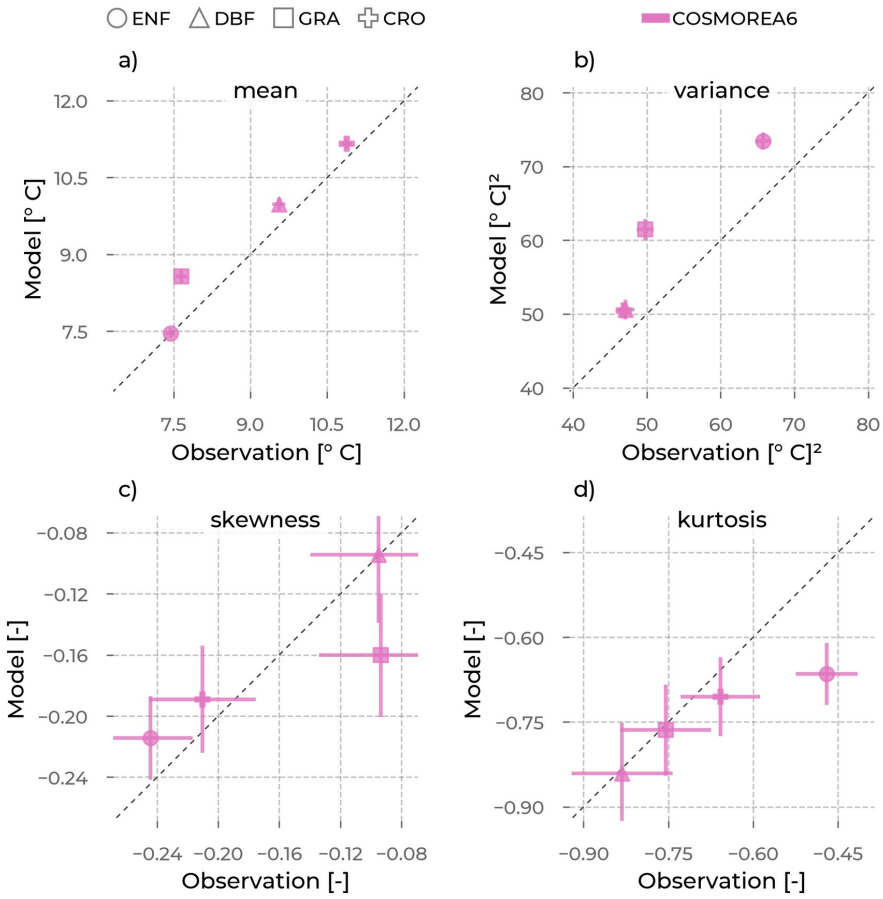

Figure B.8: The mean (a), variance (b), skewness (c), and excess kurtosis (d) of the Temp distributions (visualized in Figure B.7) from the models (color, y-axis), as opposed to the corresponding values from observations (x-axis) aggregated for each PFT (marker type): Evergreen Needleleaf Forest (ENF), Deciduous Broadleaf Forest (DBF), Grasslands (GRA), Croplands (CRO). The error bars are the standard errors of the respective moment, depending on the sample size.

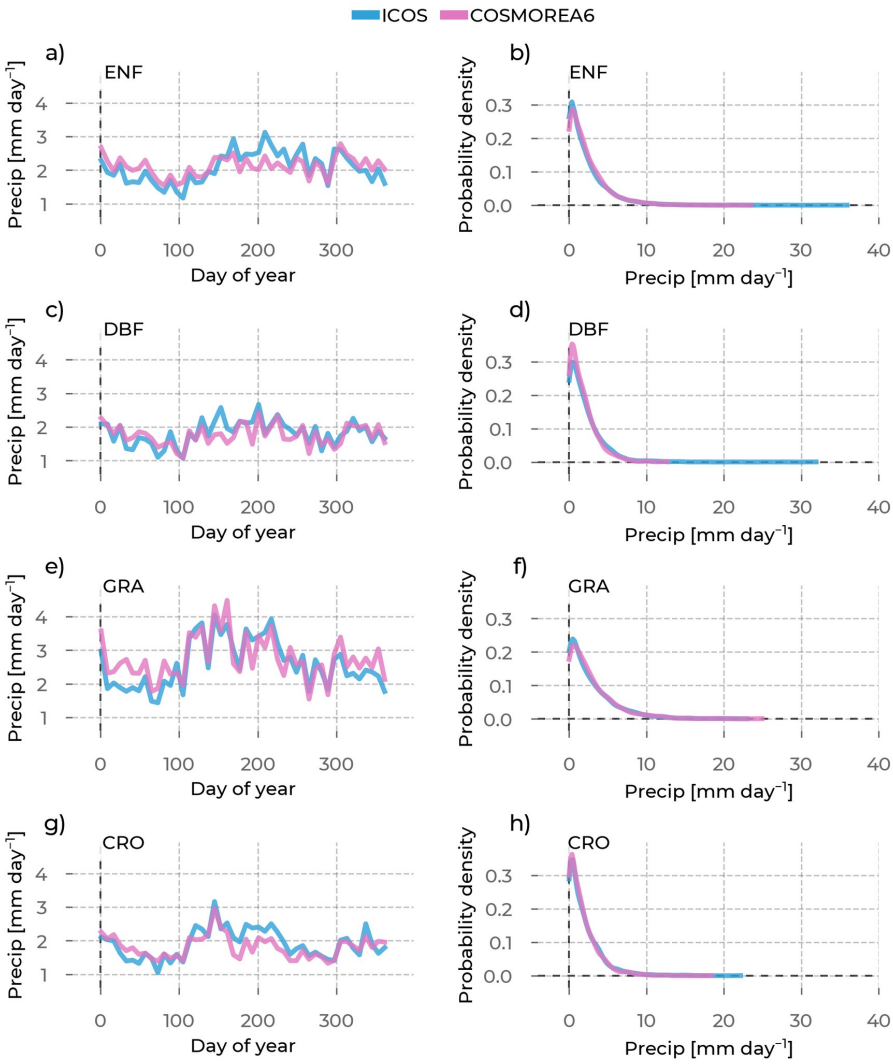

Figure B.9: In the left column are the yearly Precipitation (Precip) evolutions averaged across stations belonging to one PFT (rows). We differentiate the data source by color (ICOS observations: blue, $CLM5_{grid}$: red, $CLM5_{PFT}$: yellow, GLASS: green, $ERA5L$: brown, GLEAM: purple). The probability density curves for all Precip values from stations belonging to the selected PFT are in the right column. Each row shows these plots for one PFT: Evergreen Needleleaf Forest (ENF), Deciduous Broadleaf Forest (DBF), Grasslands (GRA), and Croplands (CRO).

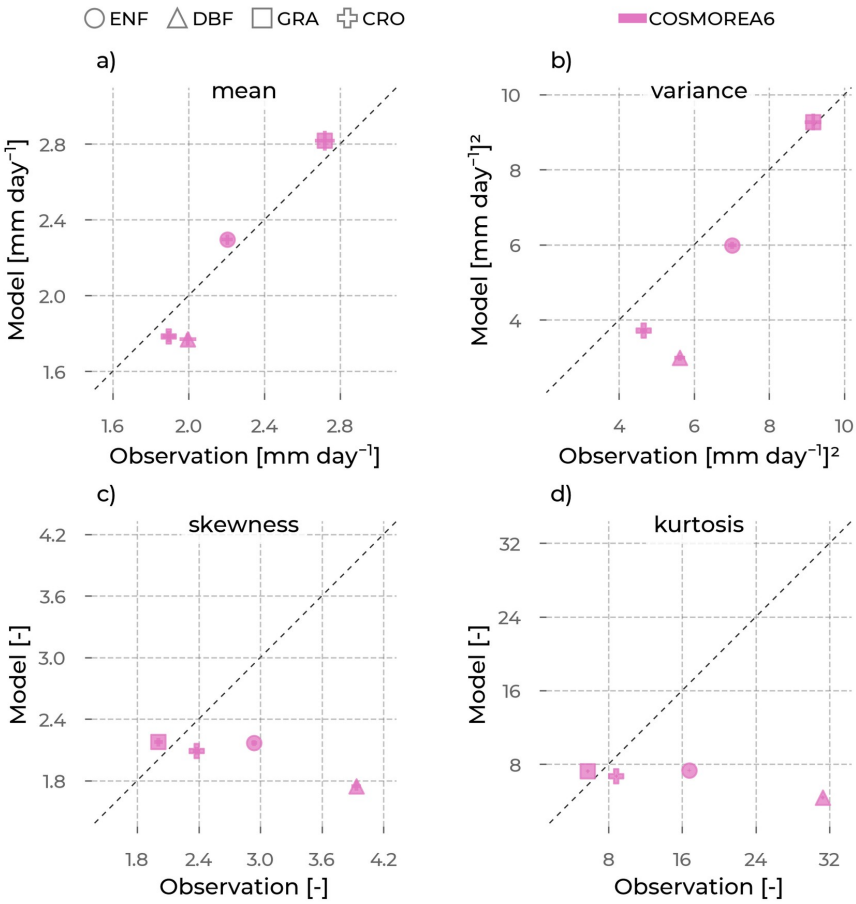

Figure B.10: The mean (a), variance (b), skewness (c), and excess kurtosis (d) of the Precip distributions (visualized in Figure B.9) from the models (color, y-axis), as opposed to the corresponding values from observations (x-axis) aggregated for each PFT (marker type): Evergreen Needleleaf Forest (ENF), Deciduous Broadleaf Forest (DBF), Grasslands (GRA), Croplands (CRO). The error bars are the standard errors of the respective moment, depending on the sample size.

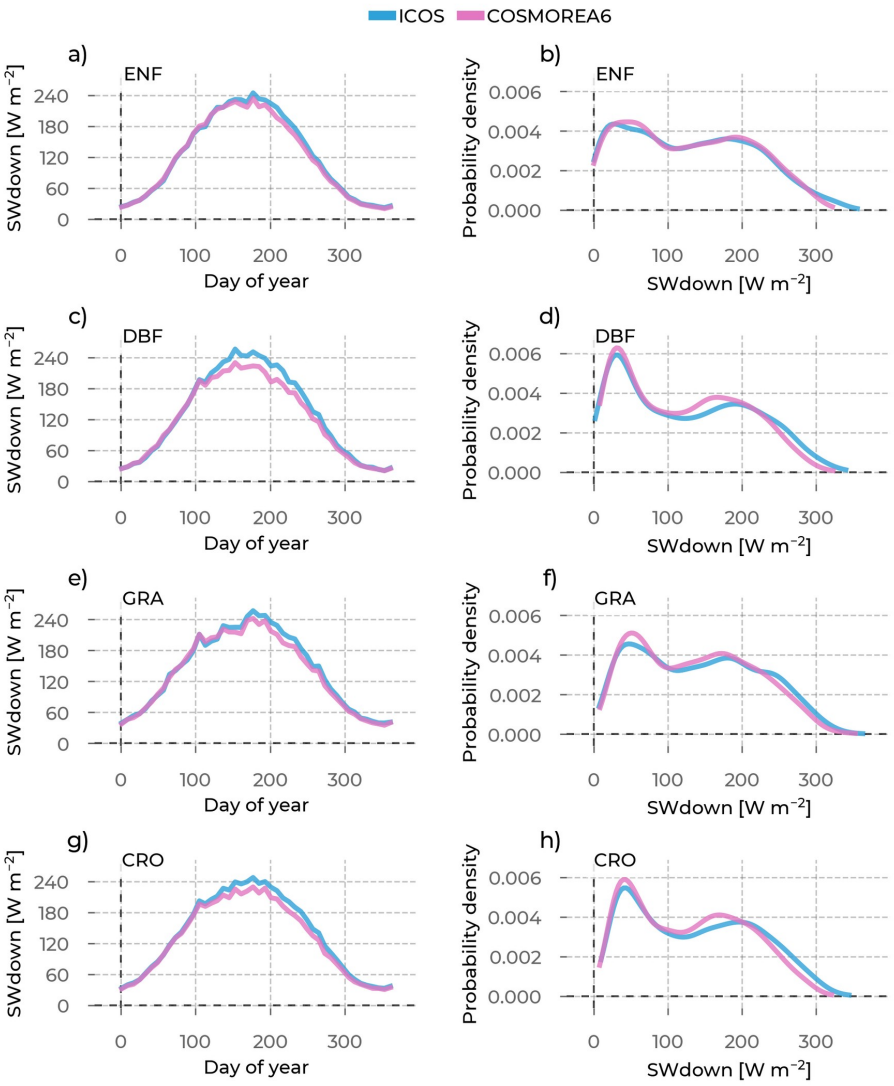

Figure B.11: In the left column are the yearly shortwave downward radiation (SWdown) evolutions averaged across stations belonging to one PFT (rows). We differentiate the data source by color (ICOS observations: blue, $CLM5_{grid}$: red, $CLM5_{PFT}$: yellow, GLASS: green, ERA5L: brown, GLEAM: purple). The probability density curves for all SWdown values from stations belonging to the selected PFT are in the right column. Each row shows these plots for one PFT: Evergreen Needleleaf Forest (ENF), Deciduous Broadleaf Forest (DBF), Grasslands (GRA), and Croplands (CRO).

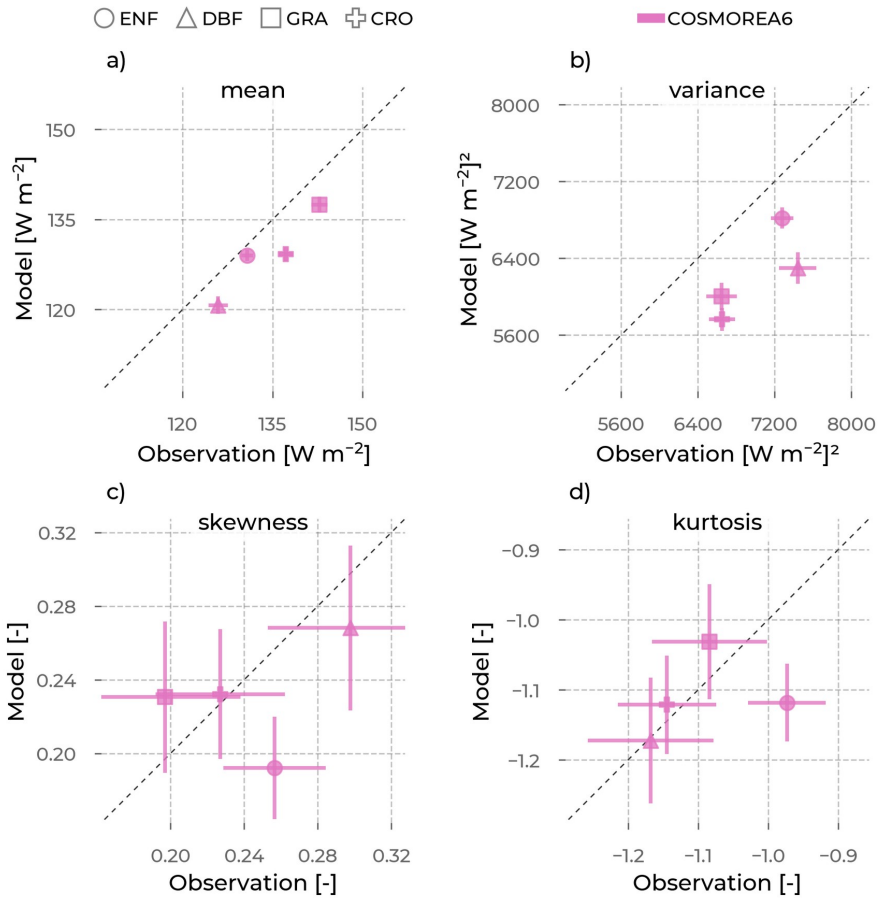

Figure B.12: The mean (a), variance (b), skewness (c), and excess kurtosis (d) of the SWdown distributions (visualized in Figure B.11) from the models (color, y-axis), as opposed to the corresponding values from observations (x-axis) aggregated for each PFT (marker type): Evergreen Needleleaf Forest (ENF), Deciduous Broadleaf Forest (DBF), Grasslands (GRA), Croplands (CRO). The error bars are the standard errors of the respective moment, depending on the sample size.

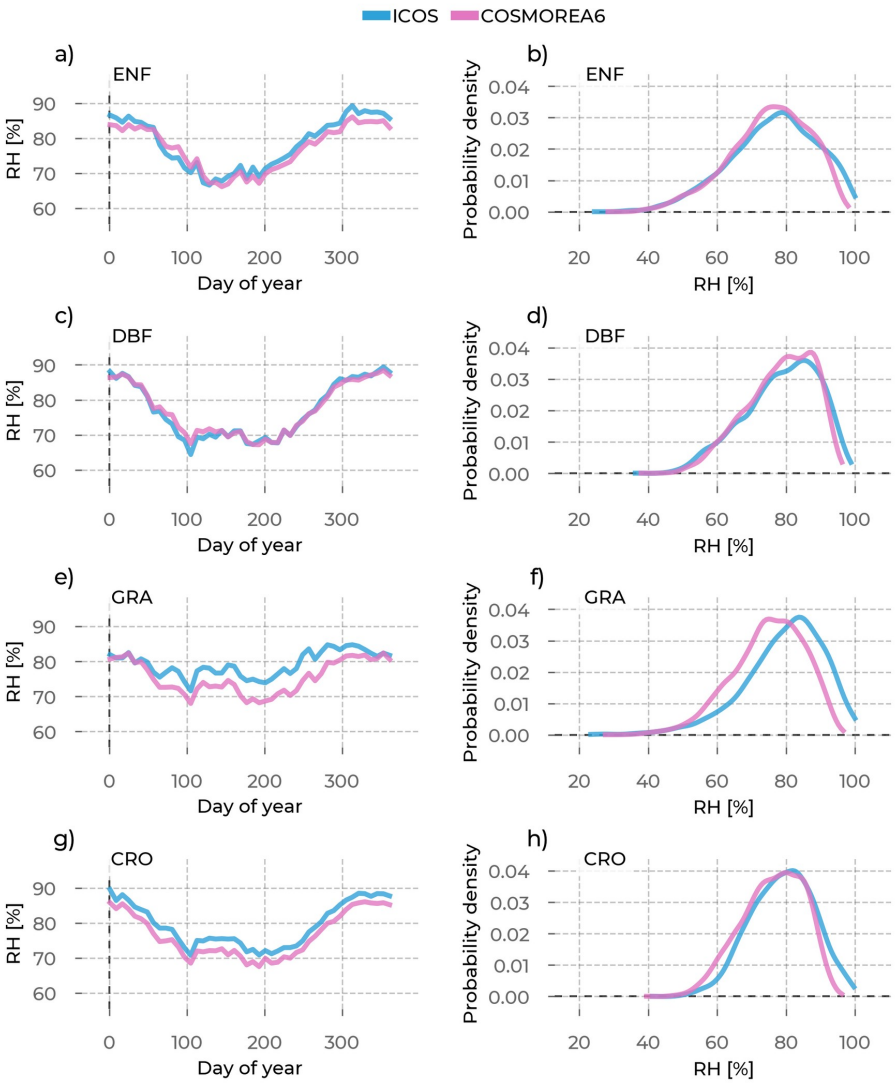

Figure B.13: In the left column are the yearly relative humidity (RH) evolutions averaged across stations belonging to one PFT (rows). We differentiate the data source by color (ICOS observations: blue, $CLM5_{grid}$: red, $CLM5_{PFT}$: yellow, GLASS: green, ERA5L: brown, GLEAM: purple). The probability density curves for all RH values from stations belonging to the selected PFT are in the right column. Each row shows these plots for one PFT: Evergreen Needleleaf Forest (ENF), Deciduous Broadleaf Forest (DBF), Grasslands (GRA), and Croplands (CRO).

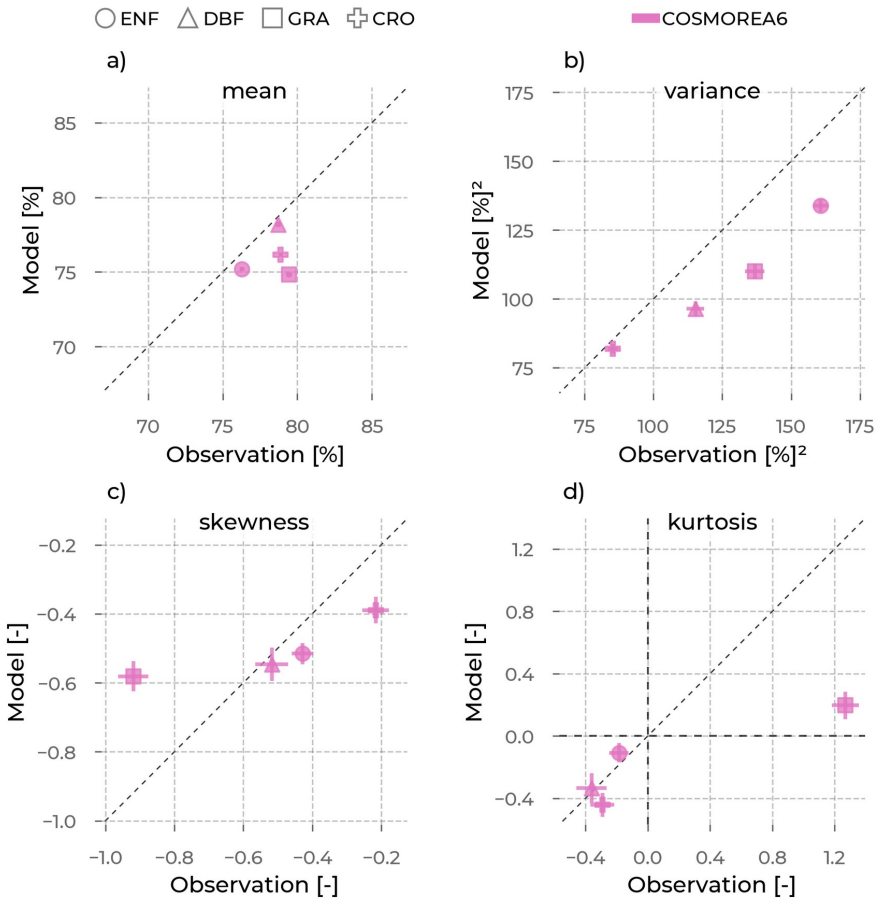

Figure B.14: The mean (a), variance (b), skewness (c), and excess kurtosis (d) of the RH distributions (visualized in Figure B.13) from the models (color, y-axis), as opposed to the corresponding values from observations (x-axis) aggregated for each PFT (marker type): Evergreen Needleleaf Forest (ENF), Deciduous Broadleaf Forest (DBF), Grasslands (GRA), Croplands (CRO). The error bars are the standard errors of the respective moment, depending on the sample size.

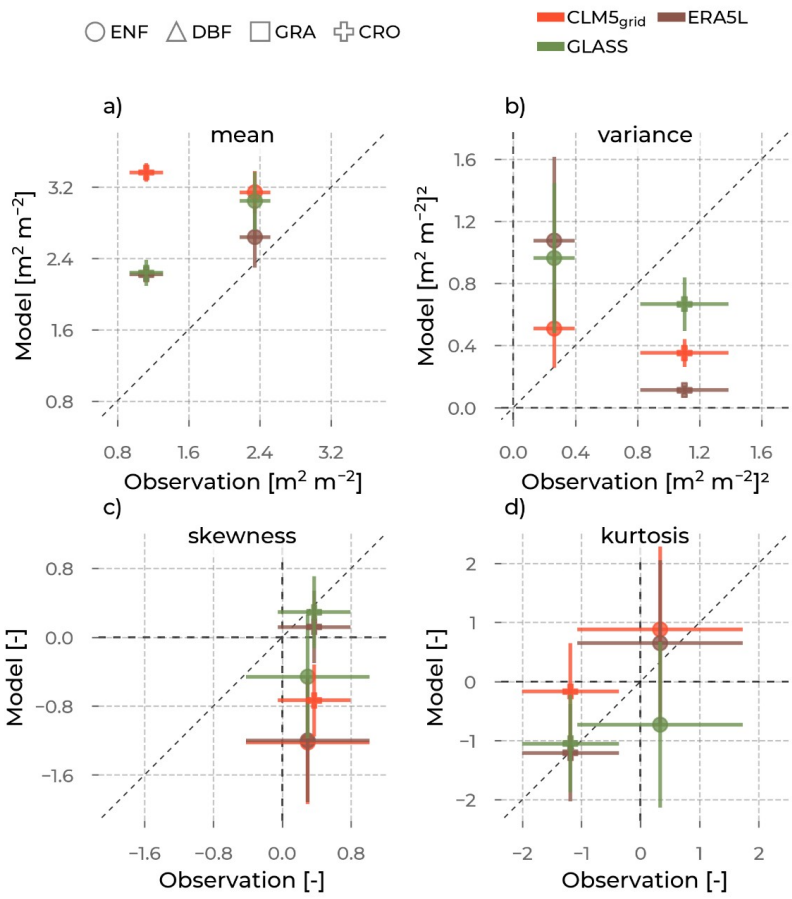

Figure B.15: The mean (a), variance (b), skewness (c), and excess kurtosis (d) of the leaf area index (LAI) distributions from the models (color, y-axis), as opposed to the corresponding values from observations (x-axis) aggregated for each plant functional type (marker type): Evergreen Needleleaf Forest (ENF), Deciduous Broadleaf Forest (DBF), Grasslands (GRA), Croplands (CRO). The error bars are the standard errors of the respective moment, depending on the sample size.

C Appendix to: The drought response of European ecosystem processes via multiple components of the hydrological cycle

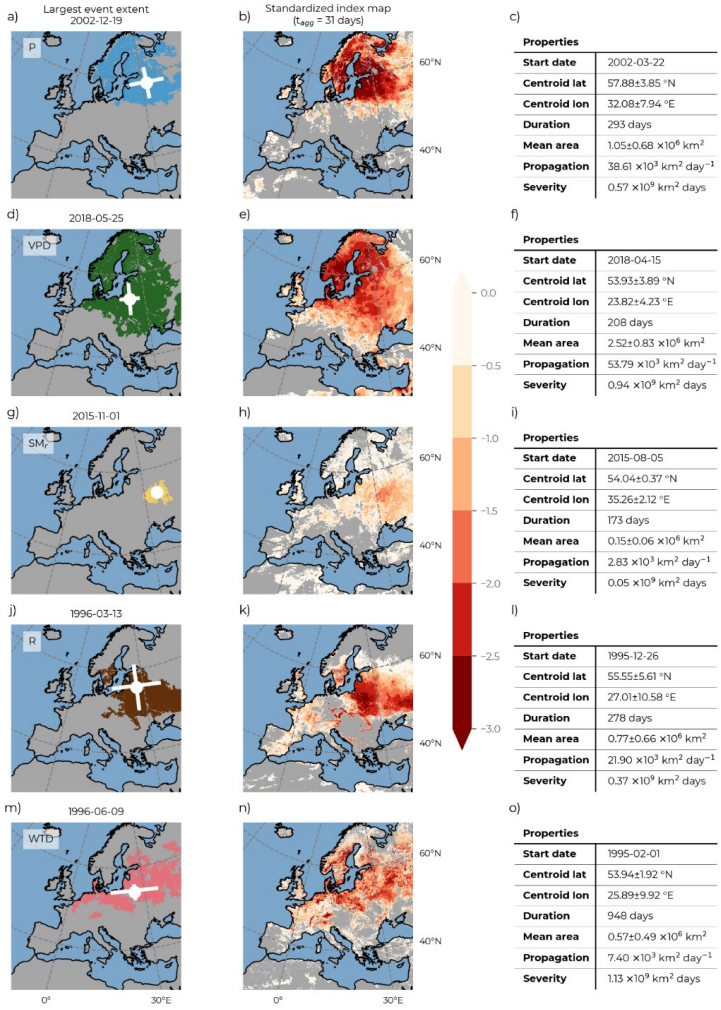

Figure C.1: For each hydrological variable, per row, precipitation (P), vapor pressure deficit (VPD), runoff (R), and groundwater (per water table depth, WTD), these are insights into the largest detected event cluster for the 1-monthly (31 days) aggregation period. The maps on the left show the maximum extent of the event, and in the center, maps with the drought indices at that corresponding point in time. On the right, the tables list the properties of the selected largest event cluster.

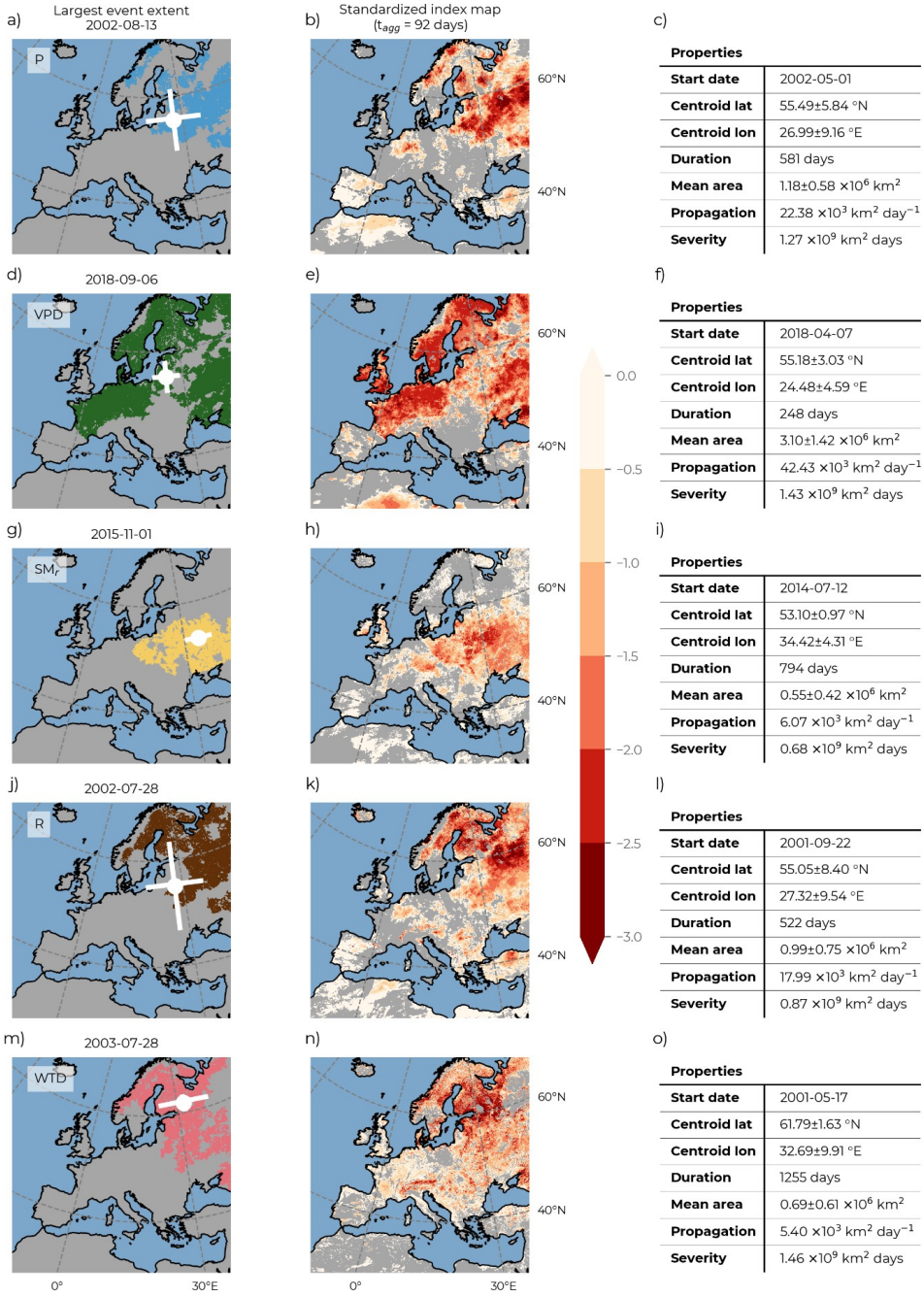

Figure C.2: For each hydrological variable, per row, precipitation (P), vapor pressure deficit (VPD), runoff (R), and groundwater (per water table depth, WTD), these are insights into the largest detected event cluster for the 3-monthly (92 days) aggregation period. The maps on the left show the maximum extent of the event,

and in the center, maps with the drought indices at the corresponding point in time. On the right, the tables list the properties of the selected largest event cluster.

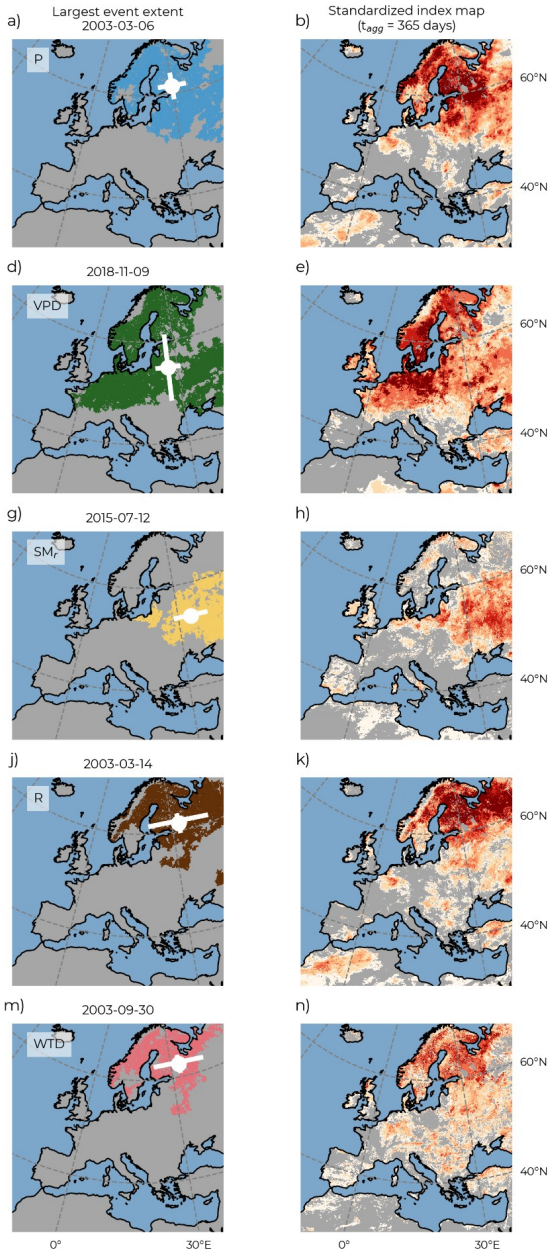

c)

Properties	
Start date	2002-03-30
Centroid lat	61.46±2.63 °N
Centroid lon	30.06±5.66 °E
Duration	794 days
Mean area	0.99±0.78 ×10^6 km^2
Propagation	10.89 ×10^3 km^2 day^{-1}
Severity	1.38 ×10^9 km^2 days

f)

Properties	
Start date	2013-06-18
Centroid lat	54.73±6.50 °N
Centroid lon	26.79±4.27 °E
Duration	2018 days
Mean area	0.83±0.97 ×10^6 km^2
Propagation	6.96 ×10^3 km^2 day^{-1}
Severity	2.74 ×10^9 km^2 days

i)

Properties	
Start date	2014-04-23
Centroid lat	53.61±1.13 °N
Centroid lon	34.13±5.68 °E
Duration	1232 days
Mean area	0.59±0.50 ×10^6 km^2
Propagation	2.44 ×10^3 km^2 day^{-1}
Severity	1.26 ×10^9 km^2 days

l)

Properties	
Start date	2001-06-10
Centroid lat	61.46±1.96 °N
Centroid lon	32.80±12.25 °E
Duration	1175 days
Mean area	0.66±0.60 ×10^6 km^2
Propagation	6.88 ×10^3 km^2 day^{-1}
Severity	1.39 ×10^9 km^2 days

o)

Properties	
Start date	1999-08-21
Centroid lat	62.49±1.81 °N
Centroid lon	33.30±10.46 °E
Duration	2184 days
Mean area	0.56±0.45 ×10^6 km^2
Propagation	1.76 ×10^3 km^2 day^{-1}
Severity	1.94 ×10^9 km^2 days

Figure C.3: For each hydrological variable, per row, precipitation (P), vapor pressure deficit (VPD), runoff (R), and groundwater (per water table depth, WTD), these are insights into the largest detected event cluster for the 12-monthly (365 days) aggregation period. The maps on the left show the maximum extent of the event, and in the center, maps with the drought indices at the corresponding point in time. On the right, the tables list the properties of the selected largest event cluster.

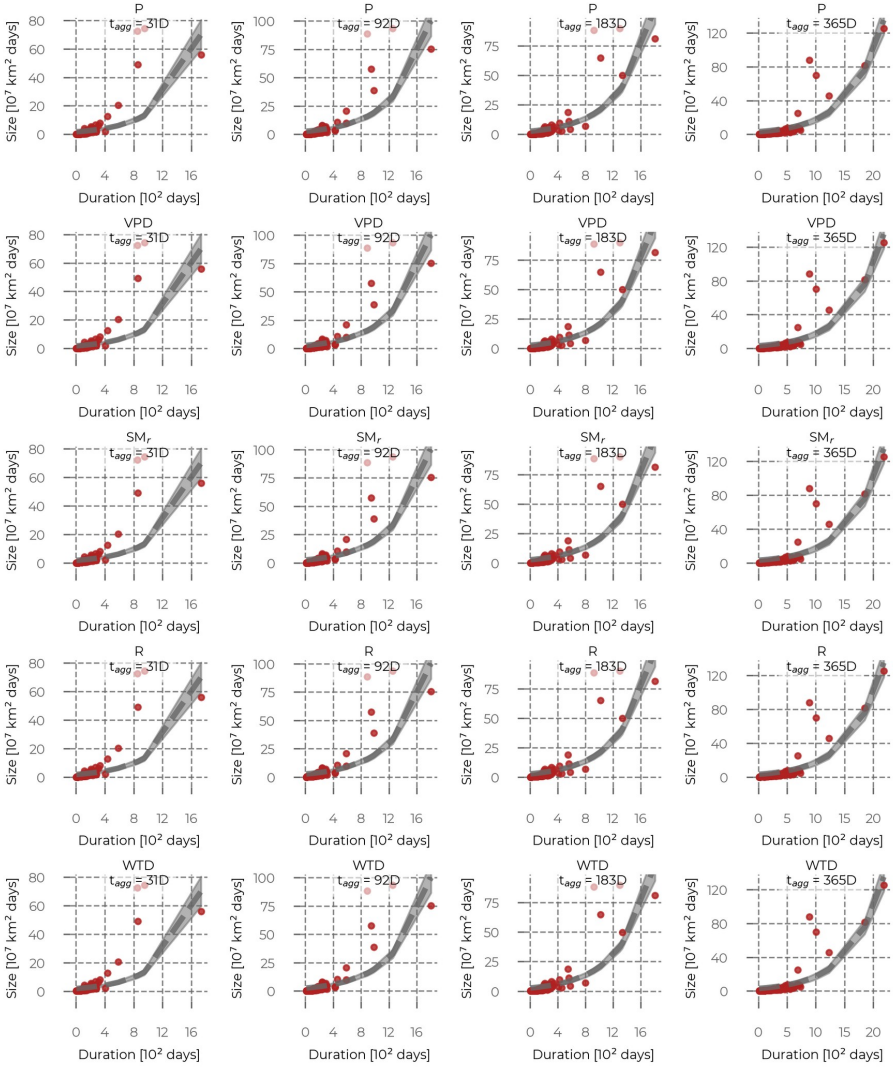

Figure C.4: Diagrams showing the size against the duration of each drought event for each hydrological variable (rows, P: precipitation, VPD: vapor pressure deficit, SMr: rootzone soil moisture, R: runoff, WTD: water table depth) and each aggregation period (t_{agg}, columns). The grey line is the fitted power curve with the 95% confidence interval.

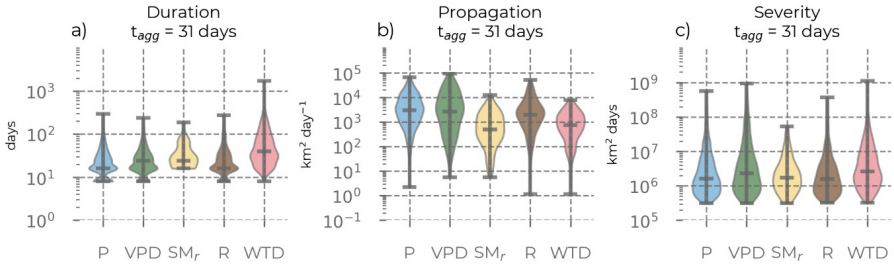

Figure C.5: The violin plots characterize the distribution of key event properties (y-axis) across all identified precipitation (P), vapor pressure deficit (VPD), rootzone soil moisture (SM_r), runoff (R), and groundwater (per water table depth, WTD) drought events (x-axis) of 1-monthly (31 days) aggregation period.

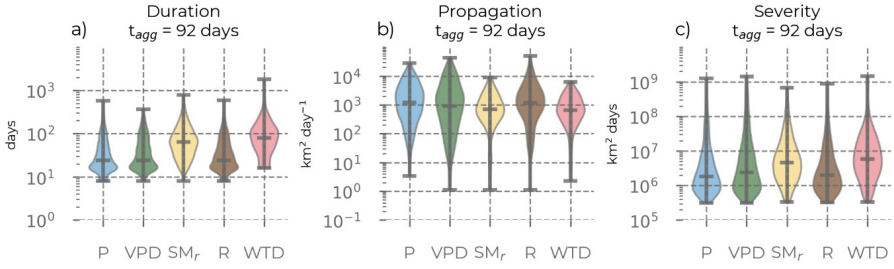

Figure C.6: The violin plots characterize the distribution of key event properties (y-axis) across all identified precipitation (P), vapor pressure deficit (VPD), rootzone soil moisture (SM_r), runoff (R), and groundwater (per water table depth, WTD) drought events (x-axis) of 3-monthly (92 days) aggregation period.

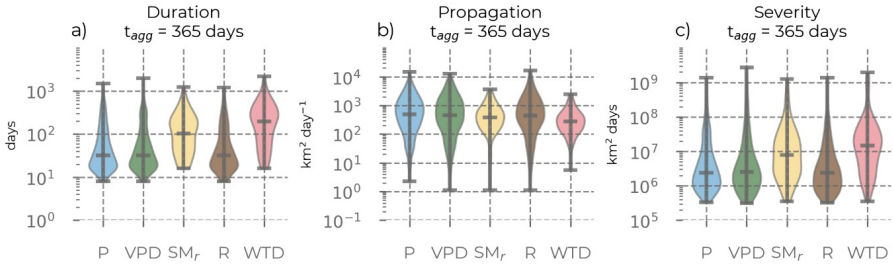

Figure C.7: The violin plots characterize the distribution of key event properties (y-axis) across all identified precipitation (P), vapor pressure deficit (VPD), rootzone soil moisture (SM_r), runoff (R), and groundwater (per water table depth, WTD) drought events (x-axis) of 1-yealy (365 days) aggregation period.

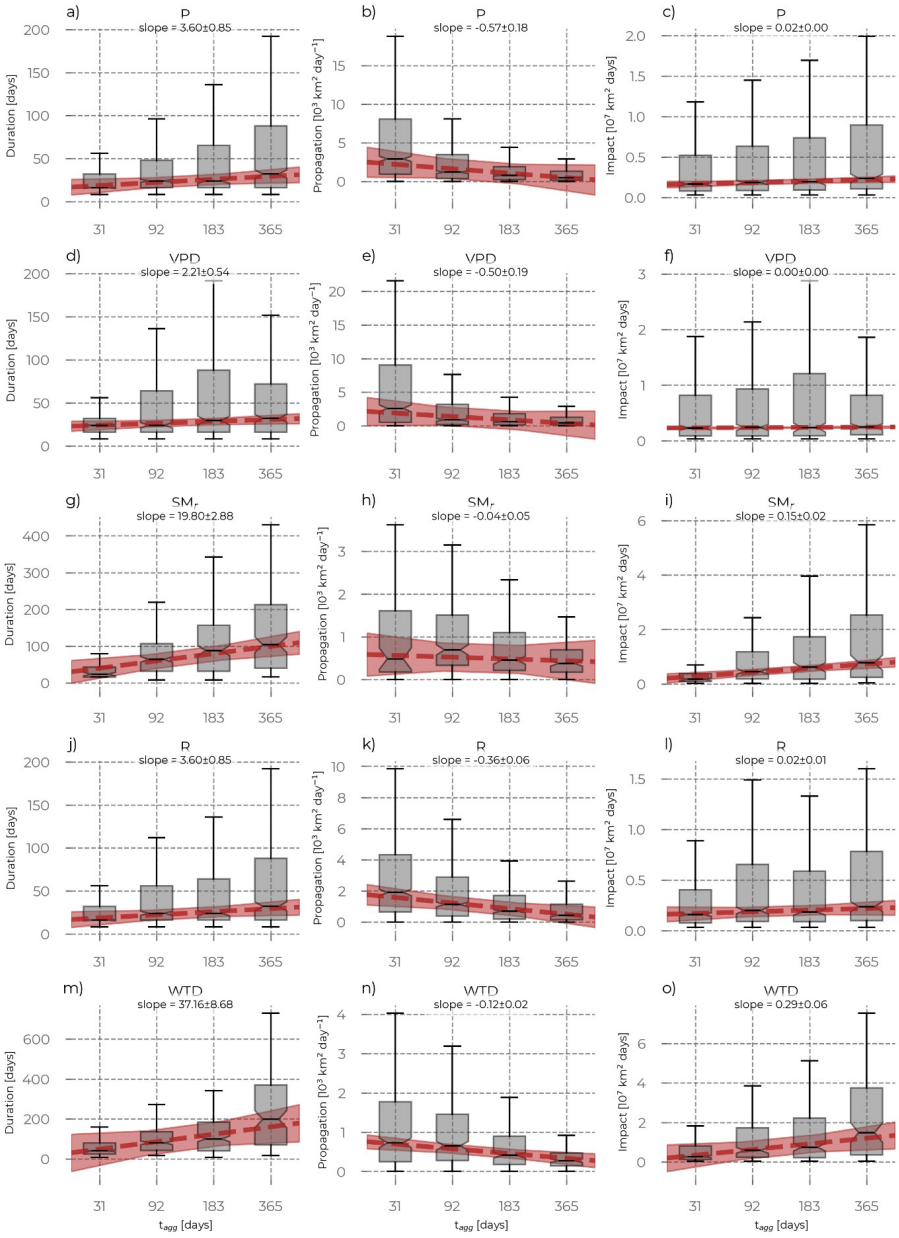

Figure C.8: Each box plot depicts the distribution of drought event properties (y-axis, in logarithmic scale. Left column: duration, center column: propagation speed, right column: severity) for each of the drought index variables precipitation (P), vapor pressure deficit (VPD), rootzone soil moisture (SM_r), surface runoff (R), and groundwater (per water table depth, WTD) and each drought deficit aggregation period (t_{agg}: 31days, 92 days, 183 days, 365 days corresponding to monthly, 3-monthly, 6-monthly and yearly). The red dashed line is a simple linear regression of the medians, exemplifying the effect of increasing t_{agg} on the drought event properties.

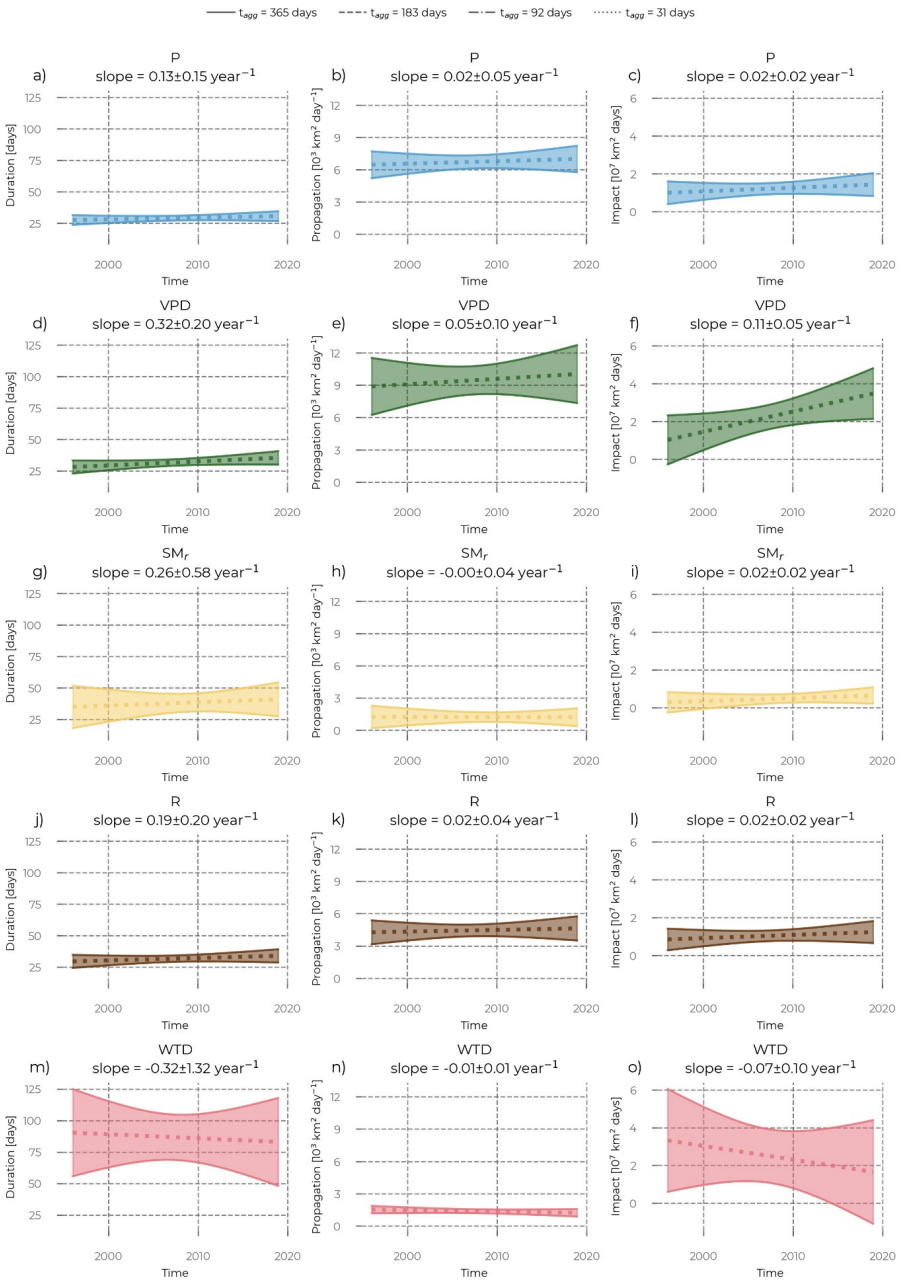

Figure C.9: Temporal trends of the drought event properties (see y-axis label) for precipitation (P), vapor pressure deficit (VPD), runoff (R), and groundwater (per water table depth, WTD) for the 31-day aggregation period. The shaded area around the line is the 95% confidence interval. The exact interception and slope values, including their uncertainty, are given in Table C.1.

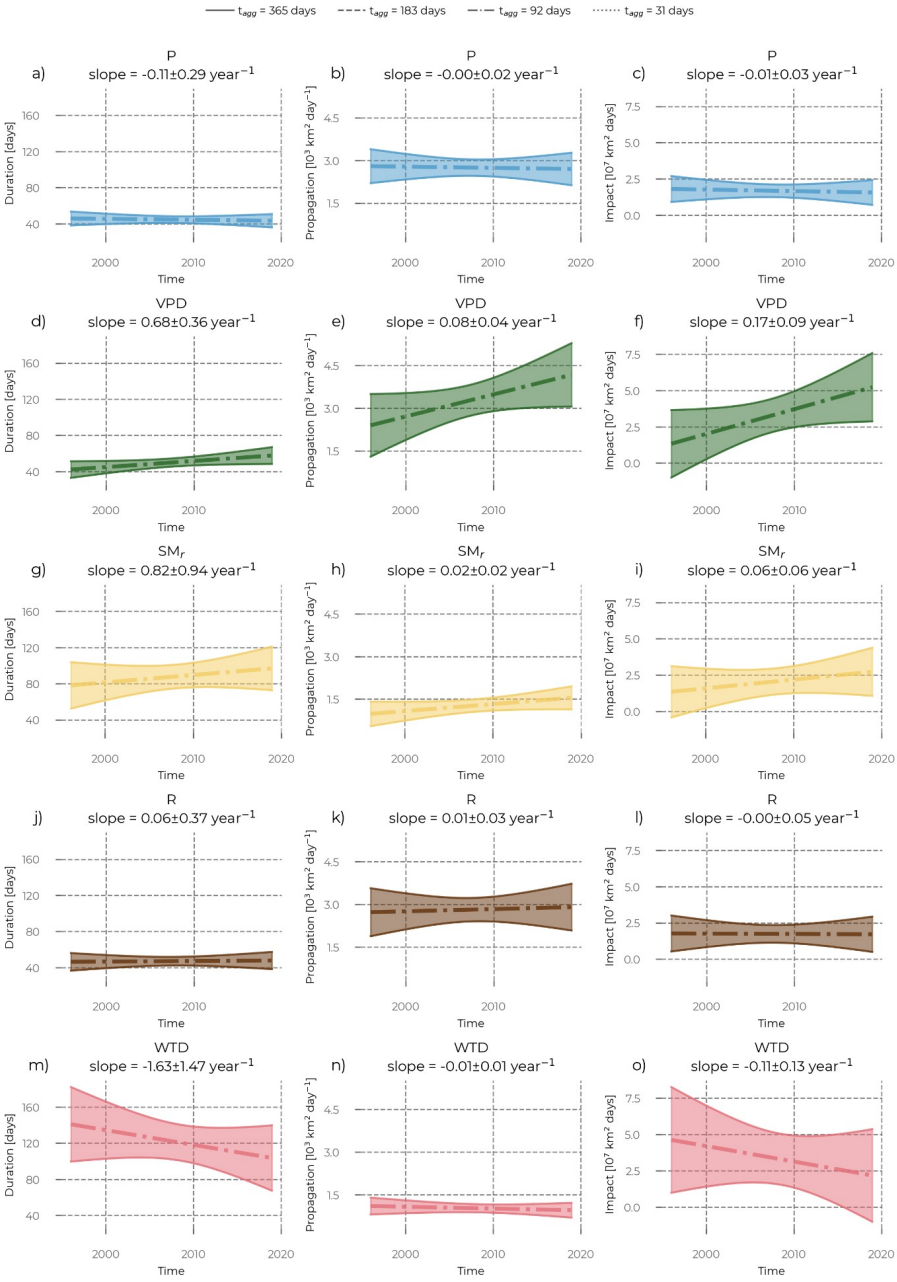

Figure C.10: Temporal trends of the drought event properties (see y-axis label) for precipitation (P), vapor pressure deficit (VPD), runoff (R), and groundwater (per water table depth, WTD) for the 92-day aggregation period. The shaded area around the line is the 95% confidence interval. The exact interception and slope values, including their uncertainty, are given in Table C.1.

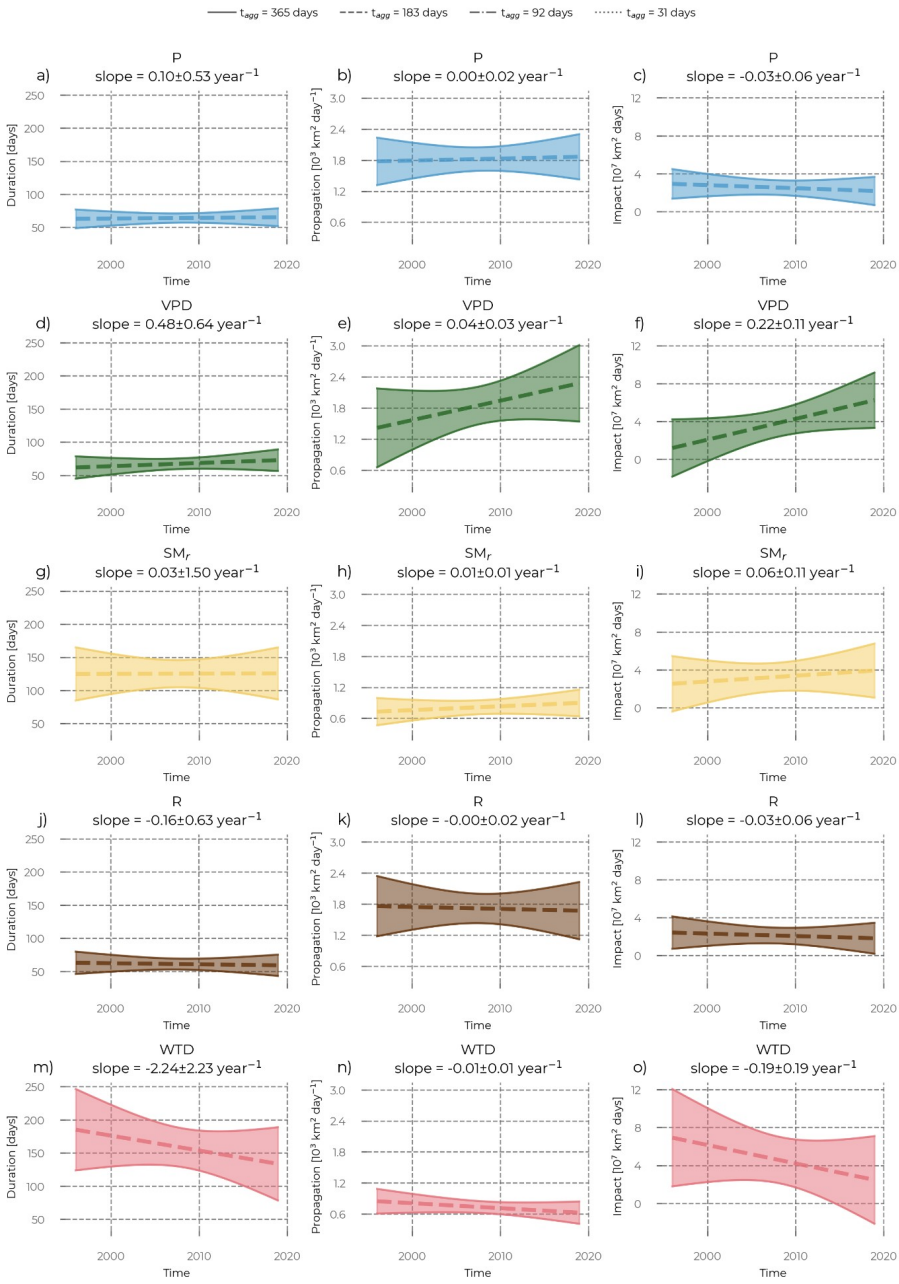

Figure C 11: Temporal trends of the drought event properties (see y-axis label) for precipitation (P), vapor pressure deficit (VPD), runoff (R), and groundwater (per water table depth, WTD) for the 183-day aggregation period. The shaded area around the line is the 95% confidence interval. The exact interception and slope values, including their uncertainty, are given in Table C.1.

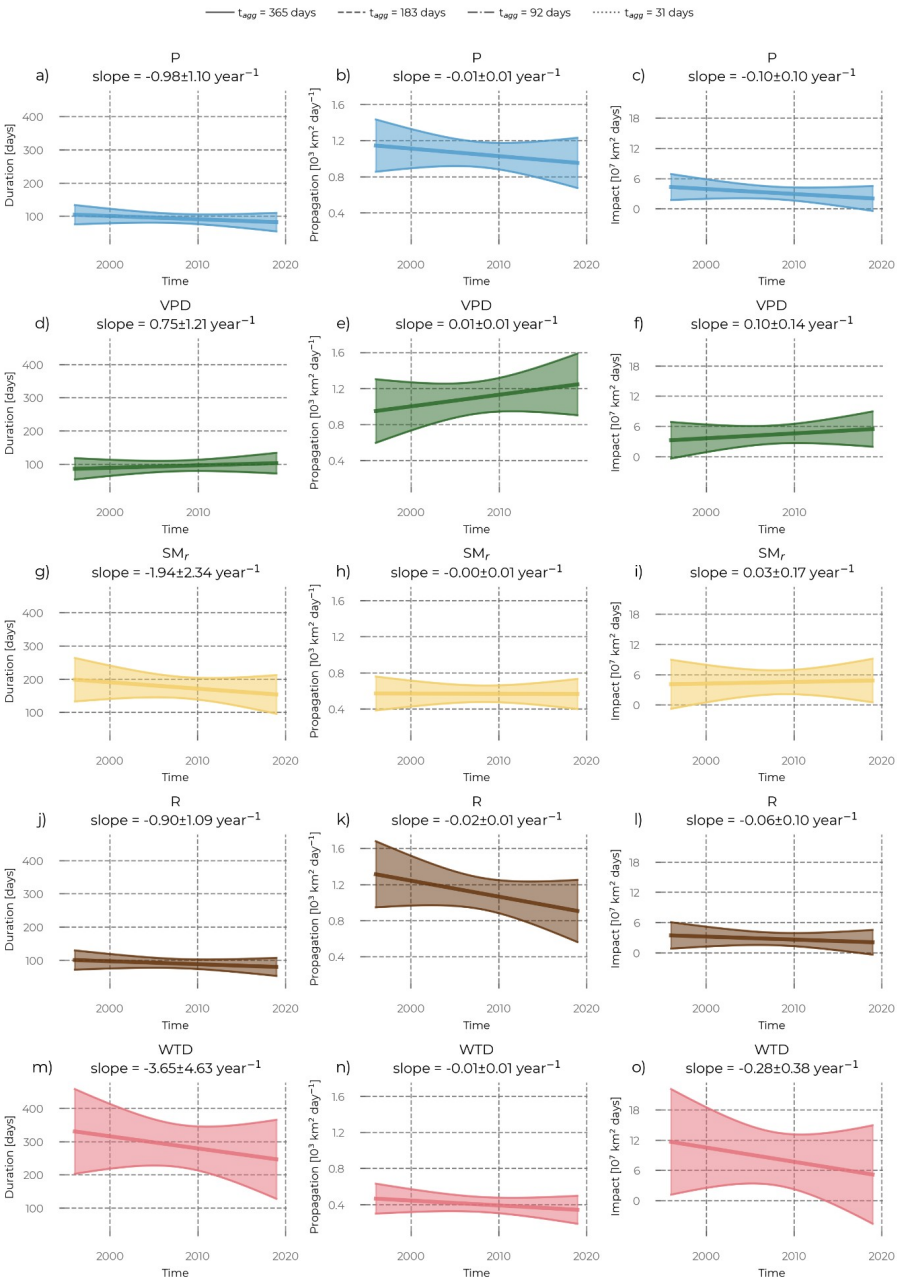

Figure C 12: Temporal trends of the drought event properties (see y-axis label) for precipitation (P), vapor pressure deficit (VPD), runoff (R), and groundwater (per water table depth, WTD) for the 365-day aggregation period. The shaded area around the line is the 95% confidence interval. The exact interception and slope values, including their uncertainty, are given in Table C.1.

Table C.1: Nominal and standard deviations of the determined intercept and slope values of the linear regression for each property (duration, propagation, impact), and each variable (P: precipitation, VPD: vapor pressure deficit, SM_r: rootzone soil moisture, WTD: water table depth), and each aggregation period.

		Duration				**Propagation**				**Impact**			
		intercept		**slope**		**intercept**		**slope**		**intercept**		**slope**	
		nominal	**std**	**nominal**	**std**	**nominal**	**std**	**nominal**	**std**	**nominal**	**std**	**nominal**	**std**
P	**31D**	27,41	2,08	0,13	0,15	6,43	0,67	0,02	0,05	0,97	0,32	0,02	0,02
	92D	45,87	4,09	-0,11	0,29	2,80	0,32	0,00	0,02	1,82	0,48	-0,01	0,03
	183D	63,05	7,40	0,10	0,53	1,77	0,24	0,00	0,02	2,94	0,82	-0,03	0,06
	365D	104,68	14,79	-0,98	1,10	1,14	0,15	-0,01	0,01	4,31	1,31	-0,10	0,10
VPD	**31D**	27,89	2,78	0,32	0,20	8,84	1,43	0,05	0,10	0,93	0,70	0,11	0,05
	92D	41,65	4,89	0,68	0,36	2,34	0,59	0,08	0,04	1,20	1,24	0,17	0,09
	183D	61,64	8,82	0,48	0,64	1,40	0,40	0,04	0,03	1,10	1,58	0,22	0,11
	365D	85,69	16,34	0,75	1,21	0,95	0,18	0,01	0,01	3,23	1,84	0,10	0,14
SM_r	**31D**	34,60	8,93	0,26	0,58	1,25	0,55	0,00	0,04	0,26	0,29	0,02	0,02
	92D	77,45	13,72	0,82	0,94	0,96	0,23	0,02	0,02	1,30	0,94	0,06	0,06
	183D	124,96	20,97	0,03	1,50	0,73	0,14	0,01	0,01	2,50	1,52	0,06	0,11
	365D	198,36	33,21	-1,94	2,34	0,57	0,10	0,00	0,01	4,09	2,47	0,03	0,17
R	**31D**	29,39	2,80	0,19	0,20	4,25	0,60	0,02	0,04	0,83	0,31	0,02	0,02
	92D	46,37	5,18	0,06	0,37	2,72	0,45	0,01	0,03	1,77	0,66	0,00	0,05
	183D	63,13	8,88	-0,16	0,63	1,76	0,31	0,00	0,02	2,44	0,90	-0,03	0,06
	365D	100,42	14,79	-0,90	1,09	1,31	0,19	-0,02	0,01	3,42	1,33	-0,06	0,10
WTD	**31D**	90,64	18,62	-0,32	1,32	1,53	0,19	-0,01	0,01	3,39	1,46	-0,07	0,10
	92D	142,07	21,90	-1,63	1,47	1,11	0,16	-0,01	0,01	4,70	1,93	-0,11	0,13
	183D	186,18	32,09	-2,24	2,23	0,85	0,12	-0,01	0,01	7,02	2,68	-0,19	0,19
	365D	330,33	64,35	-3,65	4,63	0,46	0,08	-0,01	0,01	11,63	5,29	-0,28	0,38

Figure C.13: Maps of mean responses of soil evaporation (E_s) to soil moisture (SM_r, top row) and vapor pressure deficit (VPD, second row) drought events with different aggregation periods (31, 92, 183, and 365 days). The maps in the last row depict the mean E_s response during compound events, i.e., where droughts defined by soil moisture and droughts defined by vapor pressure deficit at impactful aggregation times co-occur.

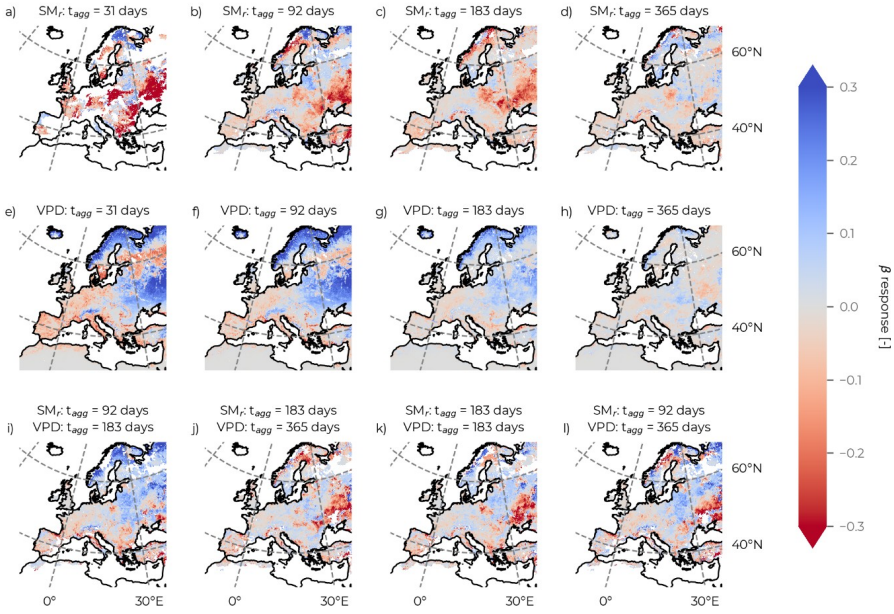

Figure C.14: Maps of mean responses of water stress (β) to soil moisture (SM_r, top row) and vapor pressure deficit (VPD, second row) drought events with different aggregation periods (31, 92, 183, and 365 days). The maps in the last row depict the mean β response during compound events, i.e., where droughts defined by soil moisture and droughts defined by vapor pressure deficit at impactful aggregation times co-occur.

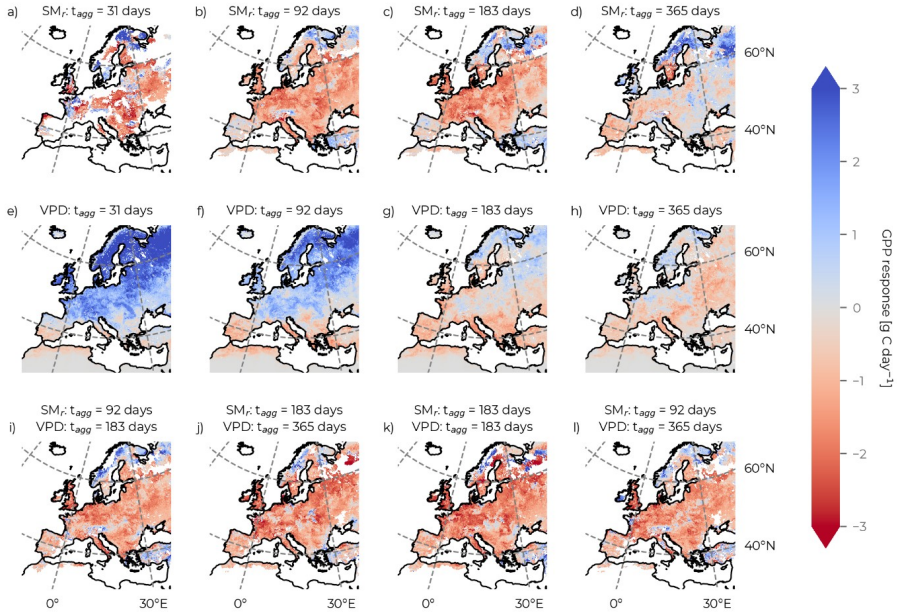

Figure C.15: Maps of mean responses of gross primary production (GPP) to soil moisture (SM_r, top row) and vapor pressure deficit (VPD, second row) drought events with different aggregation periods (31, 92, 183, and 365 days). The maps in the last row depict the mean GPP response during compound events, i.e., where droughts defined by soil moisture and droughts defined by vapor pressure deficit at impactful aggregation times co-occur.

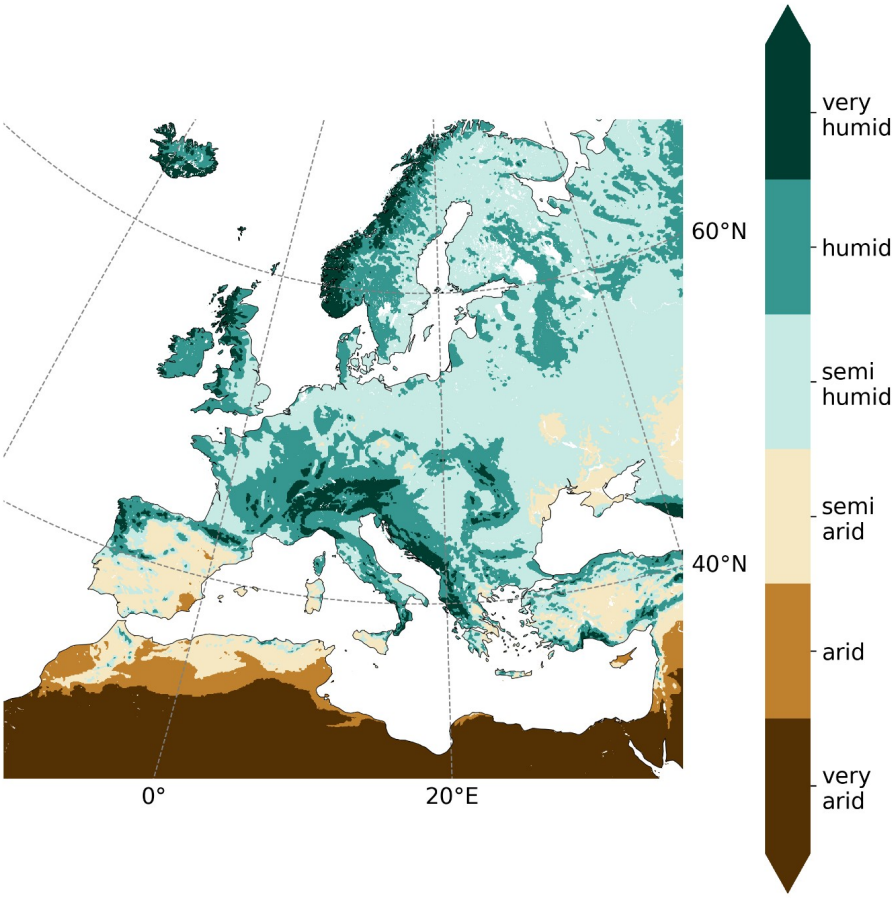

Figure C.16: Hydroclimates are defined by annual precipitation amounts (P_a [mm]). Very humid: $P_a \geq 1200$ mm, humid: $700 \leq P_a < 1200$ mm, semi humid: $500 \leq P_a < 700$ mm, semi arid: $250 \leq P_a < 500$ mm, arid: $100 \leq P_a < 250$ mm, very arid: $Pa < 100$ mm.

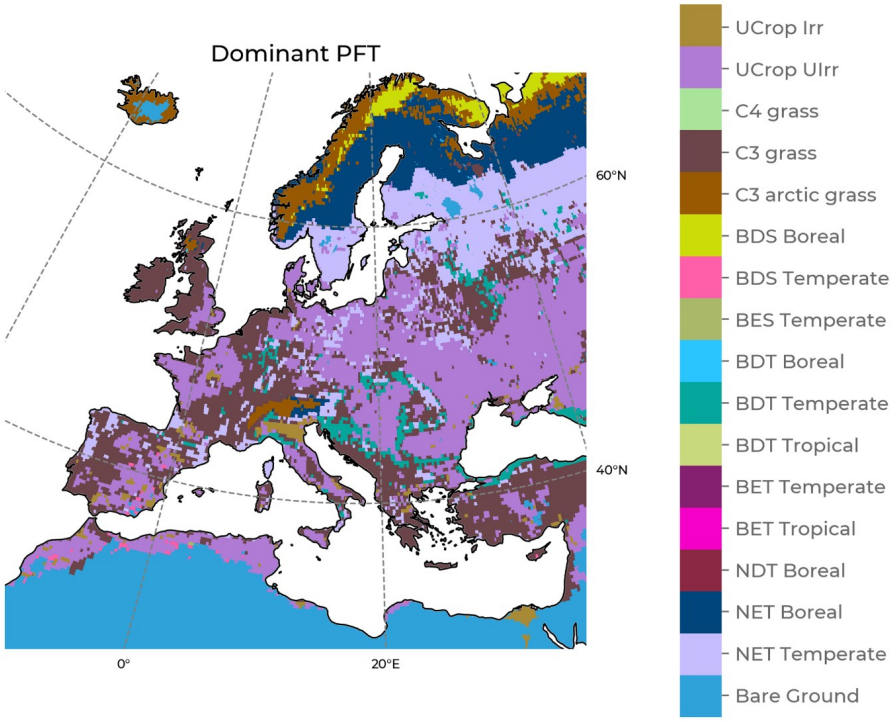

Figure C.17: Map showing the predominant Plant Functional Type (PFT) in the European CLM5 domain. Irr: irrigated. UIrr: Unirrigated, BDS: broadleaf deciduous Shrub, BES: broadleaf evergreen shrub, BDT: broadleaf deciduous tree, BET: broadleaf evergreen tree, NDT: needleleaf deciduous tree, NET: needleleaf evergreen tree.

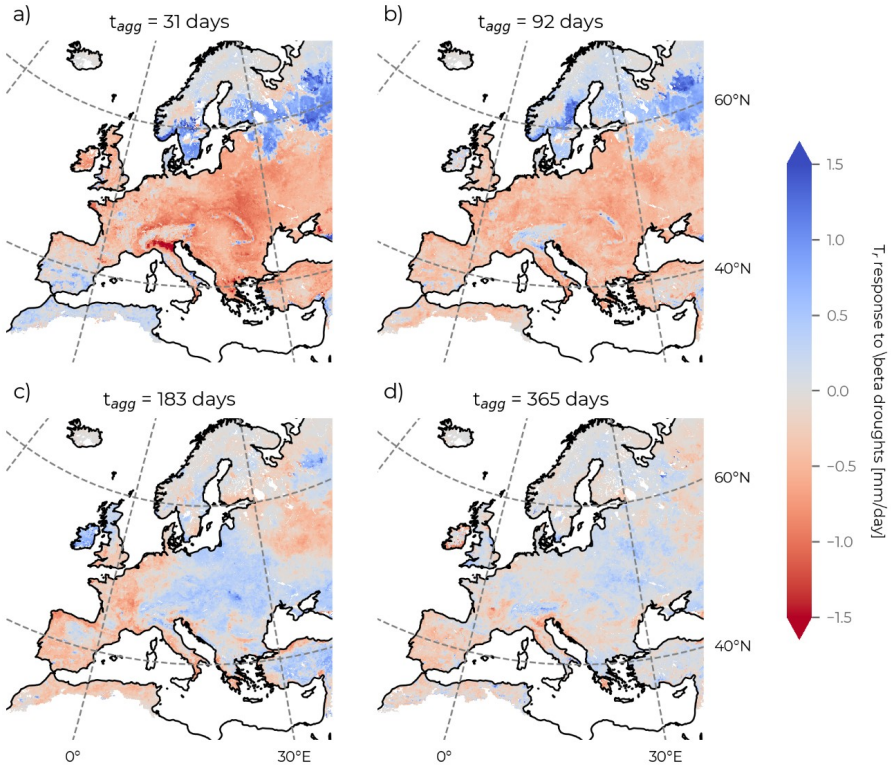

Figure C.18: Responses of transpiration (T_r) to significant water limitation events (β). Each map shows T_r responses to β droughts of a different aggregation period (t_{agg}).

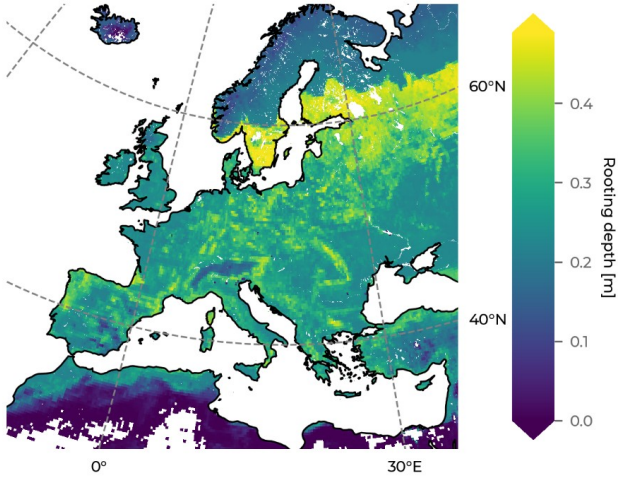

Figure C.19: Mean rooting depth of vegetation across the European CLM5 domain, resulting from rooting depths of present plant functional types weighted by their areal share in the grid cell.

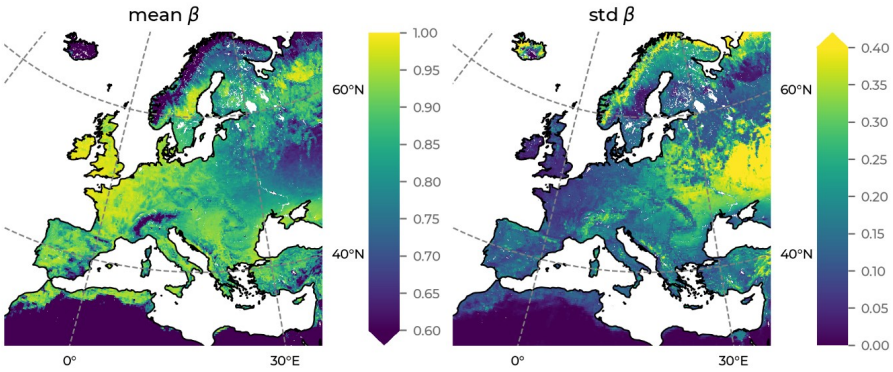

Figure C.20: Maps of the temporal mean and standard deviation of the water limitation (β), a downregulation factor to the stomatal conductance resulting from soil moisture limitation.

Band / Volume 694
Entwicklung von Korrosionsschutzschichten für Protonen-Austausch-Membran-Wasserelektrolyseure
T. Sievert (2026), 201 pp
ISBN: 978-3-95806-888-9

Band / Volume 695
Hierarchical Modeling of Electrocatalytic Reactions from a Local Perspective
X. Zhu (2026), ix, 121 pp
ISBN: 978-3-95806-889-6

Band / Volume 696
Nanocrystalline Silicon Carbide in Transparent Passivating Contact Solar Cells
A. Eberst (2026), xiii, 225 pp
ISBN: 978-3-95806-891-9

Band / Volume 697
Theory of Electronic and Ionic Perturbations at Supported Electrocatalyst Nanoparticles
Y. Zhang (2026), XI, 131 pp
ISBN: 978-3-95806-896-4

Band / Volume 698
Aufbau und Einsatz eines on-board Messsystems zur Untersuchung der Abgaszusammensetzung von Fahrzeugen betrieben mit konventionellen und alternativen Kraftstoffen
V. Polinowski (2026), VIII, 269 pp
ISBN: 978-3-95806-897-1

Band / Volume 699
Ab Initio-based large-scale Atomistic Simulations of Cathode Materials for Secondary Batteries: From Computational Methodologies to Applications towards improved Structural and Chemical Stability
K. Köster (2026), x, 204, x pp
ISBN: 978-3-95806-898-8

Band / Volume 700
Materials Design, Processing and Application of Proton-Conducting Oxides for Electrochemical Energy Conversion
Y. Zeng (2026), vii, 117 pp
ISBN: 978-3-95806-899-5

Band / Volume 701
Accelerating the discovery of alkaline-stable anion exchange membrane materials via computational exploration
F. P. Tipp (2026), xii, 135 pp
ISBN: 978-3-95806-900-8

Band / Volume 702
Methods for Investigating the Structure-Performance Correlation in Membrane Electrode Assemblies
N. Utsch (2026), XIII, 138, LXVII pp
ISBN: 978-3-95806-901-5

Band / Volume 703
Hot-Spot Formation in Cu(In,Ga)Se_2 Thin Film Solar Cells
S. Nofal (2026), xvii, 131 pp
ISBN: 978-3-95806-903-9

Band / Volume 704
Machine Learning Guidance of Manufacturing Process of Solid Oxide Cells
T. Le Dinh (2026), xxi, 122 pp
ISBN: 978-3-95806-904-6

Band / Volume 705
Drivers of spatiotemporal variability of European terrestrial ecosystem processes
C. Poppe Téran (2026), 254 pp
ISBN: 978-3-95806-905-3

Energie & Umwelt / Energy & Environment
Band / Volume 705
ISBN 978-3-95806-905-3

Mitglied der Helmholtz-Gemeinschaft

JÜLICH
Forschungszentrum